UNIVERSITY OF READING

Department of Meteorology

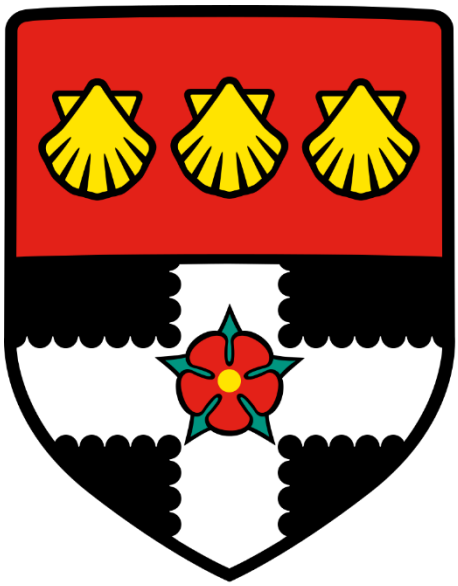

Linking Pollution, Meteorology and Climate Change

Chris Webber

A thesis submitted for the degree of Doctor of Philosophy

February 2017

Declaration of Authorship

I can confirm that this is my own work and the use of all material from other sources has been properly and fully acknowledged.

Chris Webber

Signed: Christopher Paul Webber

Date: 16th February 2017

University of Reading

Abstract

Department of Meteorology

Doctor of Philosophy

By Chris Webber

This thesis examines the relationship between synoptic meteorology and particulate matter (PM10). PM10 is a pollutant of high interest to UK health policy (DEFRA, 2016) and this study evaluates the importance of Rossby wave breaking (RWB) on UK PM10 concentration ([PM10]). RWB can result in atmospheric blocking, which is one extreme of mid-latitude synoptic meteorological variability that favours the accumulation of PM10.

This study finds significant increases ($p<0.01$) in UK Midlands [PM10] resulting from winter-time northeast Atlantic/ European RWB. Furthermore, this study shows that northeast Atlantic/ European RWB increases the probability of exceeding a hazardous [PM10] threshold. We have identified the Omega block as the most hazardous RWB subset, with a probability of exceeding a hazardous [PM10] threshold (0.383) over three times that for days without RWB (0.129).

We have implemented a tracer framework within a Hadley centre Met-Office climate model (HADGEM3-GA4) to identify flow regimes influencing the UK throughout northeast Atlantic/ European RWB events. A present-day HADGEM3-GA4 simulation, nudged to ERA-Interim reanalysis data, is used to verify the tracer framework and to identify the flow regimes influencing Omega block events. This study finds that the advection of European tracer and the accumulation of locally sourced tracer contribute to hazardous [PM10] throughout Omega block events.

This study's principal aim is to determine climatic shifts in both the frequency of synoptic meteorological conditions conducive to UK PM10 accumulation and in the corresponding flow regimes. Using a further two HADGEM3-GA4 simulations, we find a north-eastward climate shift in northeast Atlantic/ European RWB, with an overall reduction in events. Additionally, we find that future RWB events result in significantly ($p<0.01$) increased European and reduced stagnant air masses within the UK. This result indicates a reduced frequency of UK [PM10] exceedances, however a tendency for increased transport of toxic particles from Europe.

Acknowledgements

Throughout the duration of my PhD, numerous individuals have helped me both with my work and personally. I feel it only right to acknowledge these individuals before presenting my work in this thesis. Furthermore, this studentship would not have been possible without funding from NERC, for which I am hugely grateful.

The most influential people throughout my PhD and in the creation of this thesis have been my two PhD supervisors Helen Dacre and Bill Collins. I would like to thank both of you for your input in not only my work, but also my development as a researcher. You have both provided me with exciting opportunities throughout the last three years, be them in York, Italy, or even in the rain at Reading Festival.

I would also like to thank my monitoring committee Nicolas Bellouin and Sue Grimmond. Our meetings were always insightful and I'm hugely grateful for the number of ideas generated from our discussions. Further thanks must go specifically to Giacomo Masato, Laura Wilcox and Ed Hawkins. Your input has contributed at some stage to the generation of this thesis, your help was most welcome!

A big thank you must go to my office in the Lyle tower (ominous), for keeping me sane (absolutely) in the last stages of writing up and for just making work a thoroughly enjoyable place to be. I feel exceptionally privileged to work in such a sociable department, having the right environment outside of work really helped me through the PhD.

Finally on a personal level I would like to thank my family for their support throughout the last three and a half(ish) years. There have been some low times that we have stuck together through, but some really exciting times in the not too distant future that I can't wait to share with you. I would like to mention my grandpa, who passed away last year, you were always hugely supportive of my work and I know you'd have given this thesis your best efforts to read!

I would especially like to thank my wonderful fiancée for her support and sheer perseverance with me through the good times and the low times!

Alan Pardew

"For the last three years I don't know, it's science against me"

Contents

Abbreviations

ACRWB	Anticyclonic Rossby Wave Breaking
AMOC	Atlantic Meridional Overturning Circulation
APE	Available Potential Energy
AQMS	Air Quality Monitoring Site
BENELUX	Belgium Netherlands Luxembourg region
BI	Blocking Index
CEEMD	Complementary Ensemble Empirical Mode Decomposition
CI	Climate Increment
CMIP	Coupled Model Intercomparison Project
CRWB	Cyclonic Rossby Wave Breaking
DB	Direction of Breaking Index
DEFRA	Department for Environment Farming and Rural Affairs
DJF	December, January and February Months
EC	Elemental Carbon
ECMWF	European Centre for Medium-Range Weather Forecasts
EDJ	Eddy Driven Jet
EEA	European Environment Agency
EEMD	Ensemble Empirical Mode Decomposition
EMD	Empirical Mode Decomposition
ERA	ECMWF Re-Analysis
FDMS	Filter Dynamic Measurement System
GP	Grid Point
IMF	Intrinsic Mode Function
MB	Model Bias
M12	Masato et al. (2012)

M13	Masato et al. (2013a)
NMVOC	Non-Methane Volatile Organic Compound
NO_x	Reactive Species of Nitrogen ($NO + NO_2$)
OC	Organic Carbon
PBL	Planetary Boundary Layer
PM	Particulate Matter
PM1.0	Particulate Matter with Aerodynamic Diameter ≤ 1 μm
PM2.5	Particulate Matter with Aerodynamic Diameter ≤ 2.5 μm
PM10	Particulate Matter with Aerodynamic Diameter ≤ 10 μm
PV	Potential Vorticity
PVU	Potential Vorticity Units
RI	Relative Intensity of Air Masses Index
RWB	Rossby Waves Breaking
sim	simulation
SNR	Signal to Noise Ratio
SVOC	Semi-Volatile Organic Compound
TEOM	Tapered Element Oscillating Microbalance
tr	tracer
UK	United Kingdom
UKCA	United Kingdom Chemistry and Aerosol model
VOC	Volatile Organic Compound
WHO	World Health Organisation

Symbols

Symbol	Description	Unit
N	Particle number	
S	Surface Area	m^2
V	Volume	m^3
D	Particle Diameter	m
r	Particle radius	m
V_d	Dry Deposition Velocity	$m\ s^{-1}$
r_a	Aerodynamic Resistance	$s\ m^{-1}$
r_b	Quasi-laminar Resistance	$s\ m^{-1}$
g	Gravitational acceleration	$m\ s^{-2}$
ρ	Density	$kg\ m^{-3}$
ρ_p	Particle Density	$kg\ m^{-3}$
ρ_f	Fluid Density	$kg\ m^{-3}$
μ	Fluid Viscosity	$kg\ m^{-1}\ s^{-1}$
V_s	Gravitational Settling Velocity	$m\ s^{-1}$
γ	Surface Roughness Length	m
R	Rainfall Rate	$mm\ hr^{-1}$
L_m	Mean Mass Scavenging Coefficient	hr^{-1}
p	p-value	

ζ	Absolute Vorticity	s^{-1}
ξ	Relative Vorticity	s^{-1}
u	Zonal Wind Speed	$m\ s^{-1}$
v	Meridional Wind Speed	$m\ s^{-1}$
u	Horizontal Wind Velocity Vector	$m\ s^{-1}$
θ	Potential Temperature	K
φ	Latitude	^{o}N
f	Coriolis Parameter	s^{-1}
a	Radius of Earth ~ 6.3×10^{6} m	m
Ω	Rotation rate of the Earth = 7.29×10^{-5} radians s^{-1}	radians s^{-1}
θ^{*}	Dataset Mean Potential Temperature	K
$\dot{u}$	Frictional Dissipation Term	Pa s
R*	Universal Gas Constant	$8.314\ J\ K^{-1}\ mol^{-1}$
R	Specific Gas Constant for Dry Air	$287\ J\ kg^{-1}\ K^{-1}$

Chapter 1 - Aerosol Pollutants

Atmospheric pollution is one of the biggest challenges currently facing human health. The World Health Organization (WHO) recently linked 1 in 8 global premature deaths to poor air quality (WHO, 2014). This study is focussed on identifying the synoptic meteorology that is responsible for UK pollution episodes and to determine whether this will change in a future climate. The pollutants that are of most interest to UK policy and pose risks to human health are: particulate matter (PM), NO_2 and O_3, as highlighted by The Department for Environment, Food and Rural Affairs (DEFRA) (DEFRA, 2016). This study focusses on synoptic meteorology that influences UK particulate matter (PM) concentrations. No further mention of NO_2 or O_3 will be made throughout this study, however many of the sources that contribute to elevated concentrations on a regional scale are very similar to those for PM, as are the meteorological conditions that are preferable to their accumulation.

1.1 The Pollutant – PM10

Section 1.1 will focus on the chosen pollutant in this study, PM10. PM10 is a subcategory of PM, with an aerodynamic diameter of ≤ 10 μg m^{-3}, approximately a fifth of the diameter of a human hair. The aerodynamic diameter of an aerosol particle is the diameter of a perfectly spherical particle of density 1000 kg m^{-3} that has an equal settling velocity to the measured aerosol particle. This section highlights the complex nature of PM10, detailing the varied PM size distributions for PM number, surface area and volume. Sections 1.2 and 1.3 discuss PM10 sources/composition and PM10 sinks respectively.

When analyzing PM10 variety in the atmosphere, one must first define the criteria for evaluating PM10. The reason for this is because the distribution of PM10 varies for number, surface area and volume. Figure 1.1, from Fig. 1, Heal et al. (2012) shows three different particle size distributions for number (N), surface area (S) and volume (V). The metrics used to quantify the number, surface area and volume of PM are: $\frac{dN}{dlog(D)}$, $\frac{ds}{dlog(D)}$ and $\frac{dV}{dlog(D)}$ respectively, where D represents particle diameter. Each of the three distributions in Fig. 1.1 are log-normal on the x-axis. Without such a log transform, each of the distributions would be positively skewed.

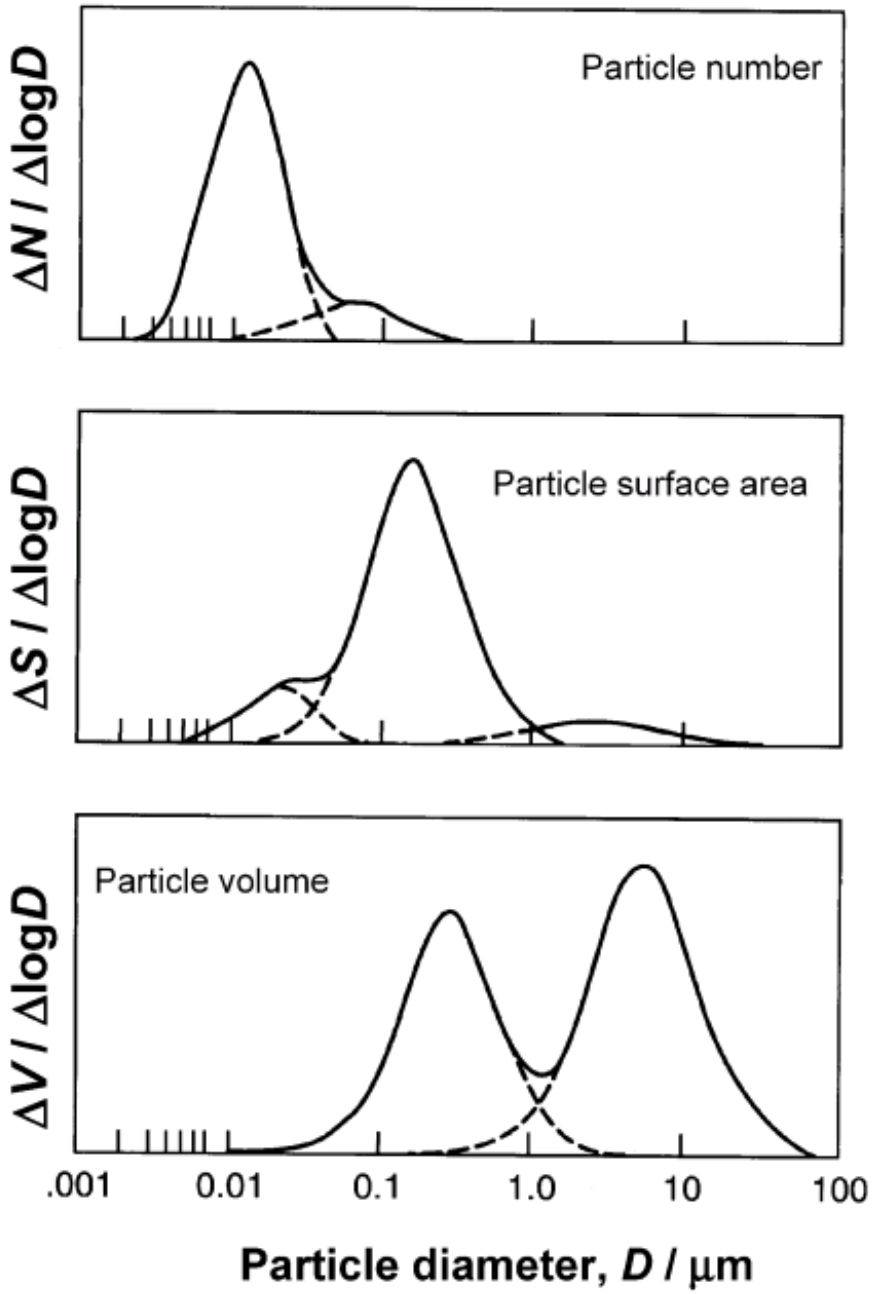

Figure 1.1 Taken from Heal et al. (2012), showing particle number, surface area and volume particulate size distributions, with a logarithmic particle diameter scale on the x-axis. These distributions are typical of an urban environment, characterized by anthropogenic aerosol.

Figure 1.1 shows the number, surface area and volume distributions against log-normal particle aerodynamic diameter. It is immediately evident how different the three distributions are. This section will explain the differences in each of the three size distributions in Fig. 1.1.

The upper panel of Fig. 1.1 shows the PM number size distribution, which is shown by two peaks. The first $\frac{dN}{dlog(D)}$ peak is centred on approximately 0.01 μm and corresponds to

nucleation mode aerosol. Nucleation occurs when a molecule condenses from the gaseous phase to the liquid phase. These nucleation mode particles are numerous within the atmosphere and their primary growth mechanism is coagulation (Kulmala et al., 2004). Coagulation reduces the number of PM particles within the atmosphere, however PM mass remains relatively constant. The second $\frac{dN}{dlog(D)}$ peak in Fig. 1.1 corresponds to Aitken mode particles. The Aitken mode predominantly constitutes of coagulated nucleation mode particles and particles emitted into the Aitken mode. These particles grow as a result of gaseous species condensing onto them or through coagulation (Lushnikov, 2009). In the upper panel of Fig. 1.1, the integrals of the nucleation and Aitken mode particles are comparable and hence contribute in comparative amounts to PM number.

The middle panel of Fig. 1.1 shows the PM surface area distribution, which is shown as a tri-modal distribution. The visually largest peak in Fig. 1.1 is centered on approximately 0.1 μm and can be described as accumulation mode aerosol. Surface area increases with particle radius^2 ($S = 4 \pi r^2$), however when multiplied by the particle number distribution in the upper panel of Fig. 1.1, the greatest particle surface area can be seen for the accumulation mode aerosol. A second peak, the integral of which is comparable (comparable due to the log-normal x-axis) to that for the accumulation mode aerosol is seen for coarse mode PM (diameter > 1 μm). It will be highlighted in Sect. 1.7 how PM with increased surface area is associated with a greater toxicity to humans. Consequently, the surface area peak in Fig.1.1 for coarse mode particles is of importance when considering the impact of PM10 on human health.

The lower panel in Fig. 1.1 represents the PM volume distribution. The PM statistic analysed in this study is PM concentration, which is determined from its mass. The particle mass distribution is comparable to that for PM volume in the lower panel of Fig. 1.1. Figure 1.1 shows that PM mass/volume is dominated by two peaks in the size distribution. These are in the accumulation mode and the coarse mode, the latter with a far greater integral (due to the log-normal x-axis). Therefore, in this study [PM10] will likely be influenced most greatly by coarse mode particles, with some influence from accumulation mode particulates.

1.2 PM10 Composition and Sources

PM10 is comprised of a number of different components, which are all unique in their size, lifetime and toxicity to humans. This section will describe some of the major components of UK PM10. Fig. 1.1 shows a common $\frac{dV}{dlog(D)}$ distribution for PM. Within this distribution there exist two peaks, one in the accumulation mode and one in the coarse mode. The

composition and the toxicity of PM in each peak is markedly different (Sect. 1.7). This study focusses on [PM10], which as Sect. 1.1 highlighted, is dominated by PM at these two distinguished peaks.

To evaluate PM sources throughout the UK, Yin and Harrison (2008) undertook a PM source attribution study for the UK Midlands region. Yin and Harrison (2008) evaluated PM composition in an urban environment within Birmingham, UK. Table 1.1 presents the results of monitored PM component analysis at Birmingham Central by Yin and Harrison (2008) for 2004 -2005.

Table 1.1 PM components at a UK Midlands urban background air quality monitoring site, Birmingham Central from Yin and Harrison (2008). The PM component mean and standard deviations are calculated for the 2004-2005 period. OC, EC, Cl^-, SO_4^{2-}, NO_3^-, Ca and Fe represent organic carbon, elemental (black) carbon, chloride, sulfate, nitrate, calcium and iron respectively. PM10, PM2.5 and PM1.0 represent Particulate Matter with an aerodynamic diameter of: ≤ 10 μg m^{-3}, ≤ 2.5 μg m^{-3} and ≤ 1.0 μg m^{-3} respectively.

Yin and Harrison (2008)	Concentration (μg m^{-3}) (Mean ± Standard Deviation)									
	PM10	PM2.5	PM1.0	EC	OC	Cl^-	SO_4^{2-}	NO_3^-	Ca	Fe
Birmingham Central	23.9 ± 11.2	16.0 ± 11.2	12.0 ± 6.7	3.8 ± 2.0	4.6 ± 2.6	0.8 ± 0.96	2.4 ± 1.69	1.7 ± 2.41	0.36 ± 0.14	1.08 ± 0.55

Table 1.1 highlights the dominant PM components that influence Birmingham, in the UK Midlands. Shown are the mean concentrations for PM10, PM2.5 and PM1.0, otherwise termed coarse, fine and ultrafine PM. Furthermore Table 1.1 presents the dominant organic and inorganic species which constitute PM10.

PM component analysis was undertaken by Querol et al. (2004) for four urban background PM10 receptor sites in London and Birmingham, including the site used by Yin and Harrison (2008). Table 1.2 shows the results of the study undertaken by Querol et al. (2004). Additional literature aids in the understanding of the composition of pollution within UK urban environments.

Table 1.2 PM components at four UK Midlands urban background air quality monitoring sites in London and Birmingham from Querol et al. (2004). The PM component mean is calculated for the 1998-2002 period. OC, EC and SIA represent organic carbon, elemental (black) carbon and secondary inorganic aerosol. PM10 and PM2.5 represent Particulate Matter with an aerodynamic diameter of: ≤ 10 μg m^{-3} and ≤ 2.5 μg m^{-3} respectively. Each PM component has been divided into a PM10 component and PM2.5 component.

Querol et al. (2004)	Concentration (μg m^{-3}) (Mean)				
Constituent	Total	OC + EC	Mineral dust	Sea salt	SIA
PM10	24	6	2	0.2-0.5	9
PM2.5	19	5	1	0.2-0.5	8

Table 1.2 supports the findings made from the study by Yin and Harrison (2008) in Table 1.1. From both studies it is clear that organic carbon (OC), elemental carbon (EC) and secondary inorganic aerosol (SIA) are major constituents of UK (London and Birmingham) PM10 and PM2.5. In both of the above tables, mean OC + EC concentrations are at least 25% of the mean [PM10] and mean total SIA concentrations such as sulfate (SO_4^{2-}) and nitrate (NO_3^-) contribute over 15% to mean [PM10]. This section will introduce each of the PM components listed in Tables 1.1 and 1.2 and detail the dominant UK sources, with help from the receptor source modelling study undertaken by Charron et al. (2013).

Elemental Carbon (EC) – EC is produced from the incomplete combustion of organic matter. EC is a large byproduct of biomass burning and the anthropogenic burning of fossil fuels. Charron et al. (2013) show that the dominant EC sources to the UK are from industrial areas of mainland Europe. An important characteristic of EC is that it has the longest atmospheric lifetime of any PM component listed in Table 1.1. This characteristic allows for EC to be transported large distances into the UK, such as from Eastern Europe.

Organic Carbon (OC) – OC describes a wide variety of PM components and can principally be dissected into primary and secondary OC. Primary OC, like EC is emitted directly from

the combustion of organic fuels. Furthermore, primary OC is also emitted from vegetation degradation and pollen. Naturally sourced primary OC is a much larger in size than OC from combustion and secondary OC. Secondary OC is formed through gas-aerosol transformations, through either nucleation or condensation of gaseous vapors onto existing aerosol. Volatile organic compounds (VOCs) are compounds which can oxidize to form semi-volatile organic compounds (SVOC) that condense to form aerosol from gaseous molecules, at temperatures below the molecules boiling point. Below this temperature, vapor pressure decreases and the vapor is more likely to condense onto a solid or liquid surface.

Mineral Dust – Mineral dust accounts for fine fragments of the Earth's lithosphere that are mechanically suspended by surface winds. Mineral dust can comprise of an array of elements, but Table 1.1 highlights two of the major components in Birmingham, UK. These two components of mineral dust are Ca and Fe. Yin and Harrison (2008) attribute the calcium salts in the Birmingham Central monitoring site to a mixture of construction/ demolition dusts and wind-blown soil. Iron dust was attributed mainly to the presence of wind-blown dust, as it was found at greater concentrations in rural environments near agricultural land. Mineral dust is larger (in size) than any of the PM components listed is this section. This characteristic inhibits the long-range transport of mineral dust from Europe into the UK, due to increased dry deposition rates (Sect. 1.3.1).

Marine/Sea Salt – Identified predominantly through elevated NaCl concentrations, however often include other ionic components such as: K and Ca. Sea salt is a considerable component of PM10 within the UK. Sea salt is generally suspended through the bursting of air bubbles at the ocean's surface and from the sea spray of breaking waves. Querol et al. (2004) find that the sea salt component of PM10 is small for the urban environments of London and Birmingham (Table 1.2). This result bares significance for Sect. 1.6, where the importance of a reduced marine influence is emphasized in the choice of this study's PM10 receptor sites.

Secondary Inorganic Aerosol (SIA) – SIA as a component is dominated within the UK by ammonium nitrate and ammonium sulfate salts. Yin and Harrison (2008) present the ionic concentrations of $SO_4^{2-}$and NO_3^- within the UK and these two components are comparable to the concentration of either OC or EC in the Birmingham urban region. Charron et al. (2013) identify that the greatest sources of $SO_4^{2-}$and NO_3^- throughout Europe are from the mainland European industrial regions. A subtlety is also seen here, as particulate NO_3^- has been attributed to more local sources than SO_4^{2-}, whose emissions are dominant throughout East Europe. Ammonia (NH_4^+) is the ion that neutralizes the majority of $SO_4^{2-}$and NO_3^- within the

UK, subsequently sequestering them within ammonium nitrate (NH_4NO_3) and ammonium sulfate $(NH_4)_2SO_4$. The dominant region of ammonia emission throughout Europe is the Belgium-Netherlands-Luxembourg (BENELUX) region. Ammonia is produced predominantly through agriculture and as the BENELUX region is one of the most agricultural regions of Europe, this region is of great importance in the generation of SIA to the UK. SIA salts are some of the smallest (in size) PM components within the troposphere and hence have the ability to transport from Europe into the UK. SO_4^{2-} and NO_3^- are of great importance within this study and subsequently have been described in more detail below.

Sulfate Aerosol (SO_4^{2-}) – Sulfate aerosol is predominantly formed through anthropogenic activities. Predominantly, European SO_4^{2-} is formed from the heterogeneous oxidation of anthropogenically generated SO_2, to form SO_4^{2-}. SO_2 is primarily sourced from the combustion of sulfur rich fuels, such as coal and oil. Historically, industrial emissions are associated with high SO_2 emissions, however shipping emissions are also a major source, surrounding the UK. Natural sources of SO_4^{2-} aerosol are through the oxidation of di-methyl sulfide, which is naturally emitted from the oceans and through volcanic activity.

Nitrate/Nitric Acid – Nitric acid is formed following the oxidation of reactive nitrogen oxides (NO_x). NO_x can be produced either naturally or anthropogenically. In Europe, the majority of NOx in the troposphere is generated anthropogenically. Anthropogenic sources include the combustion of fossil fuels and biomass burning. Nitric acid can condense onto existing aerosol, however the majority of atmospheric NO_3^- concentration in Europe is found sequestered in ammonium nitrate. Natural NO_x sources include the oxidization of the mostly inert gas N_2 by lightning, due to the high temperatures associated. Natural sources also include emissions from soils and from biomass burning (a natural and anthropogenic source).

1.3 PM10 Sinks

Section 1.2 highlighted the diverse nature of PM10, with many PM components contributing to PM10. It is therefore unsurprising that several loss mechanisms exist in the atmosphere for the varied PM components. PM10 is predominantly removed from the atmosphere through: wet and dry deposition and phase-state changes. This section will discuss each of the loss mechanisms that influence the ambient tropospheric mass of PM10.

1.3.1 Dry Deposition

Dry deposition is a process that influences all of the PM components mentioned in Sect. 1.2. It is a process whereby atmospheric pollutants are adhered to the Earth's surface through direct contact. The rate at which PM is removed from the atmosphere through dry deposition

can be determined through a flux, which is multiplicative between PM concentration and a dry deposition velocity. Equation 1.1 describes the calculation of dry deposition velocity (V_d) as used by Wesely and Hicks (1977). Dry deposition velocity can be viewed as a series of resistances ($\frac{1}{r_a+r_b+r_a r_b V_s}$) with the gravitational settling velocity (V_s) in parallel.

$$V_d(m\ s^{-1}) = \frac{1}{r_a + r_b + r_a r_b V_s} + V_s \qquad Eq.\ 1.1$$

Where:

r_a = aerodynamic resistance

r_b = quasi-laminar resistance

V_s = gravitational settling velocity

V_d = dry deposition velocity

For all particles, an increased weight is associated with an increased dry deposition velocity and this is evaluated in V_s. V_s takes into account the forces acting on a particle in the atmosphere. Ambient PM undergoes: gravitational, drag and buoyancy forces, with the latter two opposing the former. Eq. 1.2 shows the calculation of V_s (adapted from Maxey 1987), whereby all three of these forces (gravitational, buoyancy and drag) are considered. It is shown that the larger the particle, the faster it will fall to the Earth surface, however a more viscous surround fluid can act to inhibit this motion.

$$V_s(m\ s^{-1}) = \frac{gD^2(\rho_p - \rho_f)}{18\mu} \qquad Eq.\ 1.2$$

Where:

g = acceleration due to gravity = 9.81 m s^{-2}

D = particle diameter (m)

ρ_p= density of particle (kg m^{-3})

ρ_f= density of fluid (kg m^{-3})

μ = fluid viscosity (kg m^{-1} s^{-1})

V_s = gravitational settling velocity (m s^{-1})

In Eq. 1.1 it can be seen how three resistances are added in series ($\frac{1}{r_a+r_b+r_a r_b V_s}$), which all impact on the rate of dry deposition. The first resistance (r_a) represents the aerodynamic resistance to particle deposition. As the turbulence of the fluid surrounding the particle is

increased, r_a is increased. An increased turbulence provides the vertical movement of air, which aids to suspend an ambient particle (Hicks et al., 1987). Atmospheric turbulence can be seen to increase due to synoptic scale meteorological conditions, however also due to the land surface over which the particle is situated. Rougher land surface (trees, tall buildings) result in greater roughness lengths and an enhanced turbulence in the lower atmosphere, therefore supporting the suspension of ambient particles.

The second resistance term in Eq. 1.1 is the quasi-laminar resistance term (r_b). This term relates to the transport of particulates through a quasi-laminar surface adjacent to any surface that the particle will deposit on to (Wesely and Hicks, 1977). For particles, the r_b term depends on three collection efficiencies. These are the collection efficiency for: Brownian diffusion, interception and impaction. All of these properties are found to increase with increased surface roughness of the surface that the particles are being deposited onto. An increased roughness aids in increasing the turbulence of the air surrounding the surface and helps to increase transport through the quasi-laminar surface. In addition to increased roughness, a simple increase in the surface area on which the particulates are deposited onto, will increase the dry deposition velocity through all of these mechanisms. For example, dense vegetation will collect a far greater quantity of PM and atmospheric gasses than a smooth land surface, such as ice.

Particle size also impacts on the collection efficiency of: Brownian diffusion, impaction and interception. For very small particles (< 10^{-1} μm), Brownian diffusion is an efficient mechanism by which particles are transported across the quasi-laminar surface (Wesely and Hicks, 1977). Above this size, Brownian diffusion becomes less important and the mechanisms of interception and impaction become more important. These mechanisms are seen to be most important for particles > 10^{0} μm. Between 10^{-1} μm and 10^{0} μm, none of the aforementioned collection efficiencies are greatly effective and hence the dry deposition velocity for these particles is found to be at its lowest. Figure 1.2 represents this relationship graphically, from Slinn (1967).

The third resistance term in Eq. 1.1 ($r_a r_b V_s$) is a purely statistical term, which relates to the covariance between the three resistances: r_a , r_b and V_s. This term has no physical meaning, however is necessary in the calculation of V_d (Wesely and Hicks, 1977).

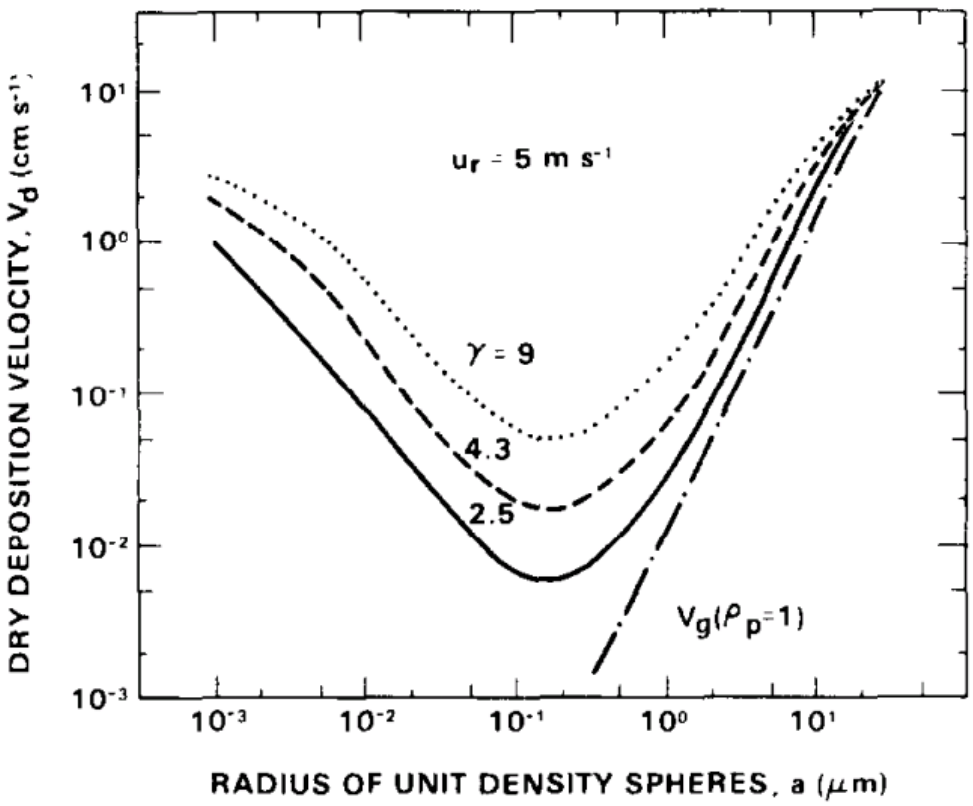

Figure 1.2 Variation of dry deposition velocity (V_d) with log-normal particle radius from Slinn, (1967). The dependence is shown over three land surface roughness lengths (γ) and at a horizontal wind velocity of 5 ms^{-1}. The dependence of dry deposition velocity on particle radius is also shown for a particle with specific density (ρ_p) = 1. Also shown is the gravitational settling velocity (V_g) of a particle with specific density = 1.

In Fig. 1.2 the lowest dry deposition velocities are seen for PM $\approx 10^{-1}$ μm. This particle size relates to accumulation mode PM. Low dry deposition velocity enables for a longer atmospheric lifetime and greater probability of longer range atmospheric transport before being deposited.

1.3.2 Wet Deposition

Wet deposition provides a very effective loss mechanism for PM throughout the atmosphere (Seinfeld and Pandis, 2006). PM is removed from both within the cloud layer and below the cloud layer through rainout and washout respectively. Washout refers to the impaction of rain droplets with aerosol particles below a cloud. Rainout refers to the condensation of water on aerosol particles and the subsequent loss of these particles to the Earth surface through precipitation. Within a cloud, the majority of hydrophilic aerosol present are removed through the rainout mechanism (Jylhä, 1999). This property makes in cloud scavenging of PM more efficient than below cloud scavenging for hydrophilic aerosol (Andronache, 2003). Below the

cloud, washout is the most effective wet deposition mechanism for hydrophobic aerosol. Figure 1.3 presents the mean mass scavenging coefficient for PM below precipitating clouds.

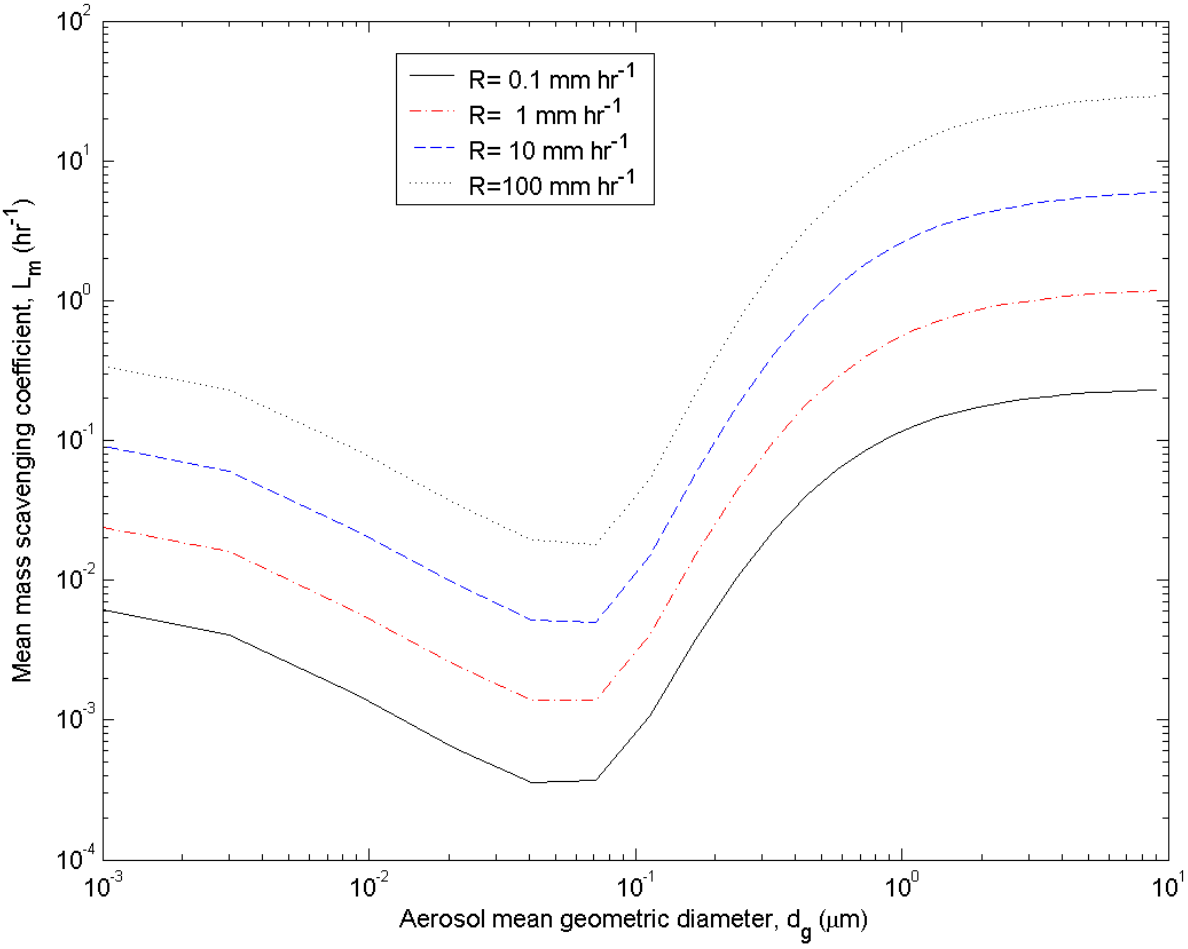

Figure 1.3 Variation of below cloud scavenging coefficient (L_m) with log-normal particle diameter (d_g) from Fig. 4 by Andronache (2003). Four lines are shown, which represent four rainfall rates (R); 0.1 mm hr^{-1} (black), 1 mm hr^{-1} (red), 10 mm hr^{-1} (blue) and 100 mm hr^{-1} (grey).

Figure 1.3 shows the aerosol mean mass scavenging coefficient with respect to aerosol diameter. The mass scavenging coefficient represents the rate at which wet deposition removes aerosol mass from the atmosphere through washout below the cloud. Most evident in Fig. 1.3 is that increasing rainfall rates, much like for in cloud scavenging, increase the below cloud mean mass scavenging coefficient.

Much like for dry deposition, in Fig. 1.3 it is seen that the lowest scavenging coefficient for

all precipitation rates, representative of the lowest PM loss rates through wet deposition, are seen for PM ~ 10^{-1} μm. The similarity in relationship between mass scavenging coefficient and aerosol diameter and dry deposition velocity and aerosol diameter is due to the driving mechanisms being essentially the same. The role of Brownian motion, impaction and interception (of aerosol and rain droplets) play an intrinsic role in the relationship between both scavenging coefficient and dry deposition velocity, and aerosol diameter.

At aerosol diameters less than approximately 10^{-1} μm there exists an increase in mean mass scavenging in Fig. 1.3. This relationship is driven by an increase in Brownian motion in smaller particles, which increases the rate of impaction with rain droplets below clouds.

Aerosol diameters > 10^{-1} μm show an increasing mean mass scavenging coefficient in Fig. 1.3. This relationship is driven by an increase of both impaction and interception of aerosol particles with rain droplets. The principle is simply that the greater aerosol cross-sectional area facilitates a greater probability of intercepting a rain droplet.

1.3.3 State Changes

Temperature increases the rate of the oxidative processes that help to form SO_4^{2-} and NO_3^-, NH_4^+ aerosol and VOCs. In addition to affecting the reaction rates of these reactions, temperature can also affect the atmospheric concentration of semi-volatile PM components. SVOCs are a PM component with high vapor pressures and subsequently low boiling points. The low boiling points of the compounds causes them to evaporate and hence change state at temperatures experienced within the lower troposphere. SVOCs comprise a not insignificant quantity of total OC (Castro et al., 1999), within the UK. Castro et al. (1999) highlight that the greatest UK Midlands OC concentrations are seen throughout the winter months, due to increased SVOC concentration with reduced temperature. This mechanism is one of the reasons why the colder winter months (DJF) are analyzed in this study.

1.4 PM10 Monitoring Techniques

In recent history, there have been a number of changes in the methods used to monitor atmospheric PM10 from in-situ air quality monitoring sites (AQMS's). Due to the relatively rapid advancements that have been made to PM10 monitoring techniques, there currently exist a vast array of operational instrumentation dedicated to determining the mass and concentration of surface PM10. The section will introduce the instrument from which measured PM10 was obtained in this study, the Tapered Element Oscillating Microbalance (TEOM). Additional analysis of the Filter Dynamics Measurement System (FDMS)

instrument will be added, as this highlights a systematic underrepresentation of measured PM10 associated with the TEOM.

1.4.1 TEOM and FDMS Methods

The most commonly used instruments to measure PM10 concentration ([PM10]) throughout the UK are the TEOM and FDMS. The TEOM calculates the air volume entering the instrument, driven by a pump. To measure PM10 mass within the instrument, the TEOM uses a glass rod that is vibrated to its natural frequency. PM10 is then deposited on this glass rod and due to the additional mass of the PM10 on the glass rod, the vibrational frequency changes. The dependency of vibrational frequency on additional mass is calculated empirically, so that when the PM10 sample has deposited on the glass rod an accurate estimate of the corresponding PM10 mass can be obtained. To ensure that only PM10 particles are measured an inlet filter removes all particles larger than 10 μm in diameter. With knowledge of PM10 mass and the volume of air through the instrument inlet, [PM10] can be calculated.

The TEOM instrument is subject to a negative instrumental PM10 mass bias and this negative bias was addressed by Green et al. (2009). It was found that at the operating temperature of the TEOM, there was a substantial loss of semi-volatile PM10 components. As these evaporated from the sample, there was a systematic underestimation of PM10 mass that was initially dealt with using correction factors. These correction factors are not dependent on atmospheric condition and therefore not dependent on atmospheric temperature, the variable with the greatest impact on the evaporation of semi-volatile PM10 components. Subsequently, an alternative is required, which Green et al. (2009) addressed with the FDMS.

The common alternative to the TEOM in the UK is the FDMS. The FDMS is based on the TEOM, however it includes an air conditioning unit at the inlet. Such a system restricts the loss of semi-volatile PM10, which is dependent on temperature. In this study all measurements were obtained from TEOM instruments, following a correction being applied by UK-AIR DEFRA, to account for the lost semi-volatiles (Green et al., 2009). It was the intention of this study to use FDMS measurements, due to the advantages in retaining semi-volatile PM10 highlighted by Green et al. (2009). Unfortunately the period of FDMS measurements does not cover the entirety of this study's PM10 dataset and therefore for consistency, a single instrument was used throughout the time-series.

1.5 Monitoring Site Classifications

An in-situ AQMS can be potentially exposed to a number of stationary and mobile PM10

sources. Which of these sources influence the site regularly is determined by the location of the AQMS. The location of an AQMS is evaluated by a site classification, of which there are many subdivisions, but four primary classifications. These are: rural, urban background, industrial and roadside sites. This study is health motivated and as such a monitoring site classification that is representative of the regions of the UK with the greatest population is appropriate. From the 2011 UK census (Office for National Statistics, 2013), 83% of the UK's population was situated within urban areas. Consequently, urban AQMSs are chosen to obtain PM10 in this study. Also of importance is that each AQMS chosen is representative of the concentration of a large area and not greatly influenced by one local source. The urban background AQMS classification is appropriate for both of these criteria and Sect. 1.5.1 will outline the criteria for an urban background AQMS, as defined by DEFRA (2014b).

1.5.1 Urban Background Sites

Urban background AQMSs are situated within urban areas, however as they are described as background sites, they are subject to restrictions in their placement:

- Not influenced significantly by a single point source or road.
- Representative of several square kilometers.
- Urban areas are defined by the building-up of the front sides of building, with at least two floors.
- Must be representative of all the sources upwind, i.e. all traffic, combustion sources and residential activity.

Urban background sites should fundamentally represent the atmospheric pollutant that the UK's urban population is inhaling on a daily basis and as stated within the criteria from DEFRA (DEFRA, 2014b), not influenced by a single source. Despite urban background sites being positioned so that they are not influenced by individual point sources, local sources may occasionally impact these sites. This study aims to gather measured [PM10] that is representative of an urban area and not of individual point sources. It is therefore important that individual point sources are removed, as these are not representative of the entire urban area. The method of removing interfering PM10 point sources from PM10 datasets is discussed in Sect. 1.6.3, through a data validation method.

1.6 UK Midlands Tri-Site Supersite

Urban background sites were chosen as the AQMS site classification used to obtain UK Midlands [PM10] in this study. The UK Midlands provide a site that is not overly sensitive

to either maritime westerly flow (See sea salt component in Table 1.2) or continental easterly flow. Furthermore, it is important that the UK region chosen has a comprehensive PM10 monitoring network, which we could use to validate PM10 from individual sites. Within the UK Midlands there exists a sufficient urban background PM10 monitoring network to enable the generation of a UK Midlands representative urban background PM10 dataset. Three sites were selected within the UK Midlands and these are outlined in Sect. 1.6.1. Obtaining [PM10] from a number of AQMSs provided the opportunity for cross-site validation, which is presented in Sect. 1.6.3. This validation process enables the removal of PM10 influenced directly by point sources from each individual site and therefore provides a PM10 dataset that is most representative of the urban background UK Midlands region.

1.6.1 Contributing Sites

Within the UK Midlands region, three urban background sites were chosen to obtain [PM10] from (DEFRA, 2014a). These sites were chosen, because these sites had almost continuous daily-mean data for the time period of this study, winter months (DJF) from January 1999 to December 2008. The three sites chosen are: Birmingham Central, Leicester Central and Leamington Spa. The daily-mean [PM10] ($\overline{[PM10]}$) at each UK urban background site is: Birmingham Central 20.26 μgm^{-3} (ln[PM10] = 3.01), Leicester Central 18.62 μgm^{-3} (ln[PM10] = 2.92), Leamington Spa 18.63 μgm^{-3} (ln[PM10] = 2.93). In this study, the motivation for using three urban background AQMS's is to enable a comparison between each of the sites. By comparing each of the three PM10 datasets, PM10 spikes at each site can be identified and removed.

1.6.2 Data Availability

One of the primary criteria for the selection of the three AQMS's shown in Sect. 1.5.1 was the data availability throughout the time period of this study (DJF 1999-2008). Fig. 1.4 shows three time-series, for each of the urban background AQMS's introduced above. Above each of the time series shown in Fig. 1.4 is the percentage of available data from the 10 years of DJF data.

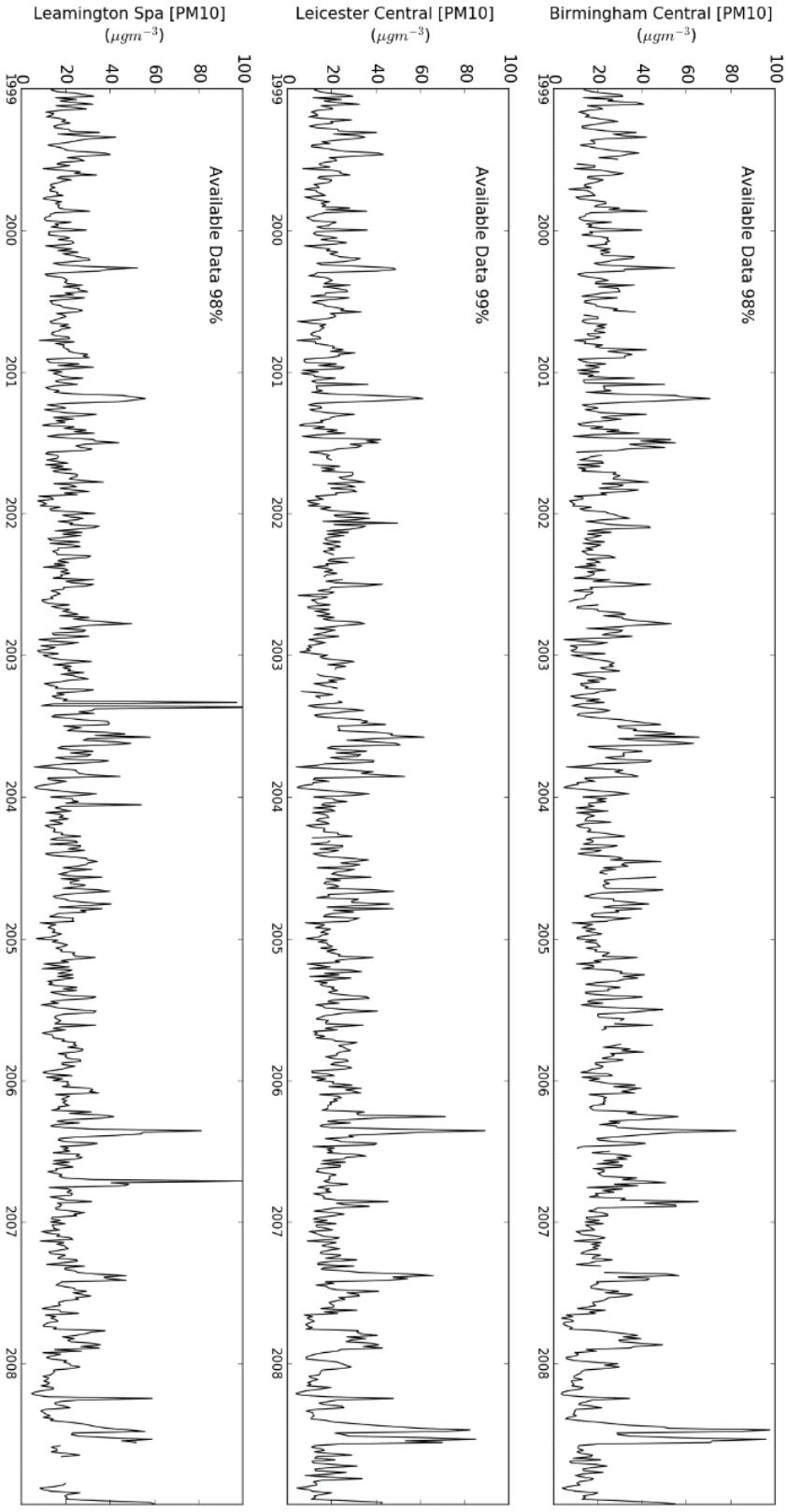

Figure 1.4 10 year (January 1999- December 2008) winter (DJF) PM10 datasets for UK Midlands three urban background AQMSs: Birmingham Central (top), Leicester Central (Middle) and Leamington Spa (lower). The available data as a percentage of the entire 10 year DJF time-series, is presented in the top left hand corner of each panel.

Figure 1.4 shows that all of the UK Midlands urban background AQMS's present data availability of at least 98%. There appears good qualitative agreement between the three sites, however PM10 spikes are visually evident, especially for the Leamington Spa PM10 dataset. A quantitative analysis was undertaken to determine the degree to which the three PM10 sites correlate. Table 1.3 shows the Pearson correlation coefficient between each of the three urban background sites.

Table 1.3 Pearson Correlation coefficients between raw [PM10] datasets from three urban background AQMS's used in this study. The PM10 datasets are obtained for winter months (DJF) between January 1999 and December 2008.

	Birmingham Central	Leicester Central	Leamington Spa
Birmingham Central		0.86	0.73
Leicester Central	0.86		0.74
Leamington Spa	0.73	0.74	

From Table 1.3 it can be seen that the poorest agreements between [PM10] datasets are associated with the Leamington Spa dataset. This was visually seen with increased PM10 spikes associated with the Leamington Spa site, in Fig. 1.4. Such spikes may be caused by local PM10 point sources or by instrumentation malfunction. As eluded to previously, a data validation step has been included (Sect. 1.6.3) to remove the PM10 spikes that are present in Fig. 1.4, as they are not representative of the wider UK Midlands area.

1.6.3 Data Validation and Verification

The data validation method undertaken in this study is a cross-validation step, between [PM10] at each of the three UK Midlands sites introduced in Sect. 1.5.1. The cross-validation step compares the tendencies of measured [PM10] at each site and is outlined below:

1. Calculate the daily time derivative of each time series ($\frac{d[PM10]}{dt}$), taking each 90 day period separately.
2. Take the difference of the derivative at each site, for each day, leaving 3 inter-site differences.
3. Define a threshold for a spike, in this study the top 10% of the magnitude of all PM10 derivatives has been defined as a spike.
4. Determine whether any of the inter-site $\frac{d[PM10]}{dt}$ differences exceeds the threshold

defined in Step 3.

5. If one of the three inter-site $\frac{d[PM10]}{dt}$ differences exceed the threshold (Step 4), identify the smallest of the three inter-site $\frac{d[PM10]}{dt}$ differences.

6. Identify the two sites that constitute the smallest $\frac{d[PM10]}{dt}$ difference and remove the [PM10] data from the third remaining site for that day.

Such a simple verification process is unlikely to identify all of the erroneous data from each of the sites, however this procedure will remove the largest spikes from the data. Spikes will show as large derivatives in the [PM10] dataset which, if inconsistent with the other two sites, will be removed following step 6 above.

To ensure that this process has improved the agreement between each of the UK Midlands [PM10] datasets, Table 1.4 has been repeated for the validated data.

Table 1.4 Pearson Correlation coefficients between validated [PM10] datasets from three urban background AQMS's used in this study. The PM10 datasets are obtained for winter months (DJF) between January 1999 and December 2008.

	Birmingham Central	Leicester Central	Leamington Spa
Birmingham Central		0.87	0.86
Leicester Central	0.87		0.86
Leamington Spa	0.86	0.86	

From Table 1.4 it is quite evident that there is an improvement between the UK [PM10] at the Leamington Spa urban background site and the other two AQMS's. This improvement was achieved following the removal of data mostly from the Leamington Spa site. The data available, following the data verification step, for each urban background site, can be seen in Fig. 1.5.

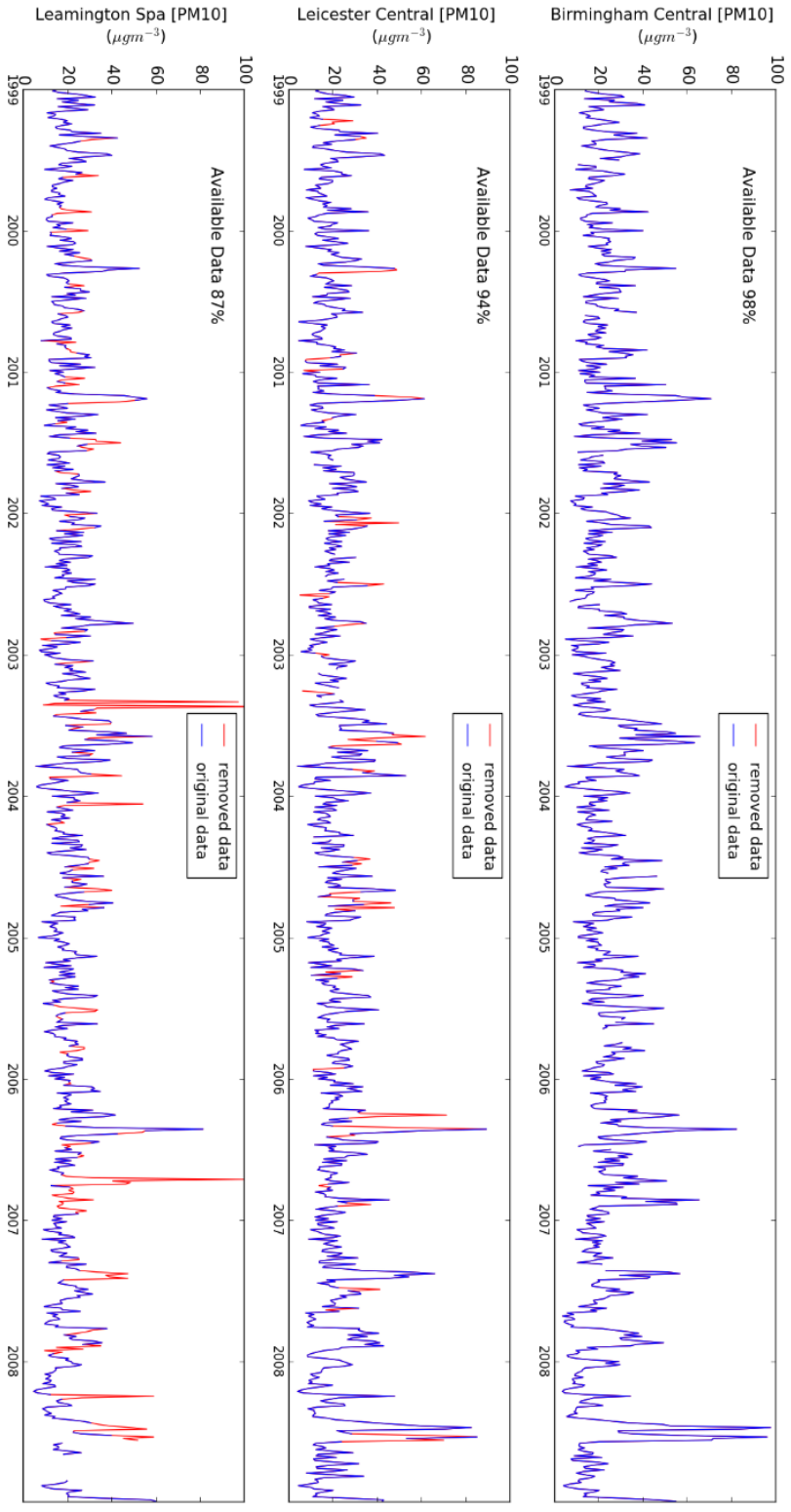

Figure 1.5 10 year (January 1999- December 2008) winter (DJF) PM10 datasets for UK Midlands three urban background AQMSs: Birmingham Central (top), Leicester Central (Middle) and Leamington Spa (lower). Shown are the raw [PM10] time series, shown in Fig. 1.3 (blue + red line) and the time series following data removal (missing data in red). The available data as a percentage of the entire 10 year DJF time-series, is presented in the top left hand corner of each panel.

Figure 1.5 can be used to identify the sources of the removed data in this study's verification step (red line). It can be seen that, while previously there was 98% data availability at Leamington Spa, following data validation, there remains 87%. The Leicester central AQMS also shows a reduction in data availability, following the data validation step. In Fig. 1.4 there was 99% data availability, whereas in Fig. 1.5 there remains 94%.

Analysing the red line in Fig. 1.5, it can be seen that the largest spikes, existent mainly within the Leamington Spa [PM10] dataset have been removed. Examples of these spikes can be seen in 2003 and 2006 for the Leamington Spa AQMS. Also evident is that differences in the timing of PM10 peaks are shown to provide a source of lost PM10 data. An example of this can be seen in the Leicester Central and Leamington Spa sites within 2008. Data is removed from both of these sites at different times, throughout a single PM10 episode in the UK Midlands, when compared to the Birmingham Central PM10 dataset.

Following the success of the data validation method in removing spikes, a singular tri-site UK Midlands [PM10] site was generated. The UK Midlands tri-site [PM10] dataset was generated by taking the mean of the three urban background sites on each day, following the removal of data in the data validation step. On days where data has been removed from a single UK Midlands AQMS, the mean is calculated from [PM10] at the remaining two UK Midlands AQMSs.

1.7 Epidemiological Studies

This study will analyze the impact of synoptic meteorology on UK [PM10]. A separate field of research that looks at the relationships between atmospheric pollutants and human health, is known as epidemiology. Epidemiology studies are used in this study to motivate a health related PM10 threshold, above which PM10 has shown to result in detrimental health impacts.

Epidemiology studies exist that explore the impact of PM10 mass as a whole, which will provide the motivation for PM10 impact thresholds used in this study. In addition to analyzing PM10 as a single quantity, epidemiology studies exist that analyze the impact of individual components of PM10 on human health. This section will explore the relative hazard of different components of PM10 as well as motivate PM10 episodes by determining a hazardous PM10 threshold. A PM10 episode corresponds to a short-term exposure of elevated [PM10] above a threshold. The EU legal PM10 threshold is 50 $\mu g\ m^{-3}$, which must not be exceeded 35 times per year.

1.7.1 Toxicity

"Sola dosis facit venenum" Paracelsus.

Toxicity relates to the hazard that a substance poses to human health. Toxicity depends on the concentration of a substance, as once stated by philosopher Paracelsus. Paracelsus recognized that any substance is poisonous to humans, but it is the dose of a substance that makes it poisonous.

It is not well known at what concentration PM10 is poisonous to humans, with Brook et al. (2010) highlighting that there is no known lower limit where PM10 ceases to have a detrimental effect on human health. This is most likely in part to the various constituents of PM10, which all impact on human health differently.

1.7.2 APHEA2 and ESCAPE Epidemiology Studies

While there exists a variety in the toxic nature of individual PM10 components, this study's metric of choice is [PM10] and therefore to identify a PM10 episode, a [PM10] threshold is required. Katsouyanni et al. (2001) and Gehring et al. (2011) showed that it is not absolute [PM10] that determines whether PM10 is hazardous or not, but [PM10] at each region, relative to that regions' $\overline{[PM10]}$. Such a measure of whether PM10 is hazardous to human health relates to Paracelsus' theory that any substance is toxic in certain doses, dependent on the resilience of the subject. In regions with comparatively elevated $\overline{[PM10]}$, it is argued by Gehring et al. (2011) that the population has a stronger resilience to PM10. Subsequently, for PM10 to become toxic, a greater concentration is required.

Katsouyanni et al. (2001) showed that for PM10, a concentration of 10 μg m^{-3} above the regions' $\overline{[PM10]}$ resulted in a significant increase in premature death ($p<0.05$). This threshold is used for the UK Midlands [PM10] dataset, with Sect. 1.7.3 detailing how a PM10 exceedance threshold is defined.

In addition to the results of Katsouyanni et al. (2001) in the APHEA2 project, Gehring et al. (2011), as part of the ESCAPE study, showed that a smaller exceedance threshold can be applied to PM2.5. Gehring et al. (2011) showed that an increase of 5 μg m^{-3} above a regions' $\overline{[PM2.5]}$ resulted in a significant decrease in peak expiratory flow ($p<0.05$). Supporting a reduced exceedance threshold for PM2.5 are Kappos et al. (2004) who showed that stronger correlations were found between premature mortality rates for PM2.5 than PM10.

1.7.3 The Increased Toxicity of Smaller Particulate Matter

Section 1.7.2 highlighted that PM2.5 is hazardous to human health given smaller exceedance thresholds than PM10. Smaller PM has a greater ability to travel further down the human respiratory tract, into the alveoli, and have a greater potential for causing infection to the subject (Waravdekar and Reynolds, 1998). Particulates of <3 μm have the ability to impact on the surfactant that creates the barrier for air exchange between the lung and the blood stream, in the alveolus (Waravdekar and Reynolds, 1998).

In addition to the reduced size of PM2.5, relative to PM10, their surface area also affects their toxicity. It was shown in Fig. 1.1 that accumulation mode PM had the greatest surface area of any mode of PM. This increased surface area provides a surface for secondary organic and inorganic species to condense upon. These species, especially organics such as the carcinogenic Benzo-a-pyrene, are notoriously the most hazardous species for human health. Accumulation mode PM constitutes a greater component of PM2.5 than PM10 and hence for this reason PM2.5 particles are more hazardous to human health. However, availability of PM2.5 measurements is not sufficient for use within this study.

1.7.4 Defining a [PM10] Exceedance

Following the findings of Katsouyanni et al. (2001), it was decided that a [PM10] exceedance threshold $[PM10]_{Ex}$ could be defined as in Eq. 1.3:

$$[PM10]_{Ex} = \overline{[PM10]} + 10\ \mu g\ m^{-3} \qquad Eq.1.3$$

An additional factor has been added for the definition of a PM10 exceedance event in this study. It was highlighted in Sect. 1.1 that PM volume has a log-normal distribution $\left(\frac{\mathrm{dV}}{\mathrm{dlogD}}\right)$. This is also the case for PM10 concentration, the metric analysed in this study. Fig. 1.1 shows how a ln[PM10] transformation accounts for the positive skew in the [PM10] dataset and this is therefore incorporated into the generation of a PM10 exceedance threshold (Eq. 1.4):

$$[PM10]_{Ex} = e^{\overline{\ln([PM10])}} + 10\ \mu g\ m^{-3} \qquad Eq.1.4$$

Equation 1.4 allows for $\overline{[PM10]}$ to be generated from a non-skewed distribution, which for further analysis in this study, is a desirable trait. In this study, the UK Midlands exceedance threshold is 29.72 μg m^{-3}, which is substantially lower than the legal exceedance threshold of 50 μg m^{-3}. Consequently, a greater number of [PM10] exceedances are classified following the use of the epidemiological threshold, with 15.7 % of all days exceeding the hazardous UK Midlands [PM10] threshold, as opposed to 2.0 % of days exceeding the 50 μg m^{-3} threshold.

1.8 Summary

Chapter 1 has introduced the pollutant of interest within this study, PM10. The diversity in the nature of PM10 components has been emphasized, with a vast distribution of component sizes and sources highlighted. Limiting the atmospheric concentration of PM10 are the loss mechanisms, of which three are described: dry deposition, wet deposition and state changes from gaseous to aqueous compounds.

83% of the UK's population live in urban areas (Office for National Statistics, 2013) and, as this study is health motivated, urban background sites were selected to obtain measured [PM10]. To monitor [PM10], the TEOM instrument was introduced and its limitations regarding the loss of semi-volatile PM were discussed. Despite this limitation, [PM10] data from TEOM instruments is widely available at multiple AQMSs and throughout the entire time period of interest in this study. Consequently, [PM10] was obtained from TEOM instruments at urban background AQMS's.

Three urban background sites were chosen for analysis: Birmingham central, Leicester Central and Leamington Spa, which are all situated within the UK Midlands. It was found that while all three sites had an almost complete daily-mean [PM10] dataset throughout the time-period for this study, DJF between January 1999 and December 2008, there was influence of local PM10 point sources at the sites. Local point sources were referred to as PM10 spikes and were removed, by using a data validation method that compared PM10 tendencies at the three UK Midlands sites.

The three [PM10] datasets were verified, following the data validation step. This verification step involved analyzing their inter-site Pearson correlation coefficients. It was seen that the lowest correlation coefficient seen prior to data validation, between Leamington Spa and Birmingham Central (0.73) was elevated to 0.86, following the data validation step. All correlation coefficients were improved by the validation step and hence the AQMSs are more representative of a non-local UK Midlands urban region.

Based on a literature review of epidemiology studies, a hazardous PM10 threshold has been determined, following results from Katsouyanni et al. (2001) as part of the APHEA2 project. The hazardous PM10 threshold used in this study is site dependent as it was found in both the APHEA2 (Katsouyanni et al., 2001) and ESCAPE (Gehring et al., 2011) projects that it is the PM10 exceedance beyond the regions mean concentration that was shown to define hazardous [PM10]. This study's hazardous [PM10] threshold is 29.72 $\mu g\ m^{-3}$, above which there exists a significantly increased probability of detrimental health effects in humans.

Chapter 2 - Synoptic Meteorological Variability Influencing UK [PM10]

Chapter 1 explored the processes determining this study's chosen pollutant, PM10. It has been shown how the lifetime of PM10, governed by deposition rates and atmospheric chemistry is heavily dependent on meteorology. Chapter 2 introduces the synoptic scale (of the order of 1000 km) meteorological patterns that dictate surface meteorology. A review of background literature in Sect. 2.1 will highlight the meteorological variables that are most important in explaining the variability in [PM10] within the UK.

Section 2.2 introduces the dynamics of atmospheric circulation, which are fundamental to the understanding of synoptic meteorology. The concept of multiple flow equilibrium will be used to introduce the variability in synoptic meteorology affecting the Northern Hemisphere Mid-Latitudes.

This study aims to analyse the impact of one state of mid-latitude synoptic variability, which is best described by atmospheric blocking. Subsequently, diagnostic metrics are introduced to identify a predominant precursor to atmospheric blocking in the Northern hemisphere winter, Rossby wave breaking (RWB) (Altenhoff et al., 2008). Three diagnostic metrics are introduced and subsequently four subsets of RWB are identified. Following this, a discussion of atmospheric blocking persistence and the effect that a temporal elongation of atmospheric blocking will have on UK [PM10] will be presented.

The remainder of this chapter explores the most frequent regions of occurrence for four RWB subsets generated in this study. The dynamics which dictate the differences in the subsets' regions of occurrence are discussed and finally the expected impact of each RWB subset on UK [PM10] is hypothesised.

2.1 Relationships between Synoptic Meteorology and UK [PM10] in Literature

The relationship between synoptic meteorology and air pollution within the UK is one that has been well studied within literature. A common technique to derive the relationship between synoptic scale meteorology and air pollution is through the clustering of synoptic weather regimes (Mcgregor and Bampzelis, 1995; Beaver et al., 2010; Buchholz et al., 2010; Pope et al. 2015; Eder et al. 1994; Kalkstein and Corrigan 1986, Barmpadimos et al., 2012).

Mcgregor and Bampzelis (1995) identify a fundamental dependence of [PM10] on synoptic meteorological regime within the UK. The result which is found within all of the

aforementioned studies is that anticyclonic conditions over a region are associated with the greatest pollutant concentrations over that region. Alternatively, cyclonic conditions are associated with a reduced UK pollutant concentration. Barmpadimos et al. (2012) expand this analysis, by using a generalised additive model to determine the meteorological variables that can explain the most [PM10] variability within five European cities. Barmpadimos et al. (2012) show that the most important meteorological variables, aside from synoptic weather regime in explaining [PM10] variability are: wind speed, wind direction, boundary layer depth, temperature and precipitation. Barmpadimos et al. (2012) found that for the UK, anomalously low wind speeds, an anomalously easterly wind direction, anomalously low winter temperatures (see Sect. 1.3.3), negligible precipitation (see Sect. 1.3.2) and anomalously low boundary layer depth are the optimum conditions for the accumulation of PM10 within the UK.

PM10 is predominantly emitted at the Earth's surface and due to its short lifetime, is found at its greatest concentrations within the planetary boundary layer. The planetary boundary layer (PBL) is a shallow region of the atmosphere that is in contact with the Earth surface through turbulent fluxes (Stull, 1988). The PBL is capped at its top by a temperature inversion, which reduces the vertical transport of pollutant out of the PBL. Throughout anticyclonic conditions, there exists a suppression of vertical mixing out of the PBL (Stull, 1988). This is one mechanism by which anticyclonic conditions increase UK [PM10] within the PBL (Barmpadimos et al., 2012).

In addition to sustaining an increased pollutant mass within the planetary boundary layer, anticyclonic events are also associated with reduced surface horizontal and vertical wind speeds. Increased surface wind speeds can increase mechanically driven turbulence, which contribute to the dispersion of atmospheric pollution throughout the planetary boundary layer and away from the surface. Furthermore, reduced mechanically driven turbulence within the planetary boundary layer favours a shallower boundary layer and hence a smaller volume of air for atmospheric pollutants to disperse within.

Cyclonic conditions (low-pressure) have been found in all aforementioned studies to be associated with the cleanest air, with respect to air pollution. Cyclonic conditions are associated with the greatest surface wind speeds, consequently enhancing the dispersion of atmospheric pollutant from the surface (Stull, 1988). In addition to the transport of atmospheric pollution away from the surface, Sect. 1.3.2 introduced the mechanisms by which precipitation effectively removes both soluble and insoluble PM10 from the atmosphere. Cyclonic conditions are associated with enhanced precipitation over the UK. It is

the increased precipitation and increased dispersion of atmospheric pollution that results in cyclonic conditions being associated with the lowest surface [PM10] in the aforementioned studies.

Barmpadimos et al. (2012) highlighted the importance of persistence of synoptic meteorological conditions that lead to elevated UK [PM10] events. Barmpadimos et al. (2012) found that a greater persistence of these events result in higher UK [PM10]. It is hypothesised that the greatest UK [PM10] events in this study will be associated with persistent anticyclonic events. Section 2.2.2 will introduce atmospheric blocking events, which represent persistent anticyclonic conditions.

All of the aforementioned studies in this section have used clustering techniques to diagnose synoptic meteorological regimes associated with the greatest surface atmospheric pollution concentrations. This study does not use a clustering technique as there exists a limitation to clustering techniques. Within a clustering framework, the amount of synoptic meteorological variability is reduced, with a (reduced) finite number of possible synoptic meteorological profiles that any one day can be attributed to. In a clustering framework, it is not possible to capture the occurrence of rare events, as within the clustering framework, these could be wrongly attributed to a cluster that is representative of a variety of synoptic meteorological conditions. This study is interested in finding the synoptic meteorological conditions that are associated with the greatest UK [PM10] events, which are themselves rare events. It is therefore necessary that the synoptic meteorological variability is not removed through a clustering technique and can be analysed in full.

This study presents a further advantage of the methodology used to determine the relationship between Northern Hemisphere Mid-Latitude variability and UK [PM10]. For clustering techniques, the resultant clustered regimes are dependent on the size of the domain that is selected. The metrics that this study uses to define synoptic meteorology are independent of the size of any domain analysed. This characteristic results in one fewer assumption made (size of analysed domain) when deriving a relationship between synoptic meteorology and UK [PM10], resulting in a reduced uncertainty in the obtained results.

2.2 The Dynamics behind Rossby Wave Breaking

2.2.1 The Potential Vorticity Budget

To understand RWB and atmospheric blocking it is important to understand the governing physics controlling atmospheric motion. Due to the Earth rotating on its axis, the fluid dynamics of the atmosphere are dictated by rotation. Potential vorticity is a measure of the

absolute vorticity of a fluid parcel between two isentropic surfaces (surfaces of equal potential temperature). This section will introduce and discuss the important aspects controlling potential vorticity and how potential vorticity can be used to identify RWB.

2.2.2 Rate of change of Absolute vorticity following a fluid parcel

The vorticity equation in a rotating frame of reference is given in Eq. 2.1 (Hoskins and James, 2014), showing the dominant processes dictating the production of absolute vorticity (ζ). It must be stated that the shallow atmosphere approximation has been applied here, indicating that the horizontal length scale is much greater than the vertical depth of the atmosphere. Furthermore, we are assuming a compressible flow for the atmosphere. In Eq. 2.1, p = pressure, ρ = density, $\boldsymbol{u}$ = horizontal wind velocity vector and $\tilde{u}$ = frictional dissipation term.

$$\frac{D\zeta}{Dt} = (\zeta.\nabla)\boldsymbol{u} - \zeta(\nabla.\boldsymbol{u}) - \nabla\left(\frac{1}{\rho}\right) \times \nabla p + \nabla \times \tilde{u} \qquad Eq.2.1$$

The left hand side of Eq. 2.1 represents the lagrangian rate of change of ζ with respect to time. The terms on the right hand side are discussed in the following sections.

2.2.3 Vortex Stretching and Tilting Terms

The first two terms on the right-hand side of Eq. 2.1 refer to the vortex stretching and tilting terms. In this context, a vortex tube can be thought of as a cylindrical column of air with radius, r and absolute vorticity, ζ. Vortex stretching and tilting mechanisms act to distort this vortex tube in such a way that either the orientation or the magnitude of ζ is changed. Equation 2.2 shows the expansion of the first two right-hand terms in Eq. 2.1, provided the vortex tube is aligned vertically along the z axis.

$$(\zeta.\nabla)\boldsymbol{u} - \zeta(\nabla.\boldsymbol{u}) = \zeta\left(\frac{\partial u}{\partial z}\underline{i} + \frac{\partial v}{\partial z}\underline{j}\right) - \zeta\underline{k}\left(\frac{\partial u}{\partial x} + \frac{\partial v}{\partial y}\right) \qquad Eq.2.2$$

Consider a case where the vertically aligned vortex tube is subject to a vertical shear of horizontal velocity and no horizontal velocity shear. Subsequently, the right-hand side of Eq. 2.2 becomes $\zeta\left(\frac{\partial u}{\partial z}\underline{i} + \frac{\partial v}{\partial z}\underline{j}\right)$. The effect of a vertical shear of horizontal flow is to tilt the vortex, in the direction of the flow. This effect acts to increase the component of vorticity in the direction of the flow. It is important to note that this term cannot generate any vorticity, however it can alter the direction of the vorticity.

A second case may also be present in the atmosphere, where a divergence/convergence of horizontal flow exists within the atmosphere. If we consider a case of no vertical shear of

horizontal velocity, the right-hand side of Eq. 2.2 becomes; $-\zeta \underline{k}\left(\frac{\partial u}{\partial x}+\frac{\partial v}{\partial y}\right)$, where $\frac{\partial u}{\partial x}+\frac{\partial v}{\partial y}$ represents the divergence of a flow field. This represents a case of vortex stretching/ squashing, as horizontal divergence/convergence within the vortex tube expands/reduces the radius of the vortex and reduces/increases its height. Equation 2.1 shows that a reduction in $(\zeta.\nabla)u-\zeta(\nabla.u)$, which is seen following a divergence of the flow field within a vortex tube, results in a reduced absolute vorticity. The opposite can be seen for a convergence, with an increase of absolute vorticity.

2.2.4 Solenoidal term (Baroclinicity)

The third term on the right-hand side of Eq. 2.1 relates to the solenoidal term and arises due to atmospheric baroclinicity. This term relates to the relative gradients of the pressure and density surfaces in a fluid. A barotropic case would result in this solenoidal term equating to zero as the pressure and density surfaces are aligned in parallel. Conversely, if the surfaces are not parallel, a baroclinic situation results and generates a horizontal component of vorticity. The solenoidal term acts to tilt the density surfaces into an orientation whereby they become more parallel to the pressure surfaces. The state whereby the pressure and density surfaces are parallel is a barotropic state and is where the fluid is in its lowest state of available potential energy (APE), where APE = 0. The act of redistributing these surfaces acts to convert APE into kinetic energy, via the redistribution of mass (Martin, 2013). Equation 2.3 shows the calculation of the solenoid term in Eq. 2.1.

$$\text{Solenoid term} = \oint \frac{\nabla \mathrm{p}}{\rho}.\mathrm{dl} \qquad Eq.\,2.3$$

Where ρ = density, p = Pressure and $\mathrm{l} =$ the closed contour of the circulation.

In the North Atlantic, the baroclinic term has its greatest magnitude within the northwest Atlantic region, where the meridional temperature gradient is at its greatest. The solenoidal term acts to generate a horizontal component of vorticity whenever there are horizontal temperature gradients (Hoskins and James, 2014). There is however potential for vortex tilting (Sect. 2.2.3) to redistribute this horizontal vorticity into a vertical vorticity component.

2.2.5 Friction term

The final term on the right hand side of Eq. 2.1 refers to the impact of friction on the vorticity equation. This term is small away from the surface, however friction can apply torque to the system, therefore naturally imparting a spin on the fluid. The friction term will always reduce the magnitude of $\frac{D\zeta}{Dt}$ anomalies calculated from Eq. 2.1, as it opposes the existing circulation.

2.2.6 Rossby-Ertel PV

Potential Vorticity (PV) is an extended application of absolute vorticity (Eq. 2.1). Throughout this study, the metrics used to diagnose synoptic meteorological conditions that influence [PM10] will be generated using PV. It is therefore important to understand the properties of PV and how it can help to identify individual air masses and their dynamics.

A representation of Rossby-Ertel PV (Rossby, 1940 and Ertel, 1942) is shown in Eq. 2.4 (Hoskins and James, 2014). The units of P are K m^2 kg^{-1} s^{-1} or more commonly defined as potential vorticity units (PVU). In Eq. 2.4, ρ is density, ζ is absolute vorticity and θ represents potential temperature.

$$P = \frac{1}{\rho}\zeta.\nabla\theta \qquad Eq.2.4$$

PV combines the dynamic (ζ) and thermodynamic ($\nabla\theta$) properties of the atmosphere and can be conserved following frictionless and adiabatic flow. The conservation of PV is a good approximation away from the surface within the free troposphere, which is of paramount important to its uses within this study. Diabatic processes and orographic forcing are two processes that can alter PV and can be quantified by evaluating the non-conservation of PV. The principal advantage of approximate PV conservation within the upper troposphere is that it becomes a good diagnostic for tracking air masses. A further useful application of PV is that it can be inverted to derive changes to the atmospheric circulation.

2.2.7 Diabatic PV Influence

The assumption of a dry atmosphere is invalid in much of the Earth's troposphere as water vapour is present. As water vapour condenses, the change of state results in a release of heat energy, otherwise called latent heat. This latent heat can act to considerably alter tropospheric thermodynamics. In the context of PV, the height of latent heat release is important in determining the resultant impact on PV. If a layer in the atmosphere above the surface experiences latent heat release and subsequent warming, the isentropes (contours of equal entropy) are displaced downwards about a region of latent heat release (Haynes and McIntyre, 1987). Consequently, $\nabla\theta$ in Eq. 2.4 is decreased above a region of latent heat release and increased below. The result of this diabatic mechanism is that PV above the region of latent heat release is decreased, while below it is increased. Studies have shown that this positive PV anomaly below the region of latent heating can be attributable to noticeably intensifying low pressure systems (Chagnon et al., 2013; Stoelinga, 1996). Furthermore the negative PV anomaly above the region of latent heat release in some cyclones has been

attributable to reinforcing large scale quasi-stationary negative PV anomalies known as blocking anticyclones (Pfahl et al., 2015). Subsequently the diabatic generation of PV could be important in sustaining atmospheric blocking mechanisms, the focus of this study.

2.2.8 Gravity Wave Drag

Gravity waves are the result of air masses passing over raised orography. The air masses are mechanically lifted and become negatively buoyant, relative to the surrounding air. These air masses adiabatically sink to a lower height, however with additional vertical momentum, overshoot their level of neutral buoyancy. Subsequently, the air mass rises adiabatically with a positive buoyancy and the process repeats itself. This is the mechanism that generates gravity waves. Such waves have been shown in idealised experiments to generate PV anomalies in the mid-troposphere (Martin and Lott, 2007).

2.2.9 The Dynamical Tropopause

Hoskins et al. (1985) pioneered the use of potential temperature (θ) on the 2 Potential vorticity units (2-PVU) surface to determine upper-level air masses on a planetary scale. Potential temperature (θ) is the temperature a fluid parcel would have if brought to the surface adiabatically. The 2-PVU surface where θ is obtained from is otherwise termed the dynamical tropopause.

There are a number of different methods of diagnosing the tropopause, be these thermal, using lapse rates (Bjeknes and Palmén, 1937), dynamically, using PV (Hoskins, 1985), or even using a tracer such as ozone concentration (Bethan et al., 1996). Wilcox et al. (2012), highlighted the potential for both a thermal and dynamical representation of the tropopause at some latitudes, by using a blended tropopause. A blended tropopause defines tropopause height using combined criteria used in defining both the dynamical and thermal tropopause height.

There are limitations to using a solely dynamical tropopause definition and Wilcox et al. (2012) highlight these limitations. Wilcox et al. (2012), showed that a dynamical representation of the tropopause is inaccurate and inappropriate at latitudes equatorward of the mid-latitudes. Appendix A examines the limitations of using a purely dynamical tropopause definition in this study. It is found that following the definition of a dynamical tropopause there exist spurious grid points, where θ-2PVU is markedly different from its neighbouring grid points. Wilcox et al. (2012) explain this effect as an artefact of tropopause folding. Tropopause folding can occur near to the subtropical jet and can result in the tropopause being diagnosed at two separate heights. To avoid this occurring, as suggested by

Wilcox et al. (2012) a 350 K θ threshold has been applied to the θ-2PVU fields analysed in this study. Appendix A highlights the improvement of using this θ threshold in Fig. A.1. Following the application of the 350 K θ threshold, the spurious grid points do remain, however their differences are much smaller, compared to neighbouring grid points. It is important to note that for the region that we are interested in (North Atlantic/ European region), the θ-2PVU field is generally not influenced by spurious grid-points.

2.3 Synoptic Meteorology influencing UK PM10

At this point the fundamentals of PV in the troposphere have been described and the significance of the dynamical tropopause identified. It is now important to understand how PV can be used to identify synoptic meteorological systems that may influence UK [PM10].

2.3.1 Multiple Flow Equilibria

The synoptic meteorological variability present in the mid-latitudes, can be encapsulated by the multiple flow equilibria. Charney and DeVore (1979) used a simple barotropic model, to determine the stable atmospheric states resulting from a topographic and stochastic thermal forcing on zonal flow. What Charney and DeVore (1979) found was that there are several stable states that include an explanation for atmospheric blocking. For zonal flow interacting with topography, such as in the case of the Rockies and the Northern-Hemisphere mid-latitude eddy-driven jet (EDJ), it was found that two stable equilibrium states were produced following the same forcing. While one of these was a high frequency/ low amplitude wave pattern that coincided with strong zonal flow, the other coincided with low frequency/ high amplitude wave pattern resulting from resonance patterns of transient Rossby waves. Subsequently Charney and DeVore (1979) show that meta-stationary (meta-stationary meaning that the flow pattern is stable to small scale disturbances) equilibrium flows can exist in zonal flow forced by topography. The meta-stationary flow is reminiscent of atmospheric blocking. The results found by Charney and DeVore (1979) regarding the two stable states following topographic forcing of zonal flow were found using a highly truncated spectral model. These results were subsequently confirmed by Charney and DeVore (1979) using a grid point model (16 x 16 grid) with a greater number of degrees of freedom and an Arakawa (1966) finite difference scheme.

It is this variability in stable equilibrium states found by Charney and DeVore (1979) that this author hypothesises will dictate synoptic meteorological patterns influencing the UK. One side of this variability, analogous to atmospheric blocking, is a phenomenon that has the potential to provide synoptic meteorological conditions conducive to PM10 accumulation.

2.3.2 Atmospheric Blocking

Following the results from Charney and DeVore (1979), it is advantageous to find a method and subsequently a metric that can diagnose the synoptic scale variability seen in their paper. As mentioned beforehand, the meta-stationary flow found by Charney and DeVore (1979) is reminiscent of blocked flow. Section 2.5 explores current metrics that are designed to identify atmospheric blocking events.

Atmospheric blocking can be described as a prolonged period where the dominant jet stream over a specified region is diverted from its climatological path. In Europe, atmospheric blocking can be viewed as persistent anticyclones that deflect the Eddy driven jet stream and subsequent storm track (Section 2.3.4) from Western Europe (Martius et al., 2007).

Section 1.3.3 highlighted the importance of the cooler winter months in UK PM10 accumulation. Therefore we have chosen to analyse the relationships between synoptic meteorology and UK [PM10] in the months surrounding the Northern hemisphere winter. Atmospheric blocking is a process that occurs all year round, however through two dominant mechanisms. Throughout the winter months, the occurrence of atmospheric blocking has been found to be linked to the prior occurrence of RWB (Altenhoff et al., 2008). In the summer months, atmospheric blocking is more influenced by the presence of stationary ridges (Tyrlis and Hoskins, 2008). In the intermediate months, a combination of the two mechanisms are responsible for atmospheric blocking.

To understand the mechanisms leading to atmospheric blocking in winter, the dynamics of Rossby waves and RWB must be understood. This section will discuss the processes of Rossby wave generation and the atmospheric jet streams, before focussing on RWB and the processes leading to persistent atmospheric blocking. It is important to reiterate that while RWB and atmospheric blocking are often dynamically linked, they are two separate meteorological phenomena. Atmospheric blocking is associated with the temporal persistence of an anticyclone over a region, which acts to divert transient synoptic weather systems. RWB is not a persistent feature, although its occurrence can result in atmospheric blocking, especially throughout Northern hemisphere winter months (DJF) (Altenhoff et al., 2008).

2.3.3 Rossby Waves

Rossby waves are a generic feature of any rotating fluid and result from the variation in the Coriolis force (f) with latitude (φ) (Hoskins and James, 2014). The Coriolis force is the force that acts on bodies moving relative to a rotating reference frame, such as Earth. The value of

Coriolis force varies with sin(φ), as in Eq.2.5. In Eq. 2.5, Ω represents the rotation rate of the Earth (7.29 x 10^{-5} radians s^{-1}).

$$f = 2\Omega\sin(\varphi) \qquad Eq.2.5$$

It is the rate of change of f with φ, referred to as the β-effect, that can explain the occurrence of Rossby waves (Atkinson, 1981).

Figure 2.1, from Fig. 9.8 by Hoskins and James (2014), shows the generation of Rossby waves in a barotropic atmosphere, due to interaction of the mean flow with a shallow (with respect to the atmospheric depth) orographic obstacle.

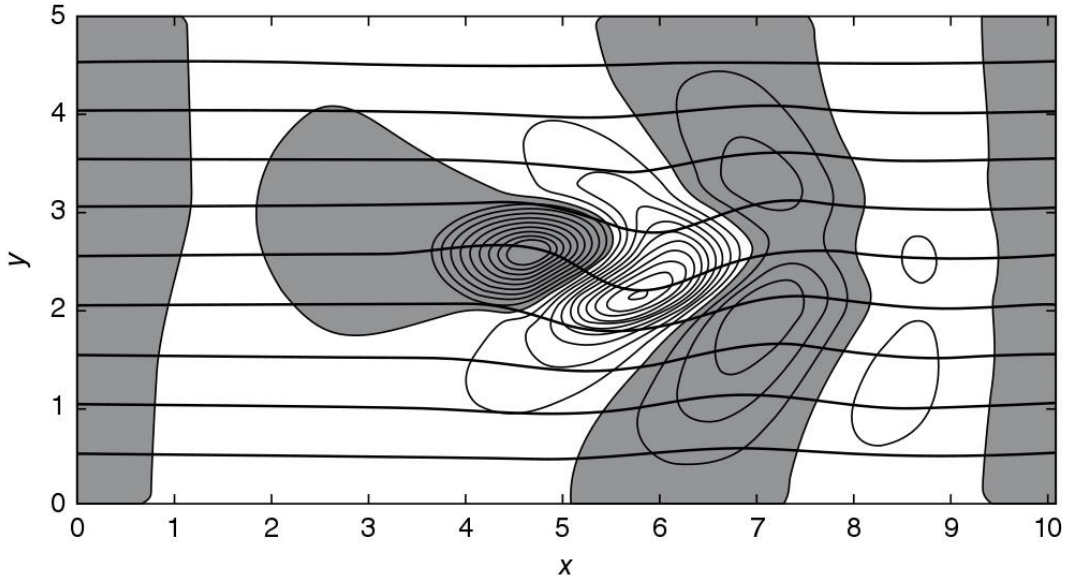

Figure 2.1 A modelled barotropic atmosphere with a shallow orographic obstruction to a west-east mean flow after 6 modelled time steps. Dark/light shading represent negative/positive PV anomalies respectively.

The wave-like pattern downstream of the small mountain is representative of a Rossby wave. The eastward propagation of the Rossby wave relative to the shallow mountain is driven by the β-effect. As air is forced over the shallow mountain, the air is squashed and a negative absolute vorticity anomaly is generated through the stretching/squashing term in Eq. 2.2. To conserve PV, following the generation of an absolute vorticity anomaly, the air mass is advected to a region of higher planetary vorticity (poleward). A consequence of this meridional advection is the generation of a downstream positive relative vorticity anomaly. The air mass consequently advects equatorward to again conserve PV. This is the process by which Rossby waves propagate following both barotropic (in Fig. 2.1) and baroclinic disturbances.

In the real world, the atmosphere is rarely barotropic, with horizontal and vertical temperature gradients creating a baroclinic atmosphere. Horizontal temperature gradients, such as those in the northwest Atlantic are responsible for a region of strong baroclinicity and subsequent horizontal PV generation (Sect. 2.2.4). Through the Rossby wave propagation mechanism above, the generated PV anomaly is compensated by a meridional advection of air masses and a Rossby wave is generated.

2.3.4 Jet Streams

Mid-latitude atmospheric variability is dictated by the strength and position of upper level westerly wind velocity maxima (Woollings et al., 2010b). These upper level wind maxima are commonly termed jet streams and in the mid-latitudes, two exist. The mechanisms generating the two jet streams are differing and therefore in many regions a latitudinal separation can be seen in their location. This latitudinal separation can be seen in the North Atlantic/ European region and hence one jet is substantially more influential on the UK than the other throughout the Northern hemisphere winter (DJF) (Eichelberger and Hartmann, 2007).

The first of the two jets that impacts the UK to a lesser extent is termed the subtropical jet (Vallis, 2006). The subtropical jet is a result of the meridional poleward transport of equatorial air in the upper branch of the Hadley cell. The Hadley cell exists due to the meridional temperature gradient on the planet and acts to equilibrate this temperature gradient. The subtropical jet is the more elevated of the two jets and marks the poleward boundary of the Hadley cell. To conserve angular momentum, the subtropical jet is formed at this boundary. Eq. 2.6 describes the conservation of momentum and what can be seen is that as latitude (φ) is increased (i.e. air migrates poleward), **u** must also increase to conserve momentum (adapted from Hoskins and James 2014). This compensatory increase in **u** is the forcing mechanism for the subtropical jet. In Eq. 2.6 a represents the radius of the Earth (approximately 6.3 x 10^6 m) and Ω is the rotation rate of the Earth = 7.29 x 10^{-5} radians s^{-1}.

$$\cos\varphi(\mathbf{u} + a\Omega\cos\varphi) = \text{constant} \qquad Eq.\,2.6$$

The position of the subtropical jet is dependent on the position of the Hadley cell in the widely recognised tri-cellular model (Rossby, 1941). During Northern hemisphere winter, the subtropical jet is positioned much further south than it is in the Northern hemisphere summer and subsequently has less impact on UK synoptic meteorology at this time.

The second of these jets is termed the eddy driven jet (EDJ). The EDJ is so named, due to the role that non-linear transient eddies play in maintaining the westerly momentum and thermal

balances within the EDJ (Vallis, 2006). Transient eddies (synoptic weather systems) maintain the EDJ via heat and momentum fluxes and therefore are crucial to the existence of the EDJ. It can also be said that the EDJ is crucial to the existence of synoptic systems in the mid-latitudes (Vallis, 2006). Mid-latitude synoptic systems are formed due to upper tropospheric convergence and divergence, which result in lower level anticyclones and cyclones respectively. Flow divergence magnitudes are greatest within the EDJ and hence the EDJ becomes an important region of synoptic system development.

On average, synoptic eddies form in the entrance region of the EDJ, which in the North Atlantic region, is in the northwest Atlantic. The northwest Atlantic region is a region of high lower level baroclinicity, caused by meridional surface temperature gradients. Thermal wind balance can explain the relationship between meridional temperature gradients and upper-level zonal wind, with an enhanced temperature gradient resulting in an enhanced zonal jet speed (Hoskins and James, 2014). Following the development of synoptic eddies, they are then steered by the EDJ towards the EDJ exit region, the statistically most probable region for synoptic eddy decay. The exit region of the North Atlantic EDJ is found over the northeast Atlantic/ European region.

The storm track is the statistically most probable region for cyclone propagation. Due to the steering mechanism of synoptic eddies by the EDJ, the position of the storm track coincides with the location of the EDJ (Brayshaw et al., 2008). Within the storm track, the higher probability of cyclones, brings with it a higher probability of precipitation and elevated wind speeds. These meteorological mechanisms lend themselves to the removal and dispersion of PM10 in the lower troposphere. Throughout this study the EDJ is referred to as a mechanism that reduces surface [PM10], due mainly to the steering of lower level synoptic systems.

2.3.5 Rossby Wave Breaking

To this point, the dynamics of the EDJ and Rossby wave generation have been discussed. Section 2.3.5 discusses RWB, the process that during the Northern Hemisphere Winter, is an important prerequisite to the formation of atmospheric blocks (Altenhoff et al., 2008).

Rossby waves are wave-like distortions in the upper tropospheric sub-tropical jet stream that are vital to the meridional transport of heat and momentum in the atmosphere (Randall, 2015). RWB occurs in regions called critical layers (Randel and Held, 1991), whereby the zonal phase velocity of the Rossby wave is equal to the zonal wind velocity at a specific region (Haynes, 2003).

Thorncroft et al. (1993) evaluated the lifecycle of RWB events and in doing so, described two categories of RWB, LC1 and LC2. LC1 and LC2 subsets are anticyclonic and cyclonic breaking Rossby waves respectively. Both of these RWB subsets are shown to break equatorward, with an equatorial advection of upper tropospheric air mass. This equatorial advection of poleward air mass is shown by Thorncroft et al. (1993) to result in a cyclonic PV anomaly equatorward of the centre of overturning, with a cut-off cyclone the prominent feature. LC1 events develop upstream of confluent flow and result in a thin filament of poleward air mass being wrapped up anticyclonically, equatorward of the centre of overturning. LC2 events develop in diffluent flow and are responsible for a greater equatorial flux of poleward air mass (Gabriel and Peters, 2008) than LC1 events. LC2 events often result in a strong cut-off cyclone equatorward of the centre of overturning.

Poleward breaking RWB subsets were added to the LC1 and LC2 subsets by Peters and Waugh (1996), called P1 and P2 RWB. P1 and P2 RWB subsets are cyclonically and anticyclonically breaking respectively. Poleward breaking Rossby waves have a greater tendency for anomalous anticyclonic air mass advection to the poleward side of the RWB event. The result of this is that a quasi-stationary anomalous anticyclone may result (Altenhoff et al., 2008), therefore resulting in atmospheric blocking conditions, as discussed in Sect. 2.3.2. P2 events occur in diffluent flow and often result in large quasi-stationary stationary anticyclones. P1 events however occur in confluent flow and are associated with a thin filament of equatorward low-PV air mass advected poleward. Consequently, P1 events are often associated with smaller anticyclonic anomalies than P2 events (Gabriel and Peters, 2008).

Gabriel and Peters (2008) showed that it is the latitude of the maxima in upper tropospheric mean kinetic energy (the EDJ maxima) that dictates the direction of RWB, with RWB occurring in both clockwise and anticlockwise directions (Masato et al., 2012; Weijenborg, et al., 2012). Gabriel and Peters (2008) show that all of the RWB subsets detailed above, experience a meridional zonal horizontal velocity shear. The LC1 and P2 events occur in regions where stronger winds exist in the background flow on the poleward side of the Rossby wave. While LC2 and P1 events experience stronger horizontal velocities on their equatorial side. Due to this horizontal velocity shear Gabriel and Peters (2008) and Masato et al., (2012) (hereafter M12) show that there is an increased probability for cyclonic/ anticyclonic RWB to the north/south of the mean-state EDJ latitude.

Figure 2.2 shows a schematic of meridional zonal shear, imparted on the background flow by the mean state EDJ. This schematic is representative of the mean-state position of the EDJ in

the North Atlantic basin, with a characteristic SW/NE tilt (Woollings et al., 2010b). This schematic can help explain the increased statistical probability for cyclonic/anticyclonic RWB on the poleward/equatorial side of the EDJ. Over a specific region, it is the sign of the meridional horizontal shear of the background flow that determines the preferential direction of RWB. In the case of Fig. 2.2, which is representative of the mean-state North Atlantic EDJ, RWB to the north/ south of the EDJ would preferentially break cyclonically/ anticyclonically (Peters and Waugh, 1996; Thorncroft et al., 1993; Masato et al., 2012; Masato et al., 2013; Gabriel and Peters, 2008; Weijenborg et al., 2012). Weijenborg et al. (2012) find this relationship between RWB direction and location relative to the mean state of the EDJ throughout the Northern Hemisphere, except for over North America. Over the North American region, Weijenborg et al. (2012) highlight that the EDJ is not well defined and hence there is no preference for cyclonic or anticyclonic RWB.

It is important to note that in the case of a propagating Rossby wave, the EDJ exhibits a wave-like pattern and therefore is not as zonally aligned as illustrated in Fig. 2.2. Despite this, the background flow remains to be sheared across the latitudinal extent of the Rossby wave, allows the Rossby wave to break. This is the case as highlighted by Gabriel and Peters (2008) for the four RWB lifecycles discussed above.

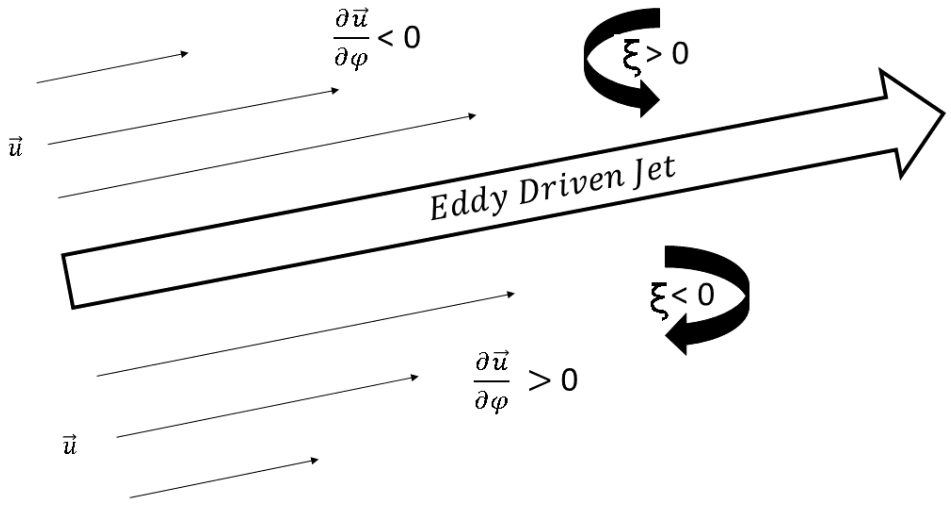

Figure 2.2. A schematic representing the impact of the eddy driven jet (EDJ) on the background flow. To the north and south of the EDJ, a cyclonic (anomalous $\xi > 0$) and anticyclonic ($\xi < 0$) shear is imparted on the background flow, as a result of meridional flow velocity shear. Meridional shear ($\frac{\partial \vec{u}}{\partial \varphi}$) is represented by $\vec{u}$ flow vectors, where the length of the arrow represents the magnitude of the vector.

Gabriel and Peters (2008) show that the P2 and LC1 RWB categories are most prominent within the northeast Atlantic, a region of high importance for UK meteorology and [PM10].

Both, the P2 and LC1 RWB subsets are shown by Gabriel and Peters (2008) to preferentially break anticyclonically, however Thorncroft et al. (1993) elucidate that Rossby waves leading to LCI-type RWB originally show cyclonic breaking tendencies. Therefore it is important to note that while a Rossby wave may exhibit cyclonic/anticyclonic breaking tendencies, this does not necessarily result in cyclonic/ anticyclonic RWB. With respect to the location of the UK, P2 events are found to be most frequent, whereas LC1 events are found to occur further south towards the Mediterranean (Gabriel and Peters, 2008). Over Western Europe, P2 events often lead to blocking anticyclones, which literature suggests (Sect. 2.1) will favour the accumulation of UK PM10.

2.4 Atmospheric Blocking Persistence

RWB can produce the synoptic meteorological conditions that are conducive to the accumulation of PM10, through the formation of a blocking anticyclone (Altenhoff et al., 2008). An important feature of this anticyclone, which can impact on UK [PM10], is its persistence. A persistent anticyclone produces a temporal elongation of synoptic conditions that are prevalent for the accumulation of PM10 (Sect. 2.1). This section will discuss the mechanisms by which anticyclones become persistent, the interaction of transient eddies on a blocking anticyclone, through the transfer of energy from small to large scales (Sect. 2.4.1) and the diabatic enhancement of blocked flow (Sect. 2.4.2).

When considering a persistent anticyclone (atmospheric block) as a negative absolute vorticity anomaly, the requirement for vorticity reinforcement becomes evident. Frictional forces at the surface apply a torque on the circulating flow, which inevitably reduce the absolute vorticity of the synoptic eddy (Eq. 2.1.5). To maintain a persistent anticyclone, reinforcement of the negative absolute vorticity anomaly is required (Illari, 1984)

2.4.1 Eddies interacting with blocked flow - Shutts – Eddy Straining

Shutts (1983) proposed a mechanism by which eddies can contribute to PV anomalies associated with an atmospheric block. The mechanism is associated with a split jet, about the atmospheric block, which can be seen in Fig. 2.3. The atmospheric block pictured is a blocking dipole, with high PV to the south of low PV. This blocking pattern is widely recognised as a classical Rex block pattern (Rex, 1950) and will be discussed in Sect. 2.5.1. Shutts (1983) identified that reinforcement of the quasi-stationary flow field, i.e. the blocking anticyclone, is achieved through an energy cascade to lower wave numbers, which ultimately allow the transfer of energy from small (eddies) to large (quasi-stationary anticyclone) scales.

Figure 2.3 shows this eddy straining mechanism, with an important feature being the eddy deformation on the upstream side of the blocking dipole. It is shown that eddies approaching the blocking dipole become meridionally elongated. Shutts (1983) showed that with respect to time, the vorticity amplitude of an eddy remains constant, regardless of meridional elongation. Therefore the energy density of the eddy will decrease once contracted. With a reduced energy density in the contracted eddy, the energy cascades to smaller scales and wavenumbers (Chemke and Kaspi, 2015). Baroclinic eddy energy transfer is the transfer of eddy energy from small to large scales and this helps to maintain the larger scale blocking dipole.

The eddy straining mechanism is a feedback mechanism, as the eddy straining is caused by a deformation field of the blocking dipole. As the blocking dipole is reinforced, the deformation field is enhanced. Illari (1984) highlighted that the frictional dissipation term, acting against the circulation of the synoptic eddy at the surface, is totally counteracted by eddy reinforcement, therefore through this mechanism the blocking dipole can persist.

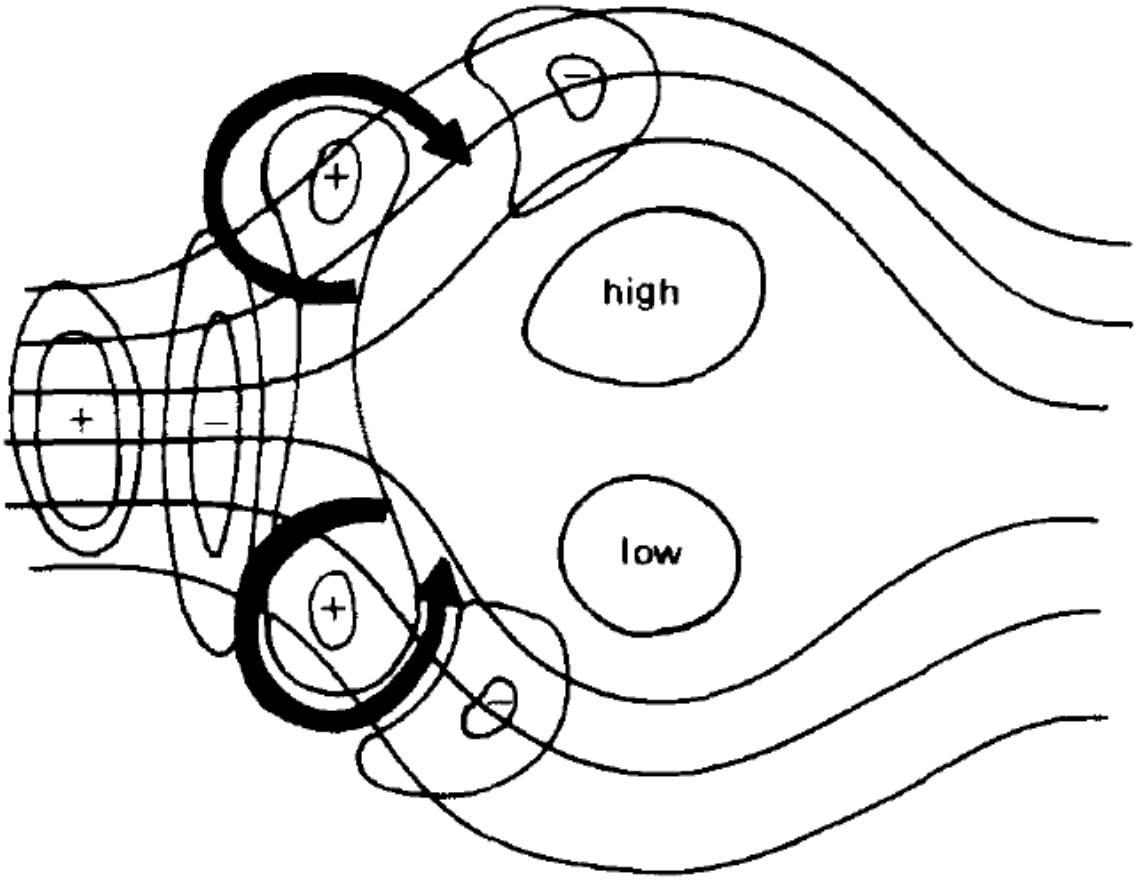

Figure 2.3. A schematic taken from Fig. 1 by Shutts et al., (1983), representing the role of eddy straining in reinforcing a blocking dipole. The high and low refer to surface pressure anomalies in a blocking dipole, with streamlines circumnavigating the blocking dipole representing the path of the displaced eddy driven jet. The + and – signs represent areas of anomalously positive and negative potential vorticity.

2.4.2 Diabatic Enhancement of Blocked flow

A mechanism that studies have demonstrated has a significant influence in not only the formation, but also the persistence of an atmospheric block, is diabatic reinforcement. Diabatic reinforcement occurs through the release of latent heat in the warm conveyor belt of cyclones that are upstream of atmospheric blocks (Pfahl et al., 2015). The warm conveyor belt is a feature of all extratropical cyclones and involves an air stream that originates at (or very close to) the surface and is elevated above the leading warm front. The characteristics of the air elevated in the warm conveyor belt are warm and moist.

The first mechanism by which upstream cyclones reinforce blocking anticyclones is seen as moist and warm air is elevated in the warm conveyor belt of a mid-latitude cyclone (Harrold, 1973). As the air is adiabatically lifted, it begins to cool and releases latent heat. This latent

heat acts to modify the PV above and below the point of latent heat release, as discussed in Section 2.2.7.

The act of adiabatically advecting low-level low PV into the upper troposphere also acts to reinforce a blocking anticyclone (Pfahl et al., 2015). As a negative PV anomaly is advected into the downstream ridge, this reinforces the (anomalously negative PV) blocking anticyclone and helps it to persist for longer.

2.4.3 Summary on Persistence

Mechanisms controlling the persistence of atmospheric blocking systems have been discussed in this section. The importance of persistence in this study is that there results a temporal elongation of conditions that may be prevalent to PM10 accumulation. The exact implications of persistent RWB on UK [PM10] are as yet unknown and will be the subject of detailed analysis in Chapters 3 and 5. The research questions regarding the persistence of RWB are:

1) Does persistent RWB lead to elevated UK [PM10]?
2) Does persistent RWB alter the dominant sources that contribute to UK PM10?

The first of these research questions will be addressed in Chapter 3, while the second will require a modelling framework described in Chapter 4, with the results demonstrated in Chapter 5.

The following section discusses the history of atmospheric blocking metrics. All of the metrics discussed include a persistence criteria. The inclusion of persistence criterion highlights the perceived importance of the persistence of atmospheric blocking on synoptic meteorology, which this study will extend to UK [PM10].

2.5 Blocking Metrics

Within literature, there exists an extensive number of metrics to diagnose atmospheric blocking and RWB. Scaife et al. (2010) showed that RWB detection is very sensitive to the metric used. Despite this finding, it is still seen that no consensus has been made regarding an optimum metric and studies being published to this date use different metrics to detect the same meteorological phenomenon. A non-exhaustive list of blocking metrics is presented in this section.

2.5.1 The Rex Block

A pioneering study on what is now well understood as an atmospheric blocking event, which follows the occurrence of RWB, was undertaken by Rex (1950). Rex (1950) identified the MSLP dipole that originates following a RWB event and quantified its impact on European

climate through a single winter month. Rex (1950) identified that atmospheric blocking, resulting from a meridional overturning of air masses, presented one half of the two extreme states of synoptic variability, as highlighted by Charney and DeVore (1979), in their multiple flow equilibria (Sect. 2.3.1). Rex (1950) identified the principles that would become the 2D blocking Index in Masato et al. (2013a) (hereafter M13), which is used in this study and discussed in Sect. 2.6.

Rex, (1950) identified a block using the following 5 criteria:

1) A meridional dissection of the mid-latitude westerly zonal wind pattern
2) A longitudinal extent over which two westerly jet maxima can be seen at different latitudes
3) A shift from zonally aligned westerlies upstream to meridionally slanted westerlies downstream.
4) An appreciable mass must be transported in each branch of westerly flow
5) The block must persist for 10 days.

The criteria used in Rex (1950) are more detailed than the 2D blocking index used by M13 and in this study and more descriptive of an idealised overturning. Using such detailed criteria for block identification will allow for 'imperfect' blocks to remain unidentified.

Following Rex (1950), having successfully diagnosed an atmospheric blocking event as a latitudinal separation of westerly flow, Lejenäs and Økland (1983) extended this analysis to create a climatology of atmospheric blocking. The criteria used to define blocking in Lejenäs and Økland (1983) was that at a central blocking latitude, defined as 50 ^{o} N, the mean zonal flow must be easterly between 40 ^{o} N and 60 ^{o} N. Furthermore, the mean wind direction averaged over 10 ^{o} W to 10 ^{o} E of the grid point of interest must be negative.

Tibaldi and Molteni (1990) made an important development on the work by Lejenäs and Økland (1983). Tibaldi and Molteni (1990) recognised that the central blocking latitude could migrate, allowing this central latitude to migrate by 4 ^{o}. Such an advancement is an important recognition of the latitudinal variability in the location of the EDJ and the resultant critical lines that dictate the regions of RWB.

2.5.2 The PV Perspective of Rossby Wave Breaking

Following the identification of PV as an important diagnostic in identifying synoptic weather systems by Hoskins et al (1985), ideas on blocking identifications changed. Instead of the Rex (1950) framework, Pelly and Hoskins (2003) identified θ on the dynamical tropopause as a diagnostic capable of capturing the overturning associated with RWB more accurately.

Pelly and Hoskins (2003) titled their paper "A New Perspective on Blocking", which has since proven to alter the manner in which blocking is identified. Equation 2.7 and accompanying Fig. 2.4 show how the θ-2PVU metric is used to calculate the blocking index, $B_{i,t}$, where φ represents latitude, φ_0 represents the central blocking latitude and $\Delta\varphi$ represents a 30° latitudinal extent.

$$B_{i,t} = \frac{2}{\Delta\varphi}\int_{\varphi_0}^{\varphi_0+\frac{\Delta\varphi}{2}} \theta_{ijt}\, d\varphi - \frac{2}{\Delta\varphi}\int_{\varphi_0-\frac{\Delta\varphi}{2}}^{\varphi_0} \theta_{ijt}\, d\varphi \qquad Eq.\,2.7$$

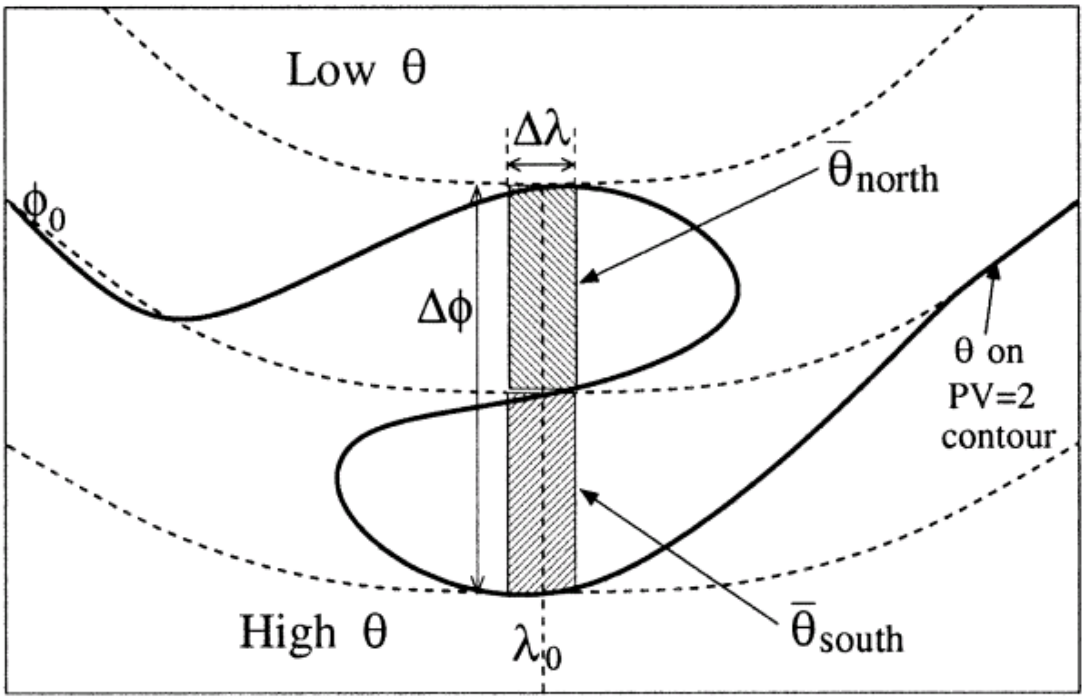

Figure 2.4. A schematic of potential temperature (θ) overturning on the dynamical tropopause (2PVU) taken from Fig. 2 in Pelly and Hoskins, (2003). The solid contour represents the θ-2PVU contour and the dashed lines represent latitude circles. The figure also depicts latitude and longitude extents, as $\Delta\Phi$ and $\Delta\lambda$, with the central longitudinal and central latitudinal points, identified as λ_0 and φ_0 respectively.

Equation 2.7 was used by Pelly and Hoskins (2003) to identify overturning of the θ-2PVU contour, as illustrated in Figure 2.4. As seen in both Eq. 2.7 and Figure 2.4, $\Delta\varphi$ represents the latitudinal extent over which Pelly and Hoskins (2003) used to identify an overturning event. The latitudinal extent that Pelly and Hoskins (2003) used was 30°, with the mean θ of the 15° north of φ_0 subtracted from the mean θ of the 15° to the south of φ_0. The central blocking latitude in Pelly and Hoskins (2003) is defined as the latitude with the greatest annual mean

high-pass transient eddy kinetic energy. This latitude is intended to represent the maxima in synoptic storm activity associated with the EDJ. If B in Eq. 2.7 is positive, this indicates a meridional reversal of the θ-2PVU contour as pictured in Fig. 2.4.

Pelly and Hoskins (2003) included a temporal persistence that must be adhered to for blocking to be identified. Pelly and Hoskins (2003) used a temporal persistence of 4 days, as opposed to the 10 days used by Rex (1950), who also used a much larger spatial scale. Furthermore, unlike Rex (1950), Pelly and Hoskins (2003) allowed the block to migrate. A sector blocking episode was defined as a longitudinal band of 20 ^{o} centred on the point of overturning, The 4 days persistence criteria is applied within this 20 ^{o} sector of blocking and if overturning reoccurs within this sector, this is seen as a continuation of the original block. Blocking episodes are therefore defined as events where blocking is identified within the migrating (after each day) sector blocking region for 4 continuous days.

2.5.3 The Blocking Index – Masato et al., (2012) & (2013)

Following the work of Pelly and Hoskins (2003), M12 generated a Blocking Index. Like Pelly and Hoskins (2003), M12 used the meridional gradient of θ-2PVU to identify RWB. Both Pelly and Hoskins (2003) and M12 identified RWB about a central blocking latitude. Consequently, as the index is confined to one latitude, this index is a 1D blocking metric. M13 spatially extended the 1D blocking index in M12 to a 2D blocking index. The 2D Blocking Index is accompanied by two further 2D metrics in M13, which aid to classify the type of RWB. These additional metrics are; the direction of breaking (DB) index and the Relative Importance of air masses (RI) index and are described in Sect. 2.6.2 and 2.6.3 respectively.

Similarly to Pelly and Hoskins (2003), M13 defined a temporal elongation for blocking to be identified again within a migrating sector blocking region. Unlike the 4 days used in Pelly and Hoskins (2003), M13 used 5 days to define a block.

2.6 Blocking Metrics used in this study

Three blocking metrics are used to identify RWB within this study. All three of these were introduced by M13 and are calculated on the $\theta - 2PVU$ surface, introduced in Sect. 2.2.10.

2.6.1 The 2D Blocking Index

The metric used in this study to represent RWB is the 2D Blocking Index (BI). The BI calculates the meridional overturning of potential temperature on the dynamical tropopause, with positive values representing overturning and RWB. Equations 2.8 and 2.9 represent mean θ ($\bar{\theta}$) in the 15^{o} latitude (φ) to the north/south of the grid point of interest, respectively.

i and j represent longitudinal and latitudinal coordinates and $\Delta\varphi$ is a 30° latitudinal extent about the latitude of the analysed grid-point (φ_0). The calculation of BI is shown in Eq. 2.10 as simply the difference between $\bar{\theta}$ in the 15° to the north and south of the grid point of interest.

$$\bar{\theta}^{n}_{i,j,t} = \frac{2}{\Delta\varphi}\int_{\varphi_0}^{\varphi_0+\frac{\Delta\varphi}{2}} \theta_{ijt}\, d\varphi \qquad Eq.2.8$$

$$\bar{\theta}^{s}_{i,j,t} = \frac{2}{\Delta\varphi}\int_{\varphi_0-\frac{\Delta\varphi}{2}}^{\varphi_0} \theta_{ijt}\, d\varphi \qquad Eq.2.9$$

$$BI_{ijt} = \bar{\theta}^{n}_{i,j,t} - \bar{\theta}^{s}_{i,j,t} \qquad Eq.2.10$$

It is important to note that for all values of θ, a longitudinal running-mean filter of 17.5 ° has been applied to the calculated fields for θ-2PVU. The longitudinal filter removes the influence of small-scale transient features, on the θ-2PVU field.

Inter-annual variability has been removed throughout the θ-2PVU dataset for each grid point. This removal procedure is important in the calculation of the RI in Sect. 2.6.3, with biases in RI corresponding to the magnitude and sign of the inter-annual trend of θ-2PVU. The inter-annual cycles have been removed by removing annual mean θ-2PVU anomalies throughout the entire dataset, relative to a 21 year mean θ-2PVU for each grid point (DJF from December 1998 to February 2009). The magnitude of the largest Northern hemispheric mean θ-2PVU removed for a single year is 0.29 K, which is 0.88% of the mean θ-2PVU value for the Northern Hemisphere of 329.98 K.

2.6.2 The Direction of Breaking Index

A concept that has received some attention in recent research (Weijenborg et al., 2012, M13 and Gabriel and Peters, 2008) is the direction in which a Rossby wave breaks. It is understood that the mechanical shear associated with the position of the EDJ (Sect. 2.3.5) will impart a cyclonic/ anticyclonic vorticity anomaly on the poleward/ equatorward flank of the EDJ. Consequently, there are contrasting most frequent regions of occurrence for both cyclonically and anticyclonically breaking Rossby waves.

The metric used to determine the direction of breaking is the 2D Direction of Breaking Index (DB Index) used in M13. Unlike the BI, which calculated the meridional θ-2PVU gradient, the DB Index measures the zonal gradient of θ-2PVU. Equation 2.11 describes the calculation of $\bar{\theta}$, which is the mean θ throughout the 30° latitude band, centred on the grid point of interest. Equation 2.11 makes use of the calculation of $\bar{\theta}^{n}_{i,j,t}$ and $\bar{\theta}^{s}_{i,j,t}$ from Eq. 2.8

and 2.9. Equation 2.12 describes the calculation of DB, which subtracts $\bar{\theta}$ to the west of the grid point of interest by $\bar{\theta}$ to the east.

$$\bar{\theta}_{i,j,t} = \frac{\bar{\theta}^{n}_{i,j,t} + \bar{\theta}^{s}_{i,j,t}}{2} \qquad Eq.2.11$$

$$DB_{i,j,t} = \bar{\theta}_{i-1,j,t} - \bar{\theta}_{i+1,j,t} \qquad Eq.2.12$$

M12 used a threshold of $|DB| > 0.2$ K to diagnose either anticyclonic RWB (ACRWB) (DB > 0.2 K) or cyclonic RWB (CRWB) (DB < -0.2 K). This threshold was implemented following an observation in M12 that overturning with weak anticyclonic or cyclonic tendency can switch between anticyclonic and cyclonic. This can occur in RWB infancy, as the wave can re-break in the opposite direction following initial breaking, given a change in the direction of the background shear.

The DB metric in this study is used to categorise the spatial patterns associated with RWB events and to not necessarily categorise RWB events themselves. In most cases a RWB event with a cyclonic (DB < -0.2 K) breaking signal will break cyclonically. Despite this there are occasions whereby a Rossby wave will exhibit both cyclonic and anticyclonic signals prior to its breaking. This is the case in the LC1 RWB lifecycle previously discussed in Sect. 2.3.5 (Thorncroft et al., 1993; Gabriel and Peters, 2008). This study will continue to use the ACRWB and CRWB terminology for RWB events which exhibit a DB > 0.2 K or DB < -0.2 K signal, however this does not necessarily mean that the signal detected is representative of the direction in which the Rossby wave breaks.

A further consideration that must also be taken into account is the use of these RWB metrics when applied to an atmospheric block. These metrics are used to classify an Omega block in Chapter 3, which has both cyclonic and anticyclonic DB signals. Therefore this study makes no attempt to re-classify atmospheric blocking types, but to use this metric in an attempt to identify atmospheric blocking events that lead to elevated UK [PM10].

2.6.3 The Relative Intensity of Air Masses Index

The third metric used in this study to categorise RWB is called the Relative Intensity of Air Masses Index (RI). M13 introduced the RI index to determine whether a RWB event is more influenced by warm or cold air masses. Aside from the study undertaken by M13, limited literature exists that discusses the concept of warm and cold RWB. Gabriel and Peters (2008) distinguished between poleward and equatorial breaking Rossby waves. This methodology is not directly comparable to the RI Index, although the intended outcome is the same. Equatorial and poleward breaking Rossby waves in Gabriel and Peters (2008) described

RWB events that resulted predominantly in cut-off cyclones and anticyclones respectively. M13 described cold and warm RWB events in a similar manner. In the RI framework, cold RWB events are described as RWB events where cold, poleward air dominates warm, equatorial air. Subsequently, these events were shown to result in dominant cut-off low pressure systems to the south of the central point of overturning. Alternatively, warm RWB events are subsequently dominated by warm, equatorial air and result in dominant cut-off high pressure systems to the north of the central point of overturning.

To calculate the RI metric, first calculate the climatological $\bar{\theta}$ for each 2D grid point. This value is then subtracted from a time-series mean $\bar{\theta}$ (θ^*) for each 2D grid point, to determine a $\bar{\theta}$ anomaly for each grid point at any given time. M13 defined θ^* from 44 years of the most recent European Centre for Medium-Range Weather Forecasts (ECMWF) re-analysis product (ERA-Interim) winter (DJF) analysis data (Dee et al., 2011). This study calculates θ^* from 19 years of winter (DJF) θ-2PVU 2D fields, between December 1990 and February 2009.

Equation 2.13 details the calculation of the RI metric. A positive/ negative RI value represents an anomalously warm/ cold RWB event.

$$RI_{i,j,t} = \bar{\theta}_{i,j,t} - \theta^*_{i,j} \qquad Eq.2.13$$

As for the DB Index, this study uses a magnitude threshold of 0.2 K to determine warm (> 0.2 K) or cold (< -0.2 K) RWB. Anything that lies between these thresholds remains unclassified, as there is no clear warm or cold signal and a potential for the sign of the RI metric to change throughout the RWB induced blocking episode.

Section 2.6.1 referred to the removal of inter-annual θ-2PVU variability and that this is important for calculation of the RI index. The magnitude of the largest annual θ-2PVU anomaly (0.285 K in DJF 2008-2009) is comparable to the magnitude of the RI values that this study classes as unclassified (-0.2 K <RI<0.2 K). A simple calculation can be made to determine how many RI values would change classification if this bias were removed. Over the UK Midlands grid point, 8.9 % of RI Index values in this year are between -0.2 K and 0.085 K , which if the 0.285 K value is subtracted would become cold RWB events as opposed to unclassified RWB events. Similarly, 18.9 % of RI Index values in this year are between 0.2 K and 0.485 K, which if 0.285 K was subtracted would become unclassified RWB events, as opposed to warm RWB events. Subsequently, in DJF 2008-2009 the removal of inter-annual cycles in this study has altered the RI Index classification of 27.8 % of days over the UK Midlands grid point.

2.6.4 Blocking Metrics Summary

As yet, the blocking metrics used to identify RWB leading to atmospheric blocking, unlike the other atmospheric blocking metrics discussed in Section 2.5, do not include a persistence criteria. Throughout the study the impact of persistence will be alluded to, however no strict persistence criterion is used. The reasoning for negating a persistence criterion is that this study intends to determine the instantaneous impact of RWB. By the instantaneous impact, this author refers to the removal of the EDJ from the UK region through the RWB mechanisms best described by Rex (1950) (a latitudinal separation of westerly flow).

As three RWB metrics are used, there exists five possible definitions and synoptic subsets. The first of these is where the BI is negative, whereby zonal flow dominates over that selected grid point. When BI is positive, the DB Index and RI Index indicate whether the RWB event belongs to one of these four subsets: warm anticyclonic, cold anticyclonic, warm cyclonic or cold cyclonic RWB. The 2D frequencies of all cyclonic and anticyclonic RWB events are discussed in Section 2.7.1. Following this a similar procedure will explore the frequencies of all warm and cold RWB in Section 2.7.3.

2.7 RWB Subset Frequencies

This section aims to present the regions of most frequent occurrence for four RWB subsets: warm anticyclonic, cold anticyclonic, warm cyclonic or cold cyclonic RWB. The mechanisms that lead to differences in the regions of most frequent occurrence, for each RWB subset, will be discussed. Table 2.1 defines the thresholds imposed on the: BI, DB and RI Indices, which are used to classify RWB into four subsets.

Table 2.1. Defining Rossby wave breaking (RWB) types using thresholds of the direction of breaking (DB) and relative influence of air masses (RI) indices. Any RWB with DB or RI values of -0.2 K ≤ DB/RI ≤0.2 K are determined as unclassified following Masato et al., (2012).

Rossby Wave Breaking Subset	Blocking Index (BI)	Direction of Breaking Index (DB)	Relative Influence of Air Masses Index (RI)
Warm Anticyclonic	> 0 K	> 0.2 K	> 0.2 K
Cold Anticyclonic	> 0 K	> 0.2 K	< -0.2 K
Warm Cyclonic	> 0 K	< -0.2 K	> 0.2 K
Cold Cyclonic	> 0 K	< -0.2 K	< -0.2 K

2.7.1 Direction of Breaking - Regions of Occurrence

Figures 2.5 (a) and (b) show this study's ACRWB and CRWB occurrence frequency throughout the Northern Hemisphere in ERA-Interim re-analysis data. RWB frequency is calculated from daily mean data between December 1990 and February 2009 and only incorporates winter (DJF) RWB.

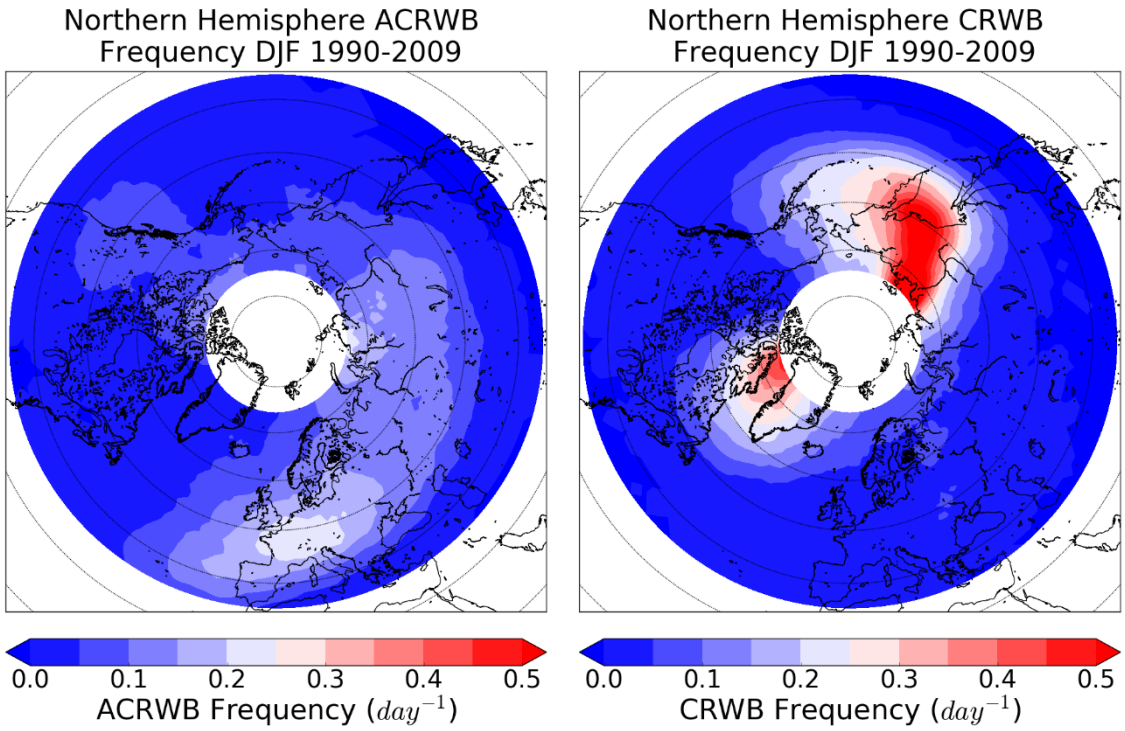

Figure 2.5. (a) Anticyclonic (ACRWB) and **(b)** cyclonic (CRWB) Rossby wave breaking daily frequency (day^{-1}) in the ERA-Interim reanalysis dataset for the winter months (DJF) between December 1990 and February 2009.

Figures 2.5 (a) and (b) show the frequency of RWB where DB > 0.2 K and DB < -0.2 K, respectively and BI> 0 K. Initially evident are the contrasting regions of frequent ACRWB and CRWB in Figures 2.5 (a) and (b). The most prominent region of ACRWB occurrence in the Northern hemisphere is seen to be over Western Europe. This region of elevated ACRWB frequency extends east from Western Europe throughout the Eurasian continent. A second maxima in ACRWB frequency can be seen at high latitudes on the Eurasian continent over Siberia. In the Pacific region, the region with greatest ACRWB frequency is shown to be the East Pacific/ west coast of North America.

The greatest region of CRWB occurrence is seen over Eastern Russia and the Pacific basin. In the North Atlantic basin, CRWB is seen to occur most frequently over the West Greenland region.

2.7.2 Dynamics and Discussion

It is shown that regions of CRWB and ACRWB are spatially separate, with CRWB occurring predominantly poleward of ACRWB. Section 2.3.5 introduced the mechanism by which a meridional zonal shear is imparted on the background flow, relative to the position of the EDJ. The latitudinal separation of ACRWB and CRWB can be attributed to the reversal in

the sign of anomalous absolute vorticity to the north and south of the EDJ, as illustrated in Fig. 2.2.

Focussing on the North Atlantic/ European region, there exists a longitudinal separation between the most frequent regions of CRWB and ACRWB occurrence. This study, M13 and Weijenborg et al. (2012) all find that, within the North Atlantic region, the most prominent region of CRWB is found in the northwest Atlantic, whereas ACRWB is most prominent over the northeast Atlantic/ European region. RWB is statistically most frequent downstream from regions of Rossby wave generation. In the North Atlantic the statistically most frequent region of Rossby wave generation is over the baroclinic region of northwest Atlantic/North America (Sect. 2.3.3). Consequently, as Rossby waves grow in scale eastward across the North Atlantic, the most frequent region of RWB is in the northeast Atlantic region. This mechanism can explain the increase of ACRWB in the northeast Atlantic region (Barnes and Hartmann, 2012), however not the CRWB frequency maxima in the northwest Atlantic.

The longitudinal separation between regions of ACRWB and CRWB occurrence can be attributed in most part due to the tilt of the EDJ across the North Atlantic basic. The EDJ is on average tilted in the southwest-northeast direction across this basin. Consequently, the EDJ is found at its most southerly latitude in the western North Atlantic basin and its most northerly latitude, in the eastern North Atlantic basin. The critical layer/latitude where RWB occurs is situated to the north and south of the EDJ and dictates where RWB occurs (Sect. 2.3.5). For CRWB occurring to the north of the EDJ, this critical layer is occasionally pushed too far poleward in the northeast Atlantic region. Hitchman and Huesmann (2006) show how the latitudinal gradient of f decreases poleward (the β-effect, Sect. 2.3.3), resulting in reduced Rossby wave propagation towards the North Pole. A reduction of Rossby wave propagation results in a reduction of RWB within the region. Instead of Rossby waves breaking to the poleward side of the EDJ, Barnes and Hartmann (2012) highlight that Rossby waves reach a turning latitude whereby their propagation becomes equatorward. These Rossby waves are subsequently seen to break on the equatorward side of the jet with an anticyclonic direction of breaking.

M13 presented the contrasting synoptic regimes resulting from West Greenland CRWB and northeast Atlantic/ European ACRWB. The synoptic responses are portrayed as geopotential height anomalies on the 500 hPa pressure field (Z500), but could as easily be presented as MSLP anomalies, which are analogous. Furthermore, in M13, the greatest Z500 responses to RWB, were found following a 2-day lag, accounting for the time between RWB occurrence at 500 hPa and the greatest surface meteorological anomalous response. Figures 2.6 (a), (b)

and (c) show the composite 2D Z500 fields for the North Atlantic/ European region, for warm and cold ACRWB and CRWB, averaged over days 0-6 following the onset of RWB. Figure 2.6 also shows the: $\theta - 2$PVU, 2 m temperature and precipitation fields, averaged over the same 6-day period.

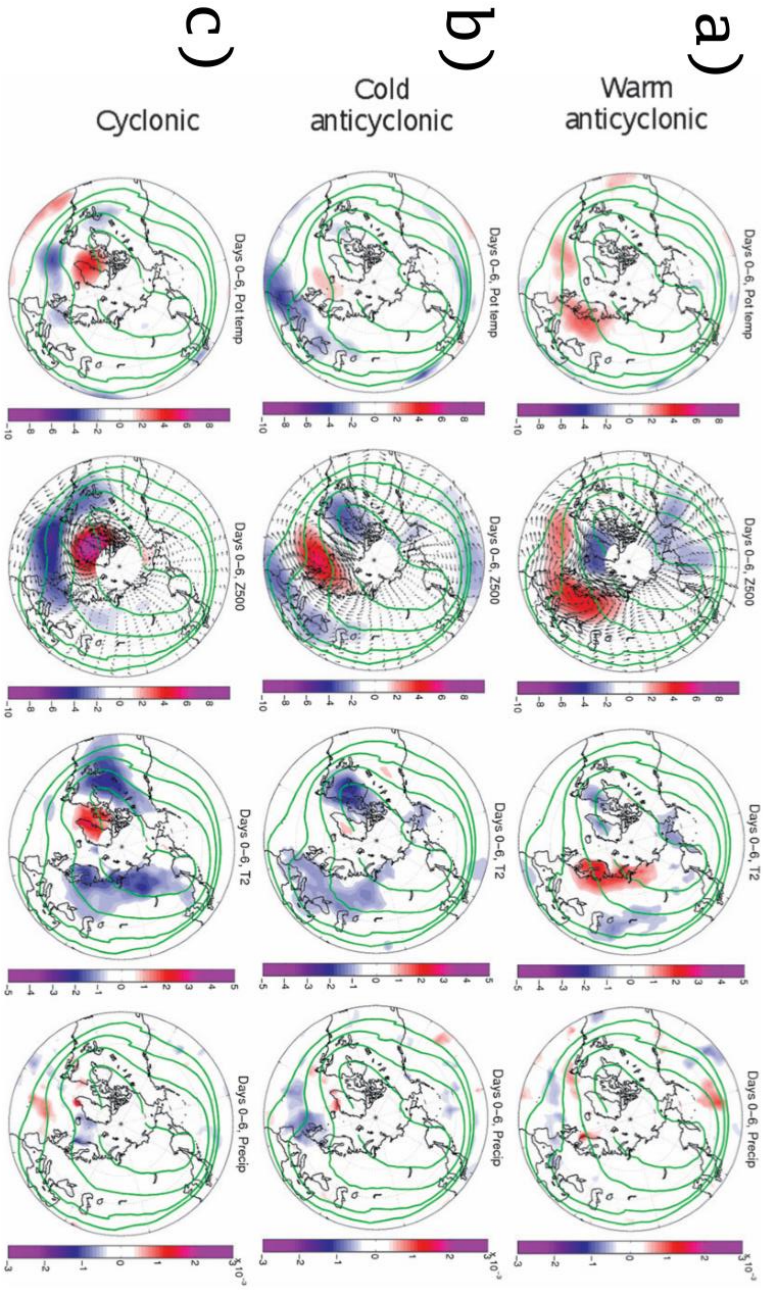

Figure 2.6 Figure 10 by Masato et al., (2013a). Four meteorological fields averaged over days 0-6 following the detection of: **(a)** Warm ACRWB, **(b)** Cold ACRWB and **(c)** CRWB events. The meteorological fields shown are: Potential temperature on the dynamical tropopause (Pot Temp, K), Geopotential height at 500 hPa (Z500, dam), temperature at 2m (T2, K) and Precipitation (Precip, m).

Figure 2.6 (a), (b) and (c) show the geopotential height at 500 hPa (Z500) response to three RWB subsets, averaged from the day of RWB detection to 6 days later. In comparing both ACRWB subsets to the CRWB subset, it is evident that there are differences in the synoptic meteorology influencing the UK. The ACRWB subsets both result in an increased Z500 over the UK, which is associated with a negative precipitation anomaly over the northeast Europe region at the same latitude as the UK. CRWB within the North Atlantic basin results in a reduction of Z500 over the UK, associated with a small positive precipitation anomaly at the latitude of the UK.

For northeast Atlantic/ European ACRWB, M13 showed that a positive Z500 anomaly over Scandinavia and the UK resulted. The associated negative UK precipitation anomaly is a result of the displacement of the EDJ and the associated storm track. This synoptic situation is the classical atmospheric block, whereby the influence of the block is felt directly by the displacement of the storm track from the blocked region.

For northwest Atlantic CRWB, M13 showed that the classical Z500 dipole pattern from Rex (1950) emerges. A Z500 dipole anomaly centred over Western Greenland, extends meridionally into the North Atlantic basin. The mechanism by which northwest Atlantic RWB influences Western European meteorology is through a displacement of the EDJ. The presence of a Z500 dipole in the northwest Atlantic acts to supress the southwest/northeast tilt of the EDJ and the jet moves into its southerly state (Woollings et al., 2010b). The result of this migration is a reduced Z500 over the UK, which is coupled with increased zonal wind speeds and precipitation over the UK.

2.7.3 Relative Importance of Air Masses Index - Regions of Occurrence

As in Sect. 2.7.1, the most frequent regions of occurrence for warm and cold RWB will be evaluated in this section, for winter months (DJF), between December 1990 and February 2009. Subsequent discussion will hypothesise the effect of each RWB subset on UK [PM10].

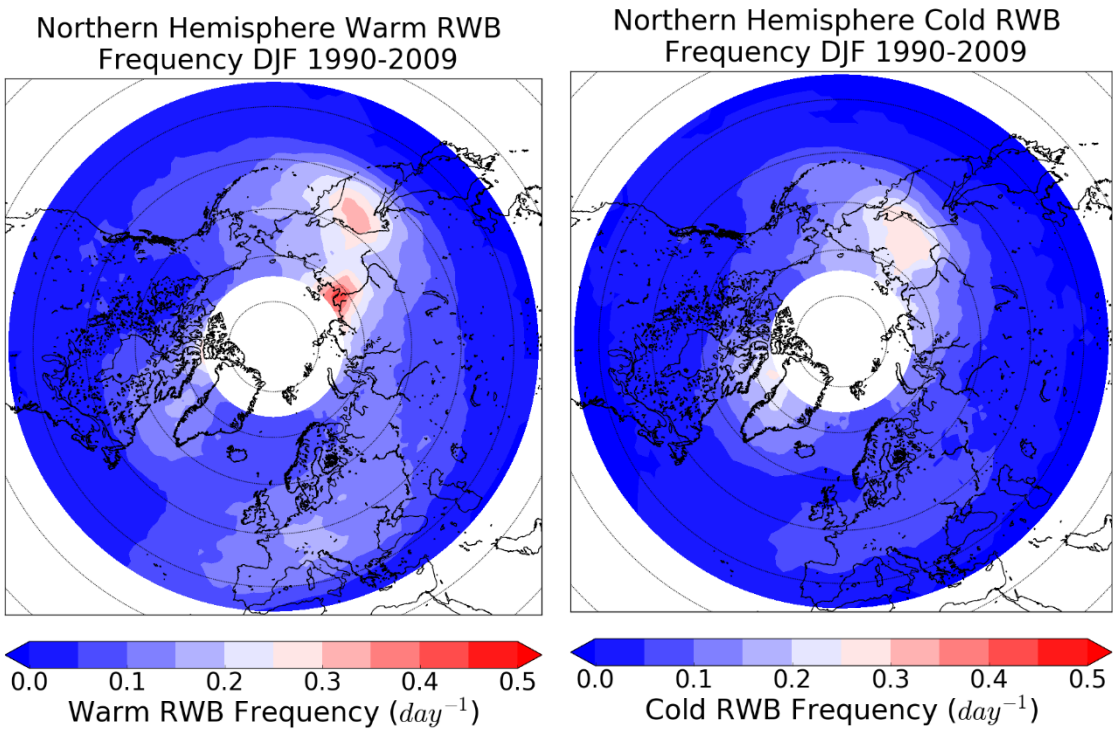

Figure 2.7. This study's **(a)** warm and **(b)** cold Rossby wave breaking daily frequency in the ERA-Interim reanalysis dataset for the winter months (DJF) between December 1990 and February 2009.

Figure 2.7 (a) and (b) show the frequency of Northern Hemisphere warm and cold RWB respectively. Much like in the case of ACRWB and CRWB, there appears to be a latitudinal separation between the regions of warm and cold RWB occurrence. In the northwest Atlantic, over Western Greenland, there appears to be a tendency towards cold RWB. Contrastingly, over the northeast Atlantic/ European region, there appears to be a tendency towards greater warm RWB occurrence.

2.7.4 Discussion & Dynamics

This study's most frequent regions of warm and cold RWB have been presented in Sect. 2.7.3. This study finds that there is a tendency towards cold RWB in the West Greenland region, coinciding with the most frequent region of CRWB in Fig. 2.5. M13 does not explore the differences in North Atlantic cold and warm CRWB, however the analogous diagnostics used by Gabriel and Peters (2008) may offer a comparison. Gabriel and Peters (2008) defined cyclonic RWB subsets as: LC2 (cold) and P1 (warm). They show that the LC2 RWB subset is more frequent than the P1 subset in the Western Greenland region, with P1 events occurring further south, which is consistent with this study's findings.

In the region identified as the most frequent region of ACRWB in Fig. 2.5, it is found in Fig. 2.7 that warm RWB is more prominent. Gabriel and Peters (2008) defined anticyclonic RWB subsets as: LC1 (cold) and P2 (warm). They show that the P2 RWB subset is more frequent than the LC1 subset in the northeast Atlantic/ European ACRWB maxima. This result is not in agreement with M13, as M13 find a preference towards a higher frequency of cold ACRWB within this region. The difference in results between M13 and Fig. 2.7 in this study is perhaps a little surprising as the same RWB metrics are used in both studies. Despite this, M13 uses a persistence criteria of 5 days, which this study does not, which may explain the difference in results. M13 find that cold ACRWB events are more persistent than warm ACRWB events and due to the 5-day RWB persistence threshold used by M13, this may suggest why M13 identify a higher frequency of cold ACRWB events in this region.

Both M13 and Gabriel and Peters (2008) find that there are marked differences in the synoptic meteorological pattern, which results from warm and cold RWB events. Both studies find that warm RWB events have a greater tendency for a more pronounced anticyclone, while cold events often lead to a more pronounced cut-off cyclone. These differences suggest that in Chapter 3, when relating RWB to UK [PM10] that warm RWB events occurring over the northeast Atlantic/ European region will result in conditions more favourable to the accumulation of UK PM10.

The differences in the locations of warm and cold RWB events are found to be less pronounced than those for the direction of RWB in Fig. 2.5. Despite this, differences in the synoptic meteorology that results from warm and cold RWB events, with regards to preferences towards a persistent anticyclone/ cyclone for warm/ cold events, may alter their effects on UK [PM10]. Chapter 3 will explore the relationships between each of the four RWB subsets and UK [PM10]. It is hypothesised that warm RWB events will be more influential on UK [PM10], due to their preference in generating a persistent anticyclone. However, Fig. 2.5 and 2.7 have shown comparatively small differences in the regions of most prominent cold and warm RWB, compared to the differences in cyclonic and anticyclonic RWB. Consequently, it is anticipated that the greatest differences in UK [PM10] will be seen when comparing CRWB and ACRWB. It is anticipated that northeast Atlantic/ European ACRWB events will be associated with the greatest UK [PM10], due to the proximity of their most frequent region of occurrence to the UK.

2.8 Summary

Chapter 2 has highlighted the synoptic meteorological variability that will likely influence UK [PM10]. Following the analysis by Charney and DeVore (1979) two principal states of synoptic meteorology, which influence the UK, have been identified. One of these is a zonally stratified flow, which is associated with the presence of the EDJ over or near the UK. This chapter has emphasised the relationship between the EDJ and the storm track, which provide synoptic meteorological conditions that are conducive to the dispersion of PM10. This study has identified RWB as the synoptic meteorological variable that can describe the two states of synoptic meteorological variability introduced by Charney and DeVore (1979).

This chapter has introduced the diagnostics used to identify RWB within this study. The diagnostics used were originally introduced by M13, however are based on diagnostic techniques that date back to Rex (1950). Three RWB metrics have been introduced, which subset RWB into four categories: warm anticyclonic, cold anticyclonic, warm cyclonic and cold cyclonic RWB.

2D frequency maps of each of the four RWB subsets listed have been presented and compared to those from M13. Clear differences in the regions of predominant CRWB and ACRWB have been identified and are associated with a meridional zonal shear on the background flow, associated with the position of the EDJ. Differences in the location of warm and cold RWB were less pronounced, however it was found that warm RWB subsets were associated with a more pronounced blocking anticyclone, whereas cold RWB subsets were associated with a more pronounced cut-off cyclone.

Chapter 3 – Relationships between UK PM10 and RWB

3.1 Introduction

The results reported in this chapter are largely based on the results published by Webber et al. (2017).

The role of synoptic meteorology on atmospheric pollutants is often overlooked in relation to the contribution of local sources, sinks and smaller scale boundary layer transport processes. This study aims to quantify the role of synoptic meteorology on this study's pollutant of interest, PM10.

Chapter 1 introduced the pollutant, PM10, and highlighted that it comprises of a number of constituents from varied source regions. PM10 was chosen as the subject of analysis in this study due to its detrimental effects on human health (Sect. 1.7), with the potential to travel down the human respiratory tract and become toxic to humans.

Chapter 2 evaluated synoptic meteorological variability that affects the Northern hemisphere mid-latitudes and the UK. Section 2.3 highlighted that two principal modes of synoptic meteorological variability exist; zonally stratified and blocked flow. The meteorological conditions associated with both of these fundamental modes of variability were discussed, with blocked flow being associated with conditions that are more conducive to the accumulation of UK PM10 (Sect. 2.1). Altenhoff et al. (2008) highlighted that in the Northern hemisphere winter months, RWB is an important precursor to atmospheric blocking. RWB was therefore selected as the metric which is used to describe the variability in Northern Hemisphere Mid-Latitude synoptic meteorology.

3.2 Method

In this chapter we examine the relationship between RWB and UK [PM10]. To diagnose RWB, three metrics were introduced in Sect. 2.6; BI (Sect. 2.6.1), DB Index (Sect. 2.6.2) and RI Index (Sect. 2.6.3). These three metrics are used to generate four RWB subsets; warm anticyclonic (WACRWB), cold anticyclonic (CACRWB), warm cyclonic (WCRWB) and cold cyclonic (CCRWB). The relationship of each of the four RWB subsets with [PM10] will be determined in this chapter.

The RWB metrics are calculated for each day on the θ-2PVU field, introduced in Sect. 2.2.10. Consistent with Wilcox et al. (2012), the study's purely dynamical definition of the tropopause is associated with limitations. Tropopause folding near the subtropical jet creates spurious grid points with a much changed θ-2PVU value to the neighbouring grid points. This effect can be seen in Appendix A, which also highlights that a 350 K threshold on the θ-2PVU field improves the magnitude of the difference of spurious θ-2PVU grid points with the neighbouring grid points. The 350 K threshold has been applied to all θ-2PVU fields within this analysis.

The PM10 dataset used in this study was introduced in Sect. 1.6. Three UK Midlands urban background PM10 sites were used to generate a tri-site urban background site. Using three urban background sites to generate a single [PM10] dataset allowed for the removal of PM10 spikes from each dataset. Section 1.6.3 showed that this procedure allowed for each contributing PM10 dataset to better compare with the other two contributing sites and subsequently be more representative of a general UK Midlands urban area.

Within this chapter, much of the focus will be on identifying RWB events that lead to an increase in UK Midlands PM10 episode frequency. Section 1.7.4 showed how this study defines a PM10 episode, as a 10 μg m^{-3} exceedance above a mean [PM10] $\left(\overline{[PM10]}\right)$. The tri-site UK Midlands $\overline{[PM10]}$ for the period of this study is 19.72 μg m^{-3} or $\ln\overline{[PM10]}$ = 2.98. An exceedance using this UK Midlands dataset is 29.72 μg m^{-3} or ln[PM10] = 3.39.

The concept of a temporal lag between RWB and UK [PM10] has been explored in this study. The strongest relationships between RWB and UK [PM10] were found following a 1-day lag between the onset of RWB and UK [PM10]. This temporal lag accounted for the time taken for European PM10 to advect into the UK and for the UK to subsequently be exposed to a new air mass. Therefore, following the diagnosis of RWB, UK Midlands [PM10] was taken one day subsequent to allow for this lag in changing flow regime. In events where RWB was not diagnosed (negative BI values), it was found that a 0-day lag provided the best relationships between RWB and [PM10]. Negative BI values are associated with westerlies entering the UK, which provide increased PM10 wet deposition (Sect. 1.3.2) and increased PM10 dispersion, both lowering [PM10]. These removal processes reduce surface [PM10] on timescales of less than a day and hence a lag of 0 days between negative BI values and resultant UK [PM10] is used in this analysis.

3.3 Results

Section 3.3 presents the main results from this study. Section 3.3.1 begins by analysing the relationship between BI and UK Midlands [PM10]. Section 3.3.2 presents regions where RWB occurrences result in significantly elevated UK [PM10]. This analysis is undertaken for four RWB subsets; warm anticyclonic, cold anticyclonic, warm cyclonic, and cold cyclonic RWB. Section 3.3.3 analyses the MSLP response to both ACRWB and CRWB, subsequently inferring the flow regimes resulting from these RWB subsets. The most important result from this study is presented in Sect. 3.3.4 and refers to the probability that days on which RWB occurs, lead to hazardous PM10 threshold exceedances. A RWB subset that results in the greatest probability of exceeding a hazardous UK [PM10] threshold is examined in more detail in Sect. 3.3.5. The mechanism dictating the occurrence of this RWB subset is presented in Fig. 3.6 and discussed from Sect. 3.3.5 onwards.

3.3.1 2D Spatial Relationship between BI and UK PM10

Figure 3.1 illustrates the relationship between BI magnitude and UK [PM10]. At each grid point the Pearson correlation coefficient between BI at that grid point and PM10 at the central UK Midlands site is shown. A region of positive correlation is found centred over the English Channel and two regions of negative correlation are found north and south of this positive correlation region. The region of positive correlation is a result of one of three potential mechanisms, (i) RWB increases the number of high [PM10] events, (ii) RWB reduces the number of low [PM10] events, or (iii) a combination of (i) and (ii). By analysing the BI-[PM10] relationship at individual grid points within the region of positive and negative correlation, we can determine which of these mechanisms dominate the relationship.

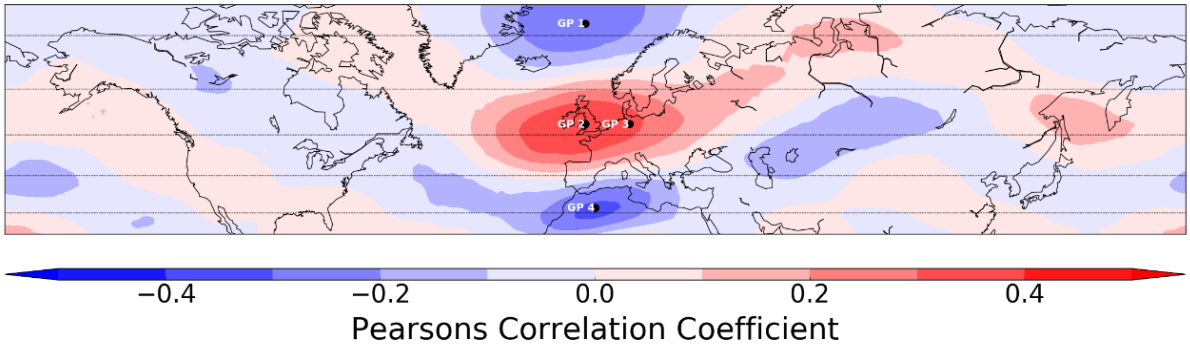

Figure 3.1 Pearson correlation coefficient between Blocking Index magnitude (Kkm^{-1}) and UK [PM10] ($\mu g\ m^{-3}$) in the UK Midlands region. All data was taken for the winter months (DJF) between January 1999 and December 2008. PM10 data following a positive/ negative BI value was lagged by 1/0 days respectively. Grid points (GP) selected for further analysis are labelled GP 1 to 4.

In order to understand the patterns in Fig. 3.1, four grid points were selected and labelled grid point (GP) 1 to 4 on Fig. 3.1. GPs 1 and 4 were selected because they lie within two separate regions of negative correlation, while GPs 2 and 3 both lie within the region of positive correlation. Figure 3.2 analyses the correlation between BI and UK [PM10] at the four selected GPs. In Fig. 3.2 the relationships between UK [PM10] and positive and negative BI values are analysed independently, which may elucidate on the mechanisms that dictate the correlations seen in Fig. 3.1.

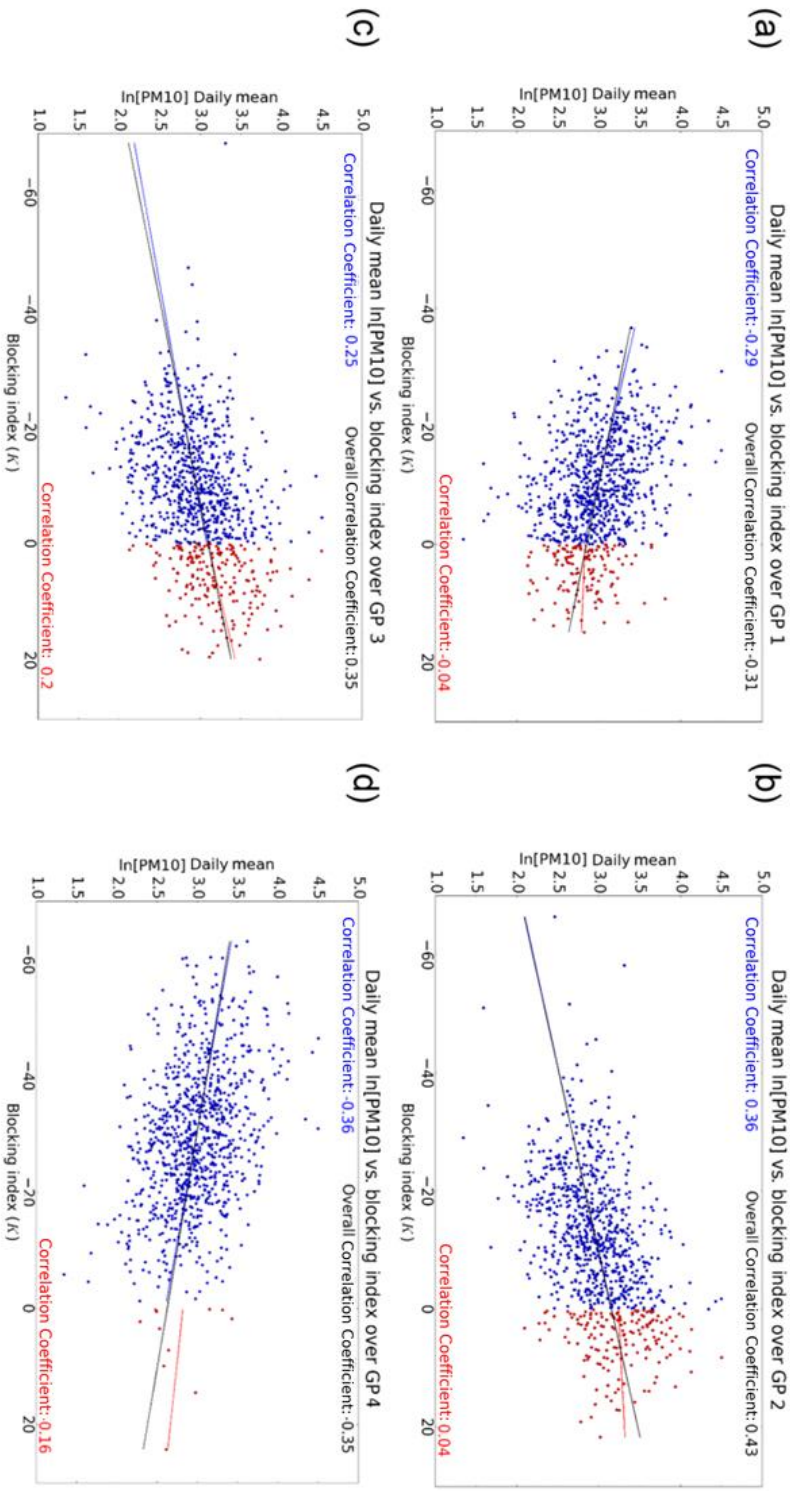

Figure 3.2 Scatter plots illustrating the relationship between daily mean Blocking Index magnitude (BI) (K) and UK [PM10] (μg m^{-3}) for four regions labelled GP 1, 2, 3 and 4 on Fig. 3.1 (Labelled a, b, c and d on Fig. 3.2). The blue/red colour corresponds to negative/ positive BI values respectively and the fitted trends are linear least-squares trends. Data was obtained for DJF January 1999 – December 2008 and [PM10] lagged by 1/0 days for positive/negative BI values respectively.

Figures 3.2 (b) and (c) highlight the positive relationships between the BI magnitude and UK [PM10] at GPs 2 and 3, with correlation coefficients (CC's) of 0.43 and 0.35 respectively. The positive relationship is a result of contributions from negative and positive BI values shown as blue and red in Fig. 3.2. In both cases, the negative BI values represent a similar positive correlation to that of the overall trend, CC = 0.36 and 0.25 for GPs 2 and 3 respectively. Based upon results of a one tailed t-test, all negative and total correlation coefficients are significantly different from zero ($p = 0.01$), with only the positive correlation coefficient for GP 3 showing a significant correlation ($p = 0.002$). For GP 2 and GP 3, variability in the negative BI values dominates the relationship between BI and [PM10]. Subsequently, with negative BI values corresponding to zonal flow, the variability in the magnitude of the zonal flow over these regions explains much of the variability in UK Midland [PM10]. GPs 1 and 4 exhibit a negative correlation between BI and PM10 (CC = -0.31 and -0.35 respectively). The negative BI values in both cases (CC = -0.29 and -0.36 respectively) display near identical relationships with UK [PM10] to the overall trend, as the correlation of BI and PM10 is dictated by negative BI values.

Despite the relationships seen between BI and UK Midlands [PM10] being dominated by negative BI values at all four selected regions, positive BI values are associated with on averaged higher [PM10] than negative BI values at GP 2 and 3. At GP 2 and 3, the increased [PM10] associated with positive BI values, indicates that RWB increases the number of high [PM10] events, despite the magnitude of positive BI values not strongly correlating with UK Midlands [PM10].

Figures 3.2 (b) and (c) are influenced by very low BI values, which appear as outliers in the general distribution. It was seen that by removing BI values < -30 K, there was very little impact on the overall CC values obtained from Fig. 3.2 (b) and (c). In Fig. 3.2 (b) and (c) the Pearson's correlation coefficient increases from 0.43 to 0.44 and from 0.35 to 0.37 respectively, following the removal of the outliers. Consequently, it has been shown that the outliers do not greatly alter the results in Fig. 3.2 (b) and (c).

With the relationship between enhanced zonal flow and low [PM10] dominating the correlations seen in Fig. 3.2, it can be presumed that the main influence upon this relationship is the EDJ. Figure 3.1 illustrates a zonal wave pattern of positive correlation between BI and UK [PM10] that is synonymous with the meandering winter EDJ location. Within this region, lie the strongest wind speeds, which are coincident with strong surface wind speeds over the

UK, during a zonal synoptic regime. As the EDJ is the dominant feature in the positive correlation between BI and UK [PM10], a positive correlation, representative of the meandering winter EDJ location, results.

3.3.2 Relationships between Rossby Wave Breaking Subsets and UK PM10

Positive BI values have been shown to be associated with above average UK [PM10] in Fig. 3.2 (b) and (c). In this section we investigate how RWB leads to raised UK [PM10]. Two criteria, described by M12 and M13, are used in this study; the DB and RI indices. Table 2.1 shows the thresholds used to define four RWB types analysed in this study.

For each day on which RWB occurs at a given grid point, the type of RWB is determined from the criteria in Table 2.1 and the corresponding ln[PM10], one day after, is stored for that RWB subset. Following this, UK $\ln[\overline{PM10}]$ for each RWB subset is calculated for every grid point. Figure 3.3 illustrates UK $\ln[\overline{PM10}]$ for the four RWB subsets listed in Table 2.1. Included in Fig. 3.3 are contoured regions representing grid points where subset $\ln[\overline{PM10}]$ is significantly greater than the $\ln[\overline{PM10}]$ for the entire dataset (described by Eq. 3.1), otherwise termed Regions of Influence. For each grid point, the standard error of the subset $\ln[\overline{PM10}]$ was calculated and multiplied by 1.96 to represent a one-tailed 99% confidence interval. Equation 3.2 describes regions where the subset $\ln[\overline{PM10}]$ is significantly less than the dataset $\ln[\overline{PM10}]$ and illustrated by a dashed black contour in Fig. 3.3. Within these equations σ represents standard deviation, N represents the number of samples within the subset or dataset, sub represents the [PM10] subset dataset and All represents the entire [PM10] dataset.

$$\overline{[PM10]}_{Sub} - \overline{[PM10]}_{All} > 1.96 \sqrt{\left(\frac{\sigma_{Sub}^2}{N_{Sub}} + \frac{\sigma_{All}^2}{N_{All}}\right)} \qquad Eq.\,3.1$$

$$\overline{[PM10]}_{All} - \overline{[PM10]}_{Sub} > 1.96 \sqrt{\left(\frac{\sigma_{Sub}^2}{N_{Sub}} + \frac{\sigma_{All}^2}{N_{All}}\right)} \qquad Eq.\,3.2$$

Contoured regions of influence were found outside of the domain shown in Fig. 3.3, but these incorporated few RWB events randomly coinciding with RWB events within the domain. To focus on the regions that are shown to be influential to UK [PM10], a longitudinal mask has been applied so that only longitudes east of 82.5° W and west of 77° E are included in this analysis.

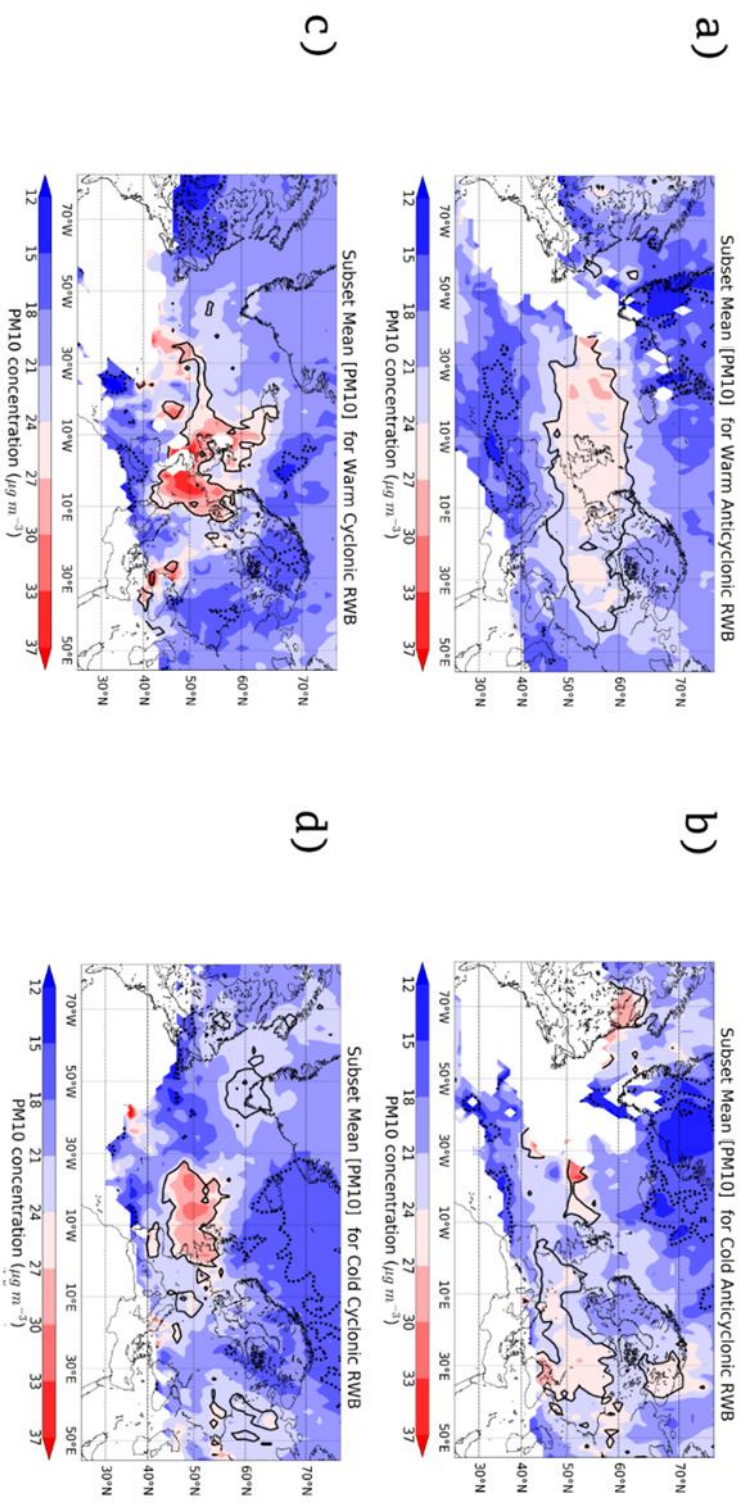

Figure 3.3 One day lagged UK Midlands mean [PM10] subset ($\overline{[PM10]}_{Sub}$) for each point within a gridded region for: (a) warm anticyclonic, (b) cold anticyclonic, **(c)** cold cyclonic and **(d)** warm cyclonic Rossby wave breaking events. Solid/dashed contours constrain regions where mean ln[PM10] for each grid point is significantly greater/lower than the entire dataset ln[PM10] mean ($p<0.01$), respectively. White grid points represent points where RWB has occurred on fewer than 2 occasions throughout DJF January 1999 – December 2008. Dataset $\overline{[PM10]}$ = 21.69 μg m^{-3}.

First of note from Fig. 3.3 are the similarities in location between the cyclonic and anticyclonic RWB regions of influence, with influential regions most prevalent within the northeast Atlantic/ European region. Climatologically CRWB occurs to the north of the EDJ, predominantly within the northeast Atlantic region (Weijenborg et al., 2012). Figure 3.3 (c) and (d) shows that warm and cold CRWB significantly raises UK [PM10], when it occurs predominantly in the northeast Atlantic/ European region and not in the northwest Atlantic region. Figure 3.3 (b) shows that warm ACRWB is the most influential RWB sub-category in terms of its regional extent, although warm CRWB exhibits the largest mean ln[PM10] magnitudes. The results from Fig. 3.3 support Fig. 3.1, as they illustrate the influence of RWB on UK [PM10], predominantly within the same region as the positive correlation in Fig. 3.1. Following Fig. 3.3, all RWB sub-categories are analysed for events occurring within their solid contoured significant regions.

3.3.3 Pressure Composites Associated with RWB Driven UK [PM10] Exceedances

M12 and M13 illustrated the climatological pressure response to each of the four RWB subsets in Table 2.1. M12 show that climatologically, CRWB exhibits a pressure dipole over West Greenland, while ACRWB results in the same dipole centred over West Europe. Fig. 3.4 illustrates composite MSLP anomalies one day after days incorporating (a) ACRWB and (b) CRWB events within their regions of influence and that lead to a UK [PM10] exceedance (ln[PM10] > 3.39) the following day.

In Fig. 3.3 for any given day, the PM10 value of that day may be placed into two or more RWB subsets, but for this analysis, only one RWB subset is elected per day based on the following criteria. Firstly the greatest BI value is found in each region of influence. This BI value must correspond to the RWB subset of the region of influence within which it was found, based on the corresponding DB and RI indices for that grid point (eg. Warm ACRWB). An occurrence threshold of 10 positive BI values, with the same DB and RI metric classifications, has been applied within the region of influence. These criteria have been applied so that the largest RWB events (greatest BI values), must occur within the region of influential RWB for that subset. Furthermore the 10 event threshold, imposes a spatial robustness for that specific RWB subset. If more than one RWB subset has occurred within its region of influence then the RWB subset occurring with the greatest magnitude of overturning (BI value) is selected as the dominant RWB type for that day. This ensures that only one RWB subset can be selected as the most influential RWB subset on any given day.

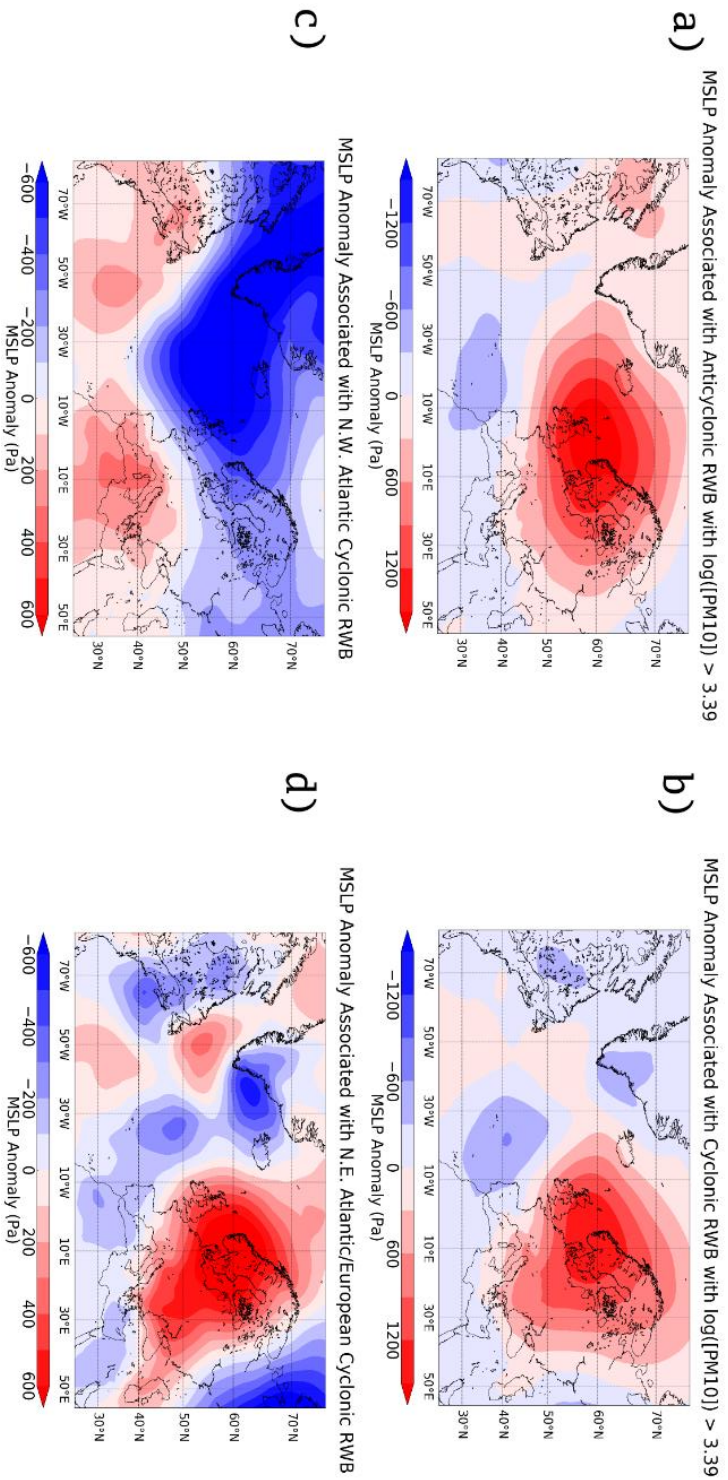

Figure 3.4 (a) and (b) Composite MSLP anomaly on the day following days incorporating; anticyclonic RWB and cyclonic RWB within the predefined regions of influence (see Fig. 3.3) respectively and on the day following RWB, ln[PM10] > 3.39. **(c) and (d)** MSLP anomaly on the day following days incorporating cyclonic RWB within the climatologically most frequent region, northwest Atlantic (135º W- 31º W longitude) and northeast Atlantic/ European (30º W - 55.5º E longitude) sectors respectively, regardless of ln[PM10]. Pressure data was taken for the winter months (DJF) between January 1999 and December 2008.

Figures 3.4 (a) and (b) are constructed using the combined warm and cold ACRWB and CRWB subsets listed in Table 2.1 and are composed of 50 and 35 contributing days respectively. The figures are similar, with a dominant high MSLP anomaly situated over Scandinavia and a low MSLP anomaly over the Azores. Together the high and low pressure anomalies complete the anomalous MSLP dipole expected of RWB. In both cases the anomalous MSLP dipole is centred over Northern France, indicating that the RWB generating this dipole occurred, on average, in this region.

Figures 3.4 (c) and (d) illustrate the composite MSLP anomaly one day after all CRWB occurrence (regardless of [PM10]) inside the regions of influence, within the northwest Atlantic and northeast Atlantic/ European sectors respectively. The decision to dissect CRWB occurrence into two sectors follows the result that the regions of influence for CRWB have a greater regional extent in the northeast Atlantic/ European sector than in the northwest Atlantic sector (Fig. 3.3 (c) and (d)). In contrast it has been highlighted in the literature that CRWB is most likely to occur in the northwest Atlantic sector and to the North of the EDJ. The purpose of Fig. 3.4 (c) and (d) is to determine the region in which CRWB occurrence is most likely to lead to [PM10] exceedances. The longitudinal sectors incorporating these two regions were 135^{o} W- 31^{o} W longitude for northwest Atlantic RWB and 30^{o} W - 55.5^{o} E longitude for northeast Atlantic/ European RWB.

The number of events in Fig. 3.4 (c) and (d) are 52 and 22 in the northwest Atlantic and northeast Atlantic/ European sectors respectively. The greater number of events in Fig. 3.4 (c) than (d), despite the much smaller regions of influence in the northeast Atlantic sector than the northeast Atlantic/ European sector (Fig. 3.3 (c) and (d)), highlight the greater density of CRWB events in the northwest Atlantic region.

Both Fig. 3.4 (b) and (d) show similar anomalous MSLP patterns, with an anomalous high MSLP system centred over the West Scandinavia region. This suggests that CRWB events leading to UK [PM10] exceedances in Fig. 3.4 (b) are predominantly northeast Atlantic/ European CRWB events. Figure 3.4 (c) however, shows a negative MSLP anomaly stretched across the North Atlantic towards the UK. This pattern would suggest that northwest Atlantic CRWB events coincide with conditions favourable for UK [PM10] dispersion and removal.

3.3.4 Importance of RWB on UK [PM10] Exceedances

In this section we focus on the RWB events leading to UK [PM10] exceedances. Section 3.3.1 highlighted that raised UK [PM10] is associated with positive BI values, showing that RWB has an effect of preventing the strongest westerly zonal winds from entering the UK region. Figure 3.3 shows the importance of RWB in significantly raising UK $\overline{[PM10]}$, but does not demonstrate the probability of individual RWB events exceeding a ln[PM10] threshold of 3.39.

Determining the probability of PM10 exceedance values is perhaps the most important result within this study, as it quantifies the importance of RWB on [PM10] levels detrimental for human health. As explained in Sect. 1.7.4 the exceedance value this study uses is 29.72 $\mu g\ m^{-3}$ (ln[PM10] = 3.39).

To illustrate the probability of exceeding a UK Midlands [PM10] threshold, Fig. 3.5 illustrates four cumulative distribution function (CDF) plots. The CDFs in Fig. 3.5 present the probability of exceeding any ln[PM10] value, for three subset [PM10] datasets. The first dataset (blue in Fig. 3.5), relates to days where no RWB of any type was detected within the region of RWB influence for that RWB subset. The black line in Fig. 3.5 represents days where RWB of the subset being analysed has occurred, following a day of no RWB (defined as onset RWB events). The red line represents continuous RWB events where RWB of the subset being analysed has followed a day of RWB of any type.

M13, Woollings et al. (2008) and Pelly and Hoskins (2003) recognised the importance of the persistence of atmospheric blocking in influencing synoptic meteorology. RWB persistence is expected to prolong the influence of atmospheric blocking and the resultant meteorological patterns. In the context of this study, it is expected that persistent events would be associated with the most hazardous UK [PM10] events.

As for Fig. 3.4, each day in Fig. 3.5 can only be associated with a single RWB subset, which has occurred with the greatest BI magnitude within its region of influence. Furthermore, as in Fig. 3.4, a threshold of 10 grid points has been used to determine RWB occurrence. Finally, following the finding in Fig. 3.4 that northwest Atlantic CRWB has a detrimental influence on meteorology leading to PM10 accumulation, only RWB within the longitudinal bounds of 30^o W - 55.5^o E is included in Fig. 3.5.

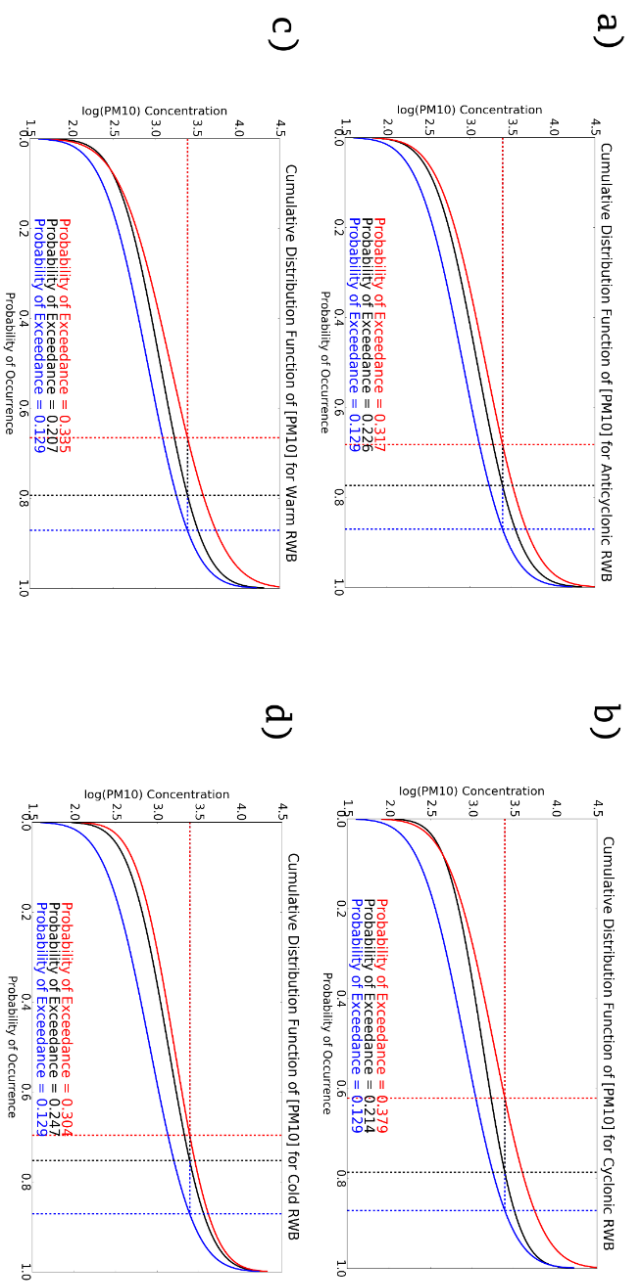

Figure 3.5 Cumulative distribution functions (CDF) for UK ln [PM10] and **(a)** Anticyclonic, **(b)** Cyclonic, **(c)** warm and **(d)** cold RWB. The red line illustrates the CDF for each RWB subset following a day with RWB of any type within the respective region of influence (continuous RWB event). The black line illustrates the CDF for each RWB subset following a day with no RWB of any type (onset event) and the blue line represents [PM10] associated with no RWB. Data was obtained for DJF January 1999 – December 2008 and [PM10] is lagged by one day following detection of RWB. Values shown for probability of exceedance are calculated as 1-α, where α is the probability of occurrence.

RWB has been analysed in four subcategories; warm, cold, anticyclonic and cyclonic. Values for probability of exceedance are shown on each figure and are calculated as 1-α, where α is the probability of occurrence, shown in Fig. 3.5. The probability of exceedance associated with no RWB is 0.129 and all RWB events can be seen to exceed this probability in Fig. 3.5. From onset (RWB within a region of influence following a day of no RWB within a region of influence) it can be seen that the probability of exceedance is greatest for cold RWB (0.247) and lowest for Warm RWB (0.207). The greatest probabilities can be seen for continuation events (RWB within a region of influence following a day of any RWB subset within its region of influence). Unlike for onset events, the probability for exceedance for CRWB events (0.379) is greater than that of ACRWB (0.317), with continuous CRWB events representing the greatest exceedance probability in Fig. 3.5. A probability of exceeding a hazardous [PM10] threshold of 0.379 represents a more than double increase in the mean exceedance probability for days with no RWB (0.129).

Sections 3.3.2 and 3.3.3 showed that CRWB is most influential when it occurs within the northeast Atlantic/ European sector, a region separated from its climatologically most frequent region. Furthermore it was shown that the anomalous MSLP pattern for influential CRWB bears great resemblance to influential ACRWB (Fig. 3.4 (a) and (b)) and within a similar region of influence (Fig. 3.3). Section 3.3.4 quantified the probability of exceedance for CRWB and showed that it has a greater UK [PM10] exceedance probability as a continuous event than ACRWB. Therefore it is hypothesised that if CRWB is to become influential upon UK PM10, it must be preceded by ACRWB within the northeast Atlantic/ European region.

3.3.5 Influential CRWB Hypothesis

The mechanism primarily dictating the direction of RWB is the meridional shear of the zonal wind, determined by the relative position of the EDJ. To the north/ south of the EDJ, a cyclonic/ anticyclonic shear is present. Consequently, the region of most frequent CRWB has been found to occur to the north of the EDJ mean-state, in the northwest Atlantic region (Sect. 2.3.5). The region of most frequent CRWB is spatially separate to the region of most frequent ACRWB, to the south of the EDJ mean-state in the northeast Atlantic/ European region. A hypothesis has been developed to explain the importance of CRWB in the northeast Atlantic/ European region. It will be shown that the majority of northeast Atlantic/ European CRWB events, which were found to significantly increase UK [PM10], are dependent on the prior occurrence of ACRWB.

Figure 3.6 shows a schematic, which illustrates how CRWB can become influential, following an ACRWB event. Figure 3.6 (a) shows the mature stage of an ACRWB event in which the mid-latitude EDJ is displaced to the south of the resultant high pressure lobe. Subsequently, with a more southerly EDJ, colder poleward air is advected into the positive potential vorticity anomaly, such as in Fig. 3.6 (b), forming an Omega block. Omega blocks are named due to the resemblance of the flow around a blocking anticyclone with the Greek letter Ω. Following the generation of an Omega block, a cut-off, formed of anomalously negative potential vorticity, warm, equatorward air, may form as in Fig. 3.6 (c). In Fig. 3.6, red shading represents regions of detected ACRWB, while CRWB is represented by blue shading. West (upstream) of the ACRWB event seen in Fig. 3.6 (b), a CRWB event is detected, which is consistent with the regions of influence seen in Fig. 3.3 (c) and (d). It is hypothesised that CRWB occurs upstream of the ACRWB due to meridional zonal velocity shear determined by the relatively southerly position of the EDJ approaching the blocking dipole. Subsequently cyclonic vorticity is imparted on the background flow to the north of the EDJ approaching the blocking dipole and CRWB can occur.

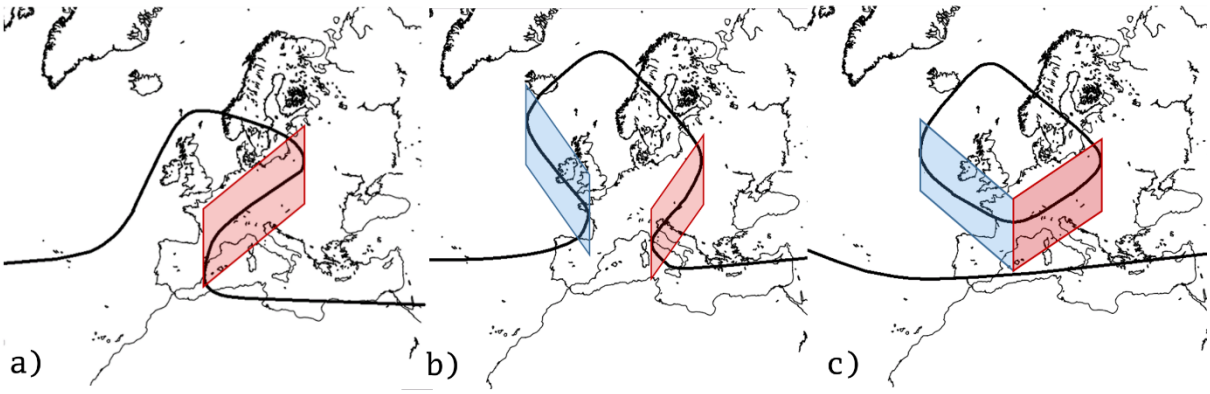

Figure 3.6 (a) Schematic of a mature warm anticyclonic Rossby wave breaking event on the dynamical tropopause, with a region of positive BI Index and anticyclonic DB Index values shaded red. The black contour portrays an arbitrary potential temperature contour representing the intermediate between anomalously cold and warm air masses. **(b)** Schematic of an Omega block with an additional cold cyclonic Rossby wave breaking event (blue shading) following **(a)**. **(c)** Schematic of a final stage warm θ cut-off.

3.3.6 Dependence of Northeast Atlantic - European CRWB upon the Prior Occurrence of ACRWB

In Fig. 3.6, CRWB occurrence within the northeast Atlantic/ European influential region follows prior ACRWB occurrence in the region. Further analysis has shown that this is the case in 94% of northeast Atlantic/ European CRWB events observed throughout January 1999-December 2008. 35 individual CRWB events were detected throughout the sampling period, using the 10 grid point threshold used for identifying RWB events in Fig. 3.4. The 10 grid point threshold helped to remove some smaller transient features. Unlike for Sect. 3.3.3 and 3.3.4 no criteria were imposed on the DB and RI metrics of the grid point with greatest BI value. In this section, it is less important to distinguish days influenced more by ACRWB and CRWB events, as Fig. 3.6 shows that both are influential in the formation of an Omega block. An ACRWB precursor was detected using the same 10 grid point threshold within ACRWB regions of influence for the four days leading up to and including the day of CRWB occurrence. This indicated that prior ACRWB was likely to be related to the occurrence of CRWB within this region.

Figure 3.7 shows the mean count of ACRWB (solid red line) and CRWB (solid blue line) grid points, on the days surrounding a CRWB event. Every event is centred on its peak CRWB grid point count and for each day a 25th and 75th percentile have been included (dashed lines) to test whether the data has been skewed by outliers.

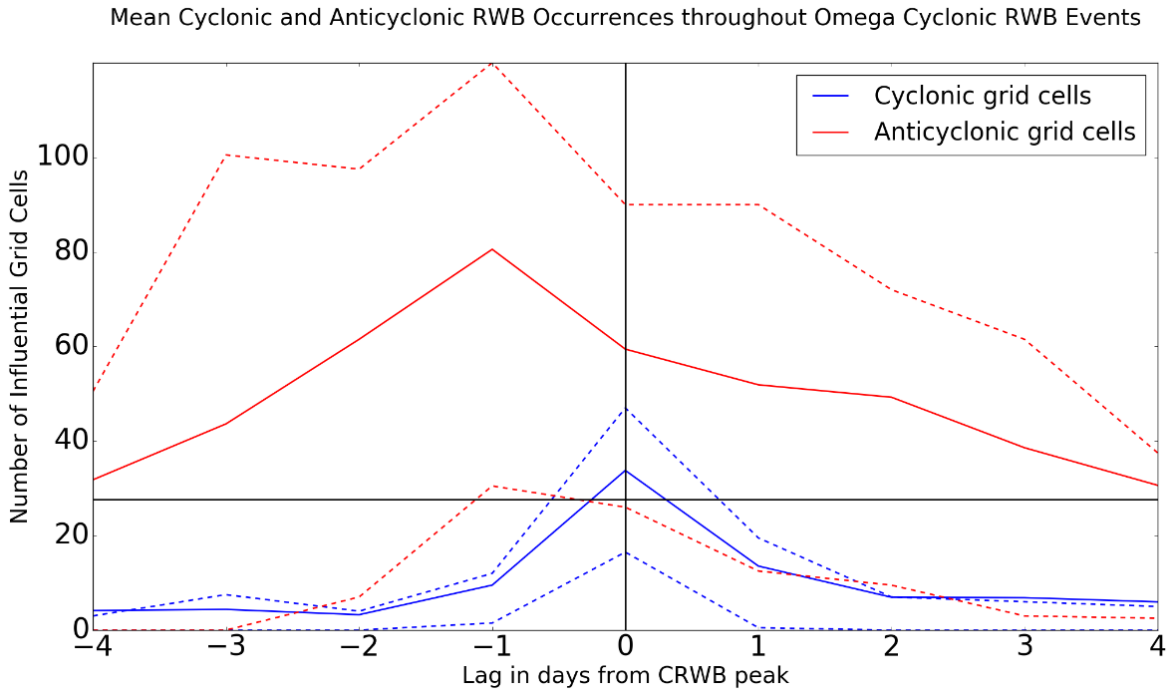

Figure 3.7 Grid points displaying RWB of (Anti)cyclonic tendency in (red)blue with time in days relative to the peak of northeast Atlantic/ European CRWB events. Solid lines represent the mean grid point count, while dashed lines represent the 25th and 75th percentile of counts for all events. In the formation of an Omega block, an ACRWB precursor is required. Of the 35 CRWB events detected within the northeast Atlantic/ European sector throughout DJF January 1999 – December 2008, 33 fulfilled the criteria of prior ACRWB occurrence. All CRWB events displayed in Fig. 3.7 include an ACRWB precursor within the four days leading up to and including the CRWB event. The black horizontal line represents the mean ACRWB count (30.07 grid points) throughout the 10-year dataset.

Figure 3.7 shows the CRWB and ACRWB counts for 94% of northeast Atlantic/ European CRWB events as defined in this study. Evident is the influence ACRWB plays upon the occurrence of CRWB, with the mean ACRWB count greater than the 10-year mean ACRWB count (black line) for the entire period of the CRWB event. The mean ACRWB count peaks one day prior to the CRWB event, with the 25th percentile for this period also exceeding the mean ACRWB count for the dataset (27.66 grid points). With the ACRWB 25th percentile above the black line in Fig. 3.7 for -1 days, this indicated that enhanced ACRWB is a robust feature for at least 75% of the northeast Atlantic/ European CRWB events.

None of the northeast Atlantic/ European CRWB events not associated with an ACRWB precursor led to a [PM10] exceedance on the day following Northeast CRWB detection. For the dataset used to generate Fig. 3.7, the probability of exceedance is 0.383, which is the greatest value found within this study. UK $\ln\overline{[PM10]} \pm \sigma$ lagged by one day following day 0 of all CRWB events contributing to Fig. 3.7 is 3.29 ± 0.35. The climatological UK $\ln\overline{[PM10]}$

$\pm \sigma$ is 2.98 ± 0.43 and subsequently the $\overline{[PM10]}$ for the dataset contributing to Fig. 3.7 is significantly greater to the 99.9th percentile ($p = 6.64 \times 10^{-5}$), using the ANOVA statistical test.

3.3.7 Blocking Anticyclone Progression throughout an Omega Block Event

Chapter 3 has identified the Omega block mechanism as the RWB subset with the greatest exceedance probability in this study. Section 3.3.6 identified ACRWB as a necessary precursor to Omega Block events in the northeast Atlantic/ European region. Section 3.3.3 showed that ACRWB events that result in UK [PM10] exceedances are associated with an anomalous high pressure system over Scandinavia. Section 3.3.7 aims to explore the progression of the anomalous anticyclone during an Omega Block event to determine why Omega Block events are associated with a greater UK Midlands [PM10] exceedance probability than ACRWB events in the same region.

It is hypothesised that the persistence associated with Omega block events is associated with the elevated probability of exceeding the hazardous [PM10] threshold. Section 2.4 highlighted the importance of atmospheric blocking persistence in elongating synoptic meteorological conditions that are favourable to the accumulation of PM10. Atmospheric blocking persistence however is only associated with elevated UK [PM10] when the atmospheric block is situated in a region that encourages the accumulation of PM10 within the UK.

Figure 3.8 explores the migration of the anomalous anticyclone throughout a composite of 33 Omega block events. To track the migration of the anomalous anticyclone, the location of the greatest positive MSLP anomaly is identified in the global mean MSLP field for the day following each day in the Omega Block composite (MSLP is lagged by 1 day as in Fig. 3.4). The Omega block events composited are identical to those analysed in Fig. 3.7, however day +4 is not shown in Fig. 3.8, as the anomalous anticyclone has diminished greatly by this stage in the Omega block event.

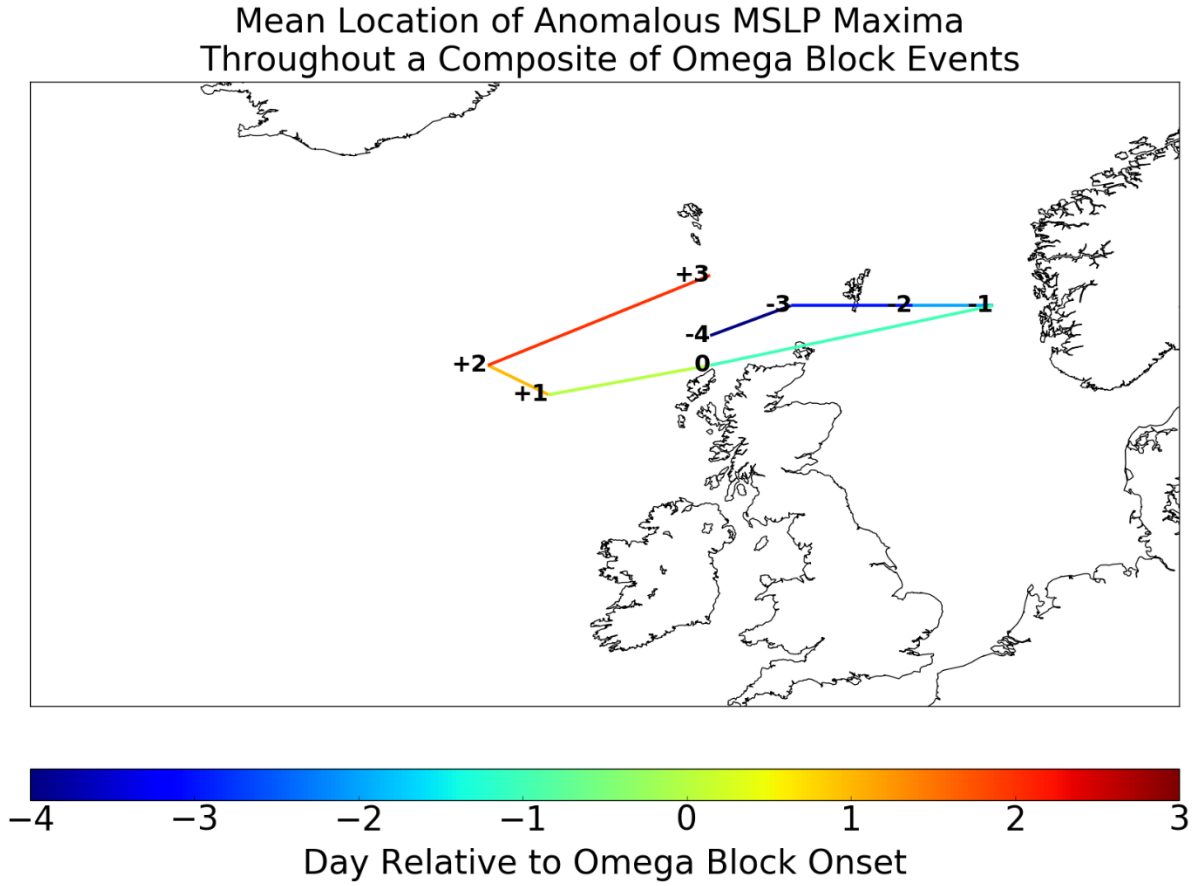

Figure 3.8 The progression of a maximum MSLP anomaly, resulting from a composite mean MSLP field on each day, relative to the onset of 33 Omega Block events. The Omega Block events used to generate this figure are identical to those used in Fig. 3.7. MSLP is lagged by 1 day relative to the RWB metrics.

Figure 3.8 shows the progression of the anomalous MSLP maxima throughout a composite of 33 Omega block events. What is shown prior to the Omega block onset, between days -4 and -1, is that the lagged MSLP anomaly maxima tracks eastwards towards the Scandinavia region. Following this period of eastward propagation, the anomalous MSLP maxima is seen to track westwards until day +2. For the onset day, the MSLP anomaly is longitudinally aligned with the UK region. Between day +2 and day +3 the migration of the MSLP maxima reverts to an eastward propagation, however, by day +3 the magnitude of the MSLP maxima is substantially smaller than that throughout the remainder of the event.

Figure 3.8 shows the progression of the mean MSLP maxima anomaly throughout an Omega block event, however to quantify the variability associated with this mechanism, Fig. 3.9 has been included. Figure 3.9 shows the MSLP anomaly over a Scandinavian and UK grid point throughout the same Omega block events as included in Fig. 3.8.

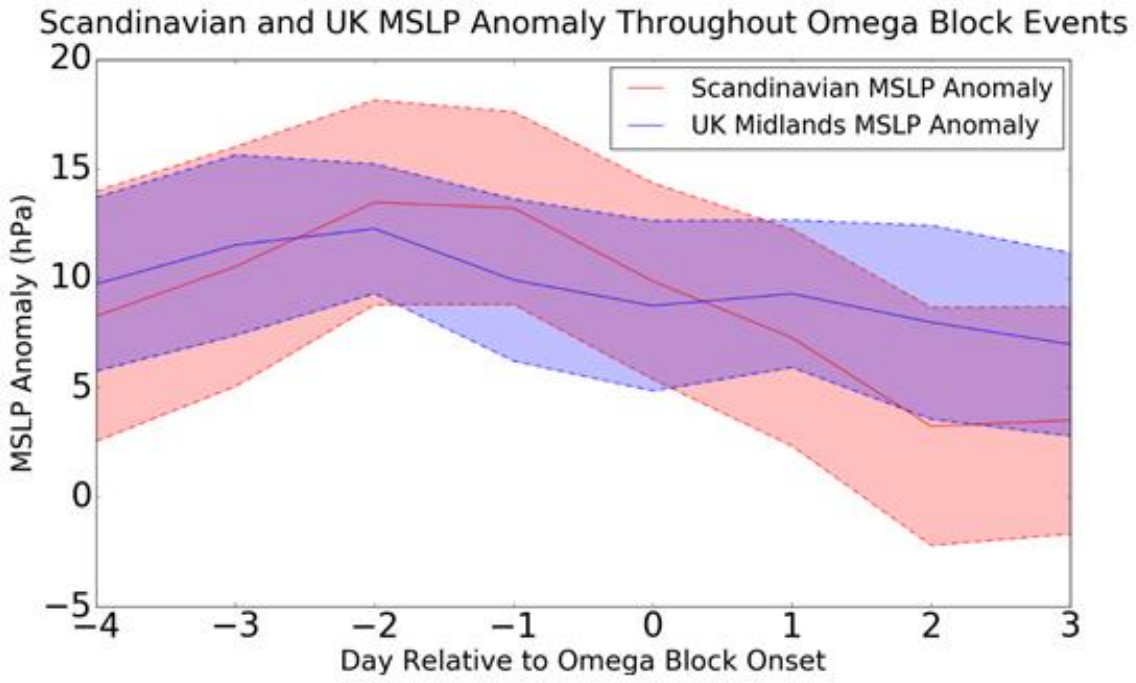

Figure 3.9 MSLP anomalies for each day, relative to the onset of 33 Omega Block events, for a grid point situated over West Scandinavia (red) and the UK Midlands (blue). The filled line represents the mean MSLP anomaly at each grid point, while the shaded regions represent the 95% confidence interval for the mean value.

Figure 3.9 shows the progression of MSLP anomalies throughout an Omega Block event at the West Scandinavian (59.29^{o} N x 13.36^{o} E) and UK Midlands (52.29^{o} N x 1.44^{o} W) grid points. The purpose of Fig. 3.9 is to elucidate on the variability in Fig. 3.8.

Throughout the Omega block event it is seen that the mean UK Midlands MSLP anomaly does not significantly ($p<0.05$) change. Despite this the Scandinavian MSLP anomaly does vary throughout the 8 days. For days -2 and -1 in Fig. 3.9, the Scandinavian MSLP anomaly reaches its greatest values. Following day -1, the Scandinavian MSLP anomaly reduces to its minima on day +2. It is found that the mean Scandinavian MSLP anomaly (solid line in Fig. 3.9) on days -2 and -1 is significantly greater ($p<0.05$) than the MSLP anomaly from day +2 and day +3, while it is likely ($p<0.33$) greater than the MSLP anomaly on day +1 (not shown).

The Scandinavian MSLP maxima in Fig. 3.9 corresponds to the period in Fig. 3.8 where the MSLP maxima is at its eastern most longitude. Following day -1 in Fig. 3.8, the anomalous MSLP maxima is seen to migrate towards its western most longitude on days +1 and +2. As the Scandinavian MSLP anomaly on days -2 and -1 is significantly ($p<0.05$) greater than on days +2 and likely ($p<0.33$) greater than on day +1, this indicates a robustness of the results from Fig. 3.8. It is therefore shown that there is a maximum in Scandinavian MSLP anomaly

prior to the onset of and Omega Block, a result of the occurrence of northeast Atlantic/ European ACRWB. This Scandinavian MSLP anomaly subsequently diminishes following the onset of an Omega block event, with the mean UK MSLP anomaly greater than the Scandinavian MSLP anomaly for days +1, +2 and +3.

3.4 Discussion

3.4.1 Do Large Scale Flow Patterns Influence UK [PM10]?

The relationship between RWB and UK [PM10] has been shown to be one that is dominated by negative BI values (Fig. 3.1 and 3.2). Negative BI values over the UK are representative of zonal flow from the Atlantic, which is associated with stronger winds and a higher probability of precipitation within the UK. The most effective PM sink is wet deposition (Sect. 1.3.2), while PM is readily dispersed by elevated surface horizontal and vertical wind speeds (McGregor and Bamzelis, 1999). Consequently, negative BI values over the UK region are associated with reduced UK [PM10]. The strongest zonal flow over the UK during winter is associated with the EDJ. At times of atmospheric blocking, resulting from RWB over the northeast Atlantic/ European sector, the EDJ is deflected to the north and/or south of the blocked region (Shutts, 1983), resulting in elevated UK [PM10] (Fig. 3.2). This study finds that there exists a correlation tripole between BI and UK [PM10], consisting of positive correlation centred over the English Channel and two negative correlations to the north and south. The two regions of negative correlation represent regions where the EDJ is deflected to during periods of blocked flow over the UK and subsequent raised UK [PM10]. Furthermore, within these regions of negative correlation, the occurrence of RWB results in these regions being blocked from the EDJ and results in a higher probability of the UK being influenced directly by the EDJ.

The use of RWB as the meteorological diagnostic differs from classical meteorological diagnostics often used, such as MSLP, wind speed and temperature (McGregor and Bamzelis, 1999; Buchholz et al., 2010; Eder et al., 1994). Justification for the use of the RWB metrics used in this paper can be sought from Woollings et al. (2008). Woollings et al. (2008) showed that RWB can account for the synoptic meteorological variability influencing the UK. The synoptic meteorological variability influencing the UK can be defined simplistically as zonal flow from the Atlantic influencing the UK or the UK being blocked from this flow (Sect. 2.3.1). Furthermore, RWB contains information relating to the spatial synoptic flow patterns and temporal variability. Temporal variability can be inferred from the upper level field and

such as in the case of the Omega block in this study, RWB metrics can tell us about the persistence of such blocked events.

3.4.2 What Large Scale Flow Patterns Lead to Raised UK $\overline{[PM10]}$?

In this study, RWB was shown to significantly ($p<0.01$) increase UK [PM10], predominantly when it occurred in the northeast Atlantic/ European region. Weijenborg et al. (2012) showed that ACRWB is most prominent within this region and this study has also shown that ACRWB in this region significantly increases UK [PM10]. Weijenborg et al. (2012) and M13 both highlighted that CRWB is most prominent in the northwest Atlantic region. However, this study has shown that CRWB occurring in the northeast Atlantic region is most influential in raising UK [PM10].

Sect. 3.3.3 showed that both CRWB and ACRWB occurring in their northeast Atlantic/ European regions of influence and that lead to UK [PM10] exceedances (>29.72 μg m^{-3}) the following day, shared near identical MSLP responses. This result suggests that ACRWB and CRWB events were influencing the UK through the same mechanisms and that they are similar events. The MSLP response seen is dominated by a positive MSLP anomaly over Scandinavia, which is hypothesised to facilitate the advection of European PM10 and produce UK conditions that are conducive to the accumulation of locally sourced PM10.

Section 3.3.1 has shown that positive BI values in the northeast Atlantic/ European region are associated with elevated UK [PM10]. Despite this, it is the relationship between negative BI values and UK [PM10] that dictate this relationship, therefore highlighting the importance of the EDJ. The EDJ is associated with the most zonally stratified flow in the North Atlantic region and subsequently the most negative BI values (and lowest UK [PM10]). Consequently, it has been shown that both CRWB and ACRWB in the northeast Atlantic/ European region raise UK [PM10] in part due to a blocking of the EDJ from the UK and associated with [PM10] removal processes.

McGregor and Bamzelis (1999) and Buchholz et al. (2010) used clustering techniques to identify low frequency weather regimes that were influential on UK [PM10]. The primary conclusion from both studies was that European anticyclonic regimes were associated with raised UK [PM10], while maritime Atlantic air masses were conducive to low UK [PM10]. The results in this paper support these findings, as we point to the dominant anomalous MSLP response to RWB that leads to elevated PM10, being an anticyclone over Scandinavia. In the method we used, each day can be classified by a number of continuous metrics, as opposed to clustering techniques, which use discrete data in the form of regimes to classify

each day. The advantage of this method is that no day can get misrepresented by using only a discrete number of clustered regimes. For example, rare, yet very important events such as Omega block events are likely to be indistinguishable in a clustering framework.

3.4.3 What Large Scale Flow Patterns Lead to the Greatest Probability of Exceeding Hazardous UK [PM10] Limits?

Katsouyanni et al. (2001) showed that episodic short term exposure of [PM10] > $\overline{[PM10]}$ + 10 μg m^{-3} led to a significant ($p<0.05$) increase in urban mortality rates. Exceedance probability analysis focuses on episodic events above a hazardous [PM10] threshold, determined following Katsouyanni et al. (2001). The exceedance probability in the UK Midlands, associated with days where no RWB has occurred within a region of influence is 0.129. The occurrence of all RWB subsets led to an increase in this probability. In this study, the Omega Block mechanism resulted in the greatest probability of exceeding a hazardous [PM10] threshold (probability = 0.383).

Section 3.3.7 analysed the migration of the anomalous MSLP maxima throughout an Omega block event. This study has found that prior to the onset of an Omega block event, the anomalous anticyclone, which is the dominant synoptic feature throughout Omega Block events, migrates from a UK centric longitude to the Scandinavian region. Prior to an Omega block event, the northeast Atlantic/ European region is most influenced by ACRWB. Fig. 3.4 (a) showed that northeast Atlantic/ European ACRWB, which resulted in UK [PM10] exceedances, resulted in an anomalous anticyclone over Scandinavia. This Scandinavian anomalous anticyclone is hypothesised to be associated with the advection of European PM10 into the UK.

Following this hypothesised advection of European PM10 into the UK, Fig. 3.8 shows a westward propagation of the anomalous MSLP maxima, back towards the UK region. An anomalous anticyclone, local to the UK region is likely to produce meteorological conditions that are favourable to the accumulation of locally sourced PM10 within the UK.

These results suggest that the occurrence of advection followed by the persistence of UK stagnation leads to the greatest PM10 exceedance probabilities in this study and subsequently the most hazardous [PM10] within the UK. Chapter 5 will analyse the flow regimes influencing the UK throughout Omega block events, with the use of a global climate model, which is introduced in Chapter 4.

The increased probability of exceedance associated with continuous events for most RWB subsets, as compared to onset events, (Sect. 3.3.4) highlights the importance of RWB

persistence in generating conditions conducive to hazardous UK [PM10]. It has been found that Omega block events are persistent RWB events and it is likely that this persistence is a key factor in determining that Omega blocks have the greatest probability of exceeding a hazardous UK [PM10] threshold in this study.

In this study, PM10 advection from Europe is hypothesised to greatly influence UK [PM10] episodes. A potential extension for this study could be to analyse the relationship between the smaller PM2.5 and RWB. PM2.5 is a smaller and subsequently lighter particle than PM10, with a reduced gravitational settling velocity. Consequently, PM2.5 is more readily advected than PM10 and RWB may therefore be more influential in facilitating the advection of PM2.5.

3.5 Limitations

3.5.1 Relating Pressure and θ-2PVU Fields

This analysis looks at large scale dynamical features affecting regional scale UK [PM10] and in this relationship there is an unconstrained intermediate. This intermediate is the pressure dipole response to RWB, which is not consistent in its proximity with the centre of overturning (maximum BI value) in a RWB event. Previous studies have shown the anomalous high pressure lobe to be located to the north of the RWB event, also found within this study. Despite latitudinal consistency, longitudinal differences in the distance between the centre of overturning and the local high pressure maxima exist. Consequently, variability exists within the results in Fig. 3.3, as UK [PM10] is not solely dependent upon the location of overturning. The relationship between location of BI maxima and high pressure maximum remains unconstrained and therefore inherent uncertainty of this relationship exists.

3.5.2 Observational Tri-Site

The observational sites used within this study are all classified as urban background sites, therefore they will be influenced by their urban environments independently. Consequently, there will be periods in the data that local influences out-weigh the effects of large scale episodes. Furthermore the tri-site is used to represent UK from its most central point and in doing this, it is likely that some events, particularly some continental advection events affecting the southeast corner of the UK will not be recorded. The extent to which three sites can represent the entire country is limited, but due to data availability, it is not possible to fully represent the entirety of the UK without large scale data interpolation methods, which are heavily influenced by the local influences of all sites used. The analysis within this paper has been repeated using data from both a rural site at Harwell, Oxfordshire and Southampton, Hampshire.

The data from Southampton showed regions of influence with reduced magnitudes of extent for all RWB subsets, but especially for the two ACRWB subsets. It is hypothesised that ACRWB facilitates the advection of European PM10, driven by a Scandinavian anticyclone. Consequently, in Southampton, where European pollution sources more regularly have a greater influence (Malcolm et al., 2000) than in the UK Midlands, the advection of European PM10 is not associated with as great a [PM10] increase. Despite the reduced magnitudes, the regions of influence were spatially co-located with those illustrated in Fig. 3.3. Conclusions gathered from the analysis of exceedance probabilities did not change. The exceedance probability for all RWB was elevated above the exceedance probability with no RWB (0.169). Continuous CRWB events led to the greatest exceedance probability (0.659) of the RWB subsets in Fig. 3.5, which was much greater than the exceedance probability for continuous ACRWB (0.323). Analysis of Omega blocks showed that these events led to the second greatest probability of exceedance in Southampton (0.604). However, as for the UK Midlands PM10 dataset, the probability of exceedance for Omega block events is similar to that for continuous CRWB events, as they comprise of many of the same events. Despite this and due to the reduced ACRWB regions of influence, only 11 out of 17 northeast Atlantic CRWB events were associated with an ACRWB precursor.

Data from the rural monitoring site in Harwell showed little difference in the shape or locations of the regions of influence for all RWB subsets, when compared with the UK Midlands dataset. Furthermore the climatological exceedance probability was slightly reduced (0.082), as the 10 μg m^{-3} increment used to define an exceedance, represented a much greater proportion of the sites' $\overline{[PM10]}$. Continuous CRWB events led to the greatest exceedance probability (0.368) of the RWB subsets illustrated in Fig. 3.5 as before. As for the two urban background sites, Omega block events led to the greatest overall exceedance probabilities (0.381), where 30/33 northeast Atlantic/ European CRWB events were identified as Omega block events.

Section 3.5.2 has highlighted the robustness of the results found in this chapter. The same mechanisms are seen to influence [PM10] variability in three datasets: Southampton (Urban background AQMS), Harwell (Rural AQMS) and the UK Midlands tri-site (Urban background AQMS). Consequently, the conclusions of this chapter are not sensitive to the choice of UK region or AQMS site classification from which PM10 is obtained.

3.6 Conclusion

The influence that RWB has on UK Midlands [PM10] has been analysed in Chapter 3, with significant relationships present. Positive correlations exist within the northeast Atlantic/ European region, between UK [PM10] and BI, a metric used to diagnose RWB. The EDJ has shown to be the dominant mechanism in the relationship between BI and UK [PM10], with northeast Atlantic/ European RWB acting to block the UK from the influence of the EDJ.

This study has shown that RWB occurring in the northeast Atlantic/ European region acts to significantly ($p<0.01$) elevate UK [PM10] above the dataset mean concentration. Furthermore, this study has found that both CRWB and ACRWB subsets are seen to significantly raise [PM10] when it occurred in the same region. The MSLP response to both CRWB and ACRWB, resulting in UK [PM10] exceedances is dominated by an anomalous anticyclone, centred over Scandinavia. This results in anomalous easterlies into the UK and a hypothesised increased advection of European PM into the UK.

The probability of exceeding an episodic [PM10] threshold value was used to evaluate the anthropogenic health hazard associated with UK PM10. All RWB subsets led to an increase in the probability of exceeding a hazardous [PM10], compared to days with no RWB occurring within the regions of influence. The occurrence of CRWB led to the greatest exceedance probability of any RWB subset. Further analysis was undertaken to determine the causes of northeast Atlantic/ European CRWB, occurring in a region separate from its most frequent North Atlantic region (northwest Atlantic).

A mechanism was hypothesised, explaining the occurrence of CRWB within a region separate from its most frequent region. The mechanism depended on the prior occurrence of ACRWB within the northeast Atlantic/ European region and was characterised by the formation of an Omega block. The persistence of these events led to the probability of exceedance in such cases exceeding that of all other RWB subsets.

The migration of a mean anomalous MSLP maxima, throughout 33 Omega Block events, led to a proposed mechanism by which Omega blocks are associated with this study's greatest probability of exceeding a hazardous UK [PM10] threshold. Prior to the onset of an Omega block, an anomalous Scandinavian anticyclone facilitates the advection of European PM10 into the UK. A westward migration of the anomalous MSLP maxima brings the anomalous anticyclone more longitudinally aligned with the UK, which could potentially facilitate the accumulation of locally sourced PM10 within the UK, through a stagnation mechanism.

Further analysis in this thesis will firstly elucidate on the flow regimes that influence the UK throughout an Omega Block event (Chapter 5). Subsequently, climate shifts in both; RWB frequency and the contributing sources to UK [PM10] throughout RWB events will be determined in Chapter 7, for a 2050 future climate.

To undertake further analysis within this study, a climate model is required. Chapter 4 introduces the climate model used in this study. The climate model enables both, a more detailed analysis of flow regimes influencing the UK throughout RWB events and a tool capable of projecting climatic trends in the frequency and dynamics of RWB events.

Chapter 4 – The Climate Model

Chapter 3 analysed the relationships between RWB and UK [PM10], with RWB found to significantly raise UK [PM10]. Furthermore, an Omega block mechanism was found to be associated with the greatest probability of exceeding a hazardous UK [PM10] threshold in this study.

Chapter 4 looks to expand on the relationships found in Chapter 3. Section 4.4 introduces a tracer framework to initially explore the PM10 sources and synoptic flow regimes that influence RWB events. In addition to analysis of the flow regimes that influence UK PM10 episodes, this study's primary research question will be addressed:

"Do UK PM10 episodes change in a future climate that is influenced by anthropogenic climate change?"

To answer this research question, a climate model is required to make projections of a future climate. The climate model used is the Met-Office HADGEM3-GA4 atmosphere-only model.

4.1 HADGEM3-GA4

The Met-Office HADGEM3-GA4 atmosphere-only climate model was used to answer this study's primary research question. HADGEM3-GA4 is the atmosphere only component of the Met-Office's HADGEM3 coupled model. The coupled model incorporates; the atmosphere model, the JULES land surface model, the NEMO ocean model and the CICE sea model. In the coupled configuration, HADGEM3 allows interaction between the aforementioned model components.

In this study, the atmosphere model is used with the JULES land surface model, which requires the other aspects of the model to be prescribed. Section 4.7 will detail the prescribed model parameters in this studies HADGEM3-GA4 simulations.

4.2 Modelling Atmospheric Pollutants in HADGEM3

To model atmospheric chemistry and aerosol processes, the United Kingdom Chemistry and Aerosol (UKCA) Model is used. The UKCA model represents the interaction of atmospheric pollutants with the atmosphere and land surface.

A feature of a climate study is the requirement that results are only extracted when the model reaches an equilibrium mean-state. The process of allowing the model to reach an equilibrium mean-state is termed model spin-up. Model spin-up allows for the model to be run prior to extracting meaningful results from it. A length of model spin-up in a coupled climate

simulation is often dependent on the time taken for the ocean and atmosphere to equilibrate. This study is an atmosphere-only model and subsequently the model spin-up is only dependent on the concentration of atmospheric pollutant within the model. The spin-up time used in this study is 3 months for each simulation, which ensures that the concentration of pollutant within the model will have reached an equilibrium state, before meaningful results are extracted from the simulations.

4.3 Modelling European PM10

To answer this study's primary research question, consideration must go into the modelling of PM10 in HADGEM3-GA4. The question arises as to whether it is desirable to model UK Midlands PM10 as accurately as possible, or to idealise PM10. It has been decided that an idealised framework, whereby inert tracers represent PM10, will enable the results from this study to be more clearly determined. By reducing the degrees of freedom that will impact on the advection of modelled PM10 into the UK, one can elucidate on the changes in flow regime that influence the UK more clearly.

4.3.2 Idealised Modelling of PM10

This study will analyse the flow regimes that influence the UK throughout northeast Atlantic/ European RWB events. These flow regimes will be identified using inert tracers that have been placed over major PM10 source regions within separate regions of Europe. The spatial distribution of tracer source regions is important, as each tracer must identify an independent flow regime. The accumulation of each flow regime in the UK will be analysed following RWB events that Chapter 3 identified as having a greatest probability of exceeding a hazardous UK [PM10] threshold. Following this method, Chapter 7 will identify whether significant shifts exist in flow regimes, due to climate change.

Aside from reducing the degrees of freedom associated with the advection of PM10 into the UK, the choice to use idealised tracers rather than attempting to accurately replicate observed PM10 is somewhat imposed by the limitations of the UKCA model. At the time that the model simulations were run, nitrate did not exist within UKCA. Nitrate sequestered in ammonium nitrate is a large component of observed PM2.5 at UK Midlands urban background and rural sites (approximately 20% of total winter PM2.5 mass at both sites in analysis by Yin et al., 2010). Consequently, even with a perfect representation of all other PM10 constituents, there would remain an underestimation of PM10 mass due to the nitrate deficit.

Mann et al. (2010) provided a comprehensive evaluation of the aerosol scheme within UKCA and found biases that existed within the model, in comparison with in-situ measurements. It was found that large model biases in OC concentration were found throughout the northern hemisphere, with a predominant negative model bias. This underestimation of OC was linked to a potential underestimation of secondary organic aerosol production. Northern Hemispheric negative model biases were also found for EC. These biases are common model biases and not specific to UKCA (Koch et al., 2009; Kipling et al., 2013).

In addition to model biases in anthropogenic aerosol mixing ratios, Mann et al. (2010) highlighted predominantly positive model biases existent in the sea-salt component. For example, a poor correlation existed between modelled annual mean sea salt concentrations and in-situ land measurements in Miami, USA (R=0.13). It was found that the sea salt component was overestimated, with the modelled sea-salt annual mean representative of sea-salt that has been sourced throughout strong wind speed events.

Analysis by Mann et al. (2010) has shown that, while UKCA can simulate many PM10 components to the correct orders of magnitude, there exist substantial model biases in some PM10 components. Such model biases, in addition to the nitrate deficit within the model, currently make UKCA incapable of replicating UK Midlands [PM10].

4.4 Modelled PM10 – The Tracer

In this study a single tracer has been implemented throughout Europe, emitted from dominant PM10 source regions that are spatially separate throughout Europe. It is important that the tracers are meaningful, so that they represent actual PM10 transported to the UK, however they must also be emitted in spatially separate regions, so to represent independent flow regimes. This study uses chemically inert tracers, which are deposited through dry and wet deposition. Removing tracer chemistry allows for a simplification of the analysis of tracer advection throughout Europe. Consequently, the tracer will much more clearly elucidate on the flow regimes influencing the UK throughout RWB events.

This study uses a gaseous tracer to model PM10 throughout Europe. The gas-phase component of UKCA was used to model the tracer that is intended to roughly represent the behaviour of long-range advected PM10 throughout Europe. A gaseous tracer was chosen to represent PM10, due to its primary purpose of representing flow regimes. By implementing a particulate tracer, one would expect no changes in any of the conclusions obtained from this study. Sections 5.3 to 5.5 evaluate the gaseous tracer, which this author feels is appropriate in representing an all-encompassing PM10 tracer throughout Europe.

It is required that the tracer has the ability to advect from the most distant of PM10 sources, as identified by the receptor source modelling study of Charron et al. (2013). Charron et al. (2013) shows that PM10 source regions exist in the Eastern European region. Most importantly therefore, the tracer must replicate a component of PM10 that is seen to advect from Eastern Europe.

Charron et al. (2013) highlighted sulfate as one of the dominant components of PM10 that undergoes long range transport from Eastern Europe. An important characteristic of SO_4^{2-} is that it is small and light in relation to the majority of PM10 components (Sect.1.2). These characteristics allow for SO_4^{2-} to undergo long-range transport within Europe and are why the lifetime of this study's tracer is representative of SO_4^{2-}.

Tracer lifetime in this study is determined by dry and wet deposition only. Section 4.4.1 and 4.4.2 present the dry and wet deposition characteristics that are attributed to the modelled gaseous tracer.

4.4.1 Dry Deposition

In this study's HADGEM3-GA4 simulations, the interactive dry deposition scheme is switched on. This scheme enables dry deposition rates to be dependent on the land surface. In this study the land surface is the same for present and future climate. Above each tiled land surface a dry deposition velocity must be prescribed. Section 1.3.1 described how the dry deposition velocity is dependent on a number of land surface properties. The prescribed dry deposition velocities in UKCA are surface specific. In UKCA there are 5 land surface types: water, forest, grass, desert and ice. Table 4.1 presents the dry deposition velocities for the modelled tracer over each of the five land surfaces, in units of cm s^{-1}. Dry deposition velocities also depend on the season and diurnal cycle and these variations in dry deposition rate have been included in Table 4.1.

Table 4.1. Dry deposition rates (cm s-1) attributed to the modelled tracer, over five model surface types in HADGEM3-GA4. Summer and winter dry deposition velocities are presented as well as day, night and daily mean dry deposition velocities for each surface type. These values are based on literature from Nho-Kim et al., (2004) and Zhou et al., (2009).

Surface Type	Summer (day)	Summer (night)	Summer (24hr avg.)	Winter (day)	Winter (night)	Winter (24hr avg.)
Water	0.1 cm s^{-1}	0.1 cm s^{-1}	0.1 cm s^{-1}	0.5 cm s^{-1}	0.5 cm s^{-1}	0.5 cm s^{-1}
Forest	0.8 cm s^{-1}	0.8 cm s^{-1}	0.8 cm s^{-1}	0.9 cm s^{-1}	0.9 cm s^{-1}	0.9 cm s^{-1}
Grass	0.4 cm s^{-1}	0.4 cm s^{-1}	0.4 cm s^{-1}	0.8 cm s^{-1}	0.8 cm s^{-1}	0.8 cm s^{-1}
Desert	0.15 cm s^{-1}	0.15 cm s^{-1}	0.15 cm s^{-1}	0.2 cm s^{-1}	0.2 cm s^{-1}	0.2 cm s^{-1}
Ice	0.02 cm s^{-1}	0.02 cm s^{-1}	0.02 cm s^{-1}	0.05 cm s^{-1}	0.05 cm s^{-1}	0.05 cm s^{-1}

Table 4.1 shows the dry deposition velocities for the modelled tracer over the five land surface types. These values are based on results by Nho-Kim et al. (2004) and Zhou et al. (2009), for fine particulate matter, representative of sulfate aerosol.

In Table 4.1 it can be seen that larger dry deposition velocities are applied throughout the winter months. Nho-Kim et al. (2004) and Zhou et al. (2009) both indicate that the deposition velocities for fine particles (PM2.5) are greatest throughout the winter. Furthermore, any diurnal variability does not influence tracer concentrations in this study, as tracer concentrations, much like UK Midlands [PM10] in Chapter 4, are daily averaged values. It is for this reason that no diurnal variability in dry deposition velocity was attributed to the tracers in this study.

It is shown in Table 4.1 that land surface type greatly influences the dry deposition velocity of a fine particle. It is seen that the greatest dry deposition velocities are prescribed for the forest. The rationale being that forests have a greater surface roughness than any of the other land surface types, thereby increasing the surface area on which PM can deposit on to. Consequently the rates of: Brownian diffusion, inertial impaction and interception (Sect. 1.3.1), which positively impact on dry deposition velocity, will all increase over forests. This rationale holds for the remainder of the land surface types, with ice being the smoothest land surface type with the smallest surface area and the lowest dry deposition velocity.

4.4.2 Wet Deposition

The most efficient method for removing particulate matter from the atmosphere is through wet deposition. The wet deposition of soluble aerosol occurs predominantly within the cloud, as aerosol particles are collected by larger water droplets. This aerosol is subsequently sequestered within the water droplet, until reaching the surface. Insoluble aerosol particles are affected by impaction with water droplets below the cloud, a process discussed in Sect. 1.3.2.

The major simplification involved with modelling UK [PM10], is the representation of all PM10 components using a single tracer. This simplification also limits the representation of wet deposition. Not all aerosol is scavenged from the troposphere at equal rates, with the solubility of different components an important characteristic. The differences in particulate solubility in the real world can be seen for organic carbon aerosol. Freshly emitted organic carbon is insoluble and hydrophobic, but after a single time step it becomes coated in inorganic species such as sulfate. This coating allows for the particle to become soluble and undergo wet deposition. Therefore a single representation of aerosol solubility is not accurately reflecting the characteristics of real-world aerosol.

This study's tracer is gaseous and consequently a wet deposition scheme is required to model the wet deposition of the tracer, as opposed to PM. The tracer was made to reflect the wet deposition characteristics of SO_2, the dominant precursor to sulfate aerosol. In UKCA, two input values are required to generate a Henry's law solubility coefficient for that species (Giannakopoulos et al., 1999). The first of these is the solubility dissociation coefficient, k(298), in units; mol atm^{-1}, while the second is a temperature dependent coefficient, $-\frac{\Delta H}{R^*}$, in units of K. The ΔH term is the change in enthalpy due to dissolution, while R* represents the universal gas constant (8.314 J K^{-1} mol^{-1}). The values obtained for SO_2 were obtained from the supplementary material of Thomas et al. (2011). This study's tracer has the following prescribed wet deposition characteristics: k(298) = 1.2 mol atm^{-1} and $-\frac{\Delta H}{R^*}$ = 3 x 10^{-3} K.

It is likely that there will be an underestimation in the quantity of tracer being deposited by wet deposition in this study, as PM10 aerosol is removed from the atmosphere at greater rates than SO_2. Despite this, by ensuring that the tracers are influenced by wet deposition, precipitation will moderate modelled tracer concentration. Much like for the dry deposition rates attributed to the tracer in Sect. 4.4.2, the wet deposition rates are consistent in all of this study's HADGEM3-GA4 simulations.

Section 4.4 has detailed the properties of this study's modelled tracer, with an attempt at best representing the behaviour of sulfate aerosol, using a gaseous tracer. Section 4.5 examines

tracer emission regions that are best representative of the greatest primary and precursor PM10 emission regions throughout Europe. Following the definition of the study's modelled tracer emissions, Sect. 4.6 will analyse tracer lifetime. An analysis of tracer lifetime will help to determine whether the tracers in the study are representing sulfate aerosol well.

4.5 Modelling Tracer Emissions throughout Europe

An idealised tracer framework was chosen for this study, however some realism of European PM10 source regions is retained. European tracers emitted in HADGEM3-GA4 are emitted from regions with elevated observed primary and precursor PM10 sources. Identifying regions with elevated PM10 emissions requires a number of PM10 precursor and primary PM10 emission inventories. These were obtained following work undertaken by the ECLIPSE project (Evaluating the Climate and Air Quality Impacts of Short-Lived Pollutants) (Stohl et al., 2015). Section 4.5 describes the steps taken in generating an idealised tracer emission map that is also semi-realistic in relation to the regions of tracer emission.

4.5.1 Chosen PM10 precursors and primary emissions

The ECLIPSE study required a representative emissions inventory to project climate and health impacts of short lived climate pollutants towards 2050. A large part of the novelty of the ECLIPSE study was the greater representativeness of the emission inventories generated. Pollutant sources that had been neglected in previous emission inventories included: gas flaring from oil production, wick lamps, high-emitting vehicles and diesel generators. It was shown that following implementation of the calculated emission inventory in four advanced Earth system models and six chemistry transport models, the concentration of short lived pollutants compared to surface and satellite observations more favourably than previous studies (Stohl et al., 2015). It was following the findings by Stohl et al. (2015) that the emission inventories representative of 2008 (the final year of analysis in Chapter 3), generated for the ECLIPSE study were chosen for this study.

4.5.2 Calculating a 2D Tracer Emission Field

It is desirable that the locations of highest PM10 emissions are identified and that the tracers are emitted from major European PM10 source regions. Consequently, this study's tracers are representative of flow regimes that have interacted with known regions of high primary and precursor PM10 emissions. An assumption used to generate the European PM10 emissions inventory is listed below:

- It was assumed that the identified primary and precursor PM10 emissions are all of equal importance, i.e. 1 kg m^{-2} s^{-1} of SO_2 and NO_x generate the same mass mixing ratio of PM.

Following this assumption it must be decided which of the emission inventories generated for the ECLIPSE study can be classified as primary or precursor PM10 emissions. Below is a list of the inventories used to generate this study's reference PM10 emission inventory.

- SO_2 emissions
- NO_x emissions
- Black Carbon Biomass burning
- Black Carbon Forest Fire emissions
- Organic Carbon Biomass burning emissions
- Organic Carbon Forest Fire emissions
- Non-Methane Volatile Organic Compound (NMVOC) emissions
- Ammonia emissions

The above assumption states that each of the above listed PM10 primary and precursor emissions are of equal importance to the mass mixing ratio of Europe. Consequently, identifying the regions where each of these primary and precursor emissions are emitted from is of high importance. With this being so, each of the above emission fields (kg m^{-2} s^{-1}) was simply added together to generate a fictional PM10 contribution factor. The emissions inventory generated for this study is shown in Fig. 4.1. In Fig. 4.1 the tracer emissions inventory is normalised with respect to the maximum PM10 contribution factor within the illustrated domain. Within the illustrated domain the greatest PM10 contribution factor was attributed to a West Poland grid point.

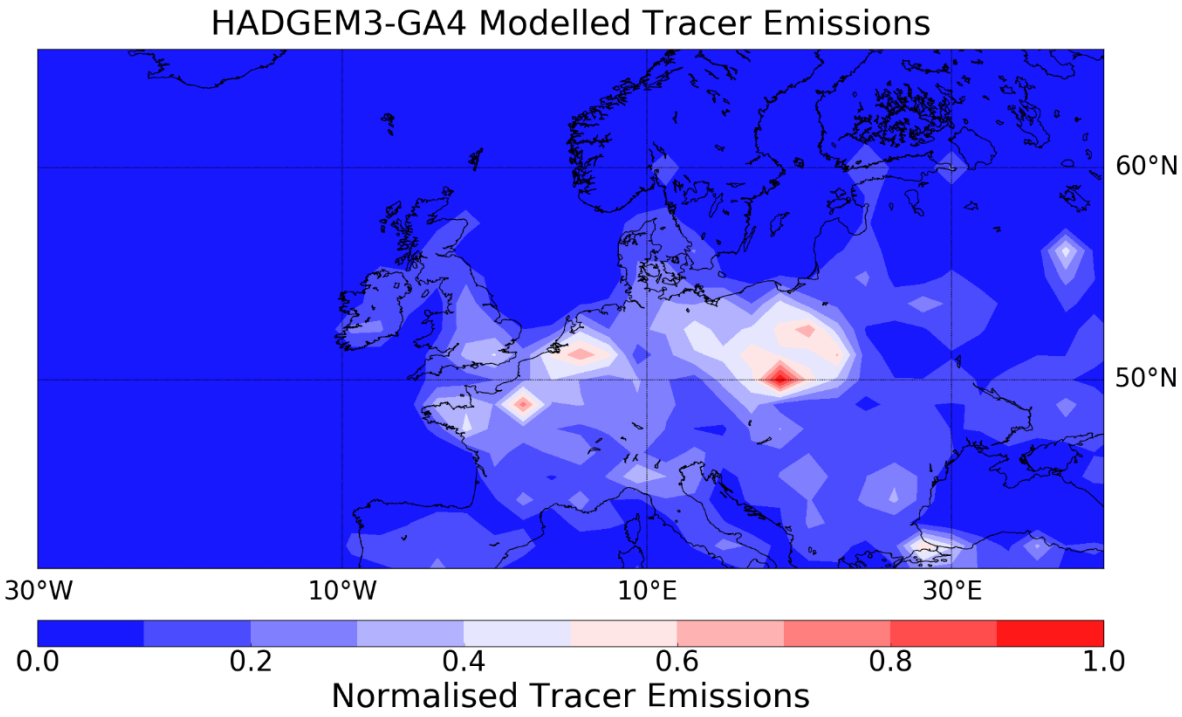

Figure 4.1 This study's normalised PM10 emissions map following evaluation of the ECLIPSE emission inventory. The normalised PM10 emissions map is generated following the addition of primary and precursor PM10 constituent emissions, with the largest value (1.0) attributed to West Poland.

Following the generation of a primary and precursor PM10 emission dataset, Fig. 4.1 identifies a few regions of elevated primary and precursor PM10 emissions. The largest and most evident of these regions is situated in West Poland. This region includes the peak normalised tracer concentration in Fig. 4.1 at 50^{o}N. The second region, with the greatest primary and precursor PM10 emissions, within the European domain selected, is in the BENELUX region. This region is characterised by three peaks, two in Northern France and the other in the Netherlands/ Belgium region. Representing the greatest normalised emissions in the southern region of this European domain is the Po Valley. Although this region shows a peak and is historically associated with elevated [PM10] (Bigi et al., 2012; Marcazzan et al., 2001), there exists a topographic barrier in the Alps mountain range, which in effect traps this pollutant. Section 4.6 explains how the Po Valley tracer was emitted in the model, so that its transport to the UK Midlands was not inhibited. The final PM10 source region highlighted was within the UK. A peak in Fig. 4.1 exists in Southeast England, corresponding to the location of the UK's most polluted city, London.

Following identifying the dominant regions of primary and precursor PM10 emissions in Fig. 4.1, this study's tracer emissions inventory was generated. The peak concentration in each of the above mentioned regions; the UK, BENELUX, Po Valley and West Poland, was used to

represent a spatially uniform tracer source region for all tracers, except the BENELUX tracer. The two long-range advected tracers (Po Valley and West Poland) and the locally sourced tracer (UK) are emitted over a 3x3 grid-point, square domain. The region in Fig. 4.1 that corresponded to an elevated BENELUX primary and precursor PM10 source, is geometrically more complex, stretching from France to South Denmark. It is due to the complex shape of the BENELUX region that the tracer emission region is more representative of the normalised PM10 emission region in Fig. 4.1. Furthermore the longitudinal extent of the BENELUX region allows for large variations in tracer emission, including three emission peaks in Fig. 4.1. Consequently the BENELUX tracer was chosen to reproduce the heterogeneity in normalised BENELUX PM10 emissions in Fig. 4.1. Figure 4.2 shows this studies tracer emission map, with the four emitted tracers, spatially separate throughout Europe.

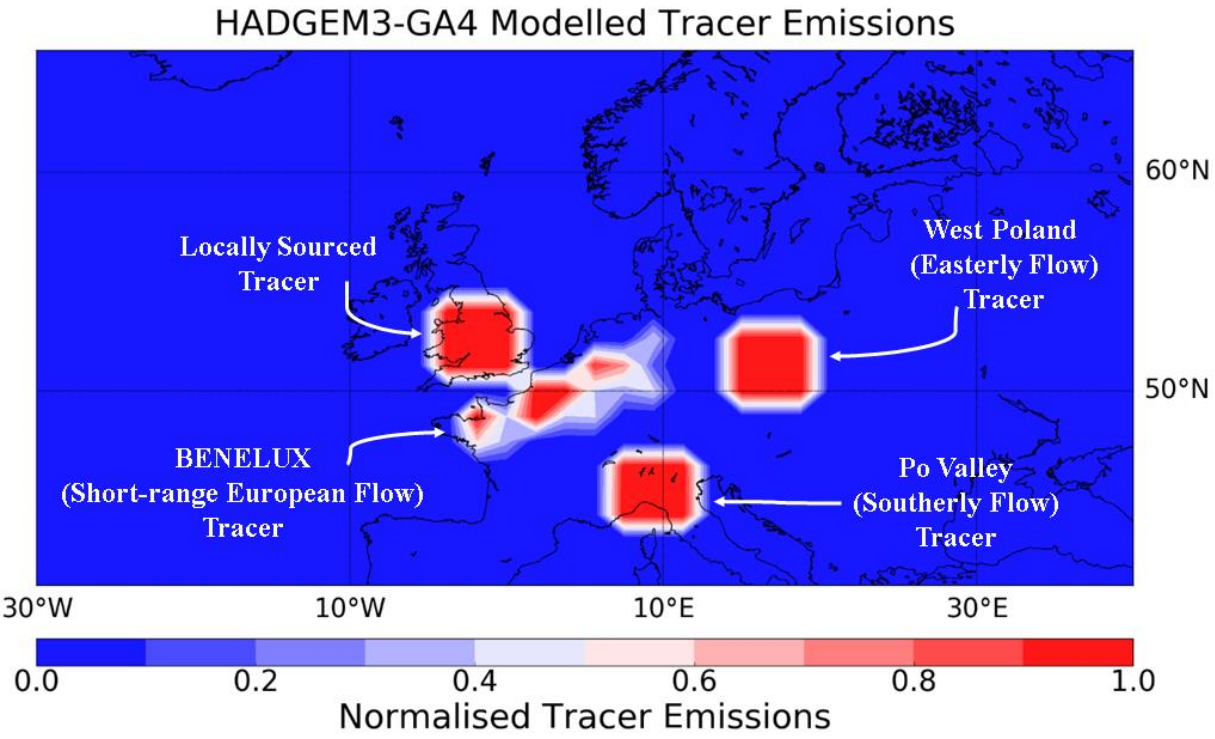

Figure 4.2 Tracer emission map, based on the regions of largest primary and precursor PM10 emissions, identified in Fig. 4.1. The map indicates four spatially distinguished tracer emissions; the locally sourced UK tracer, the BENELUX tracer, the Po Valley tracer and the West Poland tracer.

The emission regions for the UK, West Poland and Po Valley regions have been extended throughout a 9 grid point square. The BENELUX tracer region is more representative of the emission region identified in Fig. 4.1.

The decision to extend the two long-range; Eastern and Southern European source regions to a 9 grid-point peak is based on projected sensitivities to flow regime. For the two long-range

advected tracers, the UK Midlands concentration of these tracers will heavily depend on the exact flow direction between the source and the UK Midlands. By extending the regions, the sensitivity of the tracer advection into the UK to the exact flow regime is reduced.

For the locally sourced tracer, the motivation for extending the source region to a 9 grid-point domain is slightly different. At the resolution of the climate model being used (1.875^{o} longitude x 1.25^{o} latitude) there is no possibility of accurately reflecting observed urban/ rural transitions and subsequent heterogeneity in local PM10 sources. Consequently, the uniform tracer emissions throughout the locally sourced tracer emission region make no attempt to capture heterogeneities in UK PM10 emissions.

Section 4.4 disclosed the tracer characteristics that were designed to allow the tracer to simulate SO_4^{2-}, which is capable of long-range transport from Eastern Europe into the UK. Following the identification of four primary tracer emission regions, Sect. 4.6 will analyse the lifetime of these tracers in the modelled atmosphere. It is important to determine whether the prescribed variables for dry deposition velocities and wet deposition coefficients are capable of generating a tracer that is comparable in lifetime to SO_4^{2-}.

4.6 Tracer Lifetime

The tracers emitted in this study are chemically inert and therefore their only removal processes are wet and dry deposition. The characteristics of the emitted tracer attempt to mirror those of SO_4^{2-} and its gaseous precursors. SO_4^{2-} has a lifetime from 4-6 days in the boundary layer (Adams et al., 1999) to 10 days in the free-troposphere (Stevenson et al., 2003), which enables it to advect from Eastern Europe into the UK. To modulate the tracer lifetime, the dry and wet deposition must be representative of SO_4^{2-} and its precursors in the case of wet deposition. The tracer characteristics that govern dry and wet deposition were shown in Sect. 4.4.1 and 4.4.2 respectively. Equation 4.1 describes the calculation of tracer lifetime (λ) in this study.

$$\lambda\,(\mathrm{s}) = \frac{\text{Integrated Tracer atmospheric burden (kg)}}{\text{Tracer Emission Rate (kg s}^{-1}\text{)}} \qquad \text{Eq. 4.1}$$

Table 4.2 shows the mean tracer lifetime for each emitted tracer in this study's present-day nudged HADGEM3-GA4 simulation (Sect. 4.8.1). In addition to the mean tracer lifetime, significance bounds are represented as the mean tracer lifetime ± 1.96 × the standard error of the mean ($p<0.05$). Tracer lifetime is calculated for each day and hence an estimate of variability is calculated using the standard deviation of the daily tracer lifetime dataset.

Table 4.2 rows 2-5) The mean lifetime of each of the four emitted tracers in this study (days) ± 1.96 x the standard error in the tracer lifetime.

Species	Lifetime ±1.96 x Standard Error (days)
UK Tracer	6.253 ± 0.127
Elevated Po Valley Tracer	8.434 ± 0.198
West Poland Tracer	4.284 ± 0.165
BENELUX Tracer	5.808 ± 0.186

The shortest lifetime of any tracer in Table 4.2 is seen for the West Poland tracer, which lies within the bounds of SO_4^{2-} lifetime found by Adams et al. (1999). The decreased lifetime for the West Poland tracer is most likely due to the increased forest vegetation that is situated in central Europe. Section 4.4.1 showed how dry deposition rates are increased over a forest land surface type and it is likely due to this factor that the lifetime of this tracer is the shortest of all of the simulated tracers.

All of the four tracers' lifetimes lie within the bounds of SO_4^{2-} lifetime. The tracer with the greatest lifetime, the Po Valley tracer, has a lifetime more comparable to the lifetime of SO_4^{2-} in the free-troposphere. The lifetime of the Po Valley tracer is almost double that of the West Poland tracer and can probably be explained by its region of emission. The Po Valley tracer is emitted from both, within the Po Valley and the top of the simulated Alps mountain range. The rationale for this is to allow for the transport of Po Valley tracer to the UK in favourable synoptic conditions.

Due to the emissions of the Po Valley tracer on top of the Alps. The tracer is emitted from an elevated region, in comparison to the other three tracers. Figure 4.3 shows a composite of Po Valley and West Poland tracer concentration vertical profiles within the UK throughout the 10 days of highest UK Po Valley tracer concentration, in this study's present-day nudged HADGEM3-GA4 simulation (Introduced in Sect. 4.8.1).

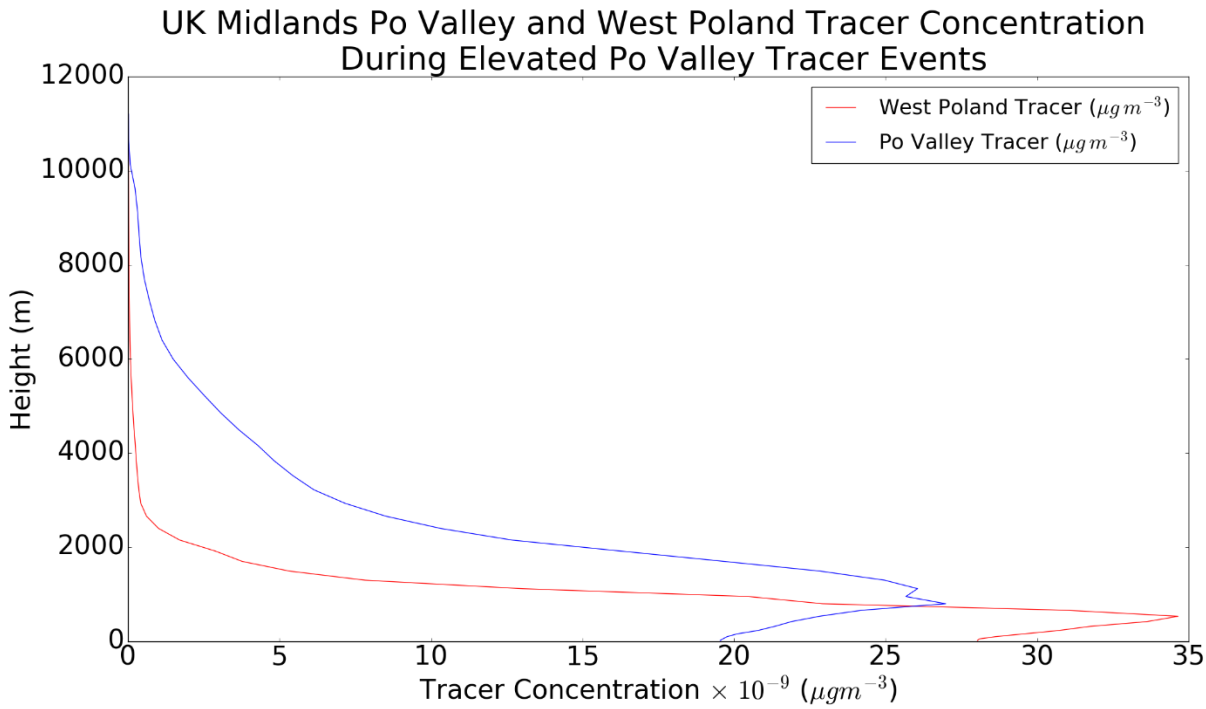

Figure 4.3 A vertical profile of West Poland (red line) and Po Valley (blue line) tracer concentration throughout the 10 days with greatest Po Valley Tracer concentration in the UK boundary layer. The profiles were obtained following this study's present-day nudged HADGEM3-GA4 simulation, which is introduced in Sect. 4.8.1. The dataset used is for 10 years between 1999 and 2008.

Figure 4.3 shows the vertical profiles of both the Po Valley and West Poland tracer at the UK Midlands grid point. Most evident from the vertical profiles in Fig. 4.3 are the different heights at which the two tracers are seen at. It is seen that the Po Valley tracer is lofted in comparison to the West Poland tracer. The Po Valley tracer peak is seen at 800m, while the peak of West Poland tracer is seen at 533m.

It was seen following the analysis of tracer lifetime in Table 4.2 that the Po Valley tracer had a lifetime more comparable to the lifetime of sulfate aerosol in the free troposphere (Stevenson et al., 2003). Contrasting this, the West Poland tracer had a lifetime in the atmosphere that was half as long and comparable to the lifetime of SO_4^{2-} in the planetary boundary layer (Adams et al., 1999). The differences in tracer lifetime are most likely explained by differences in the height of the two tracer plumes in Fig. 4.3.

One reason as to why the two tracers are advected into the UK at different heights is possibly due to the regions that they are advected within. The Po Valley tracer is advected in the lowest model level, however at a greater height above mean sea level, on the Alps mountain range. Opposing this, the West Poland tracer is emitted at a lower height, with respect to

mean sea level. Henne et al. (2004) highlighted the importance of orographic venting within the Alps mountain range and how this allows for the transport of pollutant out of the PBL into the free-troposphere. This process is also highlighted to occur at an altitude that is much elevated above sea level and hence is the suggested mechanism for why Po Valley tracer is advected towards the UK within the free-troposphere in the 10 cases seen in Fig. 4.3. Because of the efficiency of orographic regions in transporting pollutant from the boundary layer into the free-troposphere (Henne et al., 2004), much of the Po Valley tracer is found within the free-troposphere. It is therefore no surprise that the Po Valley tracer has a lifetime comparable to sulfate within the free-troposphere, as it too is seen to reside, at least for the majority of the plume within the free-troposphere.

The increased elevation of the Po Valley tracer results in reduced dry deposition rates. A tracer that is further from the model surface is less likely to interact with the surface and subsequently be deposited onto it. A consequence of decreased dry deposition velocities is an increased lifetime of Po Valley tracer.

Sections 4.2 to 4.6 have introduced this study's modelled tracer, which is representative of the atmospheric lifetime for SO_4^{2-}. The model that will be used to simulate the transport of this tracer is HADGEM3-GA4. Section 4.1 introduced HADGEM3-GA4 and highlighted that because this is an atmosphere-only model there are a number of prescribed fields that are required to replace the coupled components in HADGEM3. Section 4.7 details the most important prescribed fields used and varied within this study, namely sea ice fields and sea surface temperature (SST).

4.7 HADGEM3-GA4 Prescribed Model Fields

Section 4.1 highlighted that the climate model used in this study is the HADGEM3-GA4 atmosphere-only model. It was also stated that prescribed fields are required, which replace the coupled components of the HADGEM3 model.

To prescribe the impact of the ocean on the atmosphere model, SSTs have been prescribed within HADGEM3-GA4. The prescribed SST ancillary file is taken from the Met-Office standard ancillaries for HADGEM3-GA4 N96 simulations (Walters et al., 2014), for this study's present-day simulations. The SST field corresponds to a 1982-2006 Advanced Very High Resolution Radiometer (AVHRR) reanalysis average field (Reynolds et al., 2007).

Also in contact with the atmosphere model in HADGEM3, is the CICE, sea ice model. Sea ice plays an important role in dictating surface baroclinicity, dictated by surface temperature gradients. Sea ice thickness and sea ice depth have been prescribed in HADGEM3-GA4. The

sea ice fields have been generated from the Met-Office standard ancillary files, as for the prescribed SST ancillary file. The sea-ice fields are also calculated following AVHRR reanalysis for an average of the 1982-2006 period, in this study's present day simulations.

4.8 HADGEM3-GA4 Modelling Framework

This study's modelling framework is based around the use of three HADGEM3-GA4 simulations: present-day nudged, present-day free-running and future time-slice representative of the year 2050 HADGEM3-GA4 simulations. The first two of these simulations are present-day simulations that are concurrent to the time period used in Chapter 4, DJF between January 1999 and December 2008. A 10 year future time-slice simulation is representative of 2050 under the RCP 8.5 emissions scenario. This chapter will highlight the role of each HADGEM3-GA4 simulation in determining whether UK [PM10] episodes change in a future climate.

4.8.1 Present-day Nudged HADGEM3-GA4 Simulation

The first of the HADGEM3-GA4 simulations to be undertaken in this study is the present-day nudged HADGEM3-GA4 simulation. The nudged simulation has meteorological fields that are constrained to ERA-Interim reanalysis data. The fields are constrained through Newtonian relaxation, or nudging, which is a process that is discussed within Sect. 5.1. The intention of nudging is to ensure that the HADGEM3-GA4 simulation has the same meteorology as the ERA-Interim reanalysis dataset, used for Chapter 3. With such a constraint, the modelled tracers can be directly compared to the UK Midlands [PM10] dataset and a modelled [PM10] dataset can be generated.

The principal function of the nudged simulation is to determine the influence of each modelled tracer on the UK throughout RWB events where elevated observed UK [PM10] episodes are seen. Due to the constraints placed on meteorology in the nudged simulation, the advection of each modelled tracer can be analysed on the same days as an observed UK Midlands [PM10] episode. Subsequently, following the analysis of the present-day nudged HADGEM3-GA4 simulation, the tracers contributing to ACRWB and CRWB events in the North Atlantic/ European region can be determined. This analysis allows us to determine the contributing sources to Omega Block events, which Chapter 3 found were the RWB subset that resulted in the greatest probability of observed UK Midlands [PM10] exceeding a hazardous threshold.

In the nudged simulation the prescribed fields for SST and sea-ice are unchanged from those discussed in Sect. 4.7. In addition, there are prescribed concentrations of long lived

greenhouse gasses, such as: CH_4, N_2O and CO_2. The values given to these gasses are: 9.89 $x10^{-7}$ kg kg^{-1}, 4.91 $x10^{-7}$ kg kg^{-1} and 5.8 $x10^{-4}$ kg kg^{-1}respectively. The values were obtained from the Working Group 1 contribution to the fourth assessment report of the IPCC (IPCC, 2007).

The secondary purpose of the present-day nudged HADGEM3-GA4 simulation is to validate the ability of the modelled tracers to replicate observed UK Midlands [PM10]. In this study, the modelled tracers have been emitted in regions that have been identified as elevated European PM10 source regions. Consequently, the tracers may represent some of the variability in observed UK Midlands [PM10]. A multiple linear-regression model is undertaken to determine a modelled [PM10] dataset using the modelled tracers. It is then determined whether the relationships seen in Chapter 3 between observed UK Midlands [PM10] and ERA-Interim θ-2PVU can be replicated between modelled UK Midlands [PM10] and modelled θ-2PVU that is nudged towards ERA-Interim reanalysis. In replicating these relationships, using modelled [PM10], it would indicate that the dominant sources for observed UK [PM10] episodes have been identified by the idealised modelled tracers. Furthermore, one could argue if these relationships are replicated that variability in synoptic meteorology plays a large role in the occurrence of UK [PM10] episodes.

The results of the nudged simulation will be presented in Chapter 5 of this study.

4.8.2 Present-day Free-running simulation

The role of the present-day free-running HADGEM3-GA4 simulation (hereafter free-running simulation) is to evaluate the ability of HADGEM3-GA4, when left unconstrained by ERA-Interim reanalysis, to replicate ERA-Interim reanalysis meteorology. The free-running simulation is run for the same period as the nudged simulation (DJF from January 1999 to December 2008) and with the same prescribed fields and variables, as stated in Sect. 4.8.1. The primary purpose of the free-running simulation is to determine meteorological model biases that exist in HADGEM3-GA4.

Chapter 3 highlighted how UK [PM10] episodes increase in frequency, when associated with all RWB events. To analyse UK [PM10] episodes in a future climate, the synoptic meteorology that has been found to elevate their frequency (RWB in Chapter 3) will be analysed. The free-running simulation will be used to determine model biases that exist in the frequency of spatial distribution of RWB events in HADGEM3-GA4. This study intends to calculate climate shifts in RWB frequency and in the flow regimes that influence the UK

following northeast Atlantic/ European RWB events. To calculate these climate shifts, a model bias correction is required and these corrections are calculated in Chapter 6.

4.8.3 Future Time-slice Simulation

To answer this study's primary research question, a future climate simulation is required. A future time-slice HADGEM3-GA4 simulation (hereafter time-slice simulation) was undertaken to determine the frequency and flow regimes resulting from northeast Atlantic/ European RWB for the year 2050.

The climate scenario used in the time-slice simulation is dependent on the representative concentration pathway (RCP). This study uses RCP 8.5, which is the worst case emissions scenario in the Coupled Model Intercomparison Project Phase 5 (CMIP5) inter-comparison study (Riahi et al., 2011). The RCP8.5 emissions scenario corresponds to a projected radiative forcing of 8.5 W m^{-2}, imposed by anthropogenic pollutants by 2100. Furthermore the RCP 8.5 projection is based on an estimate that the radiative forcing imposed on the Earth's system by anthropogenic emissions will continue to increase beyond 2100.

Prescribed SST and sea ice (depth and extent) anomalies are based on future projections from a Met-Office standard HADGEM2-CC simulation for 2050-2060. These anomalies are generated by subtracting an inter-annual daily mean ancillary file in HADGEM2-CC for the 2050-2060 time period from the daily mean ancillary file for the 1989-2011 period, from the same HADGEM2-CC model simulation. The 1989-2011 period was chosen from the HADGEM2-CC simulation as it presented the closest calculated inter-annual mean time-period to the time period from the Met-Office standard ancillaries (1986-2006). The calculated anomaly is subsequently added to the original SST and Sea ice fields, from which the present-day ancillary files for SST and sea ice are generated in this study.

A caveat with regards to the sea ice field is that both the sea ice thickness and sea ice extent fields are required independently. By creating an anomaly for sea ice thickness and adding this to the original sea ice thickness field, there can exist a situation where sea ice thickness = 0 m and sea ice extent = 1 (binary field; 1 = ice, 0 = no ice). Subsequently all sea ice extent fields were generated following calculation of the sea ice thickness ancillary files, with a sea ice thickness > 0 resulting in sea ice extent for that grid point =1.

Figures 4.4 (a) and (b) illustrate the HADGEM2-CC Sea Ice fraction and SST anomalies that were applied to the present-day Sea Ice fraction and SST fields.

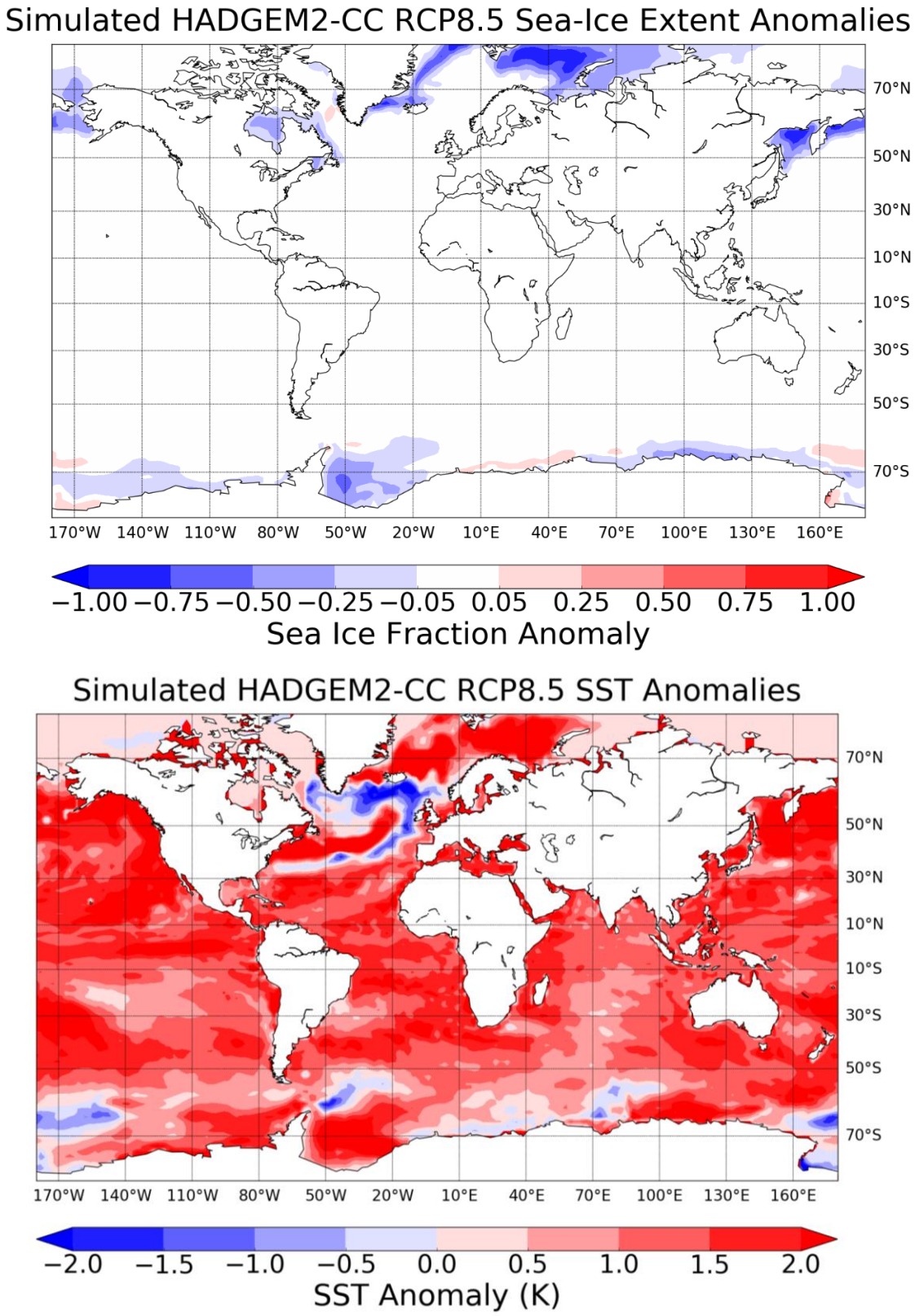

Figure 4.4 (a) Winter (DJF) sea ice extent anomalies between a present day period (1989-2011) and a future period (2050-2060) in a HADGEM2-CC simulation under emissions scenario RCP8.5. **(b)** Winter SST anomalies for the same period and in the same model as (a).

From Fig. 4.4 (a) it can be seen that following climate change under the RCP8.5 scenario that there is an evident net reduction in sea ice extent in the northern and southern hemisphere, throughout the northern hemisphere winter. This is a somewhat unsurprising result, considering that under RCP8.5 the global temperature is projected to increase by 2050. Despite this global warming, regions in Antarctica experience positive sea ice extent anomalies, which are in agreement with Shu et al., (2015), using CMIP5 models. This increase in sea ice is associated with the global circulation and reductions in poleward heat transport in the Southern Hemispheric oceans as a result from climate change.

Figure 4.4 (b) shows the projected (RCP8.5) SST response to climate change in 2050. Much of the world's ocean experiences a positive SST anomaly, however negative SST anomalies are seen in the Southern Ocean and in the North Atlantic. This cold bias in the North Atlantic Ocean is an important mediator of atmospheric dynamics in this region, due to the effects on surface baroclinicity. Analysis in Chapter 7 will refer back to Fig.4.4 to help explain climatic shifts in RWB in a future climate.

In addition to the aforementioned prescribed fields in the time-slice simulation, greenhouse gas concentrations were also prescribed. The values were again taken as anomalies from the HADGEM2-CC simulation, used for the CMIP5 inter-comparison study. The values used in the time-slice simulation for: CH_4, N_2O and CO_2 are: 1.569 $x10^{-6}$ kg kg^{-1}, 5.768 $x10^{-7}$ kg kg^{-1} and 8.5 $x10^{-4}$ kg kg^{-1} respectively. These values represent a: 37.0%, 14.9% and 31.8% increase of CO_2, CH_4 and N_2O mass mixing ratios in a future climate, compared to present-day mass mixing ratios, respectively.

4.9 Summary

Three HADGEM3-GA4 simulations will be used to answer this study's primary research question:

"Do UK PM10 episodes change in a future climate that is influenced by anthropogenic climate change?"

The present-day nudged HADGEM3-GA4 simulation is used to determine whether the relationships between ERA-Interim reanalysis RWB and observed UK Midlands [PM10] can be replicated using modelled tracers. This simulation is used to validate the idealised tracer framework, which is used to answer this study's primary research question. In addition to validating the tracers, the nudged simulation is used to identify the influential flow regimes to

the UK throughout northeast Atlantic/ European RWB events. The results from the nudged simulation are presented in Chapter 5.

A present-day free-running HADGEM3-GA4 simulation is used to evaluate the models ability to replicate synoptic meteorology from the ERA-Interim reanalysis dataset. The ability of HADGEM3-GA4 to model the process of RWB is paramount in understanding the impacts of climate change on RWB events and their subsequent impact on the flow regimes that influence the UK. The results from the free-running simulation are presented in Chapter 6. Model biases in the frequency of RWB and the flow regimes that influence the UK following northeast Atlantic/ European RWB are analysed.

The results from a future time-slice HADGEM3-GA4 simulation are presented in Chapter 7. The time-slice simulation is representative of the year 2050 and will help to determine whether the frequency of RWB or flow regimes resulting from RWB are different in a future climate.

Chapter 5 – Determining the Flow Regimes Influencing UK PM10 Episodes

Chapter 4 highlighted the framework for analysing future RWB events, using idealised tracers. The principal aim of the modelled tracers is to evaluate flow regimes that result from northeast Atlantic/ European RWB events. This chapter introduces the present-day nudged simulation, which will be used for analysis of the flow regimes influencing the UK [PM10] events, analysed in Chapter 3. The nudged simulation is constrained to ERA-Interim horizontal wind and temperature fields (u, v, T). A consequence of this is that the same UK [PM10] episodes that were identified in Chapter 3, can be analysed in the nudged simulation, using the modelled tracers. Section 5.6 will evaluate the flow regimes that influence northeast Atlantic/ European Omega block events, this study's most hazardous RWB subset (Sect. 3.3.6).

5.1 Nudging within HADGEM3-GA4

Newtonian relaxation or nudging is a data assimilation method that constrains the meteorology within a model. This study uses nudging to constrain the horizontal wind and temperature fields within HADGEM3-GA4. The purpose of nudging is to analyse the flow regimes that result from the RWB events which were analysed in Chapter 3.

To constrain the horizontal wind and temperature fields, nudging is applied to the HADGEM3-GA4 prognostic fields using Eq. 5.1, from Telford et al (2008).

$$\Delta x = F_{mt}(x) + G\Delta t(x_{ana} - x) \qquad \text{Eq. 5.1}$$

Where: Δx is the change in variable x, Δt is the dynamical time step, x_{ana} is the variable in the reanalysis dataset, x is the prognostic variable in the model, G is the relaxation parameter and $F_{mt}(x)$ is the change in variable x due to all other factors, such as model parameterisations, throughout a single time step.

The relaxation parameter, G defines the magnitude of the impact that the observations can have on the model. Telford et al (2008) highlighted that it is important for the relaxation parameter to be selected carefully. Too small and the nudging will have no impact on the modelled prognostic variables and too large values of G result in an unstable model. Telford et al. (2008) suggest that an appropriate relaxation parameter to use is:

$$G = \frac{1}{\text{Time interval in ERA} - \text{Interim}} \qquad \text{Eq. 5.2}$$

In this study the ERA-Interim reanalysis files are updated every 6 hours, therefore G = $4.6296\times 10^{-5}\ s^{-1}$.

Due to differing outputs, the temperature field from ERA-Interim reanalysis data must be converted to θ to be applied to the model θ field. There exist several differences in the grid structure and resolution between ERA-Interim reanalysis data and N96 HADGEM3 model simulations, which complicate the process of applying ERA-Interim meteorological fields onto the HADGEM3-GA4 domain. Interpolation must be undertaken to project ERA-Interim prognostic variables onto the HADGEM3-GA4 model grid. All prognostic variables are interpolated linearly onto the model log pressure field from the ECMWF hybrid pressure field. Brill et al. (1991) highlighted that more elaborate interpolation schemes brought no advantages over bi-linear interpolation.

In this study, nudging is applied in the form of Eq. 5.1 at 70 vertical levels, between model level 12 (1120 m) and model level 82 (8500 m). As in Heikkala, et al. (2011) only levels above the boundary layer were nudged, due to asymmetries between orography in the model and orography in the ERA-Interim re-analysis datasets. Telford et al. (2008) highlighted that the contrasting orographic domains in the model and ERA Interim reanalysis data become an issue as the spectral orography in the ERA-Interim reanalysis dataset does not simply interpolate onto the models grid point orography. The effect of contrasting orographic domains was seen to affect the lowest model levels and subsequently, nudging was not applied below the boundary layer. The boundary layer is by definition the lowest part of the troposphere where by surface forcings are directly felt within a timescale of about an hour or less (Stull, 2012).

5.2 Evaluating the Performance of the Nudged Simulation in Simulating RWB

This section explores the RWB frequency in the nudged simulation. There are a number of factors that may cause a discrepancy between RWB frequency in the ERA-Interim dataset and nudged simulation. These factors are detailed throughout this section.

Anstey et al., (2013) highlighted the importance of vertical resolution when calculating blocking metrics. There exist differences in the vertical resolution of both the ERA-Interim and HADGEM3-GA4 global domains. The ECMWF model used to generate the forecasts for reanalysis include 60 levels, with 37 levels represented below 18 km. The Met Office HADGEM3 simulation on the other hand has 85 vertical levels, with 50 levels below 18 km.

These vertical resolution differences in the two datasets are potentially capable of creating differences in the diagnostic θ-2PVU fields, on which the blocking metrics are calculated.

Sub-grid scale parameterisations within the nudged simulation may create differences in the diagnostic θ-2PVU field in the ERA-Interim and nudged HADGEM3-GA4 datasets. These parameterisations include diabatic processes, where for example: latent heat release and radiative cooling can greatly effect PV (Sect. 2.2.7).

Figure 5.1 shows the blocking frequency for one winter (December 1996 – February 1997) at 50° N at a longitudinal resolution of 1.5°, for the ERA-Interim reanalysis and present-day nudged HADGEM3-GA4 datasets. It is important that both RWB frequency datasets agree to a certain extent, as this author is attempting to minimise meteorological differences in the nudged simulation with the ERA-Interim reanalysis dataset.

The ERA-Interim reanalysis dataset has a horizontal resolution of 1.5 ° latitude x 1.5 ° longitude, while the HADGEM3-GA4 N96 resolution is 1.25° latitude x 1.875 ° longitude. The ECMWF ERA-Interim reanalysis dataset has been re-gridded to a 1.25° latitude x 1.875° longitude resolution, through bi-linear interpolation, to match the Met-Office model.

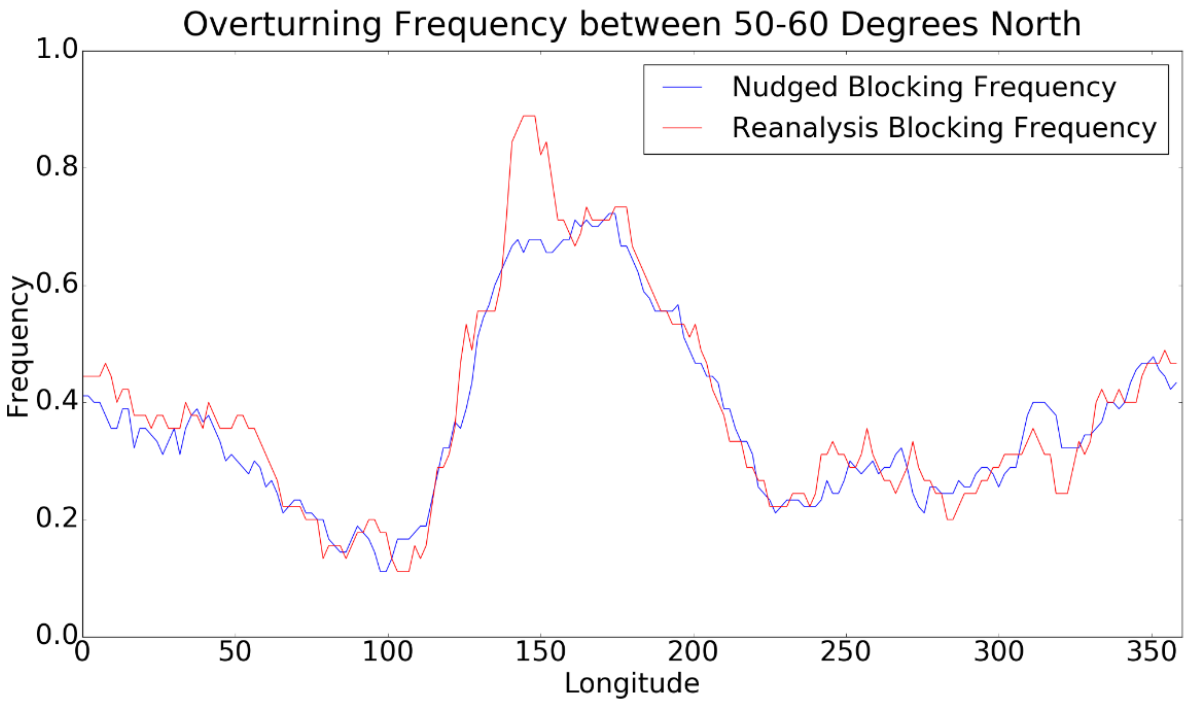

Figure 5.1. Overturning frequency averaged over a single winter (1st December 1996 – 28th February 1997) occurring within the latitudinal band 50.625° – 59.625°. Every longitudinal grid point (resolution = 1.875 °) is represented with the blue and red lines representing ERA-Interim reanalysis and present-day nudged HADGEM3-GA4 blocking frequency.

Figure 5.1 shows that the frequency of overturning in the re-gridded ECMWF reanalysis and nudged simulation are in good agreement. The largest difference in overturning frequency in Fig. 5.1 can be seen in the Pacific Ocean between 130^{o}E and 160^{o}E. The nudged simulation presents an underestimation of overturning in this region. At 149^{o}E, this overturning frequency difference corresponds to 23.75% of overturning frequency in the ERA-Interim reanalysis dataset. This study is focussed on the North Atlantic/ European region, therefore the negative bias in North Pacific overturning is not of great concern.

Within the North Atlantic sector, differences in RWB frequency are also seen. At a single grid point (320^{o} E), there exists an overestimation of RWB frequency in the nudged simulation. The overestimation accounts for 55% of the ERA-Interim reanalysis dataset RWB frequency. This overestimation in modelled overturning is longitudinally localised and reanalysis North Atlantic overturning is generally well captured by the nudged simulation.

Figure 5.1 has shown that there generally exists good agreement between RWB frequency in the ERA-Interim reanalysis dataset and the nudged simulation. Due to an oversight in the methodology, the diagnostic θ-2PVU field was not output from the nudged simulation. Consequently, to evaluate the relationship between modelled PM10 and RWB frequency, overturning metrics from the ERA-Interim reanalysis dataset were used, as in Chapter 3. As there is good agreement between RWB frequency in the ERA-Interim and nudged HADGEM3-GA4 datasets it is not expected that using the ERA-Interim θ-2PVU dataset will alter the conclusions of Chapter 5.

5.3 Relating Modelled Tracers to UK Midlands [PM10]

The primary aim of Chapter 5 is to determine the flow regimes influencing UK [PM10] episodes. Principally, this can be achieved in the nudged simulation through constraining the meteorological fields to ERA-Interim reanalysis data, as described in Sect. 5.1. Section 4.4 introduced the modelled tracers that are used to determine the flow regimes that influence the UK throughout RWB events.

A further purpose of the nudged simulation is to determine how much of the variability in UK Midlands [PM10] can be explained by our idealised modelled tracers. This chapter will attempt to replicate the relationships between UK Midlands [PM10] and RWB in Chapter 3, using the modelled tracers. If the relationships are found to be consistent in the nudged simulation, the relationships between RWB and UK [PM10] are therefore largely influenced by synoptic meteorology.

For a comparison between modelled [PM10] and observed UK Midlands [PM10], the modelled tracers must be also represented as concentrations. Initially each tracer, which is output as a mass mixing ratio ($PM10_{mmr}$), is converted to a concentration, using Eq. 5.3.

$$[PM10] = PM10_{mmr} \times \frac{p}{R \times (1 + 0.61 \times q) \times T} \qquad Eq. 5.3$$

In Eq. 5.3, p is pressure (Pa), R is the specific gas constant for dry air = 287 J kg^{-1} K^{-1}, q is specific humidity ($\frac{kg}{kg}$) and T is temperature (K).

Following the calculation of global tracer concentrations, a modelled [PM10] statistic was calculated, using the modelled tracers. It is anticipated that, due to the simplifications made in the treatment of the modelled tracers, a simple sum of all tracers at the UK Midlands receptor site would be inappropriate to create a comparable present-day nudged HADGEM3-GA4 [PM10] dataset (hereafter nudged [PM10] dataset) to observed UK Midlands [PM10] (hereafter observed [PM10] dataset). It is believed that, while each tracer will explain a percentage of the variance in the observed [PM10] dataset, some tracers may explain a greater proportion. This study uses a multiple-linear regression model to generate a modelled [PM10] dataset from four constituent tracers (locally sourced, Po Valley, West Poland and BENELUX). An extended observed [PM10] dataset (Winter months, DJF, between December 1996 and December 2008) is used to constrain the nudged [PM10] dataset. $\overline{[PM10]}$ for the extended observed [PM10] dataset is increased to 21.08 μg m^{-3}, compared with 19.72 μg m^{-3}, for the observed [PM10] dataset used in Chapter 3. The PM10 dataset was extended to match output from an initial nudged simulation used for sensitivity analysis (not included). Equation 5.4 illustrates the method by which all primary tracer concentrations and tracer covariance terms are used to generate a modelled [PM10] dataset. Each tracer (T) is scaled by an α coefficient, while their covariance terms with other tracers are scaled with a β coefficient. In Eq. 5.4, ε represents the error term, which is a single value attributed to all modelled [PM10] values.

$$[PM10] = \sum_{i=1}^{4} \alpha_i T_i + \sum_{i=1}^{4} \sum_{j=1}^{4} \beta_{ij} T_i T_j + \varepsilon \qquad Eq. 5.4$$

Equation 5.4 incorporates both the α scaled primary tracer concentration and the non-linear β scaled covariance terms. Covariance terms contain important information on the variability of the observed [PM10] dataset and have been included in the nudged [PM10] dataset for that reason. These terms are included to explain some of the variance that is unexplainable from

the first-order coefficients alone. Covariance terms are included to account for potential missing tracer sources, or missing tracer chemistry (interactions) in the tracer framework.

The α and β coefficients shown in Equation 5.4 are listed in Table 5.1. The 95% bounds for each coefficient, based on $\alpha/\beta \pm 1.96\,\sigma$ (σ is the standard deviation of each coefficient) are also shown. In Table 5.1, α coefficients are on the diagonal, all β_{ij} covariance terms off diagonal and all coefficients that are significantly greater or less than zero ($p<0.05$) are shown in bold.

Table 5.1. α and β contributing to Eq. 5.4, resulting from multiple linear regression. First order coefficients are shown as α coefficients, while β_{ij} coefficients represent covariance terms between the ith and jth tracer. Coefficients are shown as their mean value $\pm$ the 95th percentile confidence interval. Grid cells shaded red/blue correspond to coefficient means that are positive/ negative respectively. Bold values correspond to coefficients that are significantly greater than zero ($p<0.05$)

Tracer	Local Tracer α_1	Po Valley α_2	West Poland α_3	BENELUX α_4
Local Tracer	$\boldsymbol{\alpha_1 = 0.19 \pm 0.022}$	$\boldsymbol{\beta_{21} = -0.058 \pm 0.031}$	$\boldsymbol{\beta_{31} = -0.022 \pm 0.018}$	$\boldsymbol{\beta_{41} = 0.0066 \pm 0.0059}$
Po Valley		$\boldsymbol{\alpha_2 = 6.9 \pm 4.1}$	$\beta_{32} = -0.12 \pm 0.17$	$\boldsymbol{\beta_{42} = -0.27 \pm 0.17}$
West Poland			$\boldsymbol{\alpha_3 = 2.2 \pm 0.89}$	$\boldsymbol{\beta_{43} = 0.40 \pm 0.12}$
BENELUX				$\alpha_4 = 0.37 \pm 0.39$

The α coefficients for each tracer are shown in Table 5.1, with three α coefficients significantly greater than 0. The BENELUX tracer represents the only α coefficient that is not significantly greater than zero. The largest α coefficient in Table 5.1 is shown to be associated with the Po Valley tracer. While the Po Valley tracer has the largest coefficient, it also exhibits the largest uncertainty in the α coefficient, which will be discussed in the subsequent section.

The covariance terms included in Eq. 5.4, for the calculation of modelled UK [PM10] are shown to be both positive and negative. Three covariance terms in Table 5.1; β_{21} , β_{31} and

β_{42} .are shown to be significantly less than zero. Two of the three covariance terms, which involve the BENELUX tracer are shown to be significantly positive, with the Po Valley/ BENELUX tracer covariance representing the only negative BENELUX tracer covariance term.

5.3.1 Discussion

It has been shown that the largest tracer coefficient is attributed to the Po Valley tracer. This indicated that at times when the Po Valley tracer is elevated within the UK, the UK experiences elevated observed [PM10]. Associated with the elevated α coefficient is an elevated uncertainty, which indicates that the exact contribution of the Po Valley tracer on UK PM10 is uncertain. What is seen is that the advection of Po Valley tracer is associated with elevated observed [PM10] on rare occasions. Despite these being rare occasions, they raise the α coefficient associated with the advection of Po Valley tracer. Such rare occasions have been identified, when the advection of the Po Valley tracer coincides with the advection of Saharan dust from the south of the UK. Ryall et al. (2002) predict just one or two Saharan dust events per year (365 days), however are shown to be associated with elevated UK [PM10]. On these rare events, the Po Valley tracer is aliased with the influence of Saharan dust events on UK [PM10]. It is rare events such as these that raise the influence of the Po Valley tracer on modelled [PM10], raising the α coefficient (6.9) and evidenced by the elevated uncertainty associated with α (± 4.1).

Of the α coefficients attributed to the tracers in Table 5.1, the α coefficient for the BENELUX tracer is the only coefficient that is not significantly greater than zero ($p<0.05$). It is unlikely that the BENELUX tracer would be contributing negatively to nudged [PM10] and it is likely that during European advection events the BENELUX-West Poland covariance term, which is equivalent to the magnitude of the BENELUX α coefficient, is aliasing some of the BENELUX tracer. The significantly positive β_{43} covariance term from Table 5.1 highlights that during cases when the BENELUX and the West Poland tracers are advected together, there is a significant tendency for UK [PM10] to be greater than that explained by the first order tracer coefficient terms alone. A separate sensitivity study has shown that without this covariance term ($\boldsymbol{\beta_{43}}$**)**, it is seen that the BENELUX tracer α coefficient is significantly greater than zero (0.3897 ± 0.3762). This indicates that some information from periods when the BENELUX influences the UK greatest (European advection), is retained within the covariance term as opposed to the first order BENELUX coefficient (α_4).

One would expect the locally sourced tracer to have a positive impact on modelled UK [PM10], due to the proximity of the emissions to the receptor site. Table 5.1 shows that the locally sourced tracer does indeed have a positive α coefficient, albeit with the smallest magnitude of the four constituent tracers. It is seen that for the locally sourced tracer the covariance coefficient β term is negative with both long-range advected European tracers (Po Valley and West Poland). This indicates that during periods of long-range advection into the UK, there exists a reduced locally sourced tracer concentration. Furthermore, during periods of stagnation and the accumulation of locally sourced tracer, there exists little or no long-range advected tracer. The β coefficient between the locally sourced and BENELUX tracers however is positive. This result indicates that there exist meteorological conditions that both lead to elevated UK [PM10] and that facilitate the accumulation of near-continental BENELUX and locally sourced tracer.

5.3.2 Limitations

Covariance terms in Table 5.1 exist due to the existence of variance that is not represented by the linear combination of modelled tracers. These can therefore represent the variance lost from any of this study's simplifications, which include: missing PM10 sources, missing variance in the PM10 components and missing chemical processes. Consequently, the covariance terms are difficult to interpret physically and could be caused by a combination of factors. Despite being unsure as to their physical meaning, these covariance terms contain important information on the variability of the observed PM10 dataset and have been included in the nudged tracer [PM10] dataset for that reason.

5.3.3 Total Explained Tracer

Chapter 4 highlighted the simplifications used in modelling PM10 sources throughout Europe, including homogeneous and spatially extensive source regions in the tracer framework. Despite these sizeable simplifications to PM10 source regions and nudged model limitations, the tracers were able to account for 42% of the variance observed at the UK Midlands tri-site PM10 receptor site. Figure 5.2 shows a time series of the two datasets (observed and nudged tracer PM10) for the first 4 winters (360 days) of each dataset (1st December 1998 – 28th February 2002).

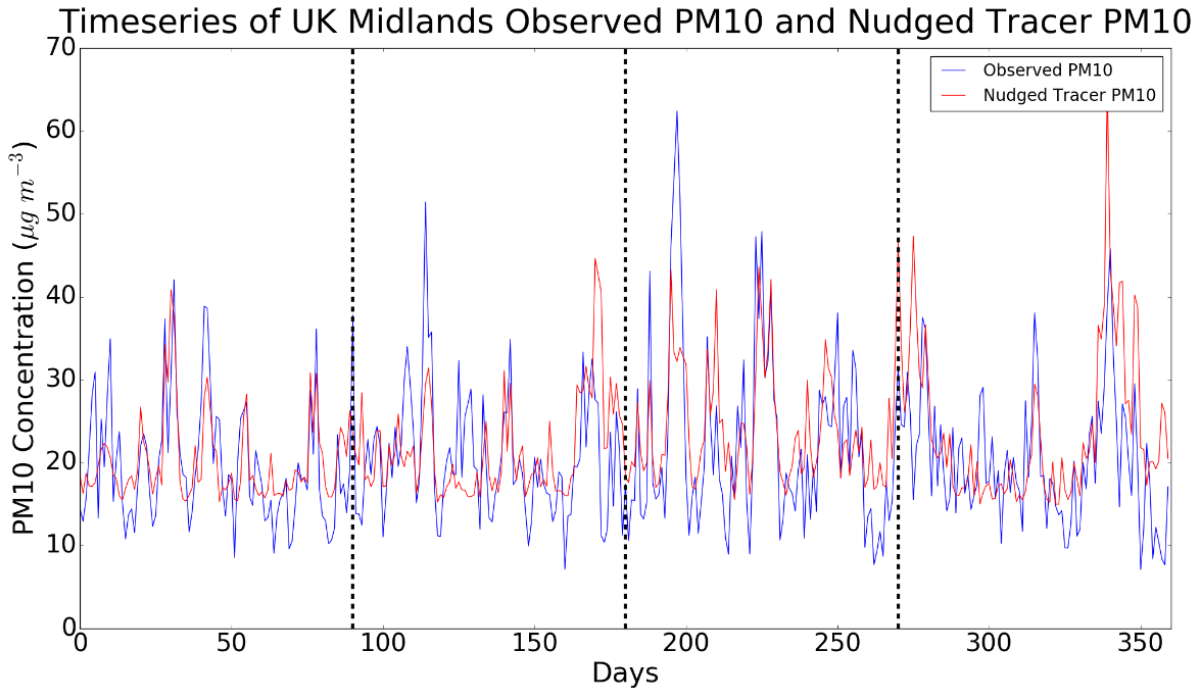

Figure 5.2. [PM10] time series for four 90 day winters (DJF) periods, divided by vertical black lines, between 1st December 1998 and 28th February 2002. The black/ red lines correspond to the observed/ nudged modelled [PM10] time series.

From Figure 5.2 it can be seen that the nudged tracer PM10 time series (red in Figure 5.2), reproduces much of the variability seen in the Observed PM10 time series (blue in Figure 5.2). This result is quite remarkable, considering the over simplified source regions, negating complex chemistry and nudged model limitations. During almost all observed PM10 episodes, there exists a peak of nudged tracer PM10.

There are also a number of times when that the nudged [PM10] dataset fails to capture observed PM10. It can be seen that the minimum values in the observed PM10 dataset are not reproduced. This is a direct result of the error term in Eq. 5.4 and results from the multiple linear regression model not being able to reproduce all of the observed [PM10] variability.

The error term in Eq. 5.4 is 13.45 μg m^{-3} and is therefore greater than the lowest observed [PM10]. Consequently, with the tracers having positive contribution on nudged [PM10] (despite negative coefficient terms), 13.45 μg m^{-3} is the minimum possible nudged [PM10] value. It is therefore seen that the nudged [PM10] cannot represent the lowest observed [PM10] values.

In addition to the [PM10] minima in Fig. 5.2, the observed [PM10] maxima are rarely captured, which may be of consequence of the fact that the observations are influenced by an urban environment (urban background sites). The homogenous source regions, discussed in Section 4.5.2 are unable to replicate urban increments in [PM10]. Urban environments significantly raise UK [PM10] (Charron et al., 2006), with $\overline{[PM10]}$ at urban AQMS sites, predominantly greater than $\overline{[PM10]}$ at rural AQMS sites. Without capturing urban PM10 sources, the maximum observed [PM10] values are unlikely to be captured in the nudged [PM10] dataset.

The following section will explore the areas of well represented and missing observed [PM10] variability. The methods used will enable analysis of nudged and observed [PM10] variability at different frequencies.

5.4 Can the Tracer [PM10] Dataset represent any UK Midlands [PM10] Variability?

The primary objective of the nudged simulation is to determine the flow regimes dominant throughout RWB events, which Chapter 3 has shown lead to increased probabilities of exceeding a hazardous PM10 threshold. This is achieved by using spatially dispersed tracers, which are representative of flow patterns that affect the UK.

Section 5.4.1 introduces a technique, which will help to determine frequencies of variability where observed [PM10] variability is and is not well represented by the nudged [PM10] dataset. Complimentary Ensemble Empirical Mode Decomposition (CEEMD) is the method used, allowing the user to decompose a time series into time series of independent frequencies, termed Intrinsic Mode Functions (IMFs), that constitute towards the original time series. As opposed to Fourier techniques, CEEMD analysis is a method of dealing with both non-stationary and nonlinear time series (Singh et al., 2015), both of which are applicable to the observed and modelled [PM10] time series.

The CEEMD methodology is presented in Appendix B and the results of the analysis, in Appendix C.

5.4.1 Complementary Ensemble Empirical Mode Decomposition

CEEMD analysis has been used to determine the frequencies at which the modelled tracers are incapable of capturing observed [PM10] variability. The results in Appendix C show that the modelled tracers are incapable of replicating observed [PM10] variance at three temporal frequencies.

The highest frequency mode of lost variability in the modelled [PM10] dataset is seen for the highest frequency constituent time-series (IMF1). This high frequency variability relates to a constituent time series period of 4 days and therefore corresponds to a similar temporal period as synoptic meteorological variability. The relationships presented in Chapter 3, between RWB and observed [PM10] were driven by variations in synoptic meteorology. Lost [PM10] variability within the nudged [PM10] dataset at this time-scale will likely impact greatly on the relationships between nudged [PM10] and RWB, as initially presented in Chapter 3.

Figure C.1 shows substantial lost variability in the modelled [PM10] dataset, when compared to the observed [PM10] dataset for a period of 7 days. The 7 days here relates to a missing weekly cycle in the modelled [PM10] time series that is present in the observed [PM10] dataset. The observed [PM10] dataset experiences a weekend effect, whereby anthropogenic activity slows at the weekend and consequently, emissions from mobile PM10 sources reduce on the weekend. Tracer emissions experience no temporal variability and subsequently no 'weekend effect' is possible within HADGEM3-GA4.

Figure C.1 shows two IMFs with periods between 123 and 584 days, representing inter-annual variability, that show a loss of nudged [PM10] variability, when compared to the observed [PM10] dataset (IMF 7 and IMF 8). A simplification in the model is the assumption of temporally constant emission rates, based on averaged primary and precursor PM10 emissions and using data from the ECLIPSE emission dataset. The assumption of constant emissions was made as a simplification in an idealised tracer experiment, although this will lead to misrepresentations of observed primary and precursor PM10 emissions. In reality, emissions of anthropogenic and natural PM10 sources vary inter-annually and it is this variability that is likely lost at IMFs 7 and 8.

Similarly to IMFs 7 and 8, the lost variance in IMF 9 (period between 779 and 1170 days) and the residual IMF (IMF 10, period = 1170 days) can be attributed to the modelled simplification of constant tracer emissions. Unlike IMFs 7 and 8, the time period of lost

variance in IMFs 9 and 10 approach the length of the [PM10] datasets (1170 days). Consequently, these IMFs highlight the long term trends of both observed and nudged modelled [PM10] time series. The observed residual (IMF 10) shows a decreasing trend between 1999-2008, which supports research undertaken by the European Environment Agency (EEA) (EEA, 2016) that shows declining European PM10 and PM2.5 emissions throughout most of the period of this analysis (1999-2008). Contrastingly nudged [PM10] does not show any such decreases, which is to be expected, due to the constant emissions used in the model. Subsequently, this result explains the lack of signal at IMFs 9 and 10 in the nudged modelled dataset, which are indistinguishable from white noise and the significant trend in the observed PM10 dataset.

Section 5.5 will analyse the relationships between nudged [PM10] and RWB to determine whether the relationships found in Chapter 3 are replicated in the nudged simulation. The ability to replicate the relationships from Chapter 3 would highlight the importance of synoptic meteorological variability in determining the frequency of UK [PM10] episodes.

5.5 Replicating the Relationships between RWB and UK [PM10] using HADGEM3-ES

Section 5.5 attempts to replicate the relationships found between RWB and observed [PM10], using modelled [PM10]. Chapter 5 has shown that the tracers emitted in the model represent 42% of observed PM10 variability. Given the simplifications associated with this HADGEM3-GA4 tracer simulation, it is somewhat surprising that this much variability can be captured. The lost variability was seen at various temporal scales in Sect. 5.4, however perhaps most relevant to this study is the high frequency lost variability. The high frequency variability corresponds to the frequency of synoptic meteorological variability, which are most relevant to the results of Chapter 3.

5.5.1 Pearson's Correlation Coefficient

In Section 3.3, spatially robust relationships were observed between the instantaneous RWB metric, BI and observed [PM10]. It was inferred that the primary driver for this relationship was the location of the EDJ in relation to the UK Midlands. Corresponding with a strong EDJ over the UK, were lower observed [PM10] observations due to; greater pollutant dispersion, a higher probability of precipitation and to a lesser extent the reduction in photochemical reactions producing secondary PM10. As the EDJ is diverted from the UK, the UK Midlands experienced conditions more conducive to PM10 accumulation. Consequently, in the regions where the EDJ was deflected to, to the north or south of the UK, a negative correlation exists between BI and observed [PM10].

Figure 5.3 (a) shows the 2D Pearson's Correlation Coefficient field between BI and observed [PM10] from Section 3.3.1. Figure 5.3 (b) shows the corresponding plot, however using the nudged [PM10] dataset.

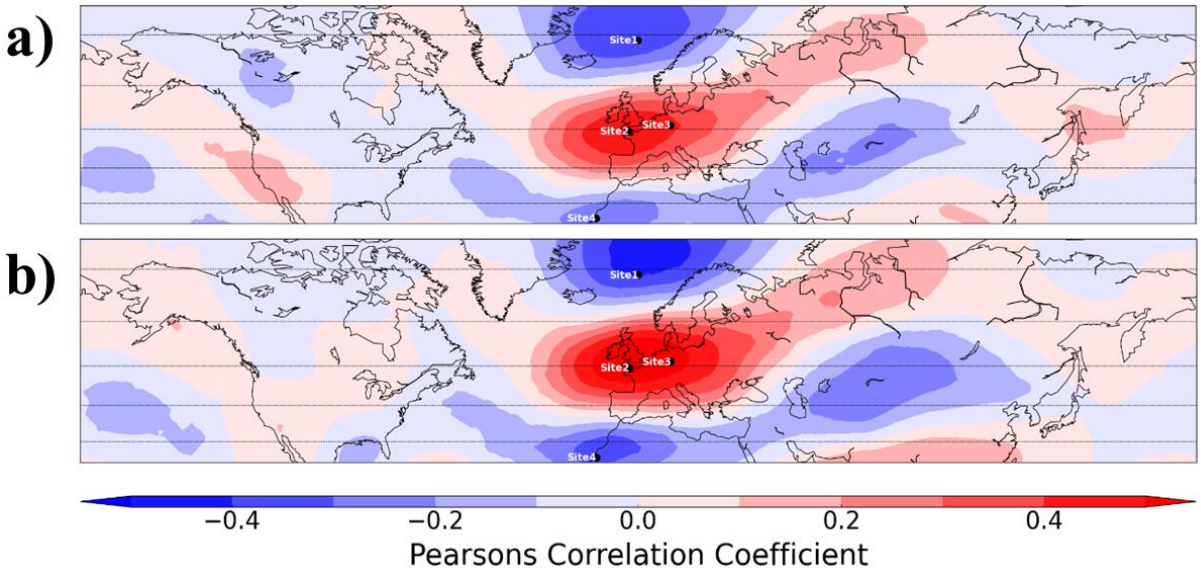

Figure 5.3 Pearson correlation coefficient between Blocking Index magnitude (K) and **(a)** observed UK Midland [PM10] (µg m^{-3}) and **(b)** nudged modelled [PM10] (µg m^{-3}). All data was taken for the winter months (DJF) between January 1999 and December 2008. PM10 data following a positive/ negative BI value was lagged by 1/0 days respectively.

Evident when comparing Figures 5.3 (a) and (b) are the similarities in the 2D Pearson correlation coefficient fields. Both 2D Pearson correlation coefficient fields result in a tripole structure centred over the UK. The spatial distribution of the Pearson's correlation coefficient seen in Fig. 5.3 (a) and (b) are very similar, however the maxima using the nudged model [PM10] dataset are greater in Fig. 5.3 (b). This suggests that the relationships between BI and [PM10] in the nudged modelled [PM10] dataset are stronger than when using the observed [PM10] dataset.

The strengthening of the relationship, using the modelled [PM10] dataset (Fig. 5.3 (a)) indicates that the variability in BI can now explain a greater proportion of the variability in [PM10] in the nudged simulation, when compared to using the observed [PM10] dataset. Although this seems counter intuitive, as the nudged [PM10] dataset can only explain 42% of the variability in the observed [PM10] dataset, this missing variability in the nudged [PM10] dataset is mostly unexplainable through synoptic meteorological processes. Sources of lost high frequency variability are likely due to unrealistically homogeneous; temporal or spatial tracer emissions. It is evident that both of these sources of variability are mostly independent

of synoptic weather conditions and therefore cannot be explained by synoptic meteorological variability. Consequently, the percentage of the total variance explained by synoptic meteorology in the nudged [PM10] dataset will be greater than that of the observed [PM10] time series.

5.5.2 Regions of Influence

Section 3.3.2 highlighted regions of influence, so called because these are regions whereby if RWB occurs within them, UK $\overline{[PM10]}$ one day after, is significantly elevated. Section 3.3.2 highlighted four such regions of influence by using two further blocking metrics, DB and RI. The DB index was used to determine whether the RWB event breaks anticyclonically or cyclonically, while the RI index distinguished between warm and cold events (Further explanation and derivation in Sections 2.6.2 and 2.6.3 respectively).

The regions of influence indicate the regions where RWB is influential to UK PM10. It is important that the regions of influence are comparable for observed and modelled [PM10], as this indicates that RWB is influential on UK [PM10] through similar mechanisms in both the observed and nudged [PM10] datasets.

The regions of influence for the nudged [PM10] dataset are shown in Figure 5.4. The methodology for creating these is identical to the method used to generate the regions of influence for the observed [PM10] dataset in Chapter 3.4. For ease of comparison, the regions of influence generated using the observed [PM10] dataset and reanalysis RWB metrics have been included in Figure 5.5.

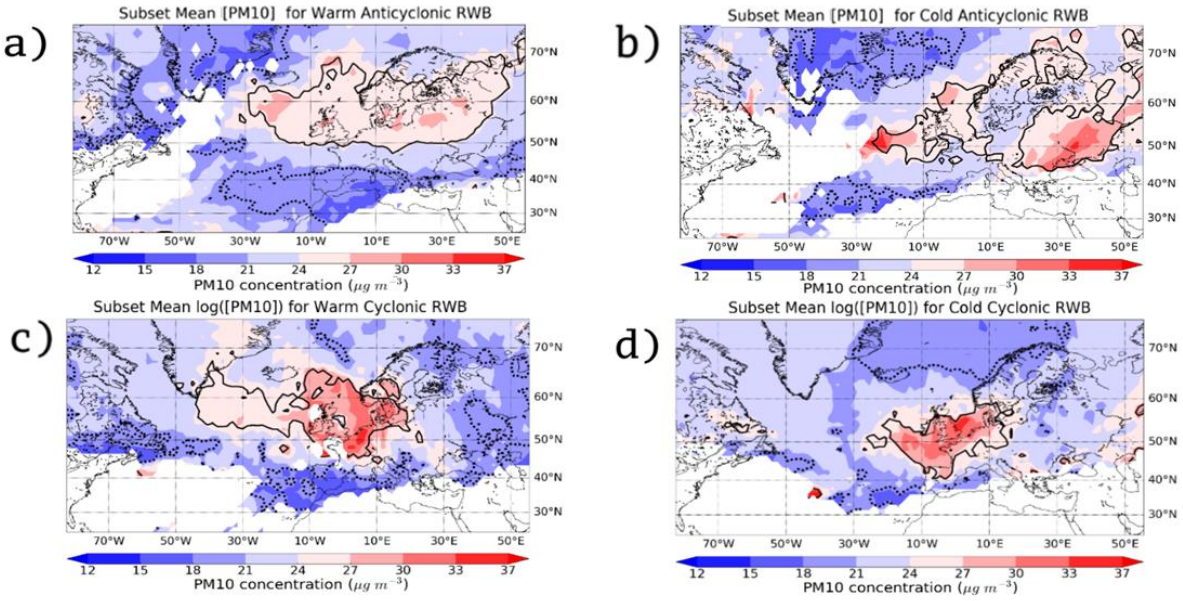

Figure 5.4 One day lagged UK mean present-day nudged HADGEM3-GA4 [PM10], for each point within a gridded region for: **(a)** warm anticyclonic, **(b)** cold anticyclonic, **(c)** warm cyclonic and **(d)** warm cyclonic Rossby wave breaking events in the ERA-Interim reanalysis dataset. Solid/dashed contours indicate regions where the illustrated ln[PM10] is significantly higher/lower than the mean ln[PM10] for the entire dataset respectively. White grid points represent points where RWB has occurred on fewer than 2 occasions throughout DJF January 1999 – December 2008. Present-day nudged HADGEM3-GA4 mean ln[PM10] = 3.05.

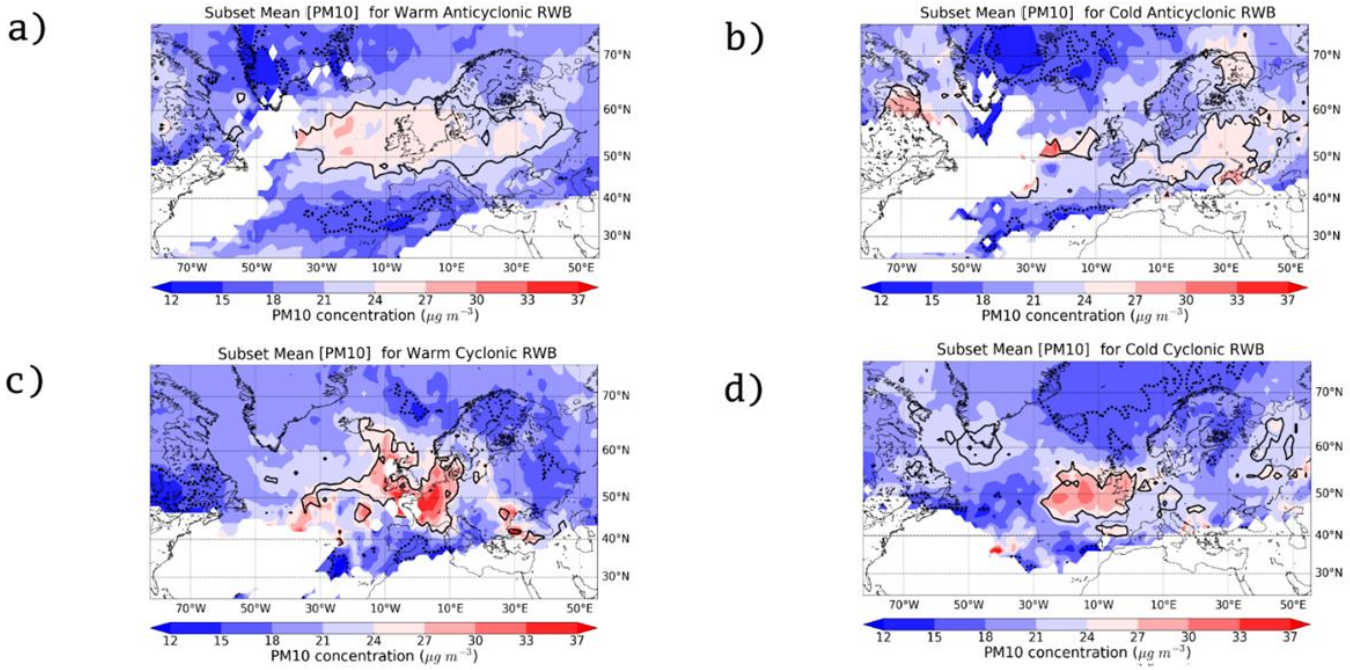

Figure 5.5 One day lagged observed UK Midlands mean [PM10] for each point within a gridded region following: **(a)** warm anticyclonic, **(b)** cold anticyclonic, **(c)** warm cyclonic and **(d)** warm cyclonic Rossby wave breaking events in the ERA-Interim reanalysis dataset. Solid/dashed contours indicate regions where the illustrated ln[PM10] is significantly higher/lower than the mean ln[PM10] for the entire dataset respectively. White grid points represent points where RWB has occurred on fewer than 2 occasions throughout DJF January 1999 – December 2008. Observed UK Midlands mean ln[PM10] = 2.98.

The regions of influence in Fig. 5.4 and 5.5 represent regions where RWB occurrence leads to UK [PM10] significantly greater than the dataset mean [PM10] ($\overline{[PM10]}$). A brief comparison of Fig. 5.4 and 5.5 highlight that the regions of influence for each RWB subset are similar in location and size for both the observed [PM10] dataset and the nudged [PM10] dataset. For both the observed [PM10] and nudged [PM10] datasets, WACRWB is the RWB subset with the greatest region of influence. Furthermore, the greatest and most coherent regions in both Fig. 5.4 and 5.5 are associated with the Warm RWB subsets. In contrast, the regions of influence for both cold RWB subsets in Fig. 5.4 and 5.5, are broken and less coherent than the warm RWB subsets, however still in a common location.

A comparison of Fig. 5.4 and 5.5 reveals more coherent regions of influence associated with the nudged [PM10] dataset in Fig. 5.4 when compared to the regions of influence in Fig. 5.5. Much like for the 2D Pearson's correlation coefficient plots in Fig. 5.3, a stronger

relationship is seen between RWB and nudged [PM10] as opposed to using the observed [PM10] dataset. The strengthening of the relationship between RWB and UK [PM10] in the nudged modelled simulation was attributed to a reduction of variability that synoptic meteorology cannot explain, as in Fig. 5.3.

The spatial patterns of ACRWB and CRWB seen in Fig. 5.4, using the nudged [PM10] dataset, are comparable to those in Fig. 5.5, when using the observed [PM10] dataset. Similarities in the regions of influence in both Fig. 5.4 and 5.5 indicate that the sources contributing to significantly elevated observed UK [PM10] are represented by the modelled tracers. Analysis of the exceedance probabilities in Sect. 5.5.3 will help elucidate whether the modelled [PM10] dataset includes episodic PM10 events and whether the probability of exceeding a hazardous [PM10] threshold is increased following RWB events. If this is the case, then it can be said that variability in synoptic meteorology plays a large role in the occurrence of UK [PM10] episodes.

5.5.3 Exceedance Probabilities

Section 3.3.4 illustrated the probabilities of exceeding a hazardous UK [PM10] threshold for four RWB subsets. This analysis has been repeated and the results displayed in Table 5.2 using the nudged [PM10] dataset.

Table 5.2 presents the probabilities of four RWB subsets exceeding a hazardous PM10 threshold one day after RWB occurrence for both the nudged [PM10] and observed [PM10] datasets. Within Table 5.2, as in Section 3.3.4, RWB is subset into continuous and onset events. The probability of exceeding the exceedance threshold without any RWB occurring within its spatially constrained region of influence is shown for the observed and nudged [PM10] datasets in the rightmost two columns. For ease of comparison, the greatest probabilities of exceedances in each column are highlighted in bold.

Table 5.2 Probabilities of exceedance resulting from cumulative distribution functions, as shown in Fig. 3.5, for four RWB subsets in the present-day nudged HADGEM3-GA4 [PM10] (Nudged [PM10]) and observed [PM10] datasets. The values displayed represent the probability of [PM10] the day following the relevant RWB subset to be greater than an exceedance threshold of 29.72 μg m^{-3}/ 31.08 μg m^{-3} for the observed and nudged [PM10] datasets respectively. The exceedance probabilities for events not associated with any RWB in the observational and modelled [PM10] datasets are shown in column 6 and 7 respectively. Bold values represent the greatest exceedance probability value for each column.

RWB Subset	Observational UK Midlands [PM10] Continuous	Observational UK Midlands [PM10] Instantaneous	Modelled Nudged [PM10] Continuous	Modelled Nudged [PM10] Instantaneous	Observational Days with no RWB	Modelled Days with no RWB
Warm	30.6	18.0	**28.6**	12.7	12.5	5.2
Cold	29.4	21.1	24.4	13.0	12.5	5.2
ACRWB	30.4	18.0	26.7	11.8	12.5	5.2
CRWB	**35.3**	**23.7**	25.6	**19.6**	12.5	5.2

Table 5.2 shows that all subsets of RWB result in an increased probability of exceeding a hazardous UK [PM10] threshold, in both the observed [PM10] and nudged [PM10] datasets. The greatest probability of exceedance values using the observed PM10 dataset were found for continuous CRWB events and attributed to the Omega block mechanism. Using the nudged [PM10] dataset, continuous CRWB events were not found to be associated with the greatest probability of exceeding a hazardous UK [PM10] threshold. Despite this, the probability of exceeding a hazardous UK [PM10] threshold for northeast Atlantic/ European CRWB events (constrained within the regions of influence in Fig. 5.4) is similar to ACRWB events in the same region.

For the nudged [PM10] dataset, instantaneous CRWB events in the northeast Atlantic/ European region are shown to be associated with the greatest exceedance probabilities of any instantaneous RWB subset in Table 5.2. These events are in fact mostly dependent on the prior occurrence of ACRWB within the northeast Atlantic/ European region, however this ACRWB occurs outside of the regions of influence used to constrain RWB in this analysis. As highlighted in Sect. 5.5.2, the regions of influence for each RWB subset are different for

the nudged [PM10] dataset and observed [PM10] dataset. These differences highlight a deficiency in the objective method of constraining RWB, as the regions are occasionally inadequate to constrain all influential RWB events. Despite this, the mechanisms dictating the occurrence of northeast Atlantic/ European CRWB are predominantly associated with the Omega block mechanism from Sect. 3.3.5.

The most hazardous RWB subset found in the nudged simulation, much like in Chapter 3 was the Omega block. In Chapter 3 the Omega block was associated with an exceedance probability of 0.373, whereas in the nudged simulation, Omega blocks are associated with an exceedance probability of 0.289.

One of the most noticeable differences between the exceedance probabilities from Chapter 3 and following the nudged simulation, are the reduced exceedance probabilities associated with the nudged [PM10] dataset. The nudged [PM10] dataset has a standard deviation of 7.45 µg m^{-3}, whereas the observed [PM10] dataset standard deviation is 11.72 µg m^{-3}. This increased variability makes PM10 episodes more frequent within the observed [PM10] dataset, even for days where no RWB has occurred.

The standard deviation of the nudged simulation (7.45 µg m^{-3}) is comparable to that for a rural background UK [PM10] AQMS in Oxfordshire, Harwell (8.10 µg m^{-3}). A background rural site must not be situated closer than 5 km from any built-up area or major road and must be representative of air quality in the surrounding 1000 km^2. This increased PM10 source homogeneity surrounding a rural site indicates that much of the lost high frequency variance in Sect. 5.4 is associated with a lack of heterogeneities in local tracer sources within this study's HADGEM3-GA4 simulations.

Following the evaluation of exceedance probabilities, it has been shown that all RWB is associated with an elevated probability of exceeding a hazardous UK [PM10] threshold. This result infers that it is the variability in synoptic meteorology and not in the PM10 source regions that is the predominant factor for generating PM10 exceedance events. Despite this, the reduced heterogeneity of local tracer sources can be attributed to a reduced exceedance probability throughout the entire nudged [PM10] dataset, when compared to the observed [PM10] dataset.

5.6 Omega Block Events – Contributing Tracers

The principal aim of this thesis chapter is to determine which flow regimes influence the UK through [PM10] exceedance events. The four tracers emitted in the HADGEM3 simulation are all representative of independent flow regimes. Using the relative contribution of each

tracer to the nudged [PM10] dataset throughout UK [PM10] events can help to determine the meteorological influence on [PM10] exceedance events.

In Chapter 3 the RWB subset associated with the greatest probability of exceedance were Omega Block events. Omega blocks are identified by CRWB on the upstream side of a blocking anticyclone, which is generated through the prior occurrence of ACRWB. It was shown in Figure 3.4 that ACRWB in this region is associated with an anticyclone over the Scandinavian region. Following this, throughout an Omega block event, the anticyclone was shown to migrate westward over the UK (Fig. 3.8). A hypothesis was generated in Section 3.3.6, as to why Omega blocks are associated with the greatest probabilities of exceedance. It is hypothesised that it is the initial advection of European PM10, followed by the stagnation of this previously advected European PM10 and locally sourced PM10 that leads to the greatest PM10 exceedance events. It is hypothesised that the ACRWB preceding the Omega block event facilitates the advection of European PM10 driven by the Scandinavian anticyclone. Following this, stagnant conditions influence the UK, due to the westward migration of the blocking anticyclone towards the UK.

Figure 5.6 shows the evolution of the nudged [PM10] and its constituent tracers during an Omega block, from 4 days prior to the onset of the Omega block to 4 days after Omega block onset. An Omega block is defined as for Fig. 3.7 and Fig. 3.8. For clarification, the methodology for diagnosing an Omega Block are listed below:

1) For each day, determine the number of grid points in each region of influence that correspond to overturning (BI > 0 K) of the RWB subset that categorises the region of influence.
2) Identify all days where at least 10 CRWB grid points are identified collectively in the warm and cold CRWB regions of influence
3) For each day of 10 CRWB grid point detection, identify the maximum CRWB grid point count in the 10 days prior to and following that day. This step will ensure that each Omega block event identified is unique and not the continuation of another Omega block event.
4) If on the four days preceding the day of the CRWB grid point maxima, 10 ACRWB grid points are identified in the warm and cold ACRWB regions of influence, an Omega block event is identified.

Of the 35 days that fulfilled criteria 3) above, 33 events fulfilled the ACRWB precursor criteria in criteria 4). All tracer concentrations in Figure 5.6 are displayed as anomalies with respect to the entire time-series mean tracer concentrations.

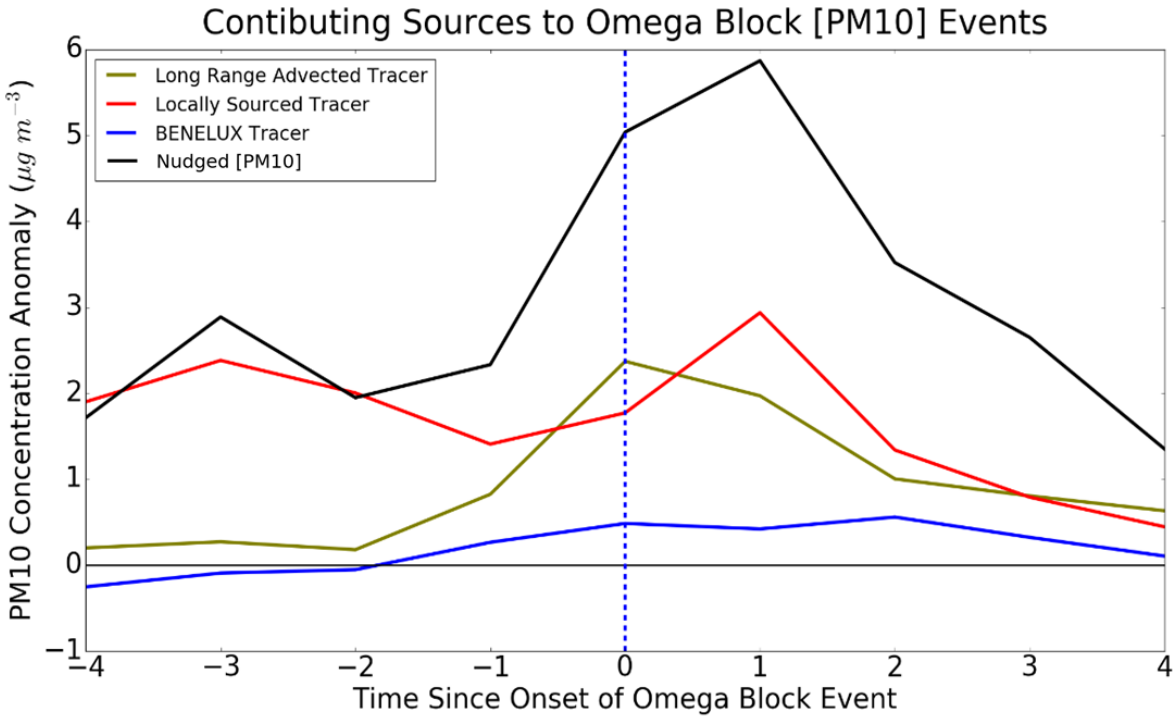

Figure 5.6 Tracer anomalies, with respect to a 10-year winter (DJF, January 1999-December 2008) time series mean, throughout an Omega block event. The Omega block event is centred on the peak CRWB grid point count in the event and must have an ACRWB precursor. Three tracers (West Poland tracer – gold line, BENELUX tracer – blue line, locally sourced tracer – red line) and the present-day nudged HADGEM3-GA4 [PM10] dataset (black line) throughout the Omega block event are illustrated.

Figure 5.6 shows the contributing PM10 sources throughout an Omega block event. The tracers shown are; the locally sourced tracer, the BENELUX (local European) tracer and the West Poland (long-range European) tracer.

Prior to Omega Block onset on day 0 in Fig. 5.6, the first tracer to peak is the locally sourced tracer on day -3. Following this initial peak, the locally sourced tracer concentration is shown to decline until a second period of locally sourced tracer concentration growth begins on day -1. Following the onset of the Omega Block event, the locally sourced tracer reaches a peak in concentration on day +1.

The second tracer to reach its maxima is the long-range European tracer on day 0. The long-range tracer concentration begins to increase from day -2, until its peak on day 0. The

BENELUX tracer, which represents the near-European tracer, steadily increases in concentration from day -4 to its peak on day 2.

Modelled [PM10], which is calculated from a combination of the four modelled tracers, is also shown in Fig. 5.6. Modelled [PM10] is shown to initially peak on day -3, coinciding with the peak of the locally sourced tracer. Following this initial peak, modelled [PM10] reduces until day -2, where it increases until its event maxima. Modelled [PM10] reaches its events maximum concentration on day +1, coinciding with the second peak of locally sourced tracer.

Despite sharing peaks with the locally sourced tracer, modelled [PM10] is shown to increase prior to the increase of locally sourced tracer, from day -2. This increase in concentration coincides with an increase of both BENELUX and long-range advected tracer.

5.6.1 The Flow Regimes that Influence the UK throughout Omega Block Events

Figure 5.6 shows the evolutions of an Omega block event and helps to answer a hypothesis made in Section 3.4.3. The hypothesis stated that an Omega block event is associated with the greatest [PM10] exceedance probabilities, as it incorporates two mechanisms of PM10 accumulation within the UK.

The results from Fig. 5.6 support this hypothesis, with influence from both European and locally sourced tracers in elevating modelled [PM10]. Initially, a brief period of locally sourced tracer accumulation on day -3 is seen. This is associated with the eastward migration of the anomalous anticyclone towards Scandinavia at this time, which can be seen in Fig. 3.8. On day -3 Fig. 3.8 shows that the anomalous MSLP maxima is longitudinally aligned with the UK, therefore providing stagnant conditions over the UK that are conducive to the accumulation of locally sourced PM10. Following the initial peak of locally sourced tracer, the long-range European tracer reaches its event maximum concentration on day 0. The accumulation of long-range European tracer in the UK prior to day 0 coincides with a Scandinavian anomalous anticyclone, seen in Fig. 3.8 and generated following ACRWB.

Following the initial advection of European PM10 into the UK, the locally sourced tracer is once again elevated on day +1. The combination of elevated long-range European tracer and locally sourced tracer predominantly causes the observed peak of modelled [PM10] on this day. On day +1, the Scandinavian anticyclone has migrated westwards, as seen in Fig. 3.8 and a period of stagnation ensues over the UK.

Throughout both the advection of European long-range tracer and the stagnation of locally-sourced tracer, the BENELUX tracer is seen to increase. The BENELUX tracer is therefore

seen to rise throughout periods of both European PM10 advection and stagnation, however its greatest increases are seen throughout the period of advection, driven by the anomalous Scandinavian anticyclone, prior to the onset of the Omega block event.

5.7 Chapter Conclusions

The present-day nudged HADGEM3-GA4 simulation presented in this chapter, has allowed for two research questions to be answered. The first of these relates to whether the relationships found in Chapter 3 between RWB and observed [PM10], remain when using a nudged [PM10] dataset. Following this, the flow regimes that influence the UK throughout this study's most hazardous RWB subset, the Omega Block, were tested.

This study has found that the variance in synoptic meteorology can explain sufficient variability in observed [PM10] to replicate the results found between RWB and observed [PM10] in Chapter 3.Consequently, variability in northeast Atlantic/ European synoptic meteorology plays a large role in the occurrence of UK [PM10] episodes. Modelled [PM10] from the nudged simulation could explain 42% of the variance within the observed [PM10] dataset. Despite replicating the results from Chapter 3, modelled [PM10] from the nudged simulation were associated with decreased probabilities of exceeding a hazardous UK [PM10] threshold. It was determined that homogenous temporal and spatial PM10 sources are the primary cause of the reduced PM10 exceedance probabilities. The nudged simulation was found to be more representative of a rural background AQMS in Harwell, with homogeneous surrounding PM10 emissions, than the urban background UK Midlands AQMS.

This study also found that this study's most hazardous RWB subset, the Omega block, influences the UK through two dominant flow regimes. An initial period of easterly advection from Europe into the UK was found to be associated with the prior occurrence of ACRWB, throughout an Omega block. Following the initial accumulation of European PM10, a period of stagnation facilitated the accumulation of locally sourced PM10. It is following both periods of advection and stagnation that modelled [PM10] reaches its event maxima. Consequently, both mechanisms are important in Omega blocks becoming this study's most hazardous RWB subset.

Chapter 6 will present the results of a present-day free-running HADGEM3-GA4 simulation. The purpose of the free-running simulation is to identify and quantify the uncertainties in the models ability to replicate observed synoptic meteorology.

Chapter 6 – Evaluating a Present-Day Free-Running HADGEM3-GA4 Simulation

6.1 Introduction

Chapter 5 addressed the effectiveness of four modelled tracers, implemented within a nudged simulation in replicating observed relationships between RWB and UK [PM10]. It was found that 42% of the variability observed in the UK Midlands tri-site PM10 dataset was explained by a weighted sum of four emitted European tracers and their covariance terms. Chapter 6 addresses the model's ability to capture synoptic meteorological variability observed in ERA-Interim reanalysis data. This chapter aims to answer two principal research questions:

1. Is the frequency and spatial distribution of ERA-Interim reanalysis RWB well replicated by HADGEM3-GA4?
2. Are the dynamics of RWB the same in present-day free-running HADGEM3-GA4 and Era-Interim reanalysis datasets?

The chapter will begin by introducing existing literature that explores model biases in synoptic meteorological variability. The modes of synoptic variability often explored within existing literature are atmospheric blocking frequencies and EDJ latitude. Model biases in RWB frequency, within the northeast Atlantic/European region will be evaluated in HADGEM3-GA4. For a comparison with existing literature, a new metric is required to evaluate the synoptic meteorology climatology of this HADGEM3-GA4 simulation. An evaluation of the latitudinal probability distribution of the EDJ was undertaken, as in Woollings et al. (2010a) and Masato et al. (2016). By analysing a metric that has been studied for past and future HADGEM model versions, we are able to determine whether HADGEM3-GA4 is behaving in a similar manner to HADGEM models used in previous studies.

Following the identification of RWB frequency biases and EDJ latitude biases, which are closely related, analysis will be undertaken to determine present-day HADGEM3-GA4 model biases in the flow regimes following RWB events. Using the modelled tracers introduced in Chapter 5, model biases in flow regimes resulting from ACRWB can be evaluated. No analysis of flow regime resulting from CRWB events will be undertaken. The low event frequency of CRWB events in the northeast Atlantic/ European region makes a detailed flow regime analysis inappropriate.

Finally, the key relationships found in Chapter 3 and replicated in Chapter 5, between RWB and UK [PM10] are shown for the free-running simulation. It is important that HADGEM3-GA4 is capable of projecting the relationships between UK PM10 and RWB, as these relationships are fundamental in determining future changes in UK [PM10] episodes, caused by synoptic meteorology.

6.2 Background Literature

Extensive literature exists on model biases with respect to atmospheric blocking (Masato et al., 2013b; Masato et al., 2016; Scaife et al., 2010; Woollings et al., 2010b). Zappa et al. (2014) and Anstey et al. (2013) analysed atmospheric blocking biases in models that contributed to the CMIP5 inter-comparison project. A model bias that is existent in almost all climate models that contribute to CMIP5 is that there exists an underestimation of atmospheric blocking in the northeast Atlantic/ European region. The Met-Office model, which contributed to CMIP5 was HADGEM2-CC, a fully coupled climate model, which uses the new-dynamics dynamical core. Anstey et al. (2013) showed that HADGEM2-CC is one of the better models, in the CMIP5 inter-comparison project, at replicating atmospheric blocking in the northeast Atlantic/ European region. Despite this, there remains a negative blocking bias in HADGEM2-CC and hence a negative blocking bias over a region that this study has shown to be most influential upon UK [PM10]. The model used in this study is HADGEM3-GA4, the atmosphere only component of the fully coupled HADGEM3-GC1, which also uses the new-dynamics dynamical core. It is expected that similar blocking biases will exist within HADGEM3-GA4.

Existing literature is used to verify the performance of HADGEM3-GA4 in this study. For direct comparisons with existing studies, a common metric is required. The studies listed above, which look at the North Atlantic/ European upper tropospheric synoptic variability in the HADGEM family of models, predominantly analyse atmospheric blocking and EDJ distribution. This study focusses on the phenomenon that is RWB, which is closely related to the location of the EDJ. The influence of the EDJ on UK [PM10] was highlighted in Fig. 3.1, which illustrates the 2D Pearson's correlation coefficient between BI and UK [PM10]. A correlation coefficient tripole was found in Fig. 3.1 and it was shown in Fig. 3.2 that these correlations are largely determined by the latitudinal position of the EDJ. The occurrence of RWB over a region acts to divert the EDJ from that region and essentially block that region from the EDJ (Sect. 2.3.2). Due to the relationship of RWB occurrence and EDJ position, analysis of the EDJ distribution has been undertaken to facilitate a direct comparison between this study and existing literature.

Unlike the comparison between EDJ position and RWB frequency, it is unwise to directly compare model biases in atmospheric blocking and RWB frequency. Atmospheric blocking requires a persistence threshold to be exceeded, while RWB frequency requires no such threshold. Additionally, while it is well recognised that throughout the Northern Hemisphere winter, an important precursor to atmospheric blocking is RWB (Altenhoff et al., 2008), this is not always the case (Cattiaux et al., 2010). Consequently, some atmospheric blocking episodes will occur without the precursor of RWB and instead due to an Atlantic ridge. In such cases as Atlantic ridge situations, the RWB and atmospheric blocking occurrences are unrelated. Despite this, it is expected that model biases in atmospheric blocking frequency and RWB frequency should be similarly signed.

Section 6.3 will explore the model biases in mid-latitude synoptic meteorological variability that are present within HADGEM3-GA4. RWB frequency and EDJ variability biases will be quantified and following this existing literature will be used in an attempt to explain these model biases.

6.3 Synoptic Meteorological HADGEM3-GA4 Model Biases

Section 6.3 analyses the biases that exist in synoptic meteorological variability within HADGEM3-GA4. This study is focussed on RWB events and subsequently this section will begin, in Sect. 6.3.1 by exploring model biases in RWB frequency. Analysis of RWB frequency biases will extend to look at ACRWB and CRWB individually in Sect. 6.3.2.

For comparison with literature, an analysis of the latitudinal frequency distribution of the EDJ will be undertaken in Sect. 6.3.3. Using this metric, a multi-model comparison can be made, including past and future HADGEM iterations, helping to determine whether model biases in synoptic meteorology are consistent with literature.

6.3.1 HADGEM3-GA4 RWB Model Frequency Biases

In this section RWB frequency was calculated for the ERA-Interim reanalysis dataset and the free-running simulation, for winter months (DJF) between January 1999 and December 2008. A model bias in RWB frequency was calculated by subtracting the ERA-Interim RWB frequency from the free-running RWB frequency, for every global grid point. Differences in horizontal resolution exist between the HADGEM3-GA4 (1.25 x 1.875) and ERA-Interim (1.5 x 1.5) θ-2PVU datasets. As in Sect.5.2, which compared ERA-Interim and present-day nudged HADGEM3-GA4 RWB frequency, the ERA-Interim θ-2PVU fields have been interpolated onto a 1.25^{o} latitude x 1.875^{o} longitude grid using bi-linear interpolation.

The present-day free-running HADGEM3-GA4 RWB frequency (hereafter free-running RWB frequency) is presented in Fig. 6.1 (a). The stereographic projection used, allows for comparison of RWB frequency in the northeast Atlantic/ European region and the most frequent region of occurrence in the northwest Pacific basin. Fig. 6.1 (b) shows the model bias in RWB frequency between the RWB frequency in the free-running simulation and ERA-Interim reanalysis dataset. Included within Fig. 6.1 (b) is the region of influence that coincides to ACRWB in the free-running simulation.

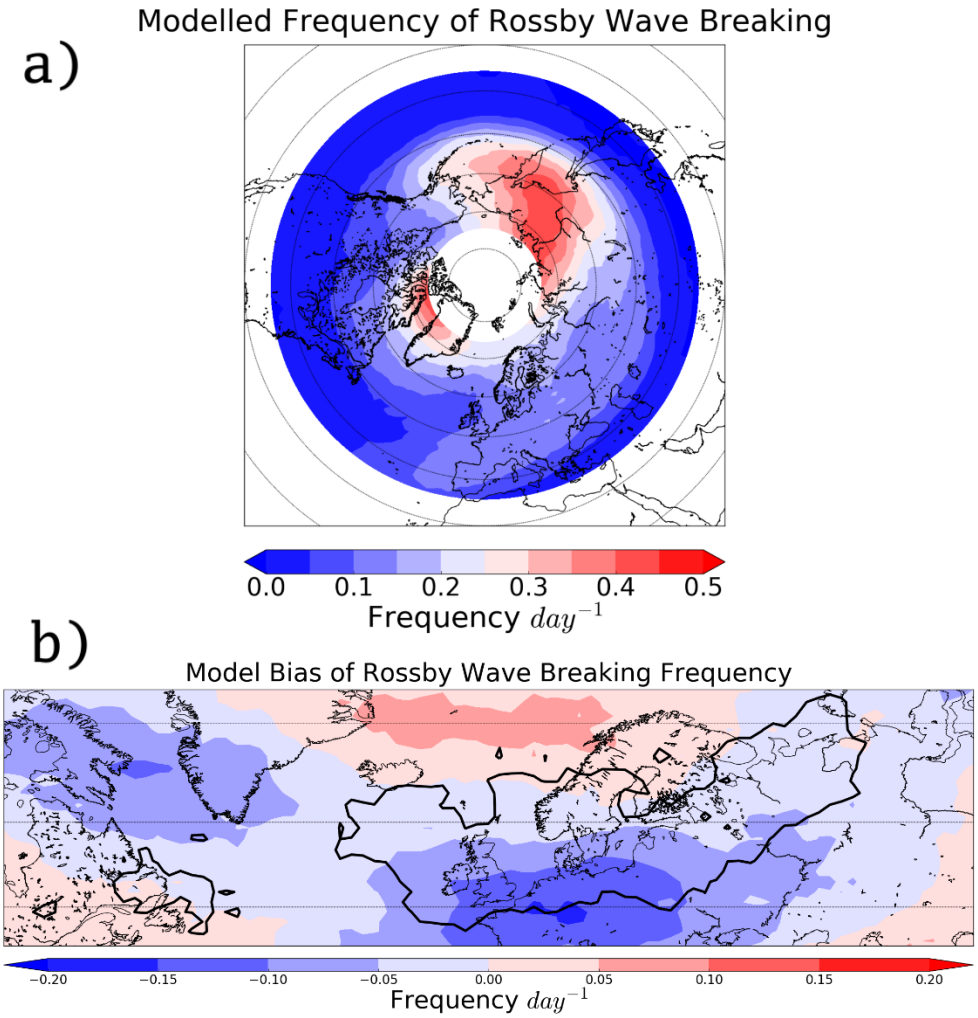

Figure 6.1. (a) The frequency of RWB in the present-day free-running HADGEM3-GA4 simulation for winter months (DJF) between January 1999 and December 2008. **(b)** The HADGEM3-GA4 model bias of RWB frequency, when compared to ERA-Interim reanalysis RWB frequency. The overlain black contour in **(b)** represents the ACRWB region of influence for the present-day free-running HADGEM3-GA4 simulation.

The RWB frequency in the free-running simulation is illustrated in Fig. 6.1 (a). This shows that, like in the ERA-Interim dataset, there exist three predominant regions of RWB occurrence. These regions include; the Northwest Pacific/ Asia region, the northwest Atlantic region and the northeast Atlantic/ European region. Chapter 3 highlighted the importance of northeast Atlantic/ European RWB on UK [PM10] and it is therefore important that HADGEM3-GA4 is able to capture this local maximum in RWB frequency.

Figure 6.1 (b) shows the HADGEM3-GA4 model bias in RWB frequency. The domain illustrated is the North Atlantic/ European region, within which Chapter 3 showed RWB is influential to UK [PM10]. Throughout the illustrated domain, much of the region exhibits a reduction in RWB frequency in HADGEM3, when compared to ERA Interim reanalysis data. The black contoured region highlights the region of influence for ACRWB on UK [PM10] in the free-running simulation. Within much of the contoured region, there exists a negative RWB frequency model bias. The greatest magnitude negative RWB frequency bias is seen in the southwest extent of the region of influence, with a bias of -0.17 day^{-1}.

The RWB frequency model bias in Fig. 6.1 (b) is shown to be negative throughout much of the illustrated domain. A region of spatially robust positive RWB frequency model bias is seen in the Norwegian Sea. This region of positive RWB frequency model bias forms the upper half of an anomalous RWB frequency dipole.

6.3.2 Anticyclonic and Cyclonic RWB Frequency Biases

This section looks at the model bias in ACRWB and CRWB frequency, in the same manner as total RWB frequency in Sect. 6.3.1. Figure 6.2 (a) and (b) show the ACRWB and CRWB model frequency biases in HADGEM3-GA4. It is important to determine the relative model biases associated with each event, as this will need to be considered when evaluating climatic shifts in ACRWB and CRWB frequency.

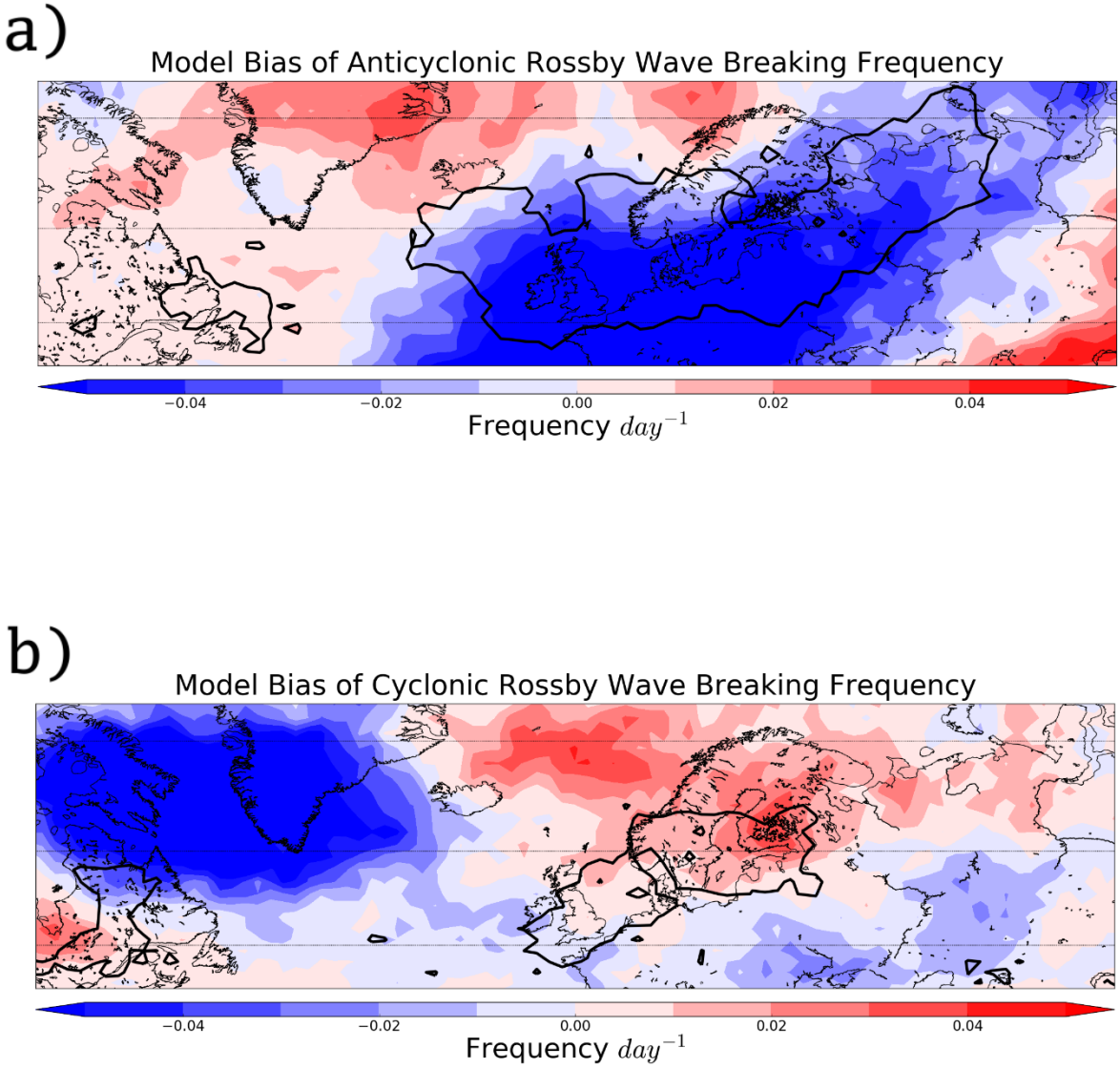

Figure 6.2. (a) The HADGEM3-GA4 model bias of ACRWB frequency, when compared to ERA-Interim reanalysis ACRWB frequency for winter months (DJF) between January 1999 and December 2008. **(b)** The HADGEM3-GA4 model bias of CRWB frequency, when compared to ERA-Interim reanalysis CRWB frequency for the same period. The overlain black contour in **(a)/ (b)** represents the ACRWB/CRWB region of influence for the free-running HADGEM3-GA4 simulation.

Figure 6.2 shows the model biases for ACRWB and CRWB in HADGEM3-GA4. The northeast Atlantic/ European model biases in RWB frequency, identified in Fig. 6.1 (b), are spatially similar to those for ACRWB frequency biases in Fig. 6.2 (a). Throughout the overlain ACRWB region of influence for the free-running simulation, there exists a negative ACRWB model bias. Furthermore, a heterogeneity exists in the model bias field, with a north-eastward shift also evident in Fig. 6.2 (a). The greatest negative ACRWB frequency model biases are seen in the southwest extent of the ACRWB region of influence and hence,

within this region the average ACRWB event will appear to have shifted north-eastward. This apparent north-eastward shift in the location of the average northeast Atlantic/ European ACRWB event can be seen more clearly, by comparing the resultant MSLP anomalies from northeast Atlantic/ European ACRWB in both the nudged and free-running HADGEM3-GA4 simulations. This analysis has been undertaken and included in Appendix D. Fig. D.1shows the model bias in MSLP anomalies, resulting from northeast Atlantic/ European ACRWB. ACRWB in both the nudged and free-running simulation is constrained to the free-running ACRWB region of influence (Fig. 6.5 (a)). Fig. D.1 shows a clear north-eastward shift in the anomalous anticyclone, resulting from northeast Atlantic/ European ACRWB (Sect. 3.3.3), with a negative model bias present over the Azores and a positive MSLP anomaly over the Scandinavian region.

Contrasting to the frequency biases for ACRWB in Fig. 6.2 (a), weak positive CRWB frequency model biases are found within the CRWB region of influence. Despite the contrasting model biases for ACRWB and CRWB, ACRWB events remain the dominant RWB subset in the northeast Atlantic/ European region.

Further analysis regarding the oppositely signed model bias for ACRWB and CRWB will be undertaken in Sect. 6.3.3 by examining model biases in the probability distribution of the EDJ in the North Atlantic. An increase in CRWB frequency within the North Atlantic/ European region coupled with a decrease in ACRWB frequency is indicative of a mean-state shift of the EDJ. Sect. 2.3.5 highlighted that the direction of RWB is dictated by the meridional zonal shear on the background flow, determined by the relative position of the EDJ. An increase of CRWB frequency and decrease of ACRWB frequency indicates that the EDJ may have a systematic equatorward model bias.

In addition to potentially providing an explanation of the HADGEM3-GA4 RWB frequency model biases in Sect. 6.3.1 and Sect. 6.3.2, Sect. 6.3.3 provides the opportunity for a comparison with literature. The latitudinal probability distribution of the EDJ is more frequently analysed within literature and hence a comparison of the model biases in synoptic meteorology, in this study, can be more readily made.

6.3.3 Model Biases in the Latitudinal Probability Distribution of the EDJ

The analysis of EDJ latitude in this study follows the analysis undertaken by Woollings et al. (2010a). EDJ latitude probability distributions were determined for both the ERA-Interim and free-running HADGEM3-GA4 datasets 10-year time series. The methodology used to calculate the EDJ latitude on each specific day is listed below:

1) Average zonal wind at every grid point between the 900, 850 and 700 hPa pressure levels. The purpose of analysing low level zonal wind fields is that the EDJ is a relatively low level feature when compared to the subtropical jet. Consequently, this avoids erroneous identification of the subtropical jet.
2) Longitudinally average the zonal wind values between 60^{o}W and 0^{o}W. The choice of this longitudinal constraint is consistent with existing literature (Woollings et al., 2010a; Masato et al., 2016). This region is chosen to analyse the variability in EDJ latitude, as the EDJ is at its most variable within this region. This region therefore best represents the variability in the latitude of the EDJ throughout the North Atlantic region.
3) Low pass filter the zonal wind data to remove the influence of transient synoptic features. This is achieved by using a 10 day Lanczos filter with 41 weights, which is consistent with Lorenz and Hartmann (2001). Increasing the number of weights decreases the likelihood of influence from variability with less than a 10 day frequency. Despite this, increasing the number of weights increases the expense of the procedure of applying the Lanczos filter. Woollings et al. (2010a) used 61 weights, however Franzke et al. (2011) applied 31 weights to the same low pass-filter and both studies generated near identical results for jet latitude variability in the ERA-40 dataset. It would appear that above a certain threshold, there is little sensitivity of the results of a low-pass Lanczos filter to the number of weights applied. Once calculated, the weights are multiplied by the days surrounding the day of interest and summed together.
4) The EDJ latitude is detected by the maximum in low-pass filtered zonal wind maxima for each day.

Figure 6.3 shows the latitudinal distribution of the EDJ in both the ERA-Interim dataset and the free-running simulation. The difference between the ERA-Interim and HADGEM3-GA4 EDJ probability distributions is shown as a black line, with negative values representing latitudes where ERA-Interim reanalysis EDJ frequency is lower than that represented by HADGEM3-GA4.

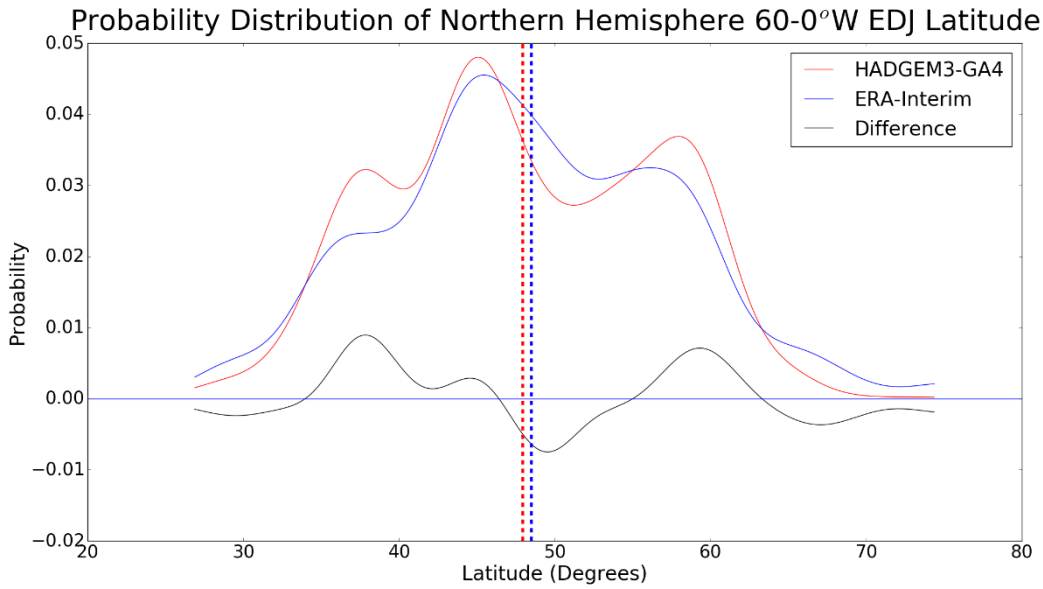

Figure 6.3 The probability distribution of Eddy Driven Jet latitude, averaged between 60°-0°W, in the present-day free-running HADGEM3-GA4 simulation (red) and ERA-Interim dataset (blue). The difference between the two distributions is shown by the black line. Data was obtained from both datasets for winter months (DJF) between January 1999 and December 2008. The vertical dashed red/blue line corresponds to the mean EDJ latitude in the free-running/ERA Interim datasets.

Figure 6.3 shows the latitudinal distribution of the EDJ in the ERA-Interim and free-running HADGEM3-GA4 datasets. Within the North Atlantic region, the tri-modal distribution of EDJ latitude is seen for both the ERA-Interim dataset and HADGEM3-GA4 simulation. At each of the three peaks in Fig. 6.3 for jet latitude (southerly, central and northerly) there exists a positive model bias in EDJ frequency. This positive EDJ frequency model bias is seen most greatly for the southern and northern EDJ latitudes.

The vertical lines in Fig. 6.3 correspond to the mean EDJ latitude in the free-running and ERA-Interim datasets. From Fig. 6.3 it can be seen that there exists an equatorward shift in EDJ latitude in the free-running dataset that corresponds to 0.56°.

6.3.4 Is Synoptic Variability Well Represented within HADGEM3-GA4?

Section 6.3.1 highlighted RWB frequency biases for the northeast Atlantic/ European region. It was shown that negative RWB frequency model biases occur throughout the regions that Chapter 3 has highlighted are influential in significantly elevating UK [PM10]. The region of greatest negative HADGEM3-GA4 model bias is seen over Western Europe, within the southwest extent of the contoured region of influence, for ACRWB, in Figure 6.2 (b). This region of negative RWB frequency model bias forms half of an anomalous RWB frequency dipole, with a positive RWB anomaly situated over the Norwegian Sea.

Although not directly comparable, existing literature for HADGEM2-CC (Anstey et al., 2013; Zappa et al., 2014) also show a negative atmospheric blocking model bias in the northeast Atlantic/ European region. Zappa et al. (2014) found increased storm track activity and subsequently reduced blocking in regions similar to those in Fig. 6.1 (b). With RWB an important precursor to atmospheric blocking in the northeast Atlantic/ European winter (Altenhoff et al., 2008), biases in RWB and atmospheric blocking are likely correlated.

Literature has shown that resolution can explain many of the observed model biases in northeast Atlantic/ European RWB frequency. Matsueda et al. (2009) and Scaife et al. (2011) showed that at coarser horizontal resolutions, such as in this study's climate model, negative atmospheric blocking biases exist. Lower resolution climate models are incapable of adequately resolving baroclinic eddies. Subsequently there results a reduction in EKE within the North Atlantic region and a reduction of northeast Atlantic atmospheric blocking (Matsueda et al., 2009). Furthermore, Scaife et al. (2011) highlighted the role of horizontal resolution in altering horizontal SST gradients in the northwest Atlantic. At relatively coarse resolutions, such as in the HADGEM3-GA4 model simulations used in this study Scaife et al. (2011) find an underestimation of horizontal SST gradients. Consequently, a reduced baroclinicity in this region and a reduced growth of baroclinic eddies results. The modelled impact on northeast Atlantic/ European blocking in Scaife et al. (2011) was an increased blocking frequency with increased resolution, due to enhanced blocking maintenance mechanisms (Sect. 2.4).

Vertical resolution is also important in the calculation of blocking metrics, as discussed in Sect. 5.2. Differences in the vertical resolutions of the ERA-Interim reanalysis and HADGEM3-GA4 datasets are however likely to lead to a positive RWB frequency model bias. The lower vertical resolution of ERA-Interim, compared to HADGEM3-GA4 (see Sect. 5.2) would result in a greater RWB frequency in the HADGEM3-GA4 dataset (Anstey et al., 2013), which opposes the negative RWB frequency model bias.

Aside from resolution, Zappa et al. (2013) find that cyclone intensity is too weak in most CMIP5 models. The result of a cyclone intensity deficiency is a reduction in a key reinforcement mechanism for atmospheric ridges and atmospheric blocks (Sect. 2.4). A weaker cyclone intensity is associated with a weaker vertical advection of air through the warm conveyor belt and a reduction in low PV being advected into a blocking anticyclone through this mechanism.

Aside from the negative model bias in RWB frequency, Sect. 6.3.2 shows a positive model bias in CRWB frequency within the northeast Atlantic/ European region. Contrasting the positive model bias of CRWB frequency, a negative ACRWB frequency model bias exists in the same region. The most likely explanation for this oppositely signed model bias is a mean-state bias within the northeast Atlantic/ European region. Sect. 6.3.3 found biases in the latitudinal probability distribution of the EDJ. It is possible an equatorward mean-state bias in the probability distribution of the northeast Atlantic/ European EDJ, would encourage a greater proportion of RWB to occur cyclonically in the region. The relative position of the EDJ determines a meridional zonal shear on the background flow, which encourages (anti)-cyclonic RWB to the (south) north of the EDJ. The consequence of an equatorward EDJ shift would be a decrease in ACRWB and an increase of CRWB within the northeast Atlantic/ European region, as seen in Fig. 6.2.

6.3.5 Can Model Biases in EDJ Variability Explain RWB Frequency Biases in HADGEM3-GA4?

Sect. 6.3.1 showed that there exists a negative model bias in northeast Atlantic/ European RWB frequency, to the south of 65^{o} N within the domain. This RWB frequency bias is shared for the ACRWB subset, however CRWB is shown to predominantly increase throughout this region. The model bias in RWB frequency, would suggest that there exists an equatorward EDJ shift within this region.

Figure 6.3 shows a southward tendency of the EDJ in HADGEM3-GA4 between 35^{o}N and 47^{o}N, upstream of the RWB frequency biases. Such a model bias in the EDJ may seem too far equatorward to explain the negative RWB frequency model bias to the south of 65^{o} N. However, within the North Atlantic, the EDJ is on average tilted in the southwest/ northeast direction, indicating that downstream of the region examined in Fig. 6.3, over the region of negative RWB frequency bias, the latitudinal EDJ model biases will be positioned further poleward than those in Fig. 6.3.

Further analysis has been undertaken to examine EDJ variability in the region between 0^{o}E and 30^{o}E. This region corresponds to the region where RWB frequency biases are evident for all RWB and ACRWB. The results (Appendix E) show that the EDJ southerly shift in Fig. 6.3, between 35^{o}N and 47^{o}N, is shifted north to between 33^{o}N and 54^{o}N (Fig. E.1). This mean-state southerly bias in the latitudinal probability distribution of the EDJ does not align perfectly with the RWB frequency biases in Fig. 6.1, however it does indicate a preference for an increase of ACRWB/CRWB equatorward/poleward of 54^{o} N. These oppositely signed model biases are seen in Fig. 6.2.

The RWB frequency model bias latitudinal dipole, in Fig. 6.1 (b) can also be coupled to this mean-state shift in the EDJ. An increased/decreased probability of the EDJ to the north/south of 54^{o} N mirrors closely the increase/reduction of RWB frequency to the north/south of 54^{o} N.

Section. 6.3.6 will be used to compare the latitudinal probability distribution of the EDJ with existing literature. From Sect. 6.3.6, an evaluation of synoptic meteorology in HADGEM3-GA4 can be made.

6.3.6 Do the synoptic Meteorological Biases Agree Well with Literature?

Masato et al. (2016) analysed jet latitude variability in the latest (at the time of writing) Met-Office HADGEM model version, HADGEM3-GC2. Alongside the coupled model, Masato et al. (2016) also evaluated EDJ latitudinal biases in the atmosphere-only component (HADGEM3-GA6). The results for both models showed that jet latitude biases exist in the North Atlantic region. Furthermore, the model biases in the atmosphere-only component (HADGEM3-GA6) were found to be much smaller than those for the coupled model. The improvement in atmosphere-only models is thought to be associated with negating ocean atmosphere coupling (Scaife et al., 2011). Scaife et al. (2011) showed that northeast Atlantic/ European atmospheric blocking frequency is very sensitive to SST biases present in the northeast Atlantic. By removing the atmosphere-ocean coupling, these SST biases are removed and it was shown by Scaife et al. (2011) that atmospheric blocking and hence, synoptic variability was better represented in the northeast Atlantic/ European region.

Figure 6.3 shows an overestimation in the probability of the EDJ to reside within its northern and southern states in HADGEM3-GA4. The model biases in the latitudinal probability distribution of the EDJ, found by Masato et al. (2016), are in agreement with those found for HADGEM3-GA4 in this study. Masato et al. (2016) also find an overestimate in HADGEM3-GA6, for the EDJ to reside in its northern and southern states (Woollings et al., 2010b).

Results from Woollings and Blackburn (2011) find a poleward shift in the latitudinal probability distribution of the EDJ, in HADGEM-GC1. This study shows that HADGEM3-GA4 (Fig. 6.3) experiences a slight equatorward bias in EDJ latitude, which is not in agreement with the model bias found in HADGEM-GC1. Despite this, the HADGEM3-GA4 model bias found for EDJ latitude is within the range of Coupled Model Intercomparison Project Phase 3 (CMIP3) model biases for mean EDJ latitude, analysed within Woollings and Blackburn (2011).

Following analysis of existing literature that explores the upper-tropospheric synoptic variability in the North Atlantic/ European region, this author is satisfied that model biases are consistent with current generation climate models. The model biases found are dominated by an equatorward model bias in the latitudinal probability distribution of the EDJ. The equatorward bias in the latitudinal probability distribution of the EDJ, most noticeably between 35^{o}N and 47^{o}N has been linked to the negative model bias in northeast Atlantic/ European RWB frequency.

6.3.7 Mid-Latitude Synoptic Meteorological Variability - Conclusions

The first research question posed in this chapter was:

"Is RWB frequency climatology well replicated by HADGEM3-GA4?"

This question has been answered, with RWB model biases evident in the northeast Atlantic/ European region. It was shown that RWB frequency is underestimated in the northeast Atlantic/ European region. Furthermore, an equatorward model bias in the latitudinal probability distribution of the EDJ is also seen, which enhances the probability of CRWB and reduces the probability of ACRWB within the northeast Atlantic/ European region. Finally, the latitudinal probability distribution of the EDJ has been compared with literature. An overestimation within HADGEM3-GA4 for the EDJ to reside within its northern and southern states agrees well with literature. Furthermore the 0.56^{o} equatorward shift that is found for the EDJ in HADGEM3-GA4 is within a range of EDJ CMIP3 model bias shifts from Woollings and Blackburn (2011). By comparing the latitudinal probability distribution of the EDJ with literature, it has been shown that the model biases in HADGEM3-GA4 agree well with existing literature.

The second research question that this chapter aims to answer is whether there are model biases in the flow regimes influencing the UK following RWB in HADGEM3-GA4. Section 6.4 will aim to evaluate the flow regimes that influence the UK following ACRWB, the most prominent RWB subset in the northeast Atlantic/ European region. Finally, the relationships between UK [PM10] and RWB will be explored in HADGEM3-GA4. It will explored whether RWB remains influential to modelled UK [PM10] and whether RWB exceedance probabilities, in Section 6.6.2, can be replicated in the free-running simulation.

6.4 Tracer Contributions to ACRWB Events

ACRWB events have been shown to be the most prominent RWB subset in the northeast Atlantic/ European region in both the ERA-Interim dataset (Sect. 2.7.1) and this is also true for the free-running simulation. Chapter 3 highlighted that ACRWB both significantly

increases observed UK [PM10] and increases the probability of exceeding a hazardous PM10 threshold. Consequently, it is important to determine whether this important feature of mid-latitude synoptic meteorological variability influences the UK through the same mechanisms in the free-running simulation.

To determine flow regimes in the free-running simulation, the modelled tracers, evaluated in Chapter 5, will be used as analogues to flow regimes. Section 6.4 presents a direct comparison between the tracer concentrations received in the UK in two present-day HADGEM3-GA4 simulations (nudged and free-running). It is hypothesised that model biases in the location of RWB occurrence throughout Europe will result in model biases in the resultant flow regimes that influence the UK.

Figure 6.2 (a) found a north-eastward model bias in ACRWB occurrence in the free-running simulation. It is therefore expected that the flow regimes, which result from northeast Atlantic/ European ACRWB will also experience a model bias.

Section 6.4.1 details the method used to determine a significant model bias (between the nudged and free-running simulations) in HADGEM3-GA4 tracer concentration, resulting from ACRWB.

6.4.1 Determining a Model Bias in Flow regime

In this study, a model bias in flow regimes is defined as the difference in tracer concentration between an unconstrained (free-running) and a constrained (nudged) present-day HADGEM3-GA4 model simulation. Model biases exist due to the model's inability to replicate observed (ERA-Interim reanalysis) dynamical mechanisms. A model bias in tracer concentration, resulting from ACRWB, is anticipated from HADGEM3-GA4, as there exist spatial differences in the location of ACRWB occurrence (Fig. 6.2 (a)). Differences in the location of ACRWB occurrence, will result in differences in the location of the resulting MSLP dipole (Sect. 3.3.3). Consequently, tracer concentrations in the UK that are dependent on synoptic flow regimes to advect into the UK, will be affected by model biases in synoptic flow pattern.

This section aims to quantify the model biases that exist in tracer concentrations in the UK, following ACRWB events. To quantify a model bias, both the absolute quantity of tracer and uncertainty associated with that tracer must be considered. Considering both the absolute concentration and error, will allow us to determine whether the model bias is statistically significant in HADGEM3-GA4. If a model bias is statistically significant, it can be stated that the model is incapable of replicating the advection/ accumulation of that tracer. Consequently

when considering climate shifts in Chapter 7, for tracers that experience a significant model bias in their concentration, it is not possible to determine a meaningful estimation of tracer concentration climate shifts.

Statistical significance is determined for the model bias (MB) in tracer concentration, using a signal to noise ratio (SNR). Significant trends are found when the signal is of a greater magnitude than the noise, i.e. internal variability, involved in the system. The calculation of the signal to noise ratio in Eq. 6.1 determines whether there exists a significant model bias in tracer concentration in HADGEM3-GA4. If $|SNR_{MB}| > 1$, there exists a significant model bias in that tracer concentration, following northeast Atlantic/ European ACRWB in HADGEM3-GA4.

$$SNR_{MB} = \frac{\overline{T_{tr}^{FR}} - \overline{T_{tr}^{N}}}{\sqrt{(\in_{FR})^2 + (\in_{N})^2}} \qquad Eq\ 6.1$$

In Eq. 6.1, there exist two mean tracer concentration terms ($\overline{T_{tr}}$) in the numerator of SNR_{MB}, associated with the nudged (N) and free-running (FR) simulations, where tr represents the tracer being analysed (locally sourced, Po Valley, West Poland and BENELUX tracers). These are both individually associated with error terms ($\in$), which are added in quadrature and shown in the denominator of SNR_{MB}.

Calculation of the tracer concentrations in the numerator of Eq. 6.4, requires information regarding two assumed independent fields. Both fields are spatially constrained by the region of influence for ACRWB in the free-running simulation (Sect. 6.6.1). For direct comparison between each HADGEM3-GA4 simulation, the same region of influence was used to constrain fields from both present-day (nudged and free-running) and the future time-slice simulation. Justification for a constant region of influence comes from the finding that this region varies very little throughout all of the simulations used.

The first field obtained for the calculation of tracer concentrations is ACRWB frequency ($freq_{ACRWB}^{Simulation}$), within the ACRWB region of influence obtained from the free-running simulation. Within this region, ACRWB frequencies are normalised so that the sum of frequencies equate to 1 (Eq. 6.2).

$$\iint freq_{ACRWB}^{Simulation}\, d\varphi d\theta = 1 \qquad Eq.6.2$$

Following the calculation of the ACRWB frequency field, a field must be generated that quantifies the effect of ACRWB at each grid point, on each modelled UK tracer. Such a field

is calculated in the generation of the regions of influence (Sect. 3.3.2). At each grid point a weighted tracer concentration is subset one day following the occurrence of ACRWB. The mean value of the subset is calculated and what results is a 2D modelled $\overline{[\text{Tracer}]}$ field. A 2D field is calculated using each tracer as the dependent variable and for each HADGEM3-GA4 simulation. This 2D $\overline{[\text{Tracer}]}$ field tells us of the mean tracer concentration which results from ACRWB throughout the northeast Atlantic/ European region. Once the normalised ACRWB frequency and the $\overline{[\text{Tracer}]}$ fields have been determined, the product of these must be taken. Equations 6.3 and 6.4 show the calculation of the mean tracer concentration, which results from multiplying the normalised ACRWB frequency and $\overline{[PM10]}$ fields and integrating over the spatially constrained 2D region.

$$\overline{T_{tr}^{FR}} = \iint freq_{ACRWB}^{FR} \times \overline{[\text{Tracer}]_{tr}^{FR}}\, d\varphi d\theta \qquad Eq.\,6.3$$

$$\overline{T_{tr}^{N}} = \iint freq_{ACRWB}^{N} \times \overline{[\text{Tracer}]_{tr}^{N}}\, d\varphi d\theta \qquad Eq.\,6.4$$

The mean model bias signal for each tracer and modelled UK [PM10] can be determined by subtracting $\overline{T_1^N}$ from $\overline{T_1^{FR}}$, where a positive value represents a positive model bias and vice-versa. This statistic relates to the numerator of Eq. 6.1, however includes no consideration of $\overline{[\text{Tracer}]}_{tr}^{Simulation}$ variability. Table 6.1 lists the HADGEM3-GA4 model bias of the mean concentration for each tracer, following ACRWB. For comparison, the mean concentration of each tracer is shown for the nudged simulation. Consideration of the magnitude of the model bias signal in relation to the absolute tracer concentration, as measured in the UK, can subsequently be made.

Table 6.1 Row 1) Model bias for each tracer concentration. **Row 2)** Mean tracer concentration for ACRWB in the nudged HADGEM3-GA4 simulation. The values in brackets represent the percentage of the mean nudged tracer concentration (row 1) represented by the magnitude of model bias in tracer increment. The subscript tr corresponds to the tracer being analysed.

Tracer	Locally Sourced Tracer	Po Valley Tracer	West Poland Tracer	BENELUX Tracer
$\overline{T_{tr}^{FR}} - \overline{T_{tr}^{N}}$	0.19 μg m^{-3}	-0.93 μg m^{-3}	-1.00 μg m^{-3}	0.05 μg m^{-3}
$\overline{T_{tr}^{N}}$	8.91 μg m^{-3} (2.13%)	3.00 μg m^{-3} (31%)	2.12 μg m^{-3} (47.2%)	0.85 μg m^{-3} (5.9%)

Table 6.1 presents the HADGEM3-GA4 model bias in tracer contribution to modelled UK [PM10] following ACRWB events. In addition the mean tracer concentration resulting from ACRWB in the nudged simulation is illustrated, with a percentage value referring to the percentage of $\overline{T_{tr}^{N}}$, which is represented by $\overline{T_{tr}^{FR}} - \overline{T_{tr}^{N}}$.

In Table 6.1 there exist two positive model bias shifts, these are the locally sourced and BENELUX tracers. The two remaining long range advected tracers (Po Valley and West Poland tracers) both show large negative model bias shifts.

6.4.2 Incorporating Error into Model Bias Estimates

In Eq. 6.1, which represents the signal to noise ratio for the HADGEM3-GA4 model bias for each tracer, there are error terms ($\in$) included in the denominator. The error terms for each simulation are calculated individually using a Jackknife resampling methodology (Hawkins et al., 2002).

The Jackknife resampling technique, calculates an estimation of the variance of each individual tracer concentration. The method involves initially dissecting a dataset into equally sized constituents, which in this study are one winter season in length. Following this, multiple subset datasets are generated from the original dataset, each concatenated with one missing constituent dataset. The result is that there exist as many subset datasets as individual constituent datasets.

In this study, tracer concentrations ($\overline{T_{tr}^{FR}}$ in Eq. 6.5) are calculated from the product of an ACRWB frequency field and resultant $\overline{[\text{Tracer}]}$ field. The Jackknife resampling technique is therefore applied to each 2D field. What results is for example, for a dataset of length 10

years (nudged simulation), there exist 10 subset ACRWB frequency fields and 10 $\overline{[\text{Tracer}]}$ fields. The tracer concentration is then calculated 10 times, using the resampled ACRWB frequency and $\overline{[\text{Tracer}]}$ fields, each with the same year removed. A mathematical representation of this for the present-day free-running HADGEM3-GA4 simulation is shown in Eq. 6.5.

$$\overline{T_{tr}^{FR}} = \frac{1}{n-1}\sum_{i=1}^{n}\iint (freq_{ACRWB}^{FR})_i \times \left(\overline{[\text{Tracer}]}_{ACRWB}^{FR}\right)_i d\Phi d\theta \qquad Eq\ 6.5$$

The number of tracer concentration estimations (n) depends on the number of subset frequency (*freq*) and mean tracer concentration ($\overline{[\text{Tracer}]}$) fields. Consequently, the resampling frequency determines the number of tracer concentration estimates. The choice of a one year re-sampling frequency in this study is one based on the temporal period of ancillary fields input into both the present-day free-running and future time-slice simulations. Ancillaries that determine SST temperatures, sea ice extent and sea ice depth, are replaced every month, although the ancillaries are constant from year to year. Subsequently, the highest frequency in which the dataset is unaffected by changing ancillaries is annually. Choosing a re-sampling frequency of one year ensures that any variability associated with the RWB and modelled [PM10] datasets will be disassociated with variability in the input prescribed model ancillary files.

Following the generation of tracer concentrations, one must extract the variance associated with the estimations. The variance associated with an estimated tracer concentration is calculated using Eq. 6.6. In Eq. 6.6, the estimated variance is calculated for the free-running simulation by determining the magnitude of the mean squared difference between an individual tracer concentration estimation $(\overline{T_{tr}^{FR}})_i$ and the tracer concentration, calculated using the original, full length frequency and $\overline{[\text{Tracer}]}$ datasets $((\overline{T_{tr}^{FR}})_o)$.

$$\text{Var} = \frac{\text{n}-1}{\text{n}}\sum_{\text{i}=1}^{\text{n}}((\overline{T_{tr}^{FR}})_i - (\overline{T_{tr}^{FR}})_o)^2 \qquad Eq.\ 6.6$$

Where: n represents the number of years in the dataset and i represents a single winter season.

The error values incorporated in Eq. 6.1, for SNR_{MB} are standard error values and can be determined following the calculation of tracer concentration variance in Eq. 6.6. The method used to calculate the standard error of each tracer concentration is consistent within this study and is shown in Eq. 6.7, using the variance calculated in Eq. 6.6.

$$\mathrm{SE} = \frac{\sqrt{Var}}{\sqrt{N}} \qquad Eq.\,6.7$$

In Eq. 6.7 N is the length of each model simulation in days, SE is the standard error of the mean in the dataset and Var is the variance as calculated in Eq. 6.6.

Once SE was calculated for each tracer concentration in the nudged ($\in_N$) and free-running ($\in_{FR}$) simulations, the calculated errors can be combined using Eq. 6.8. It is important to note that errors must be combined in quadrature, and hence the total error is not a simple sum of the two constituent errors. For Eq. 6.8, SE from Eq. 6.7 has been changed to $\in$, for consistency with Eq. 6.1.

$$\in_{MB} = \sqrt{(\in_N)^2 + (\in_{FR})^2} \qquad Eq.\,6.8$$

Following the calculation of $\in_{MB}$, the signal to noise ratio in Eq. 6.1 can be calculated.

6.4.3 Results for Model Bias Signal to Noise

Table 6.2 shows the SNR, calculated for four modelled tracers using Eq. 6.1, which will determine whether any of the tracers experience a significant model bias in their UK concentration, following northeast Atlantic/ European ACRWB. Two values are presented for each tracer. The first of these values represents the 95th percentile confidence interval of SNR for each tracer. To calculate this confidence bound, SE in Eq. 6.7 is multiplied by 1.96. The second value in Table 6.2 is presented in brackets and related to the 66th percentile confidence interval of SNR for that tracer. To calculate the 66th confidence bound, SE is calculated as in Eq. 6.7 and not multiplied by 1.96. SNR values > ±1 at the 95th/66th percentile confidence interval illustrate tracers with a very likely/likely model bias, using uncertainty terminology presented in the guidance notes for the IPCC-AR5 report (Mastrandrea et al., 2010). If a modelled tracer experiences a very likely model bias, it can be assumed that HADGEM3-GA4 is incapable of replicating the flow regimes that influence the accumulation of said tracer in the UK. It is hypothesised that elevated SNR values will be identified for the Po Valley and West Poland tracers, with the greatest $\overline{T_{tr}^{FR}} - \overline{T_{tr}^{N}}$ values, shown in Table 6.1.

Table 6.2 Calculated signal to noise ratio (SNR) for the model bias of each tracer following ACRWB. The first value in each cell represents the SNR for that tracer using a 95th percentile confidence interval (significant model bias). Values in brackets correspond to SNR values, calculated when using a 66th percentile confidence interval or one standard error of the mean (likely model bias). $|SNR| > 1$ represents a greater magnitude model bias signal than the magnitude noise associated with the model bias.

Tracer	Locally Sourced Tracer	Po Valley Tracer	West Poland Tracer	BENELUX Tracer
SNR	0.50 (0.99)	-1.90 (-3.71)	-3.17 (-6.20)	0.36 (0.70)

Of the four constituent tracers shown in Table 6.2, there exist two tracers with SNR>1 ($p<0.05$). These tracers are the long-range European tracers, sourced in the Po Valley and West Poland regions and show a very likely model bias in their measured UK concentrations. The remaining two tracers do not show a very likely, or even a likely ($p<0.33$) model bias in Table 6.2. These tracers are the locally sourced and BENELUX tracers and the absence of any discernible model bias indicates that HADGEM3-GA4 well replicates their accumulation within the UK.

6.4.4 Discussion

The purpose of this section on identifying model biases was to identify whether HADGEM3-GA4 is capable of representing the accumulation of tracers in the constrained (nudged) HADGEM3-GA4 simulation.

Table 6.2 highlighted the modelled tracers that have a significant model bias ($p<0.05$). These tracers are the Po Valley and West Poland tracers. In comparison with the remaining two tracers, these two tracers must experience long-range advection to reach the UK Midlands. Consequently, there is a greater amount of uncertainty associated with the advection of these tracers into the UK for each simulation. The advection of long range advected tracers is highly sensitive to the meteorological flow regime, which results from ACRWB. Consequently any small changes in ACRWB frequency distribution in Fig. 6.2 (a), have imposed greater changes on the concentration of advected long-range tracer in the UK. Appendix F shows that the PDFs of the two long-range advected European tracers are highly skewed in the positive direction. It was argued that an increased skew in these distributions was a signal of increased sensitivity of the tracers advecting into the UK, due to the synoptic

flow regime. Due to the sensitivities involved with simulating the advection of Eastern and Southern European tracer into the UK, any shifts in this process imposed by climate change are likely to be small in comparison to the total uncertainty in all three simulations. It is because of this that the advection of West Poland and Po Valley tracer will not be analysed in Chapter 7, analysing climatic shifts in tracer advection following ACRWB events.

Two tracers that do not experience either a very likely or likely model bias in their accumulation in the UK, following ACRWB events, are the locally sourced and BENELUX tracers. It is therefore seen that HADGEM3-GA4 is representing well, the contribution of these tracers to total modelled UK [PM10]. Table 6.1 shows the model bias shifts and relates them to the absolute concentration of said tracer in the nudged simulation. An increase of 2.13% and 5.9% of the nudged simulation tracer concentrations for the locally sourced and BENELUX tracers is seen in the free-running simulation.

While quantifying model biases is important, it is also important to understand why HADGME3-GA4 is misrepresenting the accumulation of modelled tracers. This author sees two potential causes for the change in accumulated tracer in the UK. The first of these is a change in the flow regime that influences the UK. This is extremely important in influencing the advection of European tracers into the UK. The second of these potential causes is a change in tracer lifetime. Chapter 5 highlighted how the emitted tracers are chemically inert and subsequently are only removed from the atmosphere through wet and dry deposition. No explicit information was output from the HADGEM3-GA4 simulations, relating to the breakdown of dry and wet deposition, however inferences can be made relating to the tracers calculated lifetime. Section 6.5 analyses the lifetime of each of the four modelled tracers, to determine whether significant model biases in tracer concentration can be explained by a reduced atmospheric lifetime.

6.5 Calculating Model Biases in Tracer Lifetimes

Model biases in tracer lifetime, due to changes in wet or dry deposition rates in the model could potentially explain some of the model biases in tracer concentration, seen in Table 6.1. Equation 6.9 is used to calculate tracer lifetime in days. The numerator (Tracer) is calculated for each day as the total tracer mass (kg) within the global domain. A value of tracer emission throughout a single day in the model is calculated, this remains constant in all of the HADGEM3-GA4 simulations. The tracer lifetime is calculated by dividing the mean tracer mass on each day, by the emission rate (kg day^{-1}). Uncertainty bounds on tracer lifetime (λ) are calculated as 1.96 x the mean standard error of the tracer lifetime, using daily mean values for tracer mass and tracer emission.

$$\lambda = \frac{\text{Tracer (kg)}}{\text{Emission (kg day}^{-1})} \qquad Eq.6.9$$

6.5.1 Results

Figure 6.4 shows the lifetimes of each tracer in the nudged and free-running simulation. Error bars represent the 1.96 x the mean standard error of the lifetime for each tracer.

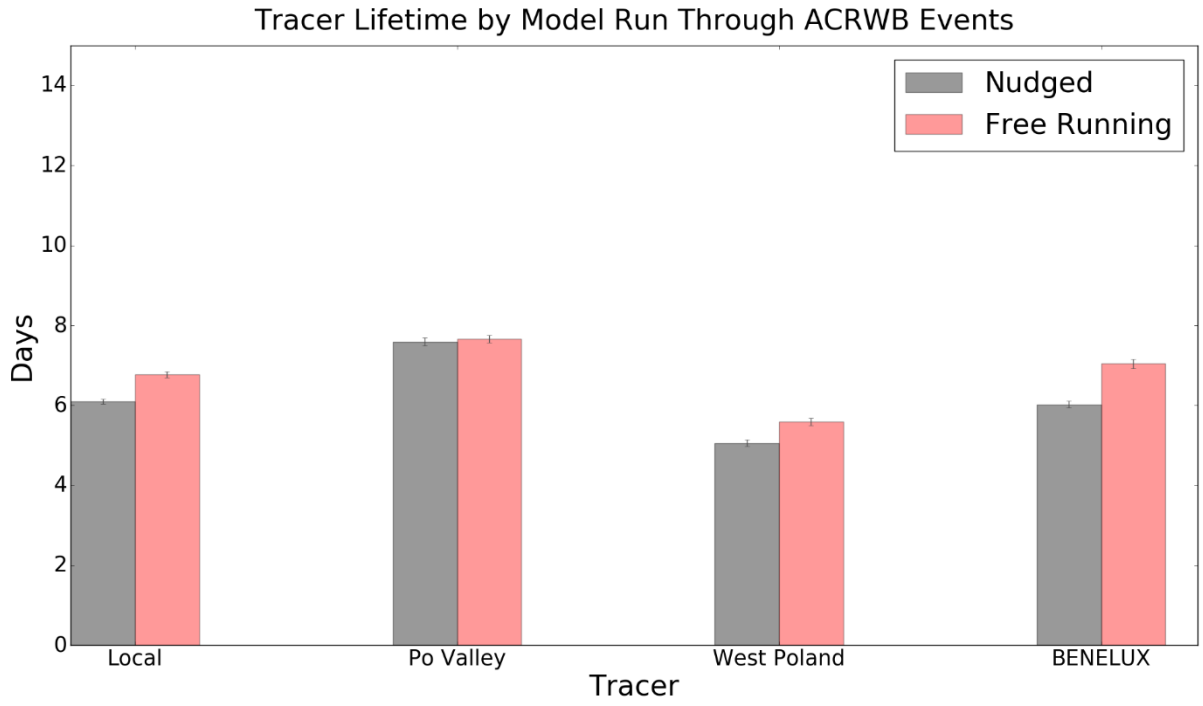

Figure 6.4 Calculated lifetimes for four modelled tracers in HADGEM3-GA4, in the nudged and free-running HADGEM3-GA4 simulations. Tracer lifetime is displayed in days and the uncertainty bounds represent the mean standard error multiplied by 1.96 for each tracer lifetime.

In Fig. 6.4 three of the four modelled tracer lifetimes experience a significant ($p<0.05$) positive model bias. The Locally sourced, Po Valley and BENELUX tracers all exhibit a significant positive model bias in HADGEM3-GA4. The Po Valley tracer does not experience significant model bias. For the locally sourced, Po Valley, West Poland and BENELUX tracers, the model bias in tracer mean represents: 9.93%, 0.91%, 9.55% and 14.49% of the mean lifetime in the nudged simulation.

Deposition diagnostics were not output from any of the simulations, however wet deposition rates, which are most likely to have influenced the significant increases in tracer lifetime, are analogous to precipitation rates. Literature exists that explores model biases in precipitation rates in HADGEM model versions.

Williams et al. (2015) explored the atmosphere-only HADGEM2 (HADGEM2-AO) model biases in precipitation. The HADGEM2-AO model is the previous generation model in the HADGEM family from the one used in this study. Figure 8 in Williams et al. (2015) shows that precipitation model biases, when compared to observations from the global precipitation climatology project. It is shown that negative precipitation biases exist in HADGEM2-AO throughout a region of Europe that coincides with the region of tracer emissions, used in this study. The precipitation model bias anomaly is heterogeneous throughout this region, however the magnitude of the negative precipitation model biases are sufficient in explaining the positive tracer lifetime biases seen in Fig. 6.4.

Analysis of tracer lifetime was undertaken to determine whether tracer concentration model biases in Table 6.2 can be explained by model biases in tracer loss mechanisms. Two tracers were shown to exhibit a significant concentration model bias in Table 6.2 (Po Valley and West Poland Traces). Of these two tracers, only one was subject to a significant tracer lifetime model biases in HADGEM3-GA4. The West Poland tracer was shown to have a significant positive lifetime model bias. The Po Valley tracer does not exhibit a significant tracer lifetime bias. This result indicates that significant negative model biases in Po Valley and West Poland tracer concentrations are unlikely to be due model biases in tracer lifetimes. Subsequently, model biases in flow regimes influencing the UK in HADGEM3-GA4, following ACRWB events, is likely to explain most of the significant tracer concentration shifts in Table 6.2.

For the locally sourced and BENELUX tracers, there exists no likely model biases in their concentration. Despite this, for the locally sourced and BENELUX tracers, the tracer lifetime shows significant increase, which would be conducive of positive tracer concentration model biases in Table 6.2. In Table 6.2 an insignificant positive model bias in locally sourced and BENELUX tracer concentration is seen, following ACRWB in HADGEM3-GA4. The increased lifetimes of these two tracers may in part explain some of the model bias in tracer concentrations following ACRWB, however the model bias in mean tracer lifetime is much greater than that for tracer concentration. This suggests that the flow regimes following ACRWB are less conducive to locally sourced and BENELUX tracer accumulation within the UK, in HADGEM3-GA4.

6.6 Relationships between RWB and modelled UK [PM10] in the present-day free-running HADGEM3-GA4 simulation.

Section 6.4 found model biases in the flow regimes influencing the UK, following northeast Atlantic/ European ACRWB. Following this, it is anticipated that there might also exist model biases in the relationships between UK [PM10] and RWB, which were originally found in Chapter 3. This section analyses these relationships and compares them to those found in Chapter 5, using the nudged simulation.

6.6.1 Regions of Influential RWB to modelled UK [PM10]

One of the most fundamental results in this project was found in Chapter 3 and regards the significant increase in observed UK [PM10] following RWB within a spatially constrained region. Through this method, Sect. 3.3.2 showed that all RWB subsets resulted in significantly increased UK [PM10]. The subsets analysed in Chapters 4 and 6 are; warm anticyclonic, cold anticyclonic, warm cyclonic, and cold cyclonic RWB. To generate these subsets, three metrics were used to categorise RWB; BI, DB and RI indices. Due to the reduction in RWB frequency in the northeast Atlantic/ European region, as evidenced by Section 6.3.1, finding coherent regions of influence became difficult. Subsequently, an alteration has been made to the metrics used to categorise RWB. The focus of the analysis in Chapter 3 was regarding the direction of RWB, determined by the DB Index. Exploration of CRWB in the northeast Atlantic/ European region helped to diagnose Omega blocks as resulting in the most hazardous RWB subset through the intermediary of RWB. Therefore, the DB Index is an important RWB characteristic for the purposes of identifying the most hazardous synoptic meteorological regimes influencing the UK. The warm and cold RWB subsets, categorised using the RI Index, were generally indistinguishable in Chapter 3. Consequently, it was decided to remove the RI metric from the categorising of RWB into subsets. Therefore, only two RWB subsets remain, ACRWB and CRWB. The number of events in each subset have increased, as a result of the decreased number of RWB subsets and coherent regions of influence have resulted.

Figure 6.5 shows the regions of influence that have been calculated for both the ACRWB and CRWB (Fig. 6.5 (a) and (b)) subsets in the present-day free-running simulation. Also shown are the equivalent ACRWB and CRWB (Fig. 6.5 (c) and (d)) subsets, calculated for the nudged simulation.

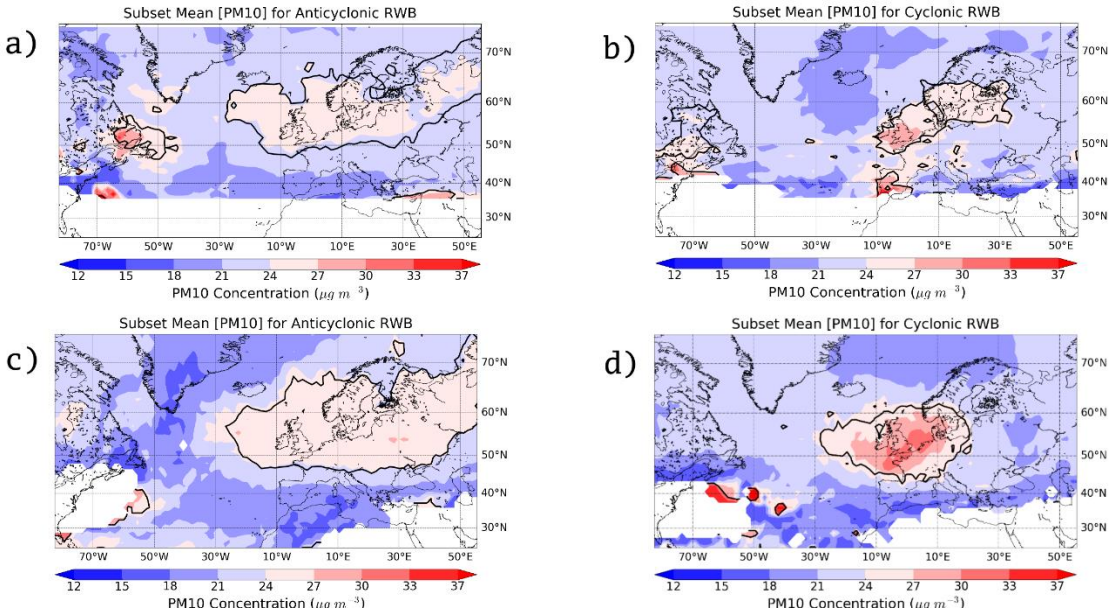

Figure 6.5 Top row) One day lagged modelled $\overline{[PM10]}$, in the 10-year present-day free-running HADGEM3-GA4 simulation, for each point within a gridded region for: **(a)** anticyclonic and **(b)** cyclonic RWB events. **Bottom row)** One day lagged modelled $\overline{[PM10]}$, in the 10-year present-day nudged HADGEM3-GA4 simulation, for each point within a gridded region for: **(c)** anticyclonic and **(d)** cyclonic RWB events. Solid contours indicate grid points where $\ln\overline{[PM10]}$ is significantly higher than $\ln\overline{[PM10]}$ for the entire dataset respectively. White grid points represent points where RWB has occurred on fewer than 2 occasions throughout DJF January 1999 - December 2008. Dataset mean [PM10] for the nudged simulation = 21.08 μg m^{-3} and free-running simulation = 22.83 μg m^{-3}.

The regions of influence used to spatially constrain RWB in the free-running simulation are illustrated in Fig. 6.5. Alongside the regions of influence calculated for the free-running simulation (a-b) are those calculated for ACRWB and CRWB in the nudged simulation (c-d). For the free-running simulation, it is shown that ACRWB results in significantly increased modelled [PM10] when it occurs in a coherent region between 30°W and 55°E. Similarities are evident when comparing the regions of influence calculated for ACRWB in the two present-day HADGEM3-GA4 simulations (nudged and free-running). Both regions are situated over a similar longitudinal extent and display spatially coherent regions. It is evident that ACRWB remains influential to modelled UK [PM10] in the free-running simulation.

Comparing the regions of influence in the nudged and free-running simulation for CRWB reveals differences. The solid contoured region in the nudged simulation (Fig. 6.5 (d)) shows greater spatial coherency than that in the free-running simulation (Fig. 6.5 (b)). The CRWB region of influence in the free-running simulation shows two centroids of influential regions.

One of these regions corresponds to a region that aligns well with the region of influence for CRWB in the nudged simulation. The second contoured region is shifted downstream into Europe, in a region not identified as influential to modelled UK [PM10] in the nudged simulation. This downstream region is thought to be associated with the eastward model bias of RWB frequency in the free-running simulation (Fig 6.1 (b)).

Figure 6.5 shows that while there are differences in the spatial extent of ACRWB and CRWB regions of influence, the magnitude of modelled UK [PM10], within the solid contoured regions of influence, is decreased within Figs. 6.5 (a) and (b), compared to Figs. 6.5 (c) and (d). Such a result infers that RWB results in less enhancement of UK [PM10] within the free-running simulation, when compared to RWB in the nudged simulation.

The results from Fig. 6.5 show that both ACRWB and CRWB significantly raise modelled UK $[\overline{PM10}]$ in the free-running simulation. This result indicates that although significant ($p<0.05$) model biases exist for the two long range advected tracers (Po Valley and West Poland tracers), RWB remains influential to modelled UK [PM10] in the free-running HADGEM3-GA4 simulation.

6.6.2 Most influential RWB subsets

Chapters 3 and 5 explored the occurrence frequency of episodic UK PM10 events, resulting from RWB. It was found that all RWB subsets resulted in an increased probability of exceeding a hazardous UK [PM10] threshold, within both of these chapters. The exceedance probabilities for ACRWB and CRWB events in both present-day HADGEM3-GA4 simulations (nudged and free-running) are displayed in Table 6.3. Much like in Sect. 6.6.1, only two RWB subsets are analysed; ACRWB and CRWB. RWB is spatially constrained within the regions of influence shown in Fig. 6.5, for the nudged and free-running simulations. The value of an exceedance in the nudged simulation is: 31.08 μg m^{-3}, while in the free-running simulation, is slightly elevated at 31.97 μg m^{-3}.

A sensitivity study was undertaken, which examines the sensitivity of the exceedance probabilities in Table 6.3, to the size of the spatially constrained regions of influence. It was shown that simulations with a greater (in area) region of influence reduce the exceedance probabilities of all RWB subsets in Table 6.3. This effect is seen due to the increased frequency of RWB events on the periphery of the regions of influence. In Fig 6.5, it can be seen that the regions of influence are greater in spatial extent for the nudged simulation, compared to the free-running simulation. To equate the spatial extent of both RWB regions of influence, a greater significance threshold was used to determine region of influence for the

nudged simulation. The ln[PM10] threshold used for the nudged simulation is 3.15, as opposed to 3.11 for the free-running simulation.

Table 6.3 Probabilities of exceeding a hazardous PM10 threshold in the nudged and free-running HADGEM3-GA4 simulations one day after; instantaneous RWB events, continuous RWB events and days not influenced by RWB. Two RWB subsets are analysed; CRWB and ACRWB. The value of an exceedance in the two present-day HADGEM3-GA4 simulations are: nudged = 31.08 μg m^{-3} and free-running = 31.97 μg m^{-3}.

RWB Subset	Instantaneous Exceedance Probability		Continuous Exceedance Probability		Days not Influenced by RWB	
	Nudged	Free-running	Nudged	Free-running	Nudged	Free-running
ACRWB	0.175	0.085	0.232	0.164	0.055	0.056
CRWB	0.158	0.075	0.325	0.417	0.055	0.056

The UK Midlands [PM10] exceedance probabilities are displayed in Table 6.3 for both the nudged and free-running simulations. Much like in Fig. 3.5 and Table 5.2, instantaneous and continuous RWB events have been identified. A result from this study has been that persistence increases the probability of exceeding a hazardous UK [PM10] threshold. Table 6.3 shows that this is also true in the free-running simulation. In the free-running simulation, continuous ACRWB/CRWB events are found to result in an 8%/34% increased probability of exceedance above instantaneous ACRWB/CRWB events.

In comparing the exceedance probabilities for RWB in the present-day nudged and free-running simulations, it is evident that the free-running simulation exceedance probabilities are reduced for all RWB subset fields in Table 6.3, aside from continuous CRWB events.

Continuous CRWB events in the free-running simulation result in the greatest exceedance probability in Table 6.3. This exceedance probability is more than twice that for continuous ACRWB and greater than that for continuous CRWB events in the nudged simulation.

6.6.3 Discussion

The analysis in Sect. 6.6.2 highlights how exceedance probabilities for all RWB subsets in the free-running simulation are elevated above days with no RWB. This result highlights that

HADGEM3-GA4 is capable of replicating a key relationship between RWB and modelled UK [PM10] found in Chapter 5, using the nudged simulation.

Table 6.3 shows that, aside from continuous CRWB events, the exceedance probability is reduced for all RWB subsets in the free-running simulation compared to the nudged simulation. Such a reduction in the exceedance probability suggests a deficiency in the model to sufficiently replicate the dynamics that lead to modelled UK [PM10] exceedances. Section 6.4.3 showed that significant negative model biases exist in the accumulation of Po Valley and West Poland tracer in the UK Midlands, during ACRWB events. The net negative model bias in modelled UK [PM10] resulting from ACRWB events has the effect of both reducing the magnitude of the [PM10] values in Fig. 6.5, illustrating the regions of influence from the free-running simulation, but also reducing the probability of reaching a hazardous modelled UK [PM10] threshold. A reduction in the exceedance probabilities for both instantaneous and continuous events can be partly explained through the significant negative model bias ($p<0.05$) of long range advected tracer.

The variance in the free-running [PM10] dataset (1.67 $\mu g\ m^{-3}$) is considerably smaller than that for the nudged [PM10] dataset (2.38 $\mu g\ m^{-3}$) and hence there is a smaller probability of exceeding a hazardous UK [PM10] threshold in the present-day free-running simulation.

The largest difference seen in Table 6.3, between the nudged and free-running simulation is the elevated continuous CRWB exceedance probability in the free-running simulation. Section 5.6 showed how with increasing time throughout an Omega Block event, the importance of the locally sourced and BENELUX tracers are elevated. Section 6.4.3 shows a slight positive model bias for these tracers, which may suggest a reason for the increased exceedance probability for continuous CRWB events in the present-day free-running simulation.

For a direct comparison between the exceedance probabilities of nudged and free-running continuous CRWB events, a comparison of the exceedance probabilities of Omega Block events must be made. In the free-running simulation, 37 CRWB events were detected, following Criteria 3) in Sect. 5.6 (CRWB grid point count > 10 grid points). Of the 37 CRWB events detected in the northeast Atlantic/ European region, 27 were identified as Omega Block events. The remaining 10 CRWB events were predominantly attributed to downstream CRWB events, independent of an ACRWB precursor. The increased number of these CRWB events in the free-running simulation, are likely due to the increased tendency of the jet to reside in its southerly state (Sect. 6.3.3) and the increased cyclonic shear

imparted on the background flow (Sect. 2.3.5). The exceedance probability for present-day nudged Omega Block events was found in Chapter 6 to be 0.373. This has been reduced in the free-running simulation, to 0.294, however this remains the most hazardous RWB subset in the free-running simulation. For completeness, the probability of exceedance associated with the 10 free-running continuous CRWB events that were not associated with Omega block events was 0.032.

Omega Block exceedance probabilities are sensitive to the event frequency of Omega block events, considering the low event frequency in each case. There exist just 31 and 27 Omega block events in the nudged and free-running simulations, throughout the 10 year datasets. Due to the low event frequency, it is not possible to state whether Omega block events are less hazardous in the free-running simulation, compared to those in the nudged simulation. Despite this, it is possible to state that Omega Block events in the free-running simulation, are likely to present the greatest probability of exceedance of any RWB subset in the free-running simulation. This statement follows the calculation of mean standard error, showing that in the free-running simulation, the $\overline{[PM10]}$ for Omega block episodes is likely ($p<0.33$) to be greater than that for continuous ACRWB episodes, as defined for Table 6.3.

6.7 Chapter Conclusions

At the beginning of this chapter there were two research questions posed:

1. Is the RWB climatology well replicated by HADGEM3-GA4?
2. Are the flow regimes resulting from northeast Atlantic/ European RWB replicated by HADGEM3-GA4?

This study has found that there exist model biases in RWB frequency throughout the northeast Atlantic/ European region. Negative RWB frequency model biases were found within the northeast Atlantic/ European region, however there exist oppositely signed model biases for ACRWB and CRWB frequency.

It has been found that ACRWB and RWB frequency show similar model biases, with negative model biases throughout the majority of the ACRWB region of influence. A positive model bias exists throughout the CRWB region of influence. Subsequent analysis in this chapter has shown that the majority of this inconsistency, between ACRWB and CRWB frequency, is due to a mean state bias in the location of the EDJ in the northeast Atlantic/ European region. An overestimation of the southerly state of the EDJ by HADGEM3-GA4 is predicted to have produced an anomalously cyclonic shear on the background flow within the

northeast Atlantic/ European region. The southerly shifted EDJ within the northeast Atlantic/ European region facilitates a greater/reduced probability for CRWB/ACRWB in this region.

The second research question outlined at the beginning of this chapter related to the flow regimes that influence the UK, following northeast Atlantic/ European RWB in the present-day free-running simulation. Due to the low event frequency of CRWB, compared to ACRWB, within the northeast Atlantic/ European region, flow regimes were determined following ACRWB events only. Subsequent analysis in Chapter 7 explores climate shifts in flow regimes that influence the UK following ACRWB. As in this section, due to a reduced event frequency, model biases in the flow regimes resulting from northeast Atlantic/ European CRWB events are not analysed.

It was found that significant ($p<0.05$) negative model biases in two long-range advected tracers (Po Valley and West Poland) existed in HADGEM3-GA4. The model biases were shown to be unexplainable due to biases in tracer lifetime and subsequently were attributed to the high sensitivities of long-range advected tracers to flow regime. Due to the high uncertainties in the advection of these two tracers within HADGEM3-GA4 and the magnitudes of the model bias being almost comparable to the nudged absolute concentration, no further analysis will be undertaken regarding the climate influence on these tracers.

In contrast, no likely ($p<0.33$) model biases were seen for the locally sourced and BENELUX tracers. The accumulation of these tracers in the UK were well represented in HADGEM3-GA4. Although there exist heterogeneous model biases in RWB frequency, both of these tracers are less sensitive to synoptic flow regime, due to their proximity to the UK Midlands measurement grid-point.

This study has found that the relationships between RWB and modelled UK [PM10] in Chapter 5, remain in the free-running simulation. Such a result is important and evidence of the fact that modelled UK [PM10] is not overly sensitive to the mean-state model biases in RWB frequency. As in Chapters 3 and 5, it was shown that all RWB events resulted in an increased probability of exceeding a hazardous modelled UK [PM10] threshold in the free-running simulation. The greatest exceedance probabilities were found for Omega block events (0.294), a consistent result with Chapters 3 and 5. Further analysis highlighted that modelled UK $\overline{[PM10]}$ following Omega block events was likely ($p<0.33$) to be greater than the modelled UK $\overline{[PM10]}$ following any other RWB subset.

6.8 Outlook to Chapter 7

In Chapter 7 the primary research question of this study will be answered:

"Do UK PM10 episodes change in a future climate that is influenced by anthropogenic climate change?"

To answer this question, a further HADGEM3-GA4 model simulation is presented, a 10 year time-slice simulation, representative of 2050 under the RCP 8.5 climate scenario (Riahi et al., 2011).

To answer the primary research question that this study poses, two subsidiary questions require answering. The first of these is to determine whether the frequency of RWB events that lead to UK [PM10] episodes changes. Subsequently, work will undergo to determine whether climate shifts in the flow regimes, resulting from RWB events, are projected.

Chapter 7 - Does Climate Change Influence the Flow Regimes that Result in UK [PM10] Exceedances?

7.1 Introduction - Overview

The work undertaken in Chapter 7 will answer the primary research question in this study:

"Do UK PM10 episodes change in a future climate that is influenced by anthropogenic climate change?"

Work has been undertaken throughout this study in an attempt to answer the above research question. Chapter 3 showed the relationships between RWB, diagnosed using ERA-Interim reanalysis data and observed UK Midlands [PM10]. In Chapter 3 it was shown that the Blocking Index (BI) is positively correlated with observed UK Midlands [PM10] in the northeast Atlantic/ European region. It was subsequently shown that the positive correlation between BI and observed UK [PM10] was mostly determined by negative BI values. Negative BI values are associated with zonally aligned flow and generally the greater magnitude negative BI values are associated with stronger zonal flow, i.e. the EDJ. Section 3.3.2 showed that RWB can significantly increase UK [PM10] when it occurs within spatially constrained regions of influence, within the northeast Atlantic/ European region. Furthermore, Sect. 3.3.4 showed that northeast Atlantic/ European RWB increased the probability of exceeding a hazardous UK [PM10] threshold. The greatest probability of exceedance was found for Omega Block events, identified from cyclonic RWB, preceded by ACRWB in the northeast Atlantic/ European region.

The relationships found in Chapter 3 are the underlying relationships that will help us to infer whether simulated climate change in this study influences UK [PM10] episodes. The climate model used is HADGEM3-GA4 and the methodology to replicate observed UK [PM10] was introduced in Chapter 5. The method used to replicate observed UK [PM10] in HADGEM3-GA4 and synoptic variability within HADGEM3-GA4 was evaluated in Chapters 5 and 6. Chapter 5 showed that 42% of the variability associated with observed UK [PM10] is replicated using an idealised tracer framework. The relationships between RWB in the ERA-Interim θ-2PVU dataset and observed UK [PM10] were replicated using modelled UK [PM10] and modelled θ-2PVU in a nudged simulation.

Chapter 6 identified model biases in the frequency and associated dynamics of RWB within HADGEM3-GA4. This study found model biases in RWB frequency, which were shown to

be influenced in part by mean-state model biases in mid-latitude synoptic variability, however it is expected that transient biases also exist in HADGEM3-GA4. Mean-state biases in the EDJ were coupled to an increase of CRWB and decrease of ACRWB within the northeast Atlantic/ European region. Heterogeneities in the ACRWB frequency model bias field resulted in spatially robust shifts in the location of ACRWB within the northeast Atlantic/ European region. Despite shifts in the region of ACRWB occurrence, this study has shown no significant or even likely model biases for the accumulation of the locally sourced or BENELUX tracers, within the UK, following ACRWB. However, the accumulation of the two long-range advected tracers within the UK (Po Valley and West Poland tracers), were shown to have significant model biases in HADGEM3-GA4.

Section 7.2 will explore the existing literature on climatic shifts of RWB events and synoptic variability within the North Atlantic/ European region. This will explore the mechanisms, which have been found to create robust climate signals in RWB frequency.

The aim of Chapter 7 is to quantitatively evaluate climate shifts in northeast Atlantic/ European RWB frequency and modelled tracer accumulation throughout ACRWB events. RWB frequency shifts are identified and discussed in Sect. 7.3.

Section 7.4 will analyse climate shifts in flow regimes, resulting from northeast Atlantic/ European ACRWB events. Knowledge of the model biases, identified in Chapter 7 are invaluable in designing a framework for identifying such climate shifts in flow regimes. It was shown how significant model biases existed for the Po Valley and West Poland tracers. These tracers were shown to be highly sensitive to synoptic flow regime and hence any misrepresentations in RWB frequency will result in large biases in the accumulation of these tracers in the UK. Section 7.4.2 will highlight an issue in evaluating the climate signals for these tracers, meaning that no climate shifts were determined for these tracers in Chapter 7.

Finally there are limitations in the method used throughout this study, to determine climate shifts in the frequency and potency of RWB events. These will be discussed in the final section of Chapter 7, which are of high importance to future studies attempting to evaluate climate shifts in a number of meteorological fields.

7.2 Background Literature

In the first half of this chapter, the focus will be on analysing climatic shifts in RWB frequency. Extensive literature exists, which analyses the climate effects on synoptic variability in the northeast Atlantic/ European region.

To understand climatic shifts in RWB frequency and in EDJ variability in the northeast Atlantic/ European region, consideration must be given to the atmospheric global circulation. In a future climate, it is well understood that the Northern Hemisphere will undergo Arctic amplification. Arctic amplification refers to the phenomena whereby the high latitudes warm at a greater rate than the low latitudes. This is an effect that can already be detected following climate change (Screen and Simmonds, 2010). Screen and Simmonds (2010) identify reductions in sea ice as the main driver for Arctic amplification. Reductions in sea ice cover result in a warming of the lower troposphere, with surface albedo decreasing and a subsequently warmer land surface. In addition to the direct effect of albedo on lower tropospheric temperatures, Screen and Simmonds (2010) highlight that increased water vapour content of the atmosphere, due in part to reduced sea ice cover, may have enhanced warming in the lower troposphere, due to water vapour being a greenhouse gas.

The global effect of anthropogenic climate change, is a reduction of the average meridional temperature gradient in the Northern hemisphere. To relate this effect into synoptic variability one must consider the impacts of a reduced meridional temperature gradient on the mid-latitude jets. As highlighted in Section 2.3.4, two mid-latitude jets exist in the Northern Hemisphere, the thermally driven upper-level subtropical jet and the lower-level EDJ. A reduction of the meridional temperature gradient due to climate change is expected to reduce the strength of the upper level jet, via thermal wind balance. In the lower troposphere, the eddy driven jet is found and its strength is determined by interaction with baroclinic eddies. Baroclinic eddies depend on baroclinic regions for their existence. Within the North Atlantic basin, the northwest Atlantic region presents the most baroclinic region. Future climate projections indicate an increase in baroclinicity in this baroclinic region (Woollings et al., 2012), due to an increase in the meridional SST gradient in this region. The change in meridional SST gradient in this region (See Fig. 4.4 (b)) opposes the hemispheric mean. This increase in baroclinicity is hypothesised to be due to a slowdown of the Atlantic Meridional Overturning Circulation (AMOC) and reduction of meridional ocean heat transport. Increased baroclinicity in this region, would present a greater conversion of baroclinic to barotropic kinetic energy and crucially a stronger EDJ (Peings and Magnusdottir, 2014; Brayshaw et al., 2009). While this mechanism is reasonably well understood, there are multiple competing mechanisms that may influence the strength of the EDJ and the resultant climatic EDJ strength shift is still uncertain (Barnes and Polvani 2013).

Barnes and Polvani, (2013), and Zappa et al. (2014) both found a clear climate signal that related to an eastward extension of the EDJ into Central Europe. The mechanisms for this

shift are unclear, with many studies pointing to a slowdown of the AMOC and increased barotropic kinetic energy in the jet, as explained above. Despite this argument, Woollings et al. (2012) also found an eastward extension in the EDJ and associated storm track when using a slab ocean model with unchanged SSTs. The mechanisms that result in this robust EDJ eastward shift are as yet undefined and remain an area of extensive research, which is beyond the scope of this PhD.

Barnes and Polvani (2013) find a poleward shift in the EDJ in a CMIP5 multi-model study. This poleward shift is not significant in the CMIP5 multi model mean although many models do show a poleward shift, with a 1^{o} poleward multi-model mean shift. Zappa et al. (2014) explored climate shifts influencing the EDJ, with results that agree with Barnes and Polvani (2013) and Dunn and Sigouin (2013). Rather than a poleward shift, an anomalous tripole of storm track activity, which is dynamically linked to EDJ location (Sect. 2.3.4), was found. It is shown by Zappa et al. (2014) that an increase in storm track activity exists over the UK region, while two regions of reduced storm track activity exist to the north and south of this region.

Masato et al. (2013b) and Zappa et al. (2014) show the climate shift of atmospheric blocking in CMIP5 models, following the RCP8.5 emission scenario, for the latter half of the 21^{st} Century. Both of these studies show that the tri-pole pattern that was identified for storm track activity (Zappa et al., 2014) also exists in atmospheric blocking frequency. The focus of this study is RWB and while strong associations are evident between RWB and atmospheric blocking in the Northern Hemisphere winter (Altenhoff et al., 2008), the two phenomena are not identical meteorological phenomena (See Sect. 2.3.2 and Sect. 2.3.5). Fortunately, Barnes and Hartmann (2012) explored the climatic shifts associated with RWB frequency, with which this study can directly compare.

Barnes and Harmann (2012) analysed climate shifts in RWB frequency. They projected a reduction in RWB frequency over the UK and Western European region and an increase over Central and Eastern Europe. This is in agreement with the eastward shift of atmospheric blocking found in the aforementioned studies. Barnes and Hartmann (2012) also divided RWB into CRWB and ACRWB events and analysed climate shifts in the frequency of each subset. Barnes and Hartmann (2012) found a poleward shift of the EDJ in 13 CMIP3 fully coupled global circulation models. This was associated with a poleward shift in the region of ACRWB occurrence, while no such shift was found for CRWB. It was argued that poleward of a northward shifted EDJ, the critical latitudes, where RWB occurs (Sect. 2.3.5) are too close to the pole and hence disappear. Critical latitudes are latitudes where Rossby wave

phase speed is equal and opposite to the background zonal wind speed, allowing Rossby waves to break. A disappearance of this critical line, reduces the CRWB frequency to the north of the EDJ and hence, no poleward shift for CRWB is evident. This signal is an amplification of the mechanism that controls the region of most frequent CRWB occurrence in the North Atlantic (Sect. 2.7.1). Section 2.7.2 discussed how a more poleward critical line in the northeast Atlantic region, when compared to the northwest Atlantic region (due to the southwest-northeast tilt of the mean EDJ), results in fewer CRWB events in the east as opposed to the west of the North Atlantic basin.

Section 7.3 will explore climate shifts in RWB frequency using HADGEM3-GA4. Within Sect. 7.3, climate shifts in RWB frequency will be divided into CRWB and ACRWB subsets, much in the same manner as Barnes and Harmann (2012).

7.3 Climate Shifts in RWB Frequency

Figure 7.1 (a) illustrates RWB frequency for the time-slice simulation, as introduced in Sect. 4.8.3. Following this, Fig. 7.1 (b) shows the difference in RWB frequency between the future time-slice and free-running simulations. The difference between the future time-slice HADGEM3 simulation and a free-running simulation for RWB frequency is referred to as the climate increment in RWB frequency.

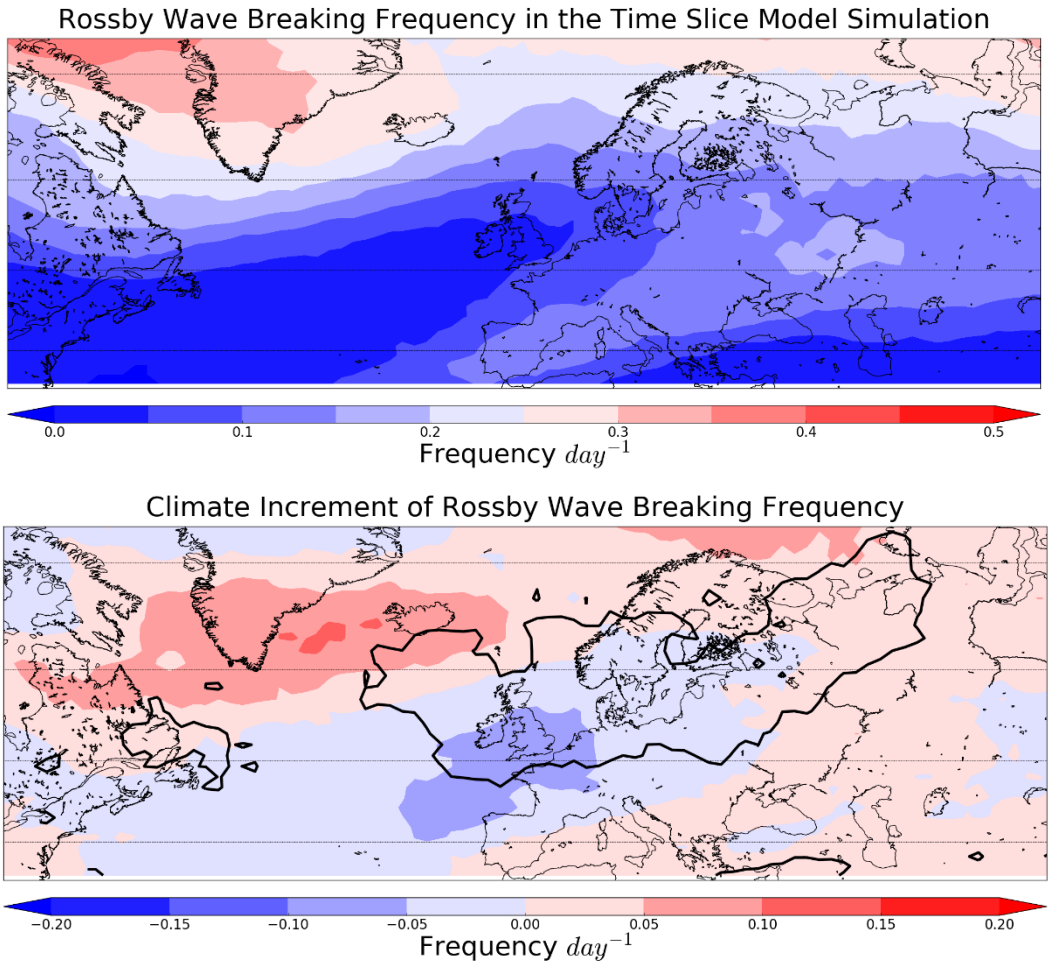

Figure 7.1 (a) Rossby wave breaking (RWB) frequency in the 10 year time-slice HADGEM3-GA4 simulation, representative of 2050. **(b)** Climate increment of RWB frequency, as calculated by subtracting the free-running from the time-slice HADGEM3-GA4 simulation. The black contoured region in Fig. 7.1 (b) represents the region of influence for ACRWB within the free-running HADGEM3-GA4 simulation.

Figure 7.1 (a) shows RWB frequency in the time-slice simulation for the North Atlantic/ European region and shows one predominant region of RWB occurrence. This region is situated over West Greenland and primarily comprises of CRWB.

Figure 7.1 (b) highlights the climate increment of RWB frequency and shows a heterogeneous pattern. Within the contoured region of ACRWB influence from the free-running simulation, there exists a spatially robust region of negative RWB frequency, situated over the UK and Western Europe. Positive climate increments in RWB frequency are found predominantly to the north of 60^{o}N, however these are longitudinally heterogeneous. Positive climate increments in RWB frequency also exist to the south of 40^{o}N, albeit with a much smaller magnitude than the positive climate increment in RWB frequency, north of 60^{o}N. At longitudes surrounding the UK and Western Europe, these climate increments in RWB

frequency present a tripolar pattern, with positive climate increments in RWB frequency to the north and south of a region of negative climate increment of RWB frequency.

Aside from latitudinal climate shifts in RWB frequency anomalies, an eastward shift of RWB frequency is highlighted from Fig. 7.1 (b). This eastward shift can be seen within the overlain free-running ACRWB region of influence. Large negative climate increments in RWB frequency to the southwest extent of this region are found alongside smaller positive climate shifts in RWB frequency to the north east of the region of influence. Within the time-slice simulation, there appears to be a greater tendency for RWB to occur further east of RWB in the free-running simulation.

7.3.1 Discussion

The results from Sect. 7.3, regarding the climate increment of RWB frequency are consistent with those found in literature. It has been shown that within a region that RWB significantly increases modelled UK [PM10] in the time-slice simulation, there exist predominantly negative climate increments in RWB frequency. Despite this, heterogeneities exist in climate RWB frequency increments, showing an anomalous latitudinal RWB frequency tripole, centred on a region of negative anomalous RWB frequency over the UK region. This result was found by Zappa et al. (2014) for storm track activity, which is directly related to the position of the EDJ (Sect. 2.3.4), much in the same way as RWB.

A robust result found in literature regarding the climate increment of; atmospheric blocking (Masato et al., 2013b), storm track activity (Zappa et al., 2014) and RWB (Barnes and Hartmann, 2012) was an eastward shift of each of these features as a result of climate change. This is a signal that is also found in Fig. 7.1 (b), most noticeably within the contoured ACRWB region of influence. There currently exists no consensus of the mechanisms that dictate this eastward migration, however the hypothesis is that it is strongly linked to the weakening of the AMOC (Peings and Magnusdottir, 2014; Brayshaw et al., 2009).

7.3.2 Climate Increments in ACRWB and CRWB

Barnes and Hartmann (2012) explored the climate increments of ACRWB and CRWB in 13 fully coupled climate models. Contrasting climate increments were found for ACRWB and CRWB, with the former experiencing a noticeable northward shift. CRWB showed no such northward shift and this was due to the poleward disappearance of the critical lines where RWB occurs.

Figure 7.2 (a) shows the climate increment for ACRWB in the Atlantic/ European region. The overlain black contour represents the ACRWB region of influence from the free-running

simulation. The climate increment associated with CRWB is shown in Fig. 7.2 (b), with the CRWB region of influence overlain from the free-running simulation.

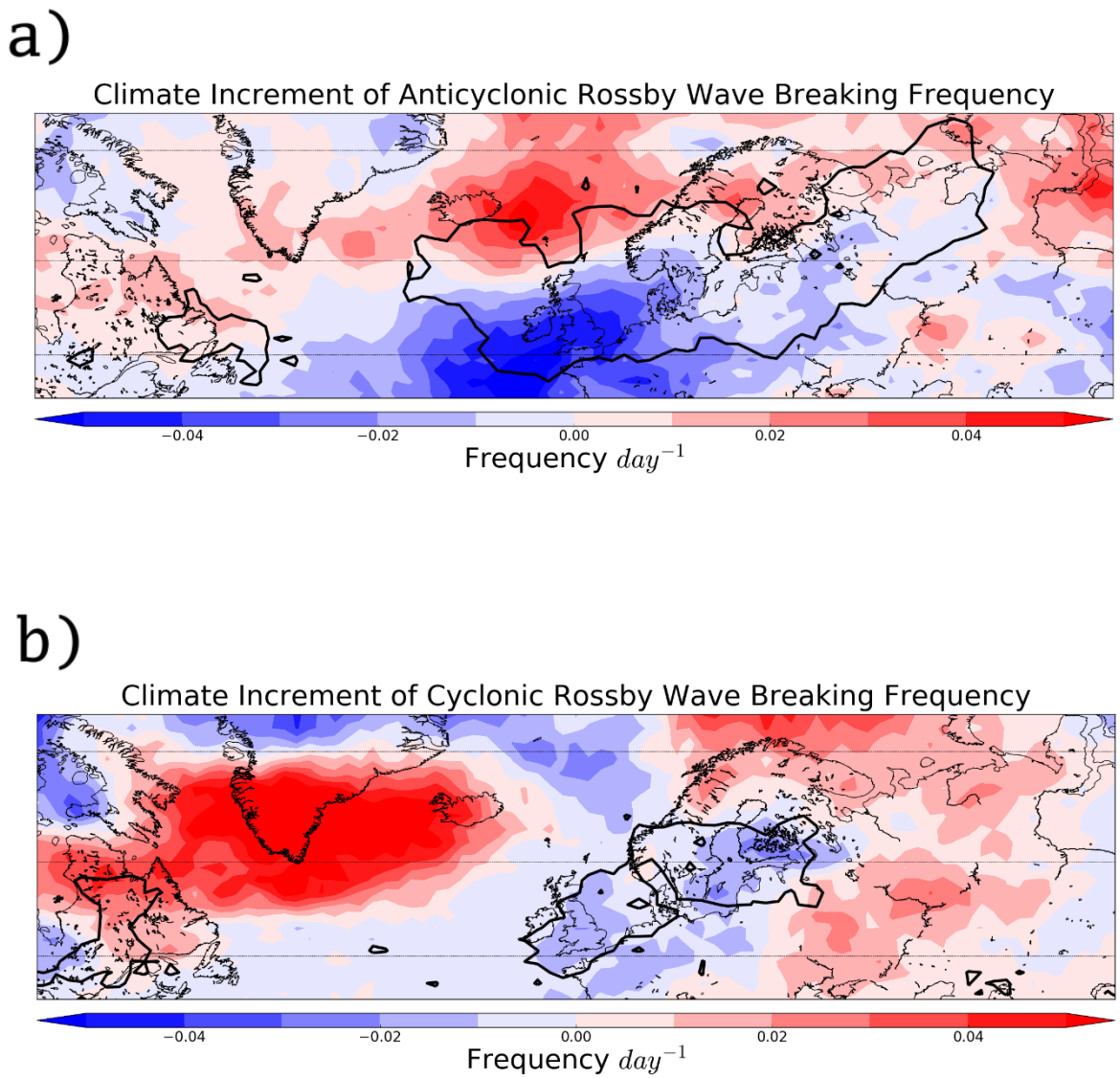

Figure 7.2 (a) Climate Increment of anticyclonic RWB frequency in HADGEM3-GA4, calculated by subtracting ACRWB frequency in the free-running HADGEM3-GA4 simulation from ACRWB frequency in the time-slice HADGEM3-GA4 simulation. **(b)** Climate increment of cyclonic RWB frequency in HADGEM3-GA4, calculated in the same manner as Fig. 7.2 (a), but for CRWB. The contoured regions in **(a)/ (b)** represent the regions where ACRWB/ CRWB significantly increases modelled UK [PM10] in the present-day free-running HADGEM3-GA4 simulation.

Figure 7.2 (a) illustrates the climate increment of ACRWB frequency in HADGEM3-GA4. It shows that ACRWB predominantly reduces in frequency when it occurs within the contoured free-running ACRWB region of influence. This reduction of ACRWB is seen equatorward of 60^{o} N, with latitudes poleward of 60^{o} N generally showing an increase in ACRWB. This pattern is suggestive of a poleward climatic shift of ACRWB in HADGEM3-GA4. Also seen

for ACRWB is that the greatest negative climate increment is situated in the southwest extent of the overlain region of influence. Within the region of ACRWB influence in Fig. 7.2 (a), there exist smaller reductions of ACRWB frequency in the east, as opposed to the west. This longitudinal RWB frequency heterogeneity results in an eastward shift of a mean ACRWB event within the region of ACRWB influence.

The eastward shift in the mean ACRWB event in a future climate, is also seen for CRWB in HADGEM3-GA4. CRWB is shown to increase in central Europe, while decreasing in the UK/ Western European region. The largest climatic shift of CRWB frequency is seen over Greenland and shows an increased signal.

A major difference evident between Fig. 7.2 (a) and (b) is the presence of a poleward anomalous RWB frequency shift. It is found that ACRWB experiences a poleward shift in RWB frequency, which is centred on approximately 60^{o} N, while unlike for ACRWB, no such latitudinal shift is seen for CRWB in Fig. 7.2 (b).

7.3.3 Discussion

Existing literature suggests that all RWB will experience an eastward shift in projected future climate (Barnes and Hartmann, 2012). This study shows that the mean ACRWB and CRWB event undergoes an eastward shift in a future climate. CRWB shows a strong robust east/west anomalous RWB frequency dipole, which is consistent with the results from a 13 member multi-model study by Barnes and Hartmann (2012).

Figure 7.2 (a) shows a poleward climate shift in ACRWB frequency, while Fig. 7.2 (b) shows no obvious poleward climate shift of CRWB frequency. Section 7.2 highlighted the mechanisms dictating the contrasting poleward climate shifts of CRWB and ACRWB. Barnes and Hartmann (2012) identified that the critical line to the north of the EDJ, where CRWB occurs, effectively disappears as it migrates poleward.

Section 7.3 has identified that there exists a negative climate shift in the frequency of both ACRWB and CRWB events within the northeast Atlantic/ European region of most influence to modelled UK [PM10]. This result indicates a future reduction in the frequency of synoptic conditions most prevalent to the accumulation of PM10 within the UK, such as Ω block events. Consequently, this study suggests a reduction of UK PM10 episodes within a future climate.

In addition to negative climate shifts in ACRWB and CRWB frequency within the northeast Atlantic/ European region, Sect. 7.3 has found that there exist robust eastward and northward climatic RWB frequency shifts. Climate shifts in the regions where RWB occurs, will likely

result in a climate shift in the flow regimes, which influence the UK, following RWB in this region. Consequently, it is uncertain at this point whether RWB influences UK [PM10] through the same mechanisms and whether different European PM10 sources become more influential during UK [PM10] episodes.

Section 7.4 analyses the flow regimes that result from ACRWB in the northeast Atlantic/ European region. A methodology has been designed to determine whether climatic shifts exist in the contribution of any of the modelled tracers to modelled UK [PM10] throughout ACRWB events.

7.4 Identifying Climate Increments in Synoptic Flow Regimes Following ACRWB

The primary research aim for this PhD project is to determine whether UK [PM10] events change in a future climate. Section 7.3 analysed climate shifts in RWB frequency and found that HADGEM3-GA4 simulates a reduction in RWB frequency within the region of most influence to UK [PM10]. This section aims to determine whether the flow regimes influencing the UK, following RWB in the northeast Atlantic/ European region, change in a future climate. Only ACRWB events are analysed, due to the comparatively low event frequency of CRWB events in the northeast Atlantic/ European region. To determine statistically significant climate shifts in flow regime, higher event frequencies are required than those seen for CRWB in the time-slice frequency (4.3 winter^{-1}). For comparison, ACRWB events are 6.12 times more common than northeast Atlantic/ European CRWB events that occur within their respective regions of influence. The flow regimes resulting from ACRWB events in the northeast Atlantic/ European region will be analysed in the time-slice simulation. These will be compared to the flow regimes in the two present-day simulations (nudged and free-running) to determine any climate shifts, following ACRWB.

Figure 7.2 (a) shows a north-eastward shift in the frequency of ACRWB in the northeast Atlantic/ European region. With this spatial shift of ACRWB, it is suggested that there may also exist a shift in the flow regime that influences the UK following ACRWB. Such a shift was noticed in Chapter 6, associated with the model bias in ACRWB frequency (Fig. 6.2 (a)). It was shown that there exists both; a northward model bias and an eastward model bias in the location of the mean northeast Atlantic/ European ACRWB event. The impact of these model biases on the flow regimes influencing the UK was identified by analysing the accumulation of advected tracers in the UK. It was found that no significant model bias shifts could be seen for the locally sourced or BENELUX tracers, however significant model biases were shown for the Po Valley and West Poland tracers.

The method undertaken to determine a climatic shift in flow regimes, is consistent with the method used to detect model biases in flow regimes, in Chapter 6. Initially the concentration of each tracer in the UK, following ACRWB, is analysed. Fundamentally, these are then compared to the tracer concentrations, which result from ACRWB in the free-running simulation. There is however, an added complexity in this chapter, which is associated with the presence of model biases in accumulated tracer concentration in the UK, following northeast Atlantic/ European ACRWB, in Chapter 6.

In Chapter 6, the accumulated UK tracer concentration, following ACRWB was calculated using Eq. 7.1. In Eq. 7.1, Sim. represents the HADGEM3-GA4 simulation (nudged, free-running, time-slice simulations) and tr represents the tracer being calculated (locally sourced, BENELUX, Po Valley, West Poland tracers). $\overline{[\mathrm{Tracer}]}$ represents the mean tracer concentration, following RWB of one subset at each grid point, throughout a 2D latitude-longitude grid. *freq* represents the latitude-longitude frequency field for one RWB subset in one simulation and $\overline{T_{tr}^{FR}}$ represents the mean tracer concentration throughout the contoured regions of influence in the free-running simulation.

$$\overline{T_{tr}^{Sim.}} = \iint freq_{ACRWB}^{Sim.} \times \overline{[\mathrm{Tracer}]}_{tr}^{Sim.} \, d\varphi d\theta \qquad Eq. 7.1$$

It is anticipated that changes in the distribution of ACRWB events, throughout the region of influence act to alter the concentration of advected tracers to the UK through the $freq_{ACRWB}^{Sim.}$ term on the right-hand side of Eq. 7.1. The $\overline{[\mathrm{Tracer}]}_{tr}^{Sim.}$ term represents the effect of RWB at each grid point on the accumulation of that tracer within the UK. It is therefore expected that a RWB event in each simulation is predominantly the same event and it is changes in the location of the event that determines changes in the flow regimes influencing the UK. These hypotheses are based on the assumption of independence between the $freq_{ACRWB}^{Sim.}$ and $\overline{[\mathrm{Tracer}]}_{tr}^{Sim.}$ terms. Section 7.4.2 elaborates on this assumption and explores whether one can assume independence between the $freq_{ACRWB}^{Sim.}$ and $\overline{[\mathrm{Tracer}]}_{tr}^{Sim.}$ terms.

To determine climate shifts in UK tracer concentration, a model bias correction must be made for both the constituent fields ($freq_{ACRWB}^{Sim.}$ and $\overline{[\mathrm{Tracer}]}_{tr}^{Sim.}$) to $\overline{T_{tr}^{Sim.}}$ in Eq. 7.1. Section 7.4.1 presents a method of applying a model bias correction in this study.

7.4.1 Applying a model bias Correction

This study uses a model bias correction method to determine the climate shift in flow regimes that influence the UK, following ACRWB. The model bias correction is not as simple as subtracting the model bias in mean tracer concentration ($\overline{T_{tr}^{MB}}$) from the free-running and time-slice simulation, therefore leaving the climate shift in tracer concentration unchanged. Rather, the model bias will alter the size of the climate shift in UK tracer concentration, following ACRWB as model biases exist in both the $freq_{ACRWB}^{Sim.}$ and $\overline{[\text{Tracer}]}_{tr}^{Sim.}$ fields.

Figures 5.4 and 6.5 both showed $\overline{[\text{Tracer}]}_{tr}^{Sim.}$ fields in the calculation of regions of influence, for the nudged and free-running simulations respectively. The $\overline{[\text{Tracer}]}_{tr}^{Sim.}$ field has been shown in both cases to be highly heterogeneous. Sect. 6.3.2 found a north-eastward model bias of ACRWB frequency, while Sect. 7.3.2 found a north-eastward climate shift of ACRWB frequency. Due to the heterogeneous nature of the $\overline{[\text{Tracer}]}_{tr}^{Sim.}$ field, the model bias in RWB frequency prior to and following the climate shift (free-running and time-slice simulations) will result in a differently sized $\overline{T_{tr}^{MB}}$.

The climate shift in modelled tracer concentration (CI) will likely be altered by the application of a model bias correction to both the free-running and time-slice simulations. This section will present the methodology for removing the model bias from both the time-slice and free-running simulations.

Equation 7.1 shows that each tracer concentration is calculated in this study as the product of the normalised ACRWB frequency and the tracer concentration that results from ACRWB at each grid point within the region of influence. This study finds model biases in both the $freq_{ACRWB}^{Sim.}$ and $\overline{[\text{Tracer}]}_{tr}^{Sim.}$ fields. The calculation of the climate increment in tracer concentration (CI_{tr}) is shown by Eq. 7.2. In Eq. 7.2, f represents the $freq_{ACRWB}^{Sim.}$ field, the subscript tr represents the tracer being analysed, the superscripts TS and FR refer to the future time-slice and free-running simulations and the superscript MB refers to the model bias calculation of the respective field. The model bias for each field ($freq_{ACRWB}^{Sim.}$ and $\overline{[\text{Tracer}]}_{tr}^{Sim.}$) is calculated by subtracting the respective field for the free-running simulation from that for the nudged simulation.

$$CI_{tr} = \iint (f_{tr}^{TS} - f_{tr}^{MB})\left(\overline{[\text{Tracer}]}_{tr}^{TS} - \overline{[\text{Tracer}]}_{tr}^{MB}\right) - (f_{tr}^{FR} - f_{tr}^{MB})\left(\overline{[\text{Tracer}]}_{rt}^{FR} - \overline{[\text{Tracer}]}_{tr}^{MB}\right) d\varphi d\theta \qquad Eq.\ 7.2$$

Where f_{tr}^{MB} and $\overline{[\text{Tracer}]}_{tr}^{MB}$ are calculated from Eq. 7.3 and 7.4 respectively.

$$f_{tr}^{MB} = f_{tr}^{FR} - f_{tr}^{N} \qquad Eq.7.3$$

$$\overline{[\text{Tracer}]}_{tr}^{MB} = \overline{[\text{Tracer}]}_{tr}^{FR} - \overline{[\text{Tracer}]}_{tr}^{N} \qquad Eq.7.4$$

Equation 7.2 describes the calculation of the climate increment for tracer tr in this framework. As in Chapter 6, to obtain an estimate of the uncertainty in CI_{tr} a Jackknife approach was applied. The calculation of *CI* was made ten times, each time one winter season of data was removed from the dataset (see Sect. 6.4.2). The variability in CI_{tr} was used to determine the uncertainty in CI_{tr} and hence help to determine whether a significant CI_{tr} was identified. The signal to noise approach, used in Chapter 6 to identify significant model biases, was used to determine whether significant climate shifts of CI_{tr} have been identified. The calculation of SNR is displayed in Eq. 7.5, where σ represents the standard deviation of CI_{tr} and N represents the number of subset datasets used to calculate CI, following this study's Jackknife approach (10 years).

$$\text{SNR} = \frac{CI_{tr}}{1.96 \times \frac{\sigma}{\sqrt{\text{N}}}} \qquad Eq.7.5$$

The model bias, which is outlined in Sect. 6.4.1 was determined following an assumption. It was assumed that the $freq_{ACRWB}^{Sim.}$ and $\overline{[\text{Tracer}]}_{tr}^{Sim.}$ fields are independent of one another. Section 7.4.2 explores this assumption and finds that model bias correction is not possible for tracer concentrations with large model biases in Sect. 6.4.3.

7.4.2 Non-Independence between [PM10] and Frequency

In Chapter 6, significant model biases were found to exist for the Po Valley and West Poland tracers. The model bias correction method, outlined in Sect. 7.4.1, would be capable of correcting these model biases, however an issue became evident with regards to an assumption made in Sect. 6.4.1. The assumption is that the $freq_{ACRWB}^{Sim.}$ and $\overline{[\text{Tracer}]}_{tr}^{Sim.}$ fields, which are used to calculate tracer concentration in Eq. 7.1, are independent. This is an important assumption, as in Eq. 7.2, the model biases are applied independently, to calculate CI_{tr}. This section will be used to argue that the assumption of non-dependence between $freq_{ACRWB}^{Sim.}$ and $\overline{[\text{Tracer}]}_{tr}^{Sim.}$ is not entirely true and that large model $freq_{ACRWB}^{Sim.}$ biases result in large uncertainties in $\overline{[\text{Tracer}]}_{tr}^{Sim.}$. This is found to be especially true for tracers whose concentrations have larger sensitivities to the location of RWB and associated synoptic flow regime.

The issue of dependence arises, due to the fundamental description of a RWB event in this study. A RWB event on any single day is unlikely to be localised to a single grid point. Instead, RWB is identified using the BI and hence a number of grid points will identify as BI > 0 K, during a single RWB event. We assume that flow regimes resulting from RWB can be best explained by the location of the centre of overturning. Consequently, corresponding grid points with BI > 0 K will share the 'influence' of this central point in relation to tracer advection into the UK.

An example of this shared influence between BI >0 K grid points can be seen in Fig. 7.3. In Fig. 7.3 the frequency (day^{-1}) of BI > 0 K values at each grid point is shown, which coincide with BI > 0 K at a North Sea grid point (frequency peak in Fig. 7.3). The North Sea grid point represents the grid point where ACRWB results in the greatest locally sourced tracer concentration, in the time-slice simulation ($\overline{[\text{Tracer}]}^{TS}_{Locally\ Sourced}$).

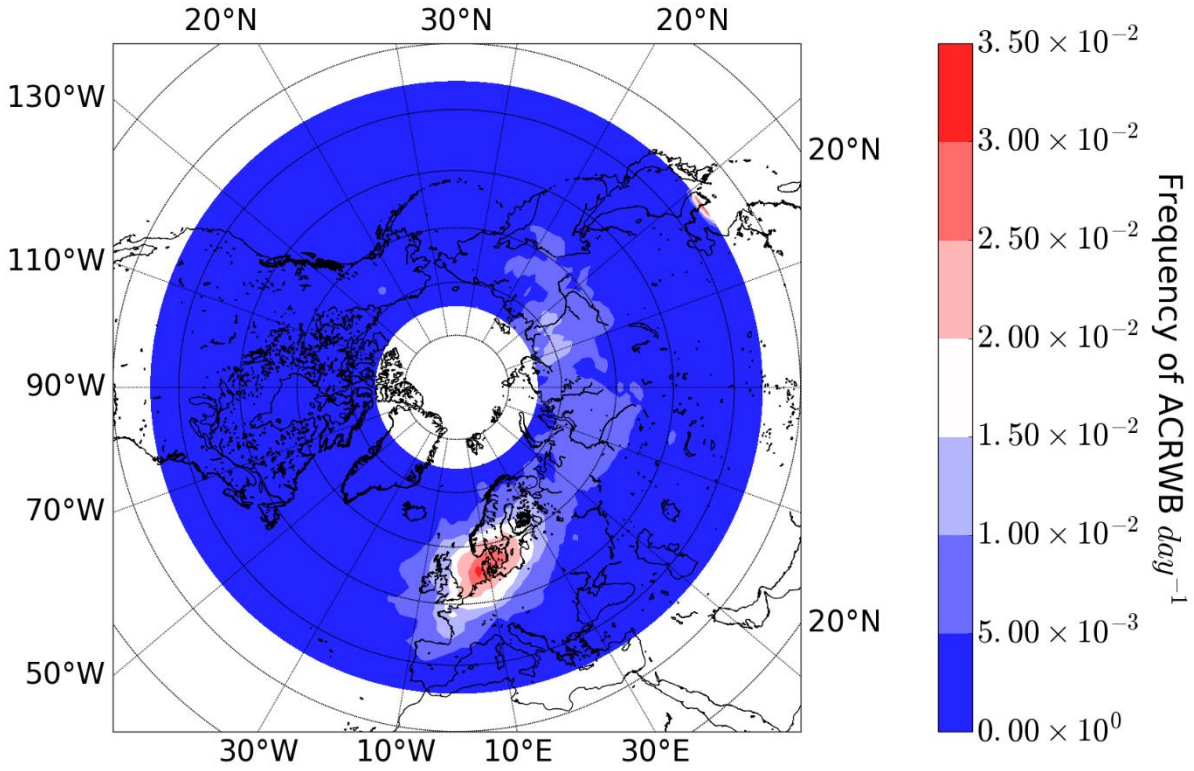

Figure 7.3 RWB frequency at each grid point, occurring concurrently with RWB over a North Sea grid point, throughout the 10 year time-slice HADGEM3-GA4 simulation.

Figure 7.3 shows the frequency of detected RWB events at each grid point that coincide with RWB detection over the North Sea grid point of maximum locally sourced tracer concentration, resulting from ACRWB in the time-slice simulation. The frequency of RWB

events at the North Sea 'hotspot' is 0.033 day^{-1} and this reduces in a concentric pattern from this grid point.

It is interesting to note that the 0.005-0.01 contour, which corresponds to 15.2%-30% of the RWB frequency at the North Sea hotspot, has a similar spatial extent as the contoured region of influence for ACRWB, from the time-slice simulation. This indicates that there exists a large covariance term (grid points with simultaneous BI > 0 K) between the frequency of RWB events throughout the region of influence.

The issue of dependence is seen between the $freq_{ACRWB}^{Sim.}$ and $\overline{[\text{Tracer}]}_{tr}^{Sim.}$ fields that constitute tracer concentration. This study has so far presented model biases in ACRWB frequency, which are heterogeneous throughout the region of ACRWB influence. These heterogeneities impose a model bias in the distribution of ACRWB throughout the region of influence and consequently on the mean flow regime pattern that results from ACRWB in HADGEM3-GA4. ACRWB events have been shown to co-vary greatly within the region of influence (Fig. 7.3). Consequently a shift in the location of the mean ACRWB event to a region where RWB results in a reduced tracer concentration, will influence the tracer concentration resulting from ACRWB, for all grid-points within the region of influence. Put simply, if the centre of overturning is likely to be associated with a reduction in tracer concentration, then the co-varying/ peripheral BI>0 K grid points will also be associated with a reduced tracer concentration in the $\overline{[\text{Tracer}]}_{tr}^{Sim.}$ field.

The consequence of this dependence between $freq_{ACRWB}^{Sim.}$ and $\overline{[\text{Tracer}]}_{tr}^{Sim.}$ fields results in an additional uncertainty. The assumption of independence allows us to apply a model bias correction to a non-linear system, by applying changes to each linear system independently ($freq_{ACRWB}^{Sim.}$ and $\overline{[\text{Tracer}]}_{tr}^{Sim.}$ fields). Without the ability to do this, the effect that the model bias has on the $\overline{[\text{Tracer}]}_{tr}^{Sim.}$ field is unknown. This author believes it to be impossible to quantify this uncertainty, which is fundamentally increased with an increasing model bias in tracer concentration.

7.4.3 Results of Signal to Noise for Each Tracer

The SNR was calculated for two of the four modelled tracers, to determine whether there exist significant climatic shifts in tracer concentration and subsequently flow regime. Table 7.1 presents both the CI_{tr} value and SNR for the tracers that did not experience a significant model bias in Chapter 6.

Table 7.1 First Row) The calculated climate increment (CI) for the locally sourced and BENELUX tracers, with positive values indicating an increased future tracer concentration **Second row)** The calculated signal to noise (SNR) ratio for the climate shifts of the two aforementioned tracers.

Tracer	Locally Sourced Tracer	BENELUX Tracer
CI	-1.74	0.66
SNR	-3.42	2.68

Table 7.1 shows both the climate increment and associated signal to noise ratio for the locally sourced and BENELUX tracers, following the methodology presented in Sect. 7.4.1. A significant climate shift ($p<0.05$) can be identified for tracers with $|S:N| > 1$, where the climate increment is greater in magnitude than the magnitude of uncertainty, associated with that value, in Eq. 7.5.

In Table 7.1, both the locally sourced and BENELUX tracers show a significant climate increment in their UK concentration, following ACRWB. The first of these is the locally sourced tracer, which shows a significantly negative climate increment in concentration. Opposing the sign of the significant climate shift for the locally sourced tracer, the BENELUX tracer shows a significantly positive climate concentration shift.

7.4.4 Discussion

The two constituent tracers to modelled UK [PM10], whose concentration were not shown to be likely ($p<0.33$) influenced by a model bias, show significant ($p<0.05$) climate shifts in concentration, following ACRWB events. It was found that the locally sourced and BENELUX tracers were influenced by oppositely signed climate shifts. This therefore suggests that HADGEM3-GA4 indicates a significant reduction of locally sourced PM10 and an increase in advected European PM10 throughout ACRWB events.

Significant model biases for the Po Valley and West Poland tracers inhibit the possibility of calculating climate increments for these two tracers. Despite this, an inference can be made, regarding the advection of European PM10 in general, from the climate shift seen for the BENELUX tracer.

7.5 Physical Interpretation of Observed Climatic Shifts

Section 7.4 highlighted a significant climate flow regime shift, associated with ACRWB. This study has shown that, following northeast Atlantic/ European ACRWB, there exists a tendency for a greater advection of European PM10 and a reduction in the accumulation of locally sourced PM10, potentially through a reduction in UK stagnation events. This section will analyse these climate shifts in tracer concentration and attempt to attach the physical explanation.

In Sect. 7.3 it was shown that there exists a spatially robust north-eastward climate shift in ACRWB frequency in HADGEM3-GA4. While it is uncertain what effect a latitudinal shift in ACRWB frequency will have on tracer concentrations in the UK, the longitudinal dependence of accumulated tracers has already been examined in this study. This analysis formed a part of the analysis of Omega blocks in Sect. 5.6. Section 5.6 showed that ACRWB over Scandinavia facilitates the advection of both West Poland and BENELUX tracers. Following the initial advection of European PM10, it was shown that the anomalous MSLP maxima (blocking anticyclone) migrates westward (Sect. 3.3.7) and a period of stagnation and locally sourced tracer accumulation ensued.

Figures 7.4 (a) and (b) respectively show the longitudinal variability in the mean latitudinal nudged locally sourced and BENELUX tracer $\overline{[\mathrm{Tracer}]}$ fields, within the free-running ACRWB regions of influence. The $\overline{[\mathrm{Tracer}]}$ field relates to the mean [Tracer] at each grid point, 1 day subsequent to ACRWB at that grid point. Both figures also show the longitudinal variability in the frequency of ACRWB in the nudged, free-running and time-slice simulations, latitudinally averaged between 50^{o}N and 60^{o}N. From Fig. 7.4 it will be shown whether a robust longitudinal shift in ACRWB is responsible for the significant increase/ decrease in BENELUX/ locally sourced tracer concentration respectively. The shading on each line corresponds to 1.96 x the standard error of the mean at each longitudinal grid point.

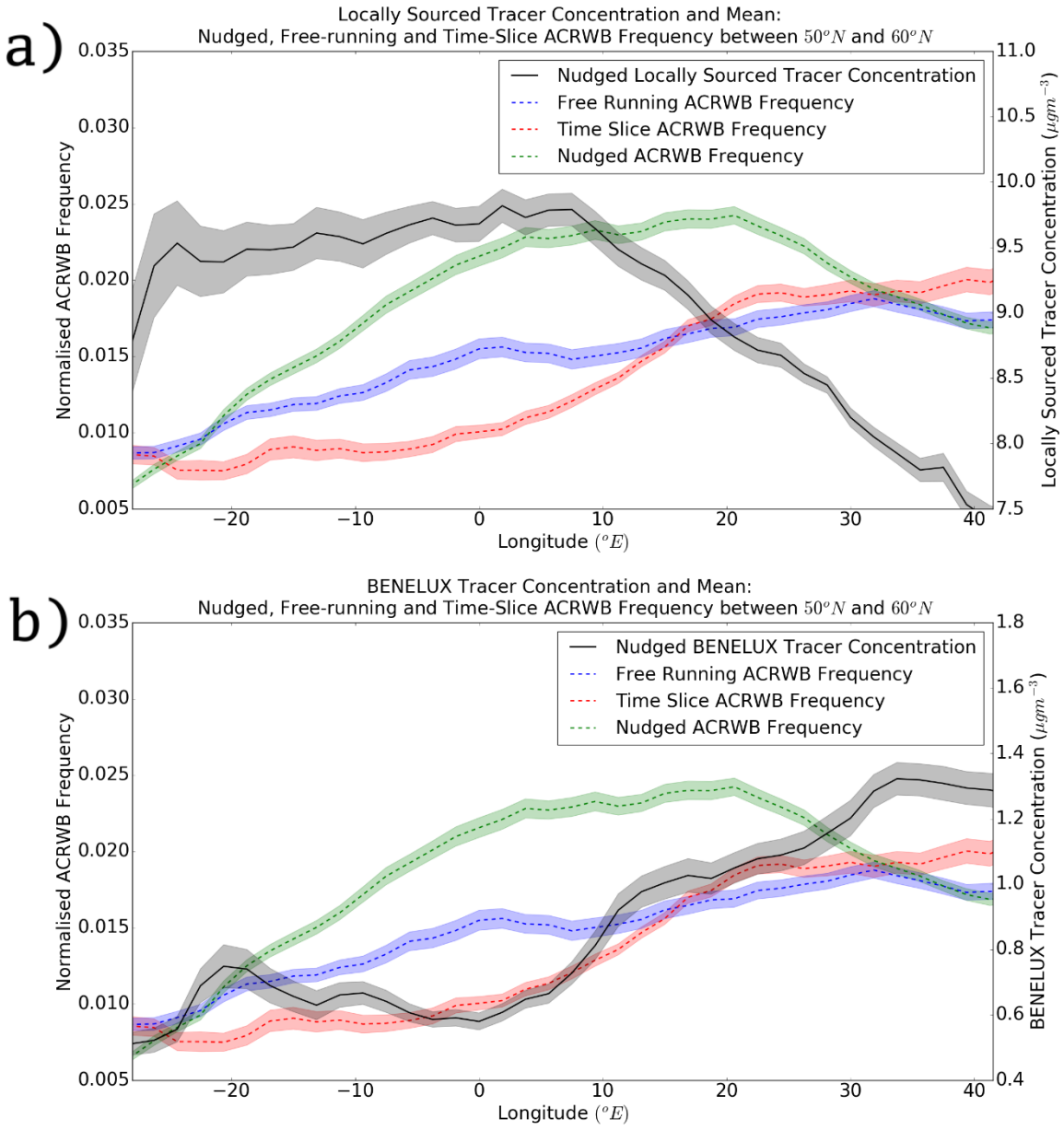

Figure 7.4 (a) The longitudinal variation, averaged between 50°N and 60°N within the time-slice HADGEM3-GA4 ACRWB region of influence, in; locally sourced tracer resulting from ACRWB (black line) and nudged (green line), free-running (blue line) and time-slice (red line) HADGE3-GA4 ACRWB frequency. ACRWB frequency lines are normalised so that the sum of each line is equal to 1. **(b)** Same as **(a)**, but with the black line representing the BENELUX tracer resulting from ACRWB. Error shading on each line represents 1.95 times the standard error of the mean.

In Fig. 7.4, the longitudinal variability in the locally sourced/ BENELUX tracer $\overline{[\text{Tracer}]}$ fields and ACRWB frequency in each model simulation can be compared. A comparison between the black lines in Fig. 7.4 (a) and (b) show two very different longitudinal dependencies. It is shown in Fig. 7.4 (a) that the locally sourced tracer concentration resulting from ACRWB in the region of influence, decreases almost linearly, eastward of 10° E.

Opposing this, the black line in Fig. 7.4 (b) increases approximately linearly from 0^{o} E to 30^{o} E.

The longitudinal variability in the black lines in Fig. 7.4 would only result in a climatic tracer concentration shift, if there exist differences in the longitudinal variability of ACRWB frequency between the free-running (blue line) and time-slice (red line) simulations. The frequency lines are normalised, so as to only analyse the distribution of ACRWB frequency within the ACRWB region of influence and are the same in Fig. 7.4 (a) and (b). It is shown that the normalised present-day free-running ACRWB frequency is greater than the normalised future time-slice ACRWB frequency between approximately -20^{o}E and 10^{o}E. Contrasting this, it is seen that the normalised time-slice frequency is greater between approximately 10^{o}E and 40^{o}E. This dipole pattern, about 10^{o}E, is consistent with the eastward shift in ACRWB (Sect. 7.3).

Discussion

In relation to the significant climate shifts in locally sourced and BENELUX tracer concentration, the above results can explain these modelled climate shifts. It is seen that a greater proportion of ACRWB in the future time-slice simulation, occurs in a region that is favourable to the accumulation of BENELUX tracer (10^{o} E to 40^{o} E). Opposing this, it is shown that fewer ACRWB events occur in the future time-slice simulation relative to the free running simulation, in a region that favours the accumulation of locally sourced tracer (-20^{o}E to 10^{o}E).

This analysis therefore shows that it is the eastward migration of ACRWB in a simulated future climate that favours the advection of European tracer and inhibits the accumulation of locally sourced tracer. Therefore based on a single atmosphere-only model simulation (HADGEM3-GA4), one can expect that following the RCP8.5 future emissions scenario, the flow regimes affecting the UK, following North-Atlantic/European ACRWB, will be significantly shifted.

Section 7.5 has shown that a significant shift in flow regimes exists and is fundamentally caused by the eastward climate shift in ACRWB events. Despite this, it must also be analysed, whether climate shifts in tracer lifetime are consistent with the climate shifts in tracer concentration. Section 7.6 will identify climate shifts in tracer lifetime and determine whether these shifts are consistent with climate shifts in tracer concentration.

7.6 Tracer Lifetime Analysis

Section 7.6 examines whether climate shifts in tracer concentration can be explained by climate shifts in tracer lifetime. Figure 7.5 shows the mean tracer lifetime for the locally sourced and BENELUX tracers in the three HADGEM3-GA4 simulations, one day after ACRWB events diagnosed within the region of influence. The tracer lifetimes were obtained following the calculation of each tracer lifetime on every day. The variability of tracer lifetime between each day provide an estimate of the uncertainty in tracer lifetime. Error bars on each column, represent the 95th confidence interval for the standard errors of each mean tracer lifetime.

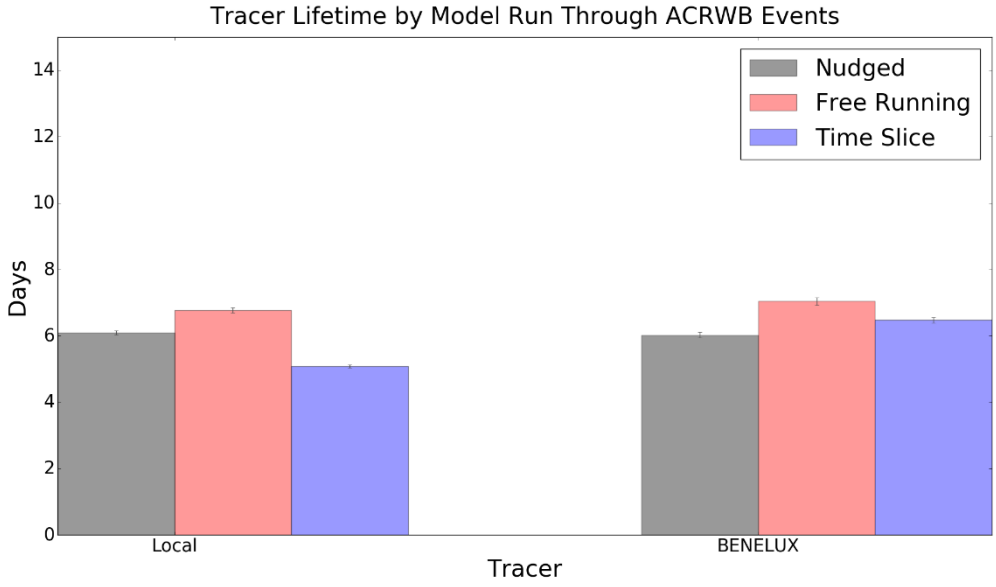

Figure 7.5 Tracer lifetime for the locally sourced and BENELUX tracers within each of the three HADGEM3-GA4 simulations: Nudged (grey bar), Free-running (red line) and time-slice (blue line). Error bars represent 1.95 times the standard error of the mean tracer concentration for each tracer in each simulation.

The mean lifetime of the locally sourced and BENELUX tracers, in three HADGEM3-GA4 simulations can be seen in Fig. 7.5. The blue bar corresponds to the time-slice simulation, which for both tracers is reduced compared to the free-running simulation (red bar). The greatest reductions in tracer lifetime between the future time-slice and free-running simulations can be seen for the locally sourced tracer.

This study has shown the locally sourced tracer to experience a significant ($p<0.05$) reduction in concentration, following ACRWB, within a future climate (Table 7.1). Locally sourced tracer lifetime also experiences a significant reduction in Fig. 7.5. Consequently, it can be

said that the negative climate shift in tracer concentration is consistent with the negative climate shift in locally sourced tracer lifetime.

This study has also found the BENELUX tracer to experience a positive climate shift in mean concentration, representative of 77.8% of the nudged mean BENELUX tracer concentration. Such a positive climate shift is not seen for tracer lifetime, with a reduction in BENELUX tracer lifetime presented in Fig. 7.5. The positive climate shift in BENELUX tracer concentration is therefore unlikely to be explained through a similar climate shift in BENELUX tracer lifetime, but to be associated with circulation changes already discussed.

7.7 Discussion on Climate Shifts

The modelled negative climate shifts in tracer lifetime are likely representative of positive climate shifts in European precipitation. Positive climate shifts in European precipitation have been found within existing literature (Williams et al., 2015; Kharin et al., 2013) as a response to anthropogenic climate change. Climate shifts in tracer lifetime are most likely due to climate shifts in precipitation, with the land surface tiles within each of the model simulation unchanged. It would therefore be unlikely that drastic differences in dry-deposition rates are experienced. Despite this, dry deposition rates will be influenced in small amounts by climate shifts in synoptic flow regimes, as tracer will likely be advected over different terrain.

The significant climate shifts in locally sourced and BENELUX tracer concentration can both be explained by climate shifts in European flow regime, following ACRWB. The climate shift seen is an easterly shift, which is consistent with the eastward shift seen for both ACRWB and CRWB by Barnes and Hartmann (2012). It is a robust feature of climate models that an eastward shift of the EDJ into Europe is identified and this is most likely due to changes in the AMOC (Peings and Magnusdottir, 2014; Brayshaw et al., 2009). This shift is the driving mechanism for the eastward shift of ACRWB in the northeast Atlantic/ European region. With an eastward shift of the EDJ into Europe, comes an eastward extension of the North Atlantic storm track. Chapter 2 highlighted that the storm track is associated with increased wind speeds and precipitation, which both reduced surface [PM10]. The increased storminess throughout Europe may in part explain the increased precipitation rates that are likely to have facilitated the negative climate shifts in tracer lifetime for all tracers.

7.8 Do RWB Events Change in a Changing Climate? (Conclusion)

The primary aim of this study was to determine whether UK [PM10] episodes would change (in frequency or dynamically) in a future climate, representative of 2050, following the

RCP8.5 emission scenario. Chapter 7 has shown that the frequency of all RWB subsets are projected to decrease in HADGEM3-GA4, in a future climate. It was found that both ACRWB and CRWB events decrease within a region that their occurrence results in significantly raised modelled UK $\overline{[PM10]}$, a result consistent with the work of Barnes and Hartmann (2012). The implication of this result is that in a future climate, synoptic meteorology will be less conducive to PM10 accumulation within the UK. Consequently this study suggests that a reduction of UK [PM10] episodes will be seen within a future climate.

Resulting from northeast Atlantic/ European ACRWB events, this study has found a reduction in the accumulation of locally sourced PM10 and an increased advection of near-continental PM10 from the BENELUX region. Spatial climate shifts in the average region of an ACRWB event in a future climate was attributed to this change. This study has found that ACRWB occurs further northward and eastwards in a future climate, with the eastward shift mostly responsible for the increased/decreased BENELUX/locally sourced tracer accumulation, following ACRWB events.

This study also examined the spatial climate shifts in the region of CRWB occurrence. We have found that CRWB experiences an eastward shift, however unlike ACRWB, this is not accompanied by a northward shift. These results are consistent with Barnes and Hartmann et al. (2012). This study does not explore the changing flow regimes in a future climate, resulting from a climatic spatial shift of CRWB occurrence. Despite this, one might infer that eastward shifted northeast Atlantic/ European CRWB events, which are predominantly explained by Omega block events may be associated with an increased European PM10 advection prior to a reduced locally sourced PM10 accumulation.

This study explored the climate shifts in tracer lifetime and found that climate shifts in tracer lifetime could not explain all of the modelled climate shifts in tracer concentration. The reduction of locally sourced tracer concentration, following ACRWB, was consistent with a reduced tracer lifetime, most likely due to increases in wet deposition rates in a future climate. All modelled tracers experienced reduced lifetimes, which for the BENELUX tracer, opposes the sign of the BENELUX concentration climate shift. It is therefore highly likely that climate shifts in flow regimes, following ACRWB, result in this modelled climate shift in BENELUX tracer concentration.

Chapter 8 - Conclusions and Discussion

This study was proposed to identify the relationships between UK pollution, synoptic meteorology and climate change. Relationships between all of the three aforementioned aspects have been found. Chapter 8 will initially detail the relationships found in this thesis. In Sect. 8.10, future work is suggested that will both, aid in the understanding of the relationships found in this study and advance the research so that further research questions can be answered. Finally, Sect. 8.11 explores the impact of this work. Much of the impact of this work is related to the climatic shifts found in Chapter 7 and these form the basis of this section.

The primary research question in this study is:

"Do UK PM10 episodes change in a future climate that is influenced by anthropogenic climate change?"

To answer this question, a number of results chapters have been included within this study, which incrementally act to answer this primary research question in Chapter 7.

8.1 Relationship between UK PM10 and RWB

This study's first aim was to determine the relationship between UK pollution concentrations and synoptic meteorology throughout the Northern hemisphere winter (DJF). The pollutant analysed was PM10, which is one of the pollutants of high interest within the UK (DEFRA, 2016). Primarily, the synoptic meteorology influencing the UK can be described as zonal or blocked flow, with the latter predominantly attributable to RWB in winter months. Atmospheric blocking is well known to be associated with conditions prevalent to the accumulation of tropospheric air pollution and hence it was anticipated that the presence of RWB over a region will result in elevated UK [PM10].

The first significant result within this study was found when relating UK [PM10] to RWB. RWB occurring over the northeast Atlantic/ European region was found to be associated with elevated UK [PM10]. It has been found that RWB has influence in raising UK [PM10] through the blocking or diverting of the EDJ from the UK region. RWB detection over a region was associated with the diversion of the EDJ from that region, which in the case of the UK region, is diverted to the north and/or south.

8.2 Can RWB Significantly Elevate UK $\overline{[PM10]}$?

This study has found that RWB occurring in a constrained northeast Atlantic/ European region resulted in significant increases of UK $\overline{[PM10]}$. Four RWB subsets: cold Anticyclonic, warm Anticyclonic, cold cyclonic and warm cyclonic RWB, were all shown to significantly increase UK [PM10] in this region.

This study has found that CRWB significantly ($p<0.05$) raises UK [PM10] when it occurs within the northeast Atlantic/ European region. This region is separate from the region of most frequent CRWB, situated in the northwest Atlantic region (M13; Weijenborg et al., 2012).

The Omega block mechanism has been found to explain the occurrence of CRWB in the northeast Atlantic/ European region. An Omega block in the northeast Atlantic/ European region requires the precursor of ACRWB to occur in the same region. Webber et al. (2017) showed that 94% of the CRWB events occurring in the northeast Atlantic/ European region, between January 1999 and December 2008, could be explained with an ACRWB precursor.

8.3 Does RWB Result in an Increased Frequency of UK PM10 Episodes?

This study has found all RWB subsets analysed lead to an increased probability of exceeding this study's hazardous PM10 threshold. In this study, continuous RWB events were found to be associated with greater hazardous PM10 exceedance probabilities than instantaneous RWB events for each RWB subset. Continuous RWB events are events that present a persistence of conditions prevalent to the accumulation of UK PM10 and it is therefore unsurprising that these events lead to the greatest hazardous PM10 exceedance probabilities.

The greatest hazardous PM10 exceedance probabilities within Chapter 3 were found to be associated with Omega blocks (0.383). Omega block events have been shown to be almost three times more likely to exceed this study's hazardous PM10 threshold than days where no RWB had occurred (0.129). Northeast Atlantic/ European Omega block events are dependent on the prior occurrence of ACRWB within the same region and hence are associated with an inherent persistence of conditions prevalent to the accumulation of PM10.

8.4 Identifying the Dominant PM10 Source Regions during European RWB events.

Following the identification of a synoptic meteorological mechanism that results in significantly elevated UK [PM10], global climate model studies were undertaken to answer this study's primary research question and some further research questions. The first question to be answered in Chapter 5 is:

"What are the dominant flow regimes influencing the UK throughout UK PM10 episodes?"

Four inert tracers were implemented to identify flow regimes throughout Europe and their UK concentrations were analysed following RWB events. ACRWB events were shown to be most influenced by the locally sourced tracer, however the European advection of tracers was found to be an important component of modelled [PM10].

Omega block events, which this study identified as the most hazardous RWB subset were found to be influenced by multiple flow regimes throughout their development. Throughout Omega block events the UK has been shown to be subject to an initial period of European tracer advection, followed by a prolonged period of locally sourced tracer accumulation. The precursor to an Omega block is the occurrence of ACRWB, which is associated with an anomalous anticyclone over Scandinavia. This Scandinavian anticyclone facilitates an increased advection of European PM10 into the UK. Following this initial European advection, the anomalous Scandinavian anticyclone migrates westwards to a location more central to the UK. The location of the anomalous anticyclone at this stage of the Omega Block (day 0 to day 1 relative to onset) provides conditions that are favourable to the accumulation of locally sourced tracer. This marks a period of stagnation that follows the initial advection of European PM10. It is therefore the initial advection of European PM10, followed by the stagnation of locally sourced PM10 that leads Omega block events to being the most hazardous RWB subset, as identified by Webber et al. (2017).

8.5 Explaining Observed PM10 Variability using Idealized Tracers

The importance of synoptic meteorology in explaining variance in UK Midlands [PM10] has been shown. The tracers implemented in this study's present-day nudged simulation are capable of replicating the relationship between RWB and PM10 found when using observed PM10. Existing literature has shown that synoptic meteorology is important in evaluating variability in observed PM10 datasets (Mcgregor and Bampzelis, 1995; Beaver et al., 2010; Buchholz, et al. 2010). This study reinforces the results from these studies, as we show, in the presence of many idealisations, that the variability in synoptic meteorology is sufficient in capturing the occurrence and frequency of episodic PM10 events. Simplifications of, PM10 source regions, PM chemistry and anthropogenic behavioural patterns, in a modelled [PM10] dataset were attributable to most of the lost variance from the observed PM10 dataset. Despite this lost variance, 42% of the variance within the UK Midlands [PM10] dataset could be explained using modelled tracers.

8.6 Can HADGEM3-GA4 Replicate RWB Climatologies

This study's primary research question is:

"Do UK PM10 episodes change in a future climate that is influenced by anthropogenic climate change?"

To answer this question, a climate model was selected, HADGEM3-GA4. To evaluate future climate shifts in RWB events that lead to UK [PM10] episodes, a model evaluation was undertaken. Model biases in RWB events can exist in the frequency or in the resulting flow regimes of RWB events.

HADGEM3-GA4 has been shown to present substantial RWB frequency biases throughout a region that RWB is significantly influential to UK [PM10]. This study has found that two-fold decreases in free-running RWB frequency can be seen throughout the south-western extent of the region where ACRWB significantly raises UK $\overline{[PM10]}$.

Negative RWB frequency biases within a region that significantly increases UK $\overline{[PM10]}$ are identified. The negative RWB frequency model biases are also found to be associated with a north-eastward spatial shift of northeast Atlantic/ European RWB events. Analysis of the probability distribution of EDJ latitude identified that RWB frequency biases were tightly coupled to latitudinal EDJ biases. A southward shifted EDJ, especially between 35^{o}N and 47^{o}N favours the cyclonic breaking of Rossby waves in the northeast Atlantic/ European region. Masato et al. (2016) found a similar overestimation of the EDJ to reside in its southern state, in HADGEM3-GA6, a more recent atmosphere-only HADGEM model. Furthermore, results from Woollings and Blackburn (2011) show that the 0.56^{o} equatorward bias of the EDJ, found in this study, is within the range of model biases found for CMIP3 climate models. These results indicate that the model bias in the latitudinal probability distribution of the EDJ, found in this study, is consistent with model biases found within literature.

8.7 Can HADGEM3-GA4 Replicate Observed Flow Regimes, Following ACRWB?

This study analysed the UK concentration of advected tracers to determine the flow regimes that influence the UK throughout ACRWB events. This study has found, like for RWB frequency, model biases exist in the flow regimes that influence the UK, following ACRWB. Significant negative model biases in the two long-range advected European tracers (Po Valley and West Poland), following ACRWB events, were found. The significant model biases were attributed to the increased sensitivity of long-range tracer advection into the UK to the location of ACRWB throughout Europe.

Such a result suggests that extreme care must be taken when using climate model output as input to offline chemistry transport models, a common practice to assess the impact of climate change on local air quality (He et al., 2016; Markakis et al., 2016; Lacressonnière et al., 2017).

Despite significant model biases in the advection of two long-range advected tracers, two tracers that are emitted more locally to the UK do not experience significant model biases. The locally sourced and BENELUX tracers exhibit no significant or even likely model biases in their accumulated UK concentration, following ACRWB events.

8.8 Do RWB Events Reduce in Frequency in a Future Climate?

Throughout much of the northeast Atlantic/ European region, negative climate shifts in RWB frequency are identified. Negative climate shifts of the order of a half the free-running RWB frequency are seen in the time-slice simulation throughout the southwestern extent of the free-running region of ACRWB influence, illustrated in Fig. 7.1 (b).

Most of the RWB reductions throughout the southwestern extent of the free-running region of influence are attributed to spatial shifts throughout the northeast Atlantic/ European region. This study finds differing climate RWB frequency spatial shifts for ACRWB and CRWB, which are in agreement with Barnes and Hartmann (2012). ACRWB was found to shift both poleward and eastward throughout the northeast Atlantic/ European region. CRWB was found to experience an eastward shift, with no poleward shift in CRWB frequency. The eastward shift in RWB frequency is associated with an eastward extension of the mid-latitude storm track, which is a robust result in multi-model climate studies (Zappa et al., 2014; Masato et al., 2013). Although the mechanisms for this shift are as yet undetermined within literature, an increase of baroclinicity in the entrance region of the North Atlantic EDJ is often cited as the most likely cause (Peings and Magnusdottir, 2014; Brayshaw et al., 2009). The poleward shift in ACRWB is attributed to a poleward migration of the EDJ, a result that is also found by Barnes and Hartmann (2012). Barnes and Hartmann (2012) indicate that the CRWB critical line, where CRWB occurs, disappears towards the pole in a future climate. It is for this reason that no such poleward shift in CRWB is observed.

8.9 Are RWB Events Dynamically Different in a Future Climate?

This study has identified two significant climate shifts in tracer concentration in a future warmer climate. A significant reduction in locally sourced tracer accumulation alongside a significant increase in advected BENELUX tracer was identified, following northeast

Atlantic/ European ACRWB. Consequently, following northeast Atlantic/ European RWB events, a significant shift in flow regimes is projected by this study.

This study is the first of its kind to identify a significant flow regime shift in a future warmer climate. The simplified inert tracer framework has allowed us to identify significant shifts in flow regime, which is independent of atmospheric chemistry and PM10 source heterogeneity. If added complexity and subsequently added variability were added to the experimental design in this study, it would be unlikely that a significant shift in flow regime could be extrapolated from the climate model simulations.

The dominant mechanism driving the significant shift in flow regimes influencing the UK following northeast Atlantic/ European ACRWB events has also been identified. An eastward shift in the location of mean ACRWB events within the northeast Atlantic/ European region results in RWB occurring in a location that enhances the advection of BENELUX tracer and reduces the accumulation of locally sourced tracer.

8.10 Suggested Future Work

In this section, improvements to the study framework have been suggested. These are aimed at reducing the noise, when calculating climate shifts in Eq. 7.5, consequently increasing the signal to noise ratio. The motivation for increasing the signal to noise ratio in a climate study is the ability to identify smaller climate shifts without being masked by excessive noise.

The most disappointing outcome of this study has been the need to neglect the Po Valley and West Poland tracers in the analysis of climate shifts. The decision was made, due to the sizeable model biases that exist in the concentrations of both of these tracers (See Sect. 6.4.3). The primary explanation for the inability of HADGEM3-GA4 to replicate the accumulation of the Po Valley and West Poland tracers within the UK, was the sensitivity associated with the long-range advection of these tracers. It is the increased sensitivity of long-range advected European tracers to the synoptic flow regime that results in large tracer concentration model biases. This result offers a warning to other studies who use more locally defined source regions in their analysis of pollutant/tracer advection in climate model studies than those defined in this study.

A methodology has been suggested to reduce the sensitivity of the two long-range advected European tracers to the location of RWB and subsequent synoptic flow regime. The tracer source regions were initally motivated by representing both primary and secondary PM10 emission regions and by representing independent flow regimes influencing the UK. It has been evident throughout this study, that both of the above tracer source dependencies conflict

in their motivation. To accurately model UK Midlands [PM10], a tracer emission map that is representative of a real European PM10 emission map would also require atmospheric chemistry, such as that currently used within the UKCA model. Contrastingly, one could idealise the emission map further, so that each tracer represented an independent flow regime and was not motivated by PM10 source regions. This emission map would worsen the representation of UK Midlands [PM10] using modelled tracers, but would enable the identification of every flow region throughout Europe. An example of the idealised tracer emission map is shown in Fig. 8.1.

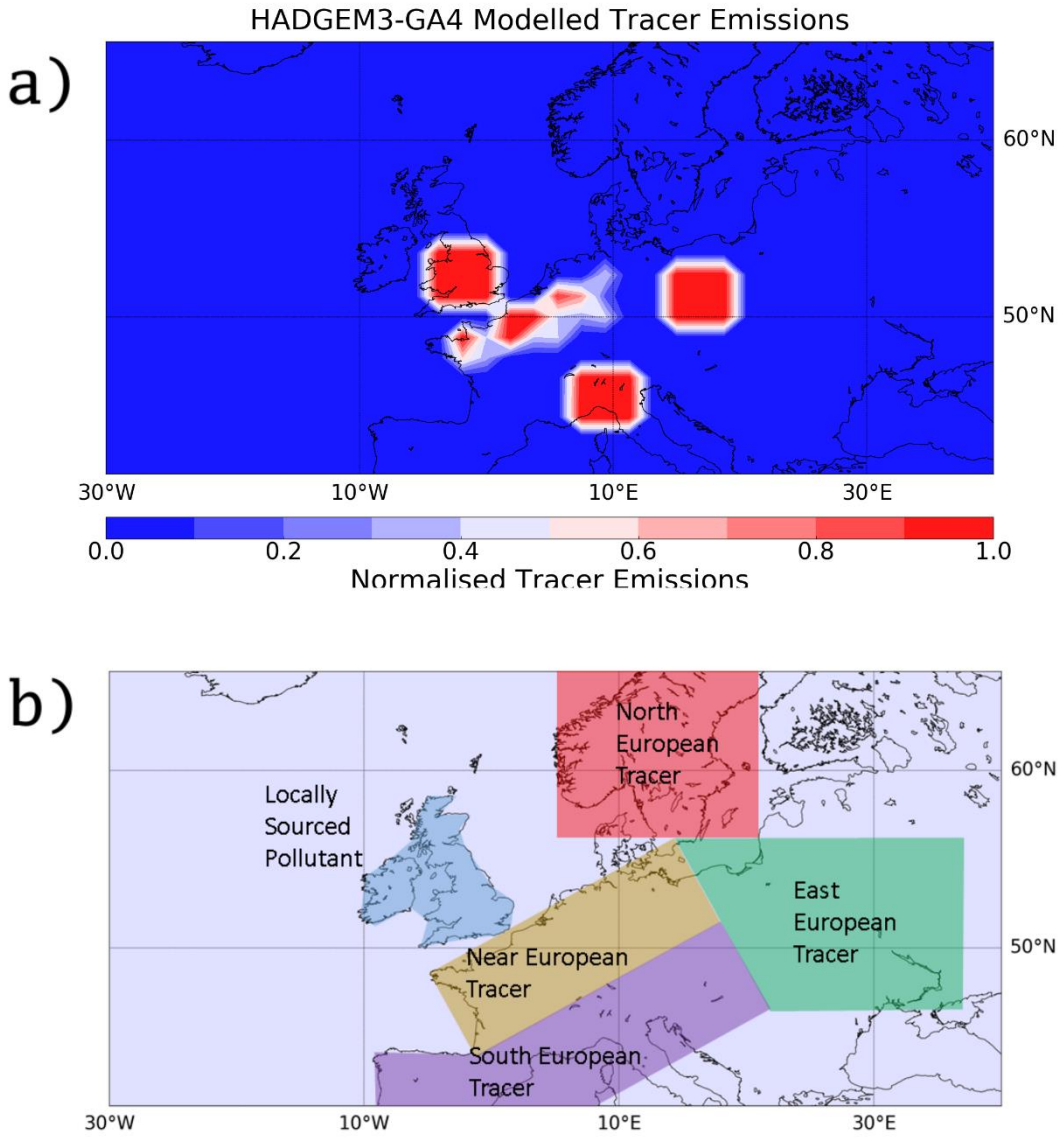

Figure 8.1 (a) This studies modelled tracer emissions (from Fig. 4.2). **(b)** An idealised proposed tracer emission map, with each tracer labelled with its respective location.

Figure 8.1 (b) shows a proposed tracer emission map that is solely motivated by representing flow regimes that influence the UK. In enlarging the regions that the tracers are emitted over, the sensitivity of the tracer advection to the UK will reduce. This should result in the analysis of long-range European tracer, with the uncertainty in model ratio SNR substantially reduced. Furthermore, additional tracers could be added, with the sole intention of identifying flow regimes (e.g. North European Tracer in Fig. 8.1 (b)).

A further issue that is not unique to this study and that effects the SNR for both the model biases and climate increment are the simulation lengths. The HADGEM3-GA4 simulation lengths were selected as 10 years for this study. 10 years provided a sufficient number of ACRWB events, to identify the resultant flow regimes and their significant trends between HADGEM3-GA4 simulations. By increasing the run length of the model simulations, the uncertainty in the tracer concentrations and ACRWB frequency estimations could be reduced. This would increase the SNR values, given that the same signal was detected. Another reason for lengthening the simulations, would be to analyse differences in flow regimes between Omega block events. Unfortunately, due to time constraints in this study, sufficient data was not gathered to analyse northeast Atlantic CRWB events in the same manner that ACRWB events were analysed. In the time-slice simulation there were approximately 7 ACRWB events per single Omega Block event, which is a similar ratio throughout each HADGEM3-GA4 simulation. Consequently, a further 60 years in each HADGEM3-GA4 simulation would be required to evaluate climate shifts in flow regime following northeast Atlantic/ European Omega Block events.

This study is a single model projection of a future climate and perhaps scope for further research is the inclusion of multiple climate models. The inclusion of multiple models would provide a range of climate flow regime shifts. From these estimations, the certainty of the flow regime climate shift seen in this chapter, can be quantitatively determined.

In this study's UK centric focus, air pollution is a major issue. The pollutant analysed in this study is PM10, while tracer characteristics have been given to model a PM2.5 particle. PM2.5 and PM10 remain issues within the UK, especially within urban areas, however other pollutants also pose significant health risks within the UK. A study similar to this could elucidate of the future trends of two priority pollutants throughout the UK: NO_x and O_3. As of 2015 NO_x has been highlighted as the priority pollutant to be reduced within the UK (DEFRA, 2016). NO_x has a shorter lifetime to that of PM10 and as such it is anticipated that local pollutant emissions are most influential to UK NO_x concentration. Based on the results

from this study one could suggest that future UK regional NO_x concentrations would decrease. This study projects a reduction in future locally sourced UK PM10, which would likely be analogous to future UK NO_x concentrations. O_3 has a longer atmospheric lifetime than most PM10 constituents and as such will be subject to longer range transport. This study finds an increase in the transport of European PM10 into the UK, which may suggest an increased transport pathway for O_3 in a future warmer climate. Despite this, there are many confounding factors and degrees of freedom that will affect the future concentration of O_3 within the UK. This author therefore recommends a future study of O_3 concentrations throughout a UK or European domain. A similar tracer study would be sufficient, however for O_3, it is important that atmospheric chemistry be incorporated within the global climate model simulations.

8.11 Application of Results

This study set out to determine whether climate change would influence the frequency or sources contributing to UK PM10 episodes. RWB frequency has been shown in this study and in Barnes and Hartmann (2012), to reduce in a future climate influenced by climate change. With RWB frequency reduced, this suggests that the UK in a future winter climate will experience conditions conducive to the dispersion of UK PM10 on a more frequent basis.

Despite the results from this study indicating that UK air quality may improve following climate change, this author is not suggesting that authorities become more relaxed about the mitigation of greenhouse gasses. Air pollution is but one of a number of potential areas that climate change can effect, with: temperature rise, sea rise, precipitation increase (flash flooding) and tropical storm changes expected consequences of climate change. Furthermore, while climate change can be seen to positively influence UK air quality, the same is unlikely to be said for Central and Eastern Europe, where our study and Barnes and Hartmann (2012) both project future increases of RWB. Increases in RWB indicate an increase of atmospheric blocking and conditions that are favourable for the accumulation of PM10 in these regions. One might suggest an increase of Eastern European pollution would be advected into in Central Europe and Scandinavian regions following northeast Atlantic/ European RWB events, as the most frequent regions of RWB migrate eastward into Europe in a future climate.

It has been shown that climate change can act to improve the UK's air quality through the reduction of northeast Atlantic/ European events and subsequent atmospheric blocking. Despite this, analysis of flow regimes in this study may in some respect contradict this message. It was shown that resulting from an eastward shift of ACRWB in the northeast

Atlantic/ European region, there is an increased tendency for the advection of European PM10 and a reduction in the accumulation of locally sourced pollutant. Consequently, the topics of PM10 source attribution, composition and toxicity must be considered.

In Chapter 1, PM10 components were introduced and their relative toxicity towards humans discussed. It was highlighted in Sect. 1.7.4 how especially accumulation mode PM, are more toxic to human health, due to a small particle size and large particle surface area (Fig. 1.1). Furthermore, accumulation mode PM, as shown in Fig. 1.2 and 1.3 have the lowest dry and wet deposition rates of all PM size categories. Consequently, this hazardous PM component is capable of advecting long distances, due to its increased atmospheric lifetime. In this study it was found that ACRWB in a future climate favours the advection of European PM, more than in the present-day climate. This increased advection facilitates a greater long-range advection of smaller particles from mainland Europe into the UK. Subsequently, the composition of PM within the UK, in a future climate, may become more hazardous to human health.

The conclusions of this study indicate that, while the frequency of RWB events that significantly raise UK [PM10] will likely decrease, the toxicity of each individual event might increase. Such a conclusion might have large implications on the politics involved with trans-national pollution advection. It must however be emphasised that this study is a single model study, with a single projection of a future climate and while it has been idealised to remove uncertainty in the chemical processes involved with PM10, there remains a need for further analysis. For robust conclusions to be made on changing PM composition within the UK, a multi-model study would be required. From this, an idea of the sensitivity of the climate signals found in this study can be gauged. Despite this, the climate shift of RWB frequency is one that is also seen in the multi-model CMIP5 study by Barnes and Hartmann (2012). Consequently one might suggest, given the spatially robust result, within a nudged simulation, that the advection of BENELUX tracer increases with easterly shifted RWB and that the eastward shift of ACRWB is robust between CMIP5 models, the climate shift towards enhanced European advection of PM is also a robust signal.

References

Adams, P.J., Seinfeld, J.H., Koch, D.M., 1999. Global concentrations of tropospheric sulfate, nitrate, and ammonium aerosol simulated in a general circulation model. J. Geophys. Res.-Atmos. 104, 13791-13823.

Arakawa, A., 1966. Computational design for long-term numerical integration of the equations of fluid motion: Two-dimensional incompressible flow. Part I., J. Comput. Phys., 1, no 1, 119-143.

Altenhoff, A.M., Martius, O., Croci-Maspoli, M.I., Schwierz, C., Davies, H.C., 2008. Linkage of atmospheric blocks and synoptic-scale Rossby waves: a climatological analysis. Tellus A, 60, no 5, 1053-1063.

Andronache, C., 2003. Estimated variability of below-cloud aerosol removal by rainfall for observed aerosol size distributions. Atmos. Chem. Phys. 3, 131-143.

Anstey, J.A., Davini, P., Gray, L.J., Woollings, T.J., Butchart, N., Cagnazzo, C., Christiansen, B., Hardiman, S.C., Osprey, S.M., Yang, S.T., 2013. Multi-model analysis of Northern Hemisphere winter blocking: Model biases and the role of resolution. J. Geophys. Res.-Atmos. 118, 3956-3971.

Atkinson, B., Meso-scale atmospheric circulations. Academic Press, Chap. 1, 1989.

Barmpadimos, I., Keller, J., Oderbolz, D., Hueglin, C., Prevot, A.S.H., 2012. One decade of parallel fine (PM2.5) and coarse (PM10-PM2.5) particulate matter measurements in Europe: trends and variability. Atmos. Chem. Phys. 12, 3189-3203.

Barnes, E.A., Hartmann, D.L., 2012. Detection of Rossby wave breaking and its response to shifts of the midlatitude jet with climate change. J. Geophys. Res.-Atmos. 117, no. D9.

Barnes, E.A., Polvani, L., 2013. Response of the Midlatitude Jets, and of Their Variability, to Increased Greenhouse Gases in the CMIP5 Models. J. Climate 26, 7117-7135.

Beaver, S., Palazoglu, A., Singh, A., Soong, S.T., Tanrikulu, S., 2010. Identification of weather patterns impacting 24-h average fine particulate matter pollution. Atmos. Environ. 44, 1761-1771.

Beelen, R., Raaschou-Nielsen, O., Stafoggia, M., Andersen, Z.J., Weinmayr, G., Hoffmann, B., Wolf, K., Samoli, E., Fischer, P., Nieuwenhuijsen, M., Vineis, P., Xun, W.W., Katsouyanni, K., Dimakopoulou, K., Oudin, A., Forsberg, B., Modig, L., Havulinna, A.S., Lanki, T.,

Turunen, A., Oftedal, B., Nystad, W., Nafstad, P., De Faire, U., Pedersen, N.L., Ostenson, C.G., Fratiglioni, L., Penell, J., Korek, M., Pershagen, G., Eriksen, K.T., Overvad, K., Ellermann, T., Eeftens, M., Peeters, P.H., Meliefste, K., Wang, M., Bueno-de-Mesquita, B., Sugiri, D., Kramer, U., Heinrich, J., de Hoogh, K., Key, T., Peters, A., Hampel, R., Concin, H., Nagel, G., Ineichen, A., Schaffner, E., Probst-Hensch, N., Kunzli, N., Schindler, C., Schikowski, T., Adam, M., Phuleria, H., Vilier, A., Clavel-Chapelon, F., Declercq, C., Grioni, S., Krogh, V., Tsai, M.Y., Ricceri, F., Sacerdote, C., Galassi, C., Migliore, E., Ranzi, A., Cesaroni, G., Badaloni, C., Forastiere, F., Tamayo, I., Amiano, P., Dorronsoro, M., Katsoulis, M., Trichopoulou, A., Brunekreef, B., Hoek, G., 2014. Effects of long-term exposure to air pollution on natural-cause mortality: an analysis of 22 European cohorts within the multicentre ESCAPE project. Lancet 383, 785-795.

Berrisford, P., Hoskins, B.J., Tyrlis, E., 2007. Blocking and Rossby wave breaking on the dynamical tropopause in the Southern Hemisphere. J. Atmos. Sci. 64, 2881-2898.

Bethan, S., Vaughan, G., Reid, S.J., 1996. A comparison of ozone and thermal tropopause heights and the impact of tropopause definition on quantifying the ozone content of the troposphere. Q. J. Roy. Meteor. Soc. 122, 929-944.

Bigi, A., Ghermandi, G., Harrison, R.M., 2012. Analysis of the air pollution climate at a background site in the Po valley. J. Environ. Monitor. 14, 552-563.

Bjerknes, J., Palmen, E., 1937. Investigation of Selected European Cyclones by Means of Serial Ascent. Am. Meteorol. Soc. 12, 62.

Brayshaw, D.J., Hoskins, B.J. Blackburn, M., 2008. The storm-track response to idealized SST perturbations in an aquaplanet GCM. J. Atmos. Sci., 65, no. 9, 2842-2860.

Brayshaw, D.J., Woollings, T., Vellinga, M., 2009. Tropical and Extratropical Responses of the North Atlantic Atmospheric Circulation to a Sustained Weakening of the MOC. J. Climate 22, 3146-3155.

Brill, K.F., Uccellini, L.W., Manobianco, J., Kocin, P.J., Homan, J.H., 1991. The Use of Successive Dynamic Initialization by Nudging to Simulate Cyclogenesis during Gale Iop-1. Meteorol. Atmos. Phys. 45, 15-40.

Brook, R.D., Rajagopalan, S., Pope, C.A., Brook, J.R., Bhatnagar, A., Diez-Roux, A.V., Holguin, F., Hong, Y.L., Luepker, R.V., Mittleman, M.A., Peters, A., Siscovick, D., Smith, S.C., Whitsel, L., Kaufman, J.D., Epidemiol, A.H.A.C., Dis, C.K.C., Metab, C.N.P.A., 2010. Particulate

Matter Air Pollution and Cardiovascular Disease An Update to the Scientific Statement From the American Heart Association. Circulation 121, 2331-2378.

Buchholz, S., Junk, J., Krein, A., Heinemann, G., Hoffmann, L., 2010. Air pollution characteristics associated with mesoscale atmospheric patterns in northwest continental Europe. Atmos. Environ. 44, 5183-5190.

Cattiaux, J., Vautard, R., Cassou, C., Yiou, P., Masson-Delmotte, V., Codron, F., 2010. Winter 2010 in Europe: A cold extreme in a warming climate. Geophys. Res. Lett. 37.

Chagnon, J.M., Gray, S.L., Methven, J., 2013. Diabatic processes modifying potential vorticity in a North Atlantic cyclone. Q. J. Roy. Meteor. Soc. 139, 1270-1282.

Charney, J.G., Devore, J.G., 1979. Multiple Flow Equilibria in the Atmosphere and Blocking. J. Atmos. Sci. 36, 1205-1216.

Charron, A., Degrendele, C., Laongsri, B., Harrison, R.M., 2013. Receptor modelling of secondary and carbonaceous particulate matter at a southern UK site. Atmos. Chem. Phys. 13, 1879-1894.

Chemke, R., Kaspi, Y., 2015. The Latitudinal Dependence of Atmospheric Jet Scales and Macroturbulent Energy Cascades. J. Atmos. Sci. 72, 3891-3907.

Council of the European Union and Parliament of the European Union, 2008. Ambient air quality and cleaner air for Europe, 2008/50/EC, European Parliament and the Council of 21 May 2008.

Dee, D.P., Uppala, S.M., Simmons, A.J., Berrisford, P., Poli, P., Kobayashi, S., Andrae, U., Balmaseda, M.A., Balsamo, G., Bauer, P., Bechtold, P., Beljaars, A.C.M., van de Berg, L., Bidlot, J., Bormann, N., Delsol, C., Dragani, R., Fuentes, M., Geer, A.J., Haimberger, L., Healy, S.B., Hersbach, H., Holm, E.V., Isaksen, L., Kallberg, P., Kohler, M., Matricardi, M., McNally, A.P., Monge-Sanz, B.M., Morcrette, J.J., Park, B.K., Peubey, C., de Rosnay, P., Tavolato, C., Thepaut, J.N., Vitart, F., 2011. The ERA-Interim reanalysis: configuration and performance of the data assimilation system. Q. J. Roy. Meteor. Soc. 137, 553-597.

DEFRA: Department for Environment, Farming and Rural Affairs 2014a. UK-air.defra.gov.UK/data/data_selector. [Accessed October 2013].

DEFRA: Department for Environment, Farming and Rural Affairs 2014b. UK-air.defra.gov.UK. [Accessed October 2013].

DEFRA: Department for Environment, Food and Rural Affairs in partnership with the Scottish Executive, Welsh Assembly Government and Department of the Environment Northern Ireland (2016) 'Air Pollution in the UK 2015' Available at https://uk-air.defra.gov.uk/library/annualreport/viewonline?year=2015_issue_1&jump=tp [Accessed September 2016].

Eder, B.K., Davis, J.M., Bloomfield, P., 1994. An Automated Classification Scheme Designed to Better Elucidate the Dependence of Ozone on Meteorology. J. Appl. Meteorol. 33, 1182-1199.

EEA, 2016, European Union emission inventory report 1990–2014 under the UNECE Convention on Long-range Transboundary Air Pollution (LRTAP), EEA Report No 16/2016, European Environment Agency.

Eichelberger, S.J., Hartmann, D.L., 2007. Zonal jet structure and the leading mode of variability. J. Clim., 20, no 20, 5149-5163.

Ertel, H., 1942. Ein neuer hydrodynamischer Wirbelsatz. Meteorol. Z. 59, 277-281.

Flandrin, P., Goncalves, P., Rilling, G., 2005. EMD equivalent filter banks, from interpretation to applications. Interd. Math. Sci. 5, 57-74.

Franzke, C., Woollings, T., Martius, O., 2011. Persistent Circulation Regimes and Preferred Regime Transitions in the North Atlantic. J. Atmos. Sci. 68, 2809-2825.

Gabriel, A., Peters, D., 2008. A Diagnostic Study of Different Types of Rossby Wave Breaking Events in the Northern Extratropics. J. Meteorol. Soc. Jpn., 86, 613-631.

Gehring, U., Gruzieva, O., Agius, R.M., Beelen, R., Custovic, A., Cyrys, J., Eeftens, M., Flexeder, C., Fuertes, E., Heinrich, J., Hoffmann, B., de Jongste, J.C., Kerkhof, M., Klumper, C., Korek, M., Molter, A., Schultz, E.S., Simpson, A., Sugiri, D., Svartengren, M., von Berg, A., Wijga, A.H., Pershagen, G., Brunekreef, B., 2013. Air Pollution Exposure and Lung Function in Children: The ESCAPE Project. Environ. Health. Persp. 121, 1357-1364.

Giannakopoulos, C.M., Chipperfield, M.P., Law, K.S., Pyle, J.A., 1999. Validation and intercomparison of wet and dry deposition schemes using 210Pb in a global three-dimensional off-line chemical transport model, J. Geophys. Res., 104(D9), 23761-23784.

Green, D.C., Fuller, G.W., Baker, T., 2009. Development and validation of the volatile correction model for PM10 - An empirical method for adjusting TEOM measurements for their loss of volatile particulate matter. Atmos. Environ. 43, 2132-2141.

Harrold, T.W., 1973. Mechanisms influencing the distribution of precipitation within baroclinic disturbances. Quart. J. Roy. Meteor. Soc., 99, 232-251.

Hawkins, E., Maddox, S.J., Merrifield, M.R., 2002. No periodicities in 2dF redshift survey data. Mon. Not. R. Astron. Soc, 336, no. 1, L13-L16.

Haynes, P.H., McIntyre, M.E., 1987. On the evolution of vorticity and potential vorticity in the presence of diabatic heating and frictional or other forces. J. Atmos. Sci., 45, no. 5, 828-841.

Haynes, P.H., 2003. CRITICAL LAYERS, In: Holton, J.R. (Ed.), Encyclopaedia of Atmospheric Sciences. Academic Press, Oxford.

Heal, M.R., Kumar, P., Harrison, R.M., 2012. Particles, air quality, policy and health. Chem. Soc. Rev. 41, 6606-6630.

He, H., Liang, X. Z., Lei, H., Wuebbles, D. J., 2016. Future US ozone projections dependence on regional emissions, climate change, long-range transport and differences in modelling design. Atmos. Env. 128, 124-133.

Heikkila, U., Sandvik, A., Sorteberg, A., 2011. Dynamical downscaling of ERA-40 in complex terrain using the WRF regional climate model. Clim. Dynam. 37, 1551-1564.

Henne, S., Furger, M., Nyeki, S., Steinbacher, M., Neininger, B., de Wekker, S.F.J., Dommen, J., Spichtinger, N., Stohl, A., Prevot, A.S.H., 2004. Quantification of topographic venting of boundary layer air to the free troposphere. Atmos. Chem. Phys. 4, 497-509.

Hicks, B.B., Baldocchi, D.D., Meyers, T.P., Hosker, R.P., Matt, D.R., 1987. A preliminary multiple resistance routine for deriving dry deposition velocities from measured quantities. Water Air Soil Pollut., 36, 311-330.

Hitchman, M. H. and Huesmann, A. S., 2007. A seasonal climatology of Rossby wave breaking in the 320-2000-K layer. J. Atmos. Sci. 64, 1922-1940.

Hoskins, B.J., Mcintyre, M.E., Robertson, A.W., 1985. On the Use and Significance of Isentropic Potential Vorticity Maps. Q. J. Roy. Meteor. Soc. 111, 877-946.

Hoskins, B.J., James, I. N., 2014. Vorticity and the Barotropic Vorticity Equation, Fluid Dynamics of the Mid-Latitude Atmosphere. Wiley-Blackwell, Published Online.

Hu, X.Y., Peng, S.L., Hwang, W.L., 2012. EMD Revisited: A New Understanding of the Envelope and Resolving the Mode-Mixing Problem in AM-FM Signals. IEEE T. Signal Proces. 60, 1075-1086.

Huang, N.E., Shen, Z., Long, S.R., Wu, M.L.C., Shih, H.H., Zheng, Q.N., Yen, N.C., Tung, C.C., Liu, H.H., 1998. The empirical mode decomposition and the Hilbert spectrum for nonlinear and non-stationary time series analysis. P. Roy. Soc. A.-Math. Phy. 454, 903-995.

Illari, L., 1984. A Diagnostic Study of the Potential Vorticity in a Warm Blocking Anticyclone. J. Atmos. Sci. 41, 3518-3526.

IPCC, 2007. Climate Change 2007: The Physical Science Basis. (eds.) Solomon, S., Qin, D., Manning, M., Chen, Z., Marquis, M., Averyt, K., Tignor, M. M. B. and Miller, H. L. Working Group 1 Contribution to the Fourth Assessment Report of the Intergovernmental Panel on Climate Change (IPCC). Technical Summary and Chapter 10 (Global Climate Projections). Cambridge University Press.

Jylha, K., 1999. Relationship between the scavenging coefficient for pollutants in precipitation and the radar reflectivity factor. Part I: Derivation. J. Appl. Meteorol. 38, 1421-1434.

Kappos, A.D., Bruckmann, P., Eikmann, T., Englert, N., Heinrich, U., Hoppe, P., Koch, E., Krause, G.H.M., Kreyling, W.G., Rauchfuss, K., Rombout, P., Schulz-Klemp, V., Thiel, W.R., Wichmann, H.E., 2004. Health effects of particles in ambient air. Int. J. Hyg. Envir. Heal. 207, 399-407.

Katsouyanni, K., Touloumi, G., Samoli, E., Gryparis, A., Le Tertre, A., Monopolis, Y., Rossi, G., Zmirou, D., Ballester, F., Boumghar, A., Anderson, H.R., Wojtyniak, B., Paldy, A., Braunstein, R., Pekkanen, J., Schindler, C., Schwartz, J., 2001. Confounding and effect modification in the short-term effects of ambient particles on total mortality: Results from 29 European cities within the APHEA2 project. Epidemiology 12, 521-531.

Kharin, V.V., Zwiers, F.W., Zhang, X., Wehner, M., 2013. Changes in temperature and precipitation extremes in the CMIP5 ensemble. Climatic Change 119, 345-357.

Kulmala, M. Vehkamäki, H., Petäjä, T., Dal Maso, M., Lauri, A., Kerminen, V.M., Birmili, W., McMurry, P.H., 2004. Formation and growth rates of ultrafine atmospheric particles: a review of observations. J. Atmos. Sci., 35, no. 2, 143-176.

Lacressonnière, G., Watson, L., Gauss, M., Engardt, M., Andersson, C., Beekman, M., Colette, A., Foret, G., Josse, B., Marécal, V., Nyiri, A., 2017. Particulate matter air pollution in Europe in a + 2^{o} C warming world. Atmos. Env. 154, 129-140.

Lejenas, H., Okland, H., 1983. Characteristics of Northern Hemisphere Blocking as Determined from a Long-Time Series of Observational Data. Tellus A 35, 350-362.

Liao, K.J., Tagaris, E., Manomaiphiboon, K., Napelenok, S.L., Woo, J.H., He, S., Amar, P., Russell, A.G., 2007. Sensitivities of ozone and fine particulate matter formation to emissions under the impact of potential future climate change. Environ. Sci. Technol. 41, 8355-8361.

Lorenz, D.J., Hartmann, D.L., 2001. Eddy-zonal flow feedback in the Southern Hemisphere. J. Atmos. Sci. 58, 3312-3327.

Lushnikov, A.A., 2009. Introduction to aerosols, in Aerosols – Science and Technology. Edited by Igor Agranovski, Wiley-VCH Verlag GmbH & Co, KGaA, Weinheim, Germany.

Malcolm, A.L., Derwent, R.G., Maryon, R.H., 2000. Modelling the long-range transport of secondary PM10 to the UK. Atmos. Environ. 34, 881-894.

Mann, G.W., Carslaw, K.S., Spracklen, D.V., Ridley, D.A., Manktelow, P.T., Chipperfield, M.P., Pickering, S.J., Johnson, C.E., 2010. Description and evaluation of GLOMAP-mode: a modal global aerosol microphysics model for the UKCA composition-climate model. Geosci. Model Dev. 3, 519-551.

Marcazzan, G.M., Vaccaro, S., Valli, G., Vecchi, R., 2001. Characterisation of PM10 and PM2.5 particulate matter in the ambient air of Milan (Italy). Atmos. Environ. 35, 4639-4650.

Markakis, K., Valari, M., Engardt, M., Lacressonnière, G., Vautard, R., Andersson, C., 2016. Mid-21st century air quality at the urban scale under the influence of changed climate and emissions-case studies for Paris and Stockholm. Atmos. Chem. And Phy. 16(4), 1877-1894.

Martin, A., Lott, F., 2007. Synoptic responses to mountain gravity waves encountering directional critical levels. J. Atmos. Sci. 64, 828-848.

Martin, J.E., 2013. Mid-latitude atmospheric dynamics: a first course. John Wiley and Sons.

Martius, O., Schwierz, C., Davies, H.C., 2007. Breaking waves at the tropopause in the wintertime Northern Hemisphere: Climatological analyses of the orientation and the theoretical LC1/2 classification. J. Atmos. Sci. 64, 2576-2592.

Masato, G., Hoskins, B.J., Woollings, T., 2013a. Wave-Breaking Characteristics of Northern Hemisphere Winter Blocking: A Two-Dimensional Approach. J. Climate 26, 4535-4549.

Masato, G., Hoskins, B.J., Woollings, T., 2013b. Winter and Summer Northern Hemisphere Blocking in CMIP5 Models. J. Climate 26, 7044-7059.

Masato, G., Hoskins, B.J., Woollings, T.J., 2012. Wave-breaking characteristics of midlatitude blocking. Q. J. Roy. Meteor. Soc. 138, 1285-1296.

Masato, G., Woollings, T., Williams, K.D., Hoskins, B.J., Lee, R.W., 2016. A regime analysis of Atlantic winter jet variability applied to evaluate HadGEM3-GC2. Q. J. Roy. Meteor. Soc. 142, 3162-3170.

Matsueda, M., Mizuta, R., Kusunoki, S., 2009. Future change in wintertime atmospheric blocking simulated using a 20-km-mesh atmospheric global circulation model. J. Geophys. Res.-Atmos. 114, no. D12.

Maxey, M.R., 1987. The gravitational settling of aerosol particles in homogeneous turbulence and random flow fields. J. Fluid Mech. 174, 441-465

Mcgregor, G.R., Bamzelis, D., 1995. Synoptic Typing and Its Application to the Investigation of Weather Air-Pollution Relationships, Birmingham, United-Kingdom. Theor. Appl. Climatol. 51, 223-236.

Morgan, M.C., Nielsen-Gammon, J.W., 1998. Using tropopause maps to diagnose midlatitude weather systems. Mon. Weather Rev. 126, 2555-2579.

Nho-Kim, E.Y., Michou, M., Peuch, V.H., 2004. Parameterization of size-dependent particle dry deposition velocities for global modeling. Atmos. Environ. 38, 1933-1942.

Noll, K.E., Jackson, M.M., Oskouie, A.K., 2001. Development of an atmospheric particle dry deposition model. Aerosol Sci. Tech. 35, 627-636.

Office for National Statistics, 2013. 2011 Census: Characteristics of Built-Up Areas. Government Statistical Service, Available Online at https://www.ons.gov.uk/peoplepopulationandcommunity/housing/articles/characteristicsofbuiltupareas/2013-06-28

Peings, Y., Magnusdottir, G., 2014. Response of the Wintertime Northern Hemisphere Atmospheric Circulation to Current and Projected Arctic Sea Ice Decline: A Numerical Study with CAM5. J. Climate 27, 244-264.

Pelly, J.L., Hoskins, B.J., 2003. A new perspective on blocking. J. Atmos. Sci. 60, 743-755.

Pfahl, S., Schwierz, C., Croci-Maspoli, M., Grams, C.M., Wernli, H., 2015. Importance of latent heat release in ascending air streams for atmospheric blocking. Nat. Geosci. 8, 610-614.

Pope, R.J., Savage, N.H., Chipperfield, M.P., Ordonez, C., Neal, L.S., 2015. The influence of synoptic weather regimes on UK air quality: regional model studies of tropospheric column NO2. Atmos. Chem. Phys. 15, 11201-11215.

Querol, X., Alastuey, A., Ruiz, C.R., Artinano, B., Hansson, H.C., Harrison, R.M., Buringh, E., ten Brink, H.M., Lutz, M., Bruckmann, P., Straehl, P., Schneider, J., 2004. Speciation and origin of PM10 and PM2.5 in selected European cities. Atmos. Environ. 38, 6547-6555.

Randall, D., 2015. An introduction to the global circulation of the atmosphere. Princeton University Press.

Randel, W.J., Held, I.M., 1991. Phase Speed Spectra of Transient Eddy Fluxes and Critical Layer Absorption. J. Atmos. Sci. 48, 688-697.

Reynolds, R.W., Smith, T.M., Liu, C., Chelton, D.B., Casey, K.S., Schlax, M.G., 2007. Daily high-resolution-blended analyses for sea surface temperature. J. Climate 20, 5473-5496.

Rex, D.F., 1950. Blocking action in the middle troposphere and its effect upon regional climate. Tellus A 2, 275-301.

Riahi, K., Rao, S., Krey, V., Cho, C.H., Chirkov, V., Fischer, G., Kindermann, G., Nakicenovic, N., Rafaj, P., 2011. RCP 8.5-A scenario of comparatively high greenhouse gas emissions. Climatic Change 109, 33-57.

Rossby, C.G., 1940. Planetary flow patterns in the atmosphere. Q. J. R. Meteorol. Soc. 66, 68-87

Ryall, D. B., Derwent, R. G., Manning, A. J., Redington, A. L., Corden, J., Millington, W., Simmonds, P. G., O'Doherty, S., Carslaw, N. and Fuller, G. W., 2002. The origin of high particulate concentrations over the United Kingdom, March 2000. Atmos. Env. 36(8), 1363-1378.

Scaife, A.A., Woollings, T., Knight, J., Martin, G., Hinton, T., 2010. Atmospheric Blocking and Mean Biases in Climate Models. J. Climate 23, 6143-6152.

Screen, J.A., Simmonds, I., 2010. The central role of diminishing sea ice in recent Arctic temperature amplification. Nature 464, 1334-1337.

Seinfeld, J.H., Pandis, S.N., 2006. Atmospheric Chemistry and Physics-from Air Pollution to Climate Change. John Wiley & Sons, New Jersey.

Shutts, G.J., 1983. The Propagation of Eddies in Diffluent Jetstreams - Eddy Vorticity Forcing of Blocking Flow-Fields. Q. J. Roy. Meteor. Soc. 109, 737-761.

Singh, P., Joshi, S. D., Patney, R. K., Saha, K, 2015. The Hilbert spectrum and the Energy Preserving Empirical Mode Decomposition. arXiv preprint arXiv:1504.04104.

Slinn, W.G.N., 1982. Predictions for Particle Deposition to Vegetative Canopies. Atmos. Environ. 16, 1785-1794.

Stevenson, D.S., Johnson, C.E., Collins, W.J., Derwent, R.G., 2003. The tropospheric sulphur cycle and the role of volcanic SO(2). Geol. Soc. Spec. Publ. 213, 295-305.

Stoelinga, M.T., 1996. A potential vorticity-based study of the role of diabatic heating and friction in a numerically simulated baroclinic cyclone. Mon. Weather Rev. 124, 849-874.

Stohl, A., Aamaas, B., Amann, M., Baker, L.H., Bellouin, N., Berntsen, T.K., Boucher, O., Cherian, R., Collins, W., Daskalakis, N., Dusinska, M., Eckhardt, S., Fuglestvedt, J.S., Harju, M., Heyes, C., Hodnebrog, O., Hao, J., Im, U., Kanakidou, M., Klimont, Z., Kupiainen, K., Law, K.S., Lund, M.T., Maas, R., MacIntosh, C.R., Myhre, G., Myriokefalitakis, S., Olivie, D., Quaas, J., Quennehen, B., Raut, J.C., Rumbold, S.T., Samset, B.H., Schulz, M., Seland, O., Shine, K.P., Skeie, R.B., Wang, S., Yttri, K.E., Zhu, T., 2015. Evaluating the climate and air quality impacts of short-lived pollutants. Atmos. Chem. Phys. 15, 10529-10566.

Stull, R.B., 2012. An introduction to boundary layer meteorology. Vol. 13, Springer Science and Business Media.

Telford, P.J., Braesicke, P., Morgenstern, O., Pyle, J.A., 2008. Technical Note: Description and assessment of a nudged version of the new dynamics Unified Model. Atmos. Chem. Phys. 8, 1701-1712.

Thomas, J.L., Stutz, J., Lefer, B., Huey, L.G., Toyota, K., Dibb, J.E., von Glasow, R., 2011. Modeling chemistry in and above snow at Summit, Greenland - Part 1: Model description and results. Atmos. Chem. Phys. 11, 4899-4914.

Tibaldi, S. and Molteni, F., 1990. On the operational predictability of blocking. Tellus A 42, 343-365.

Tyrlis, E., Hoskins, B.J., 2008. The morphology of Northern Hemisphere blocking. J. Atmos. Sci. 65, 1653-1665.

Vallis, G.K., 2006. Atmosphere and oceanic fluid dynamics: fundamentals and large-scale circulation. Cambridge University Press.

Waravdekar, N.V.L. and Reynolds, H.Y, 1998. Respiratory defences against infection, Infectious Diseases of the Respiratory Tract. Cambridge University Press, Cambridge, pp. 52-62.

Webber, C. P., Dacre, H. F., Collins, W. J., Masato, G., 2017. The dynamical impact of Rossby wave breaking upon UK PM_{10} concentration. Atmos. Chem. Phys. 17, 867-881.

Weijenborg, C., de Vries, H., Haarsma, R.J., 2012. On the direction of Rossby wave breaking in blocking. Clim. Dynam. 39, 2823-2831.

Wesely, M.L., Hicks, B.B., 1977. Some factors that affect the deposition rates of sulfur dioxide and similar gases on vegetation. JAPCA. 27, 1110-1116.

Wilcox, L.J., Hoskins, B.J., Shine, K.P., 2012. A global blended tropopause based on ERA data. Part I: Climatology. Q. J. Roy. Meteor. Soc. 138, 561-575.

Williams, K.D., Harris, C.M., Bodas-Salcedo, A., Camp, J., Comer, R.E., Copsey, D., Fereday, D., Graham, T., Hill, R., Hinton, T., Hyder, P., Ineson, S., Masato, G., Milton, S.F., Roberts, M.J., Rowell, D.P., Sanchez, C., Shelly, A., Sinha, B., Walters, D.N., West, A., Woollings, T., Xavier, P.K., 2015. The Met Office Global Coupled model 2.0 (GC2) configuration. Geosci. Model Dev. 8, 1509-1524.

Woollings, T., Hoskins, B., Blackburn, M., Berrisford, P., 2008. A new Rossby wave-breaking interpretation of the North Atlantic Oscillation. J. Atmos. Sci. 65, 609-626.

Woollings, T., 2010a. Dynamical influences on European climate: an uncertain future. Philos. T. R. Soc. A 368, 3733-3756.

Woollings, T., Hannachi, A., Hoskins, B., 2010b. Variability of the North Atlantic eddy-driven jet stream. Q. J. Roy. Meteor. Soc. 136, 856-868.

Woollings, T., Blackburn, M., 2012. The North Atlantic Jet Stream under Climate Change and Its Relation to the NAO and EA Patterns. J. Climate 25, 886-902.

Xie, G., Guo, Y.M., Tong, S.L., Ma, L., 2014. Calculate excess mortality during heatwaves using Hilbert-Huang transform algorithm. Bmc. Med. Res. Methodol. 14(1), 35.

Yin, J.X., Harrison, R.M., 2008. Pragmatic mass closure study for PM1.0, PM2.5 and PM10 at roadside, urban background and rural sites. Atmos. Environ. 42, 980-988.

Zappa, G., Shaffrey, L.C., Hodges, K.I., 2013. The Ability of CMIP5 Models to Simulate North Atlantic Extratropical Cyclones. J. Climate 26, 5379-5396.

Zappa, G., Shaffrey, L.C., Hodges, K.I., Sansom, P.G., Stephenson, D.B., 2013. A Multimodel Assessment of Future Projections of North Atlantic and European Extratropical Cyclones in the CMIP5 Climate Models. J. Climate 26, 5846-5862.

Zhou, J., Cui, J.A., Fan, J.L., Liang, J.N., Wang, T.J., 2010. Dry deposition velocity of atmospheric nitrogen in a typical red soil agro-ecosystem in Southeastern China. Environ. Monit. Assess. 167, 105-113.

Appendix A

Implementing a 350 K Threshold in the Calculation of θ-2PVU

Section 2.2.10 highlights the use of a purely dynamical definition of the tropopause in this study. The 2 Potential Vorticity Units (2PVU) surface is identified as the dynamical tropopause.

Wilcox et al. (2012) highlight limitations in using a solely dynamical tropopause definition, such as in this study. At latitudes equatorward of the mid-latitudes, there exist large gradients in the height of the tropopause (z) with respect to latitude (φ) ($\frac{\partial z}{\partial \varphi}$). Throughout a process called tropopause folding, the dynamical tropopause can be diagnosed at two heights, whereby the tropopause overturns in a vertical frame of reference. Vertical overturning events can result in the dynamical tropopause being identified at two heights for a single grid point. In regions with high $\frac{\partial z}{\partial \varphi}$, the consequence of the dynamical tropopause being identified at two heights is that there may be a large vertical distance between the two tropopause heights. Subsequently, as θ-2PVU is being calculated, θ can vary greatly at these two diagnosed tropopause heights.

This study finds spurious grid-points, where θ-2PVU is greatly different from the neighbouring grid points. In this study, to constrain the dynamical tropopause to a single level, a threshold on θ has been imposed. The threshold used, follows the recommendation of Wilcox et al. (2012), of 350 K. Figure 3.1 (a) and (b) show θ on 2-PVU fields when using no threshold and when using a 350 K threshold.

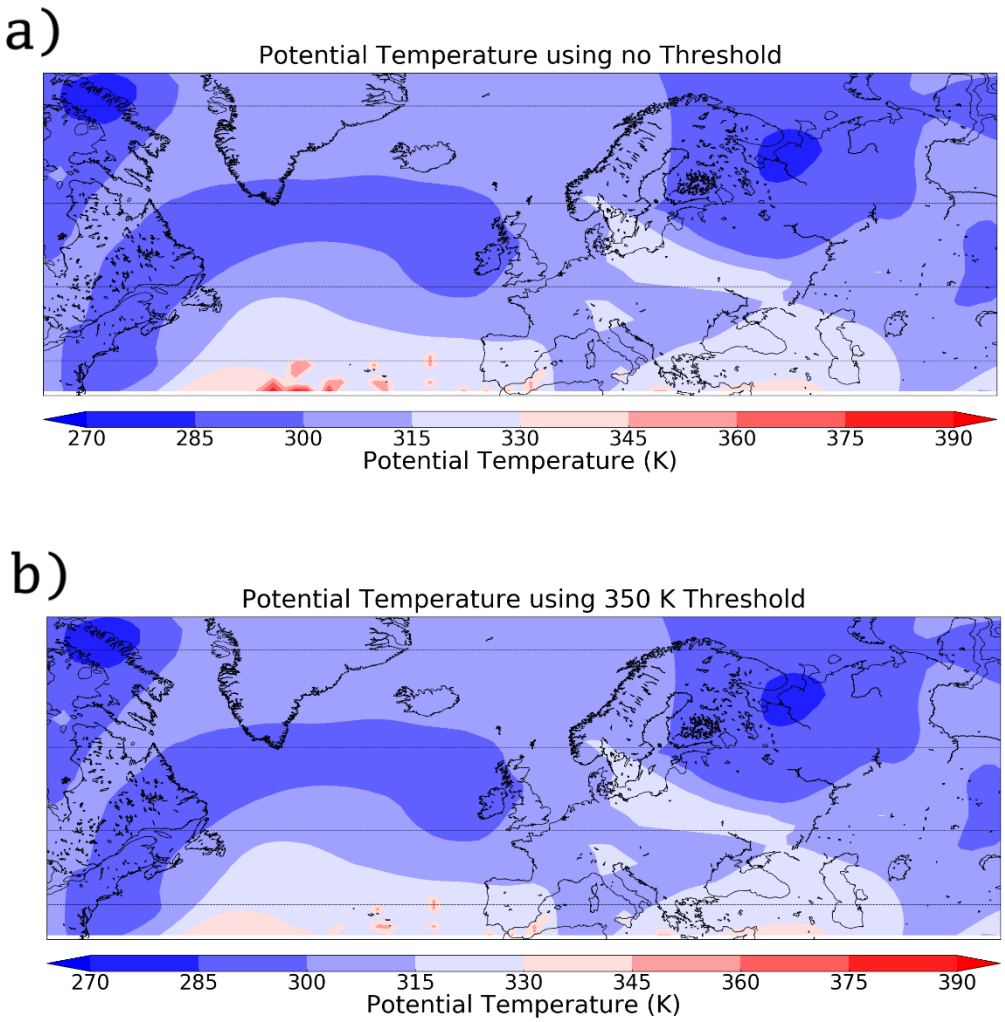

Figure A.1. Potential temperature on the dynamical tropopause (θ-2PVU) surface for a single modelled day, in a present-day nudged HADGEM3-GA4 simulation, see Sect. 4.8.1. **(a)** Corresponds to θ-2PVU, with no filter or threshold applied. **(b)** Corresponds to θ-2PVU with a 350 K maximum threshold placed on the potential temperature field.

Figure A.1 highlights the effect of using a θ threshold, when analysing θ-2PVU fields. In the subtropical region in Figure A.1 (a) spurious grid points of very high θ are visible. These spurious grid points can be attributed to the tropopause folding effect, highlighted in Wilcox et al. 2012.

Figure A.1 (b) shows the same field, with a 350 K threshold imposed. This threshold acts to remove the greatest magnitude spurious grid points from the 2D θ-2PVU field. Despite this, some outliers remain, but these outliers are of a similar magnitude to the remainder of the 2D field. While this projects more clearly onto a 2D plot as in Figure A.1, the remaining spurious points carry far less influence on the calculation of this studies' metrics in Section 2.5.

Appendix B

EMD Analysis (Method)

Empirical mode decomposition (EMD) analysis was chosen to decompose both the observed and modelled PM10 datasets into constituent time series called intrinsic mode functions (IMFs). 10 constituent IMFs were generated, each with the same length as the original time series. To generate the IMFs, a sifting process was undertaken. The sifting process starts by generating a cubic spline that connects each of the peaks and troughs of the original time series. This cubic spine is subtracted from the original time series and the sifting process is repeated on the resultant time series. This process is repeated until the number of time series maxima or minima ($\frac{\partial[PM10]}{\partial t} = 0$) differs from the number of zero crossings by more than 1.

EMD analysis acts as a dyadic filter bank, where a dyadic fraction is a rational number with a denominator to the power of 2 (Eq. B.1). Subsequently the time period of oscillation will halve per subsequent filter bank, as n increases by 1. Therefore the time period of oscillation for each IMF should be approximately double the previous IMF (Huang et al., 1998), leaving the final IMF as the residual of the time series. In Eq. B.1 n represents the corresponding filter bank.

$$\frac{1}{2^n} \qquad Eq.B.1$$

An advantage of using EMD analysis is that the constituent time series account for all of the original time series. The original time series can be reconstituted using Eq. B.2.

$$O = \sum_{i=1}^{n} d_i + r \qquad Eq.B.2$$

Where O is the original time series, d_i represents the ith IMF and r represents the residual or final IMF.

Hu et al. (2012) and Xie et al. (2014), highlighted an issue, which is common when using EMD analysis on noisy data. An intermittent signal or noisy data may result in a phenomenon known as mode mixing. Mode mixing restricts the EMD analysis acting like a dyadic filter. Mode mixing is the result of the EMD analysis not being capable of distinguishing IMFs at periods, as in Eq. B.1. Instead, variance contained within a single IMF, may be placed within neighbouring IMFs, hence creating mode-mixing.

A method of reducing mode-mixing was suggested by Xie et al. (2014), called ensemble EMD (EEMD). EEMD entails adding white noise, with standard deviation 0.1 times that of the original time series, to each of the constituent IMFs. This process is repeated multiple times in an ensemble and each time a new set of IMFs are generated. The white noise added to each IMF, after sufficient ensemble members, should cancel, due to the added white noises zero mean property and subsequently reduce mode-mixing. Equation B.3 shows how white noise is added to the original dataset with amplitude, a, to generate N members of a time series ensemble. The white noise time series is simply a time series of random numbers between 1 and 0.

$$x_i = O + an_i\,, \qquad (i = 1,2,\dots,N) \qquad Eq.B.3$$

Where O is the original [PM10] time series, a is the amplitude applied to the white noise, n_i is a generated white noise time series of the same length as O, x_i is a time series ensemble member and N is the number of ensemble members.

Zheng, et al. (2014) highlighted an issue when using EEMD analysis. Occasionally when using EEMD analysis, the white noise added does not cancel exactly. Complementary EEMD (CEEMD) analysis inputs this noise in positive and negative pairs, therefore ensuring a final cancellation when averaging (Equations B.4 – B.6). The time series with added noise ($x_i^+ \; and \; x_i^-$) are detailed in Equations B.4 and B.5 and individually decomposed into j IMFs (d_{ij}^+ and d_{ij}^-) using EMD. For CEEMD to eliminate white noise from the time series and eliminate mode mixing, N positive and negative noise IMFs are averaged together in Equation B.6, resulting in M IMFs. CCEMD is the method used to analyse the frequencies of variability lost in the modelled [PM10] time series, when compared to the UK Midlands [PM10] time series.

$$x_i^+ = O + an_i\,, \qquad (i = 1,2,\dots,N) \qquad Eq.B.4$$

$$x_i^- = O - an_i\,, \qquad (i = 1,2,\dots,N) \qquad Eq.B.5$$

$$I_j = \frac{1}{2N}\sum_{i=1}^{N}[d_{ij}^+ + d_{ij}^-], \qquad (j = 1,2,\dots,M) \qquad Eq.B.6$$

Once the original time series is decomposed into its constituent frequencies, the energy (variance) contained within each IMF must be extracted. Equation C.7 illustrates the method by which energy is extracted from an IMF using CEEMD, from Xie et al. (2014).

$$E_j = \sum_{k=1}^{n} [I_j(k)]^2, \qquad (k = 1,2, \dots, P) \qquad Eq.B.7$$

Where $I_j(k)$ is the kth element of the jth IMF and P is the total number of elements in the time series.

Figures B.1 and B.2 show the 10 constituent IMFs, which together explain all of the variance from the modelled and UK Midlands [PM10] datasets respectively. The first IMF has the highest frequency in both cases, while the tenth IMF has the lowest frequency and is otherwise referred to as the residual.

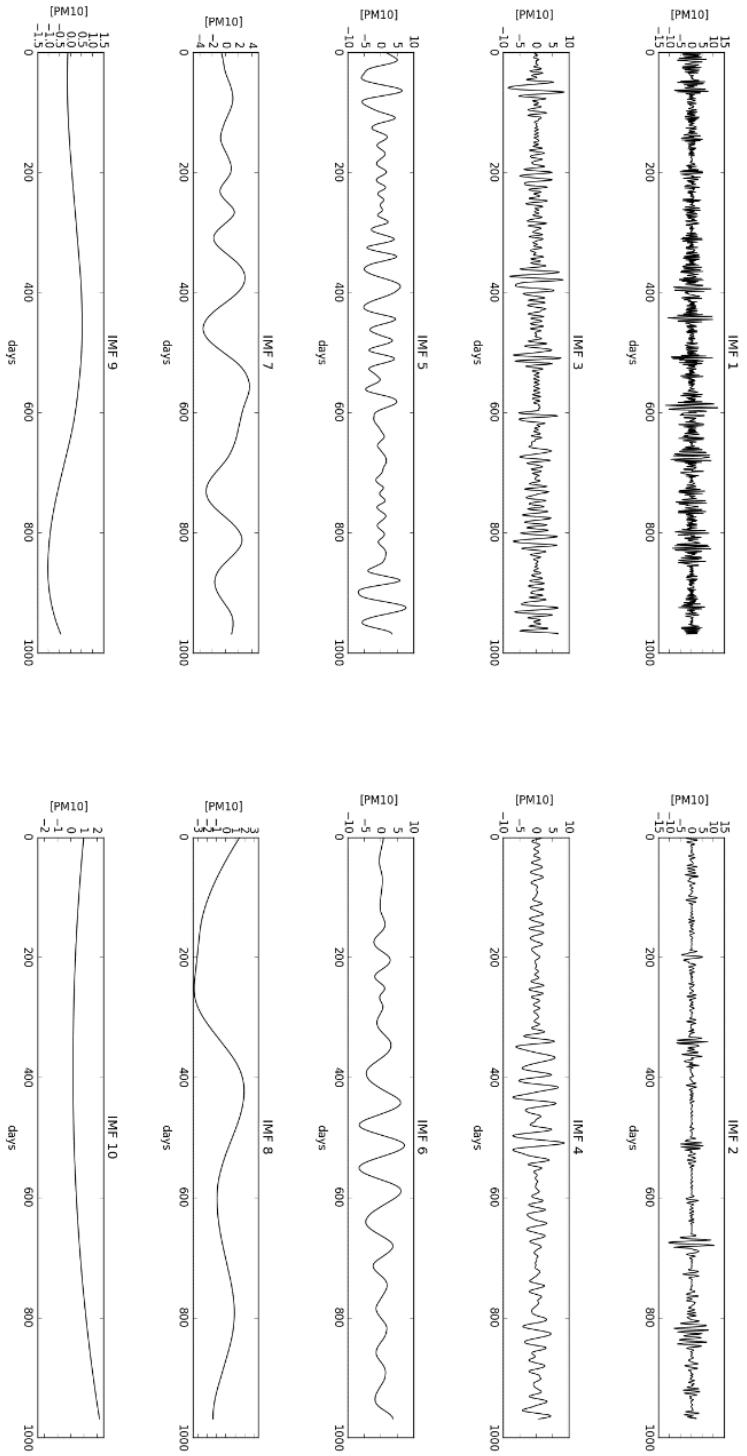

Figure B.1 Intrinsic mode functions following CEEMD analysis on the present-day nudged HADGEM3-GA4 [PM10] dataset. IMF 1-10 are shown, with decreasing Frequencies for increasing IMFs.

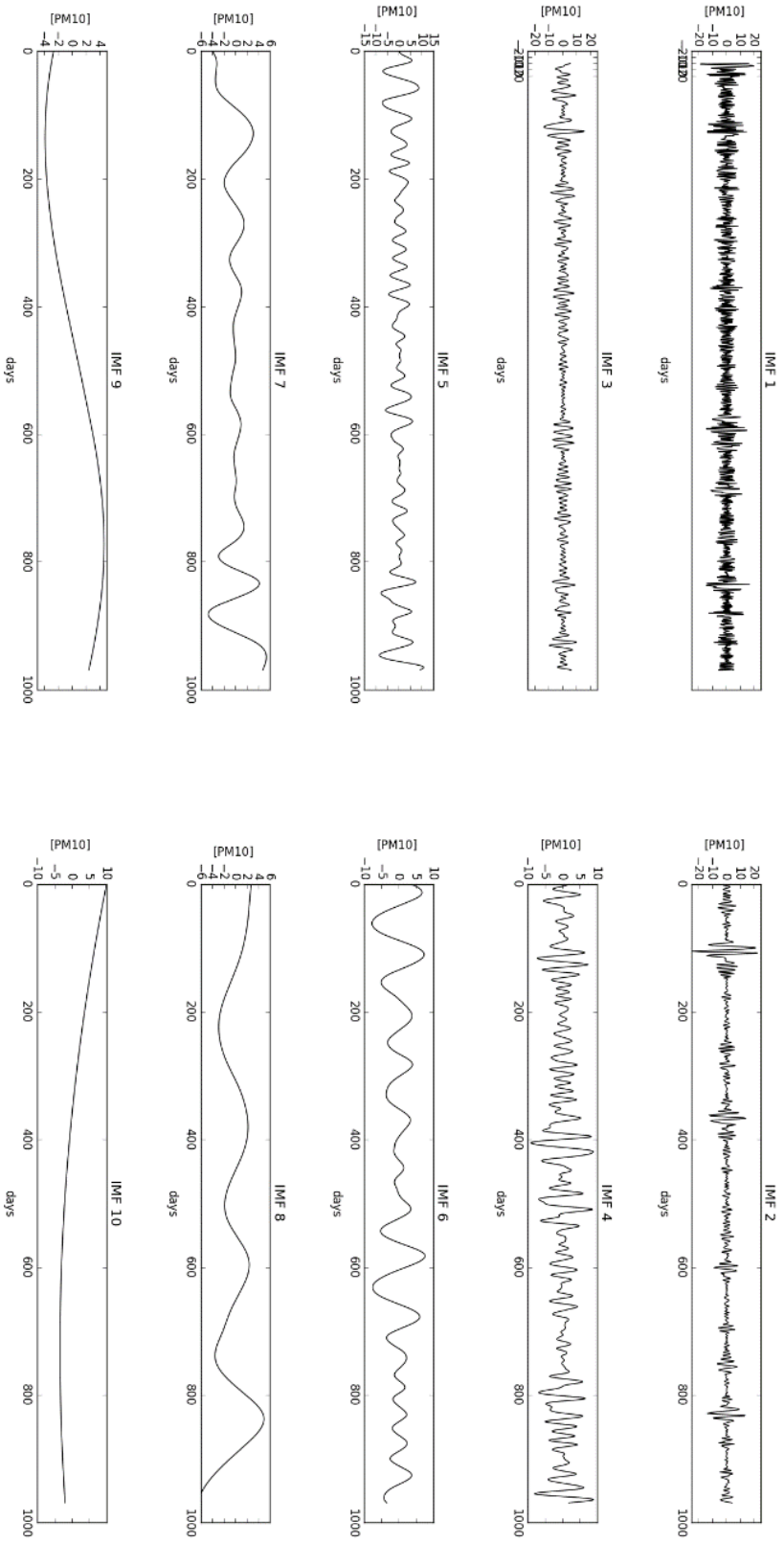

Figure B.2 Intrinsic mode functions following CEEMD analysis on the UK Midlands [PM10] dataset. IMF 1-10 are shown, with decreasing frequencies for increasing IMFs.

All of the above constituent IMFs were tested against the approximated energy (E_j) from white noise for each IMF. This test determines whether there exists more energy in each IMF than a white noise (random) process, i.e. whether there is a trend within the IMF. Flandrin et al. (2005) generated an empirical formula for calculating this white noise energy that was subsequently used in Xie et al. (2014). This formula is detailed in Equation B.8, following the nomenclature used thus far in this section.

$$W_j = \frac{E_1}{0.719} \times 2.01^{-j}, \qquad (j = 2,3, \dots, M) \qquad Eq.B.8$$

Equation B.9 illustrates the method in Xie et al. (2014) to calculate a statistical (p=0.01) upper limit on white noise.

$$W_j(99) = log_2\left(W_j\right) + 2^{0.460j-1.919}, \qquad (j = 1,2, \dots, M) \qquad Eq.B.9$$

For this analysis each IMF is associated with a corresponding W_j and $W_j(99)$ value. The IMF is only considered a 'trend' IMF if its energy is greater than the value obtained by $W_j(99)$ for that IMF.

Appendix C

EMD Analysis (Results)

Figure C.1 shows the results following CEEMD analysis on both the nudged and UK Midlands [PM10] datasets. The frequencies where most observed [PM10] variance is lost in the modelled PM10 time series, are those that show the greatest $log_2(energy)$ discrepancies between the nudged and UK Midlands PM10 time series. It is important to note that both time series analysed using CEEMD analysis are not continuous datasets. Both time series are created by concatenating thirteen 90 day DJF time series together. Subsequently any differences between the observed and modelled time series at time periods greater than ½ the length of each DJF time series (90 days), are considered as inter-annual differences. The solid diagonal line represents W_j for both the nudged and UK Midlands [PM10] datasets, while the dashed line represents$W_j(99)$.

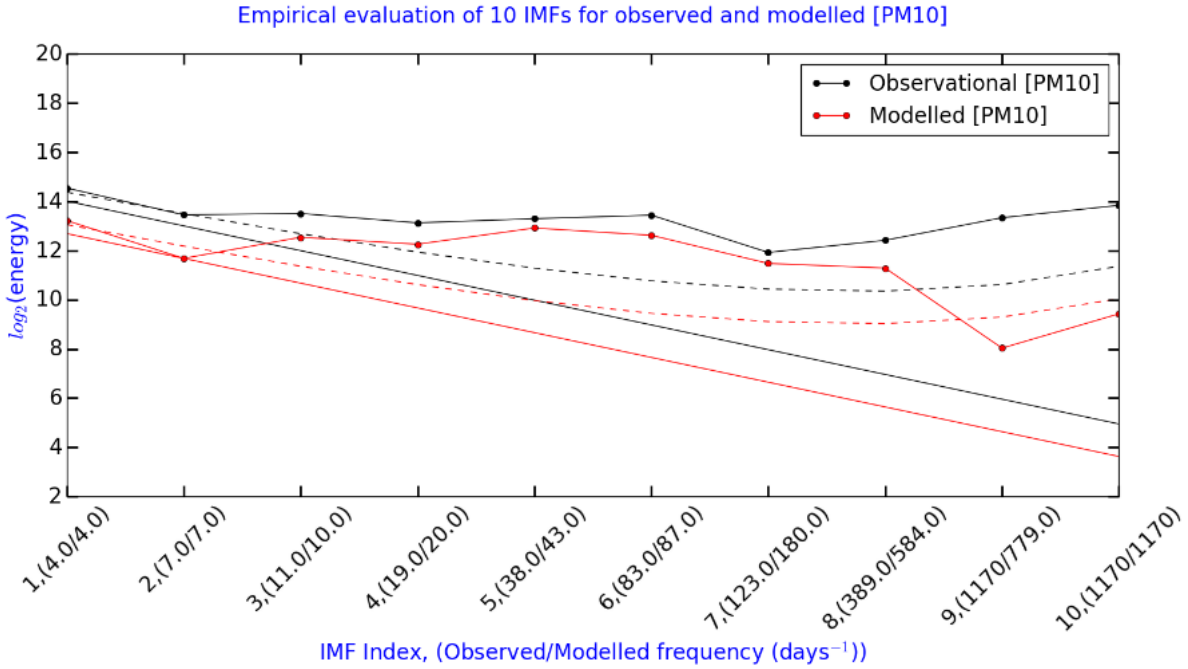

Figure C.1 The variance encapsulated in 10 Intrinsic Mode Functions (IMFs), for the observed and nudged tracer [PM10] datasets (black and red respectively) for Complementary Ensemble Empirical Mode Decomposition analysis. IMF Periods are shown in brackets on the x axis in the form (Observed/ Modelled Period). The black/red solid line represents the variance expected for a white noise process for the observed/ nudged tracer [PM10] datasets respectively. The dashed lines represent the 99th confidence interval for variance expected from the white noise process.

Figure C.1 shows the results from the CEEMD analysis, with IMF energies for 10 IMFs plotted alongside the energy expected from a purely white noise process. Trend IMFs that lie

above or at the $W_j(99)$ dashed line include all of the UK Midlands [PM10] IMFs and IMFs 1, 3, 4, 5, 6, 7 and 8 from the nudged [PM10] dataset. Consequently, it can be said that these IMFs are significantly different from white noise ($p \leq 0.01$). The primary purpose of CEEMD analysis was to identify IMFs that showed the greatest $log_2(energy)$ differences between the UK Midlands and nudged [PM10] datasets. IMFs with the greatest $log_2(energy)$ differences between the UK Midlands and nudged [PM10] datasets highlight frequencies of lost variability.

This author would like to draw the reader to four distinct frequencies of lost variability. The first of these exists at IMFs 7 and 8, with periods of oscillation of 123 days and greater. As stated previously, any lost variance at time periods greater than ½ the length of one winter, is representative of inter-annual lost variance. The second of these is seen at IMFs 9 and IMF 10, the latter representing the residual. Both IMF 9 and 10 from the nudged modelled time series are indistinguishable from white noise, however there exist significant trends in the observational [PM10] IMFs. The third IMF indicating underestimated observed variance in the nudged model is at IMF 2. Again the nudged modelled IMF is indistinguishable from white noise, while the observed IMF is statistically significantly different from white noise. The time period of the lost frequency for IMF 2 is 7 days. Finally IMF 1 also indicates lost frequency within the nudged modelled [PM10] time series.

Appendix D

Model Bias in MSLP Anomalies resulting from northeast Atlantic ACRWB

The purpose of Appendix D is to elucidate on the model bias in the location of the mean ACRWB event, as highlighted in Sect. 6.3.2. Figure 6.2 (a) showed how within the region of influence for ACRWB in the free-running HADGEM3-GA4 simulation, there exists a north-eastward model bias in the location of the mean ACRWB event.

Figure D.1 highlights the north-eastward shift in the location of the mean northeast Atlantic/ European ACRWB event, by comparing the anomalous MSLP plots following northeast Atlantic/ European ACRWB in the nudged and free-running HADGEM3-GA4 simulations. Figure 3.4 (a) shows that the most prominent feature following northeast Atlantic/ European ACRWB, in the ERA-Interim dataset, is an anomalous anticyclone situated over Scandinavia. Following the north-eastward model bias in the location of the mean northeast Atlantic/ European ACRWB event, it is hypothesised that anomalous anticyclone is shifted north-eastward also.

For Fig. D.1, nudged and free-running ACRWB events are both constrained by the free-running ACRWB region of influence. This step ensures that the model bias in RWB frequency within the free-running ACRWB region of influence is best illustrated.

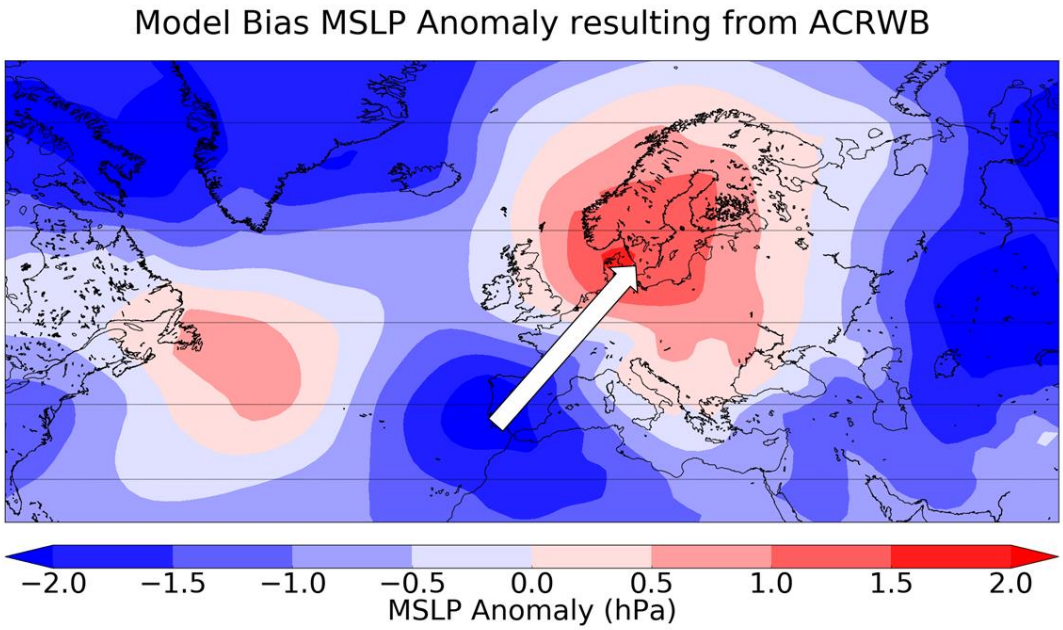

Figure D.1 The model bias in the anomalous MSLP anomaly field (hPa), resulting from northeast Atlantic/ European ACRWB in the nudged and free-running HADGEM3-GA4 simulations. Composite anomaly MSLP fields for the nudged and free-running simulations were generated with a one-day lag following ACRWB detection. The occurrence of both nudged and free-running ACRWB is constrained by the free-running ACRWB region of influence (Fig. 6.5 (a)). The white arrow highlights the observed north-eastward shift in the MSLP anomaly.

Figure D.1 highlights more clearly the north-eastward shift in the location of the mean northeast Atlantic/ European ACRWB event (white arrow). It is shown that in the free-running simulation, ACRWB results in a greater magnitude anomalous Scandinavian anticyclone, while reductions in MSLP anomaly can be seen about the Azores region. The reduction in MSLP anomaly in the Azores is dictated by the north-eastward migration of a negative MSLP anomaly in the free-running simulation. The negative MSLP anomaly, as highlighted in Fig. 2.3 is closely coupled to the location of the positive MSLP anomaly, which Fig. 3.4 (a) found over Scandinavia, following ACRWB events that lead to UK [PM10] exceedances. For clarification, ACRWB events analysed in Fig. D.1 are not required to lead to UK [PM10] exceedances

Appendix E

The latitudinal probability distribution of the EDJ between 0º E and 30º E

Additional analysis was undertaken to analyse the latitudinal variability of the EDJ within a region that Sect. 6.3 find RWB frequency biases within HADGEM3-GA4. Figure E.1 shows the latitudinal probability distribution of the EDJ between 0º E and 30º E, calculated using the same method as for Fig. 6.3.

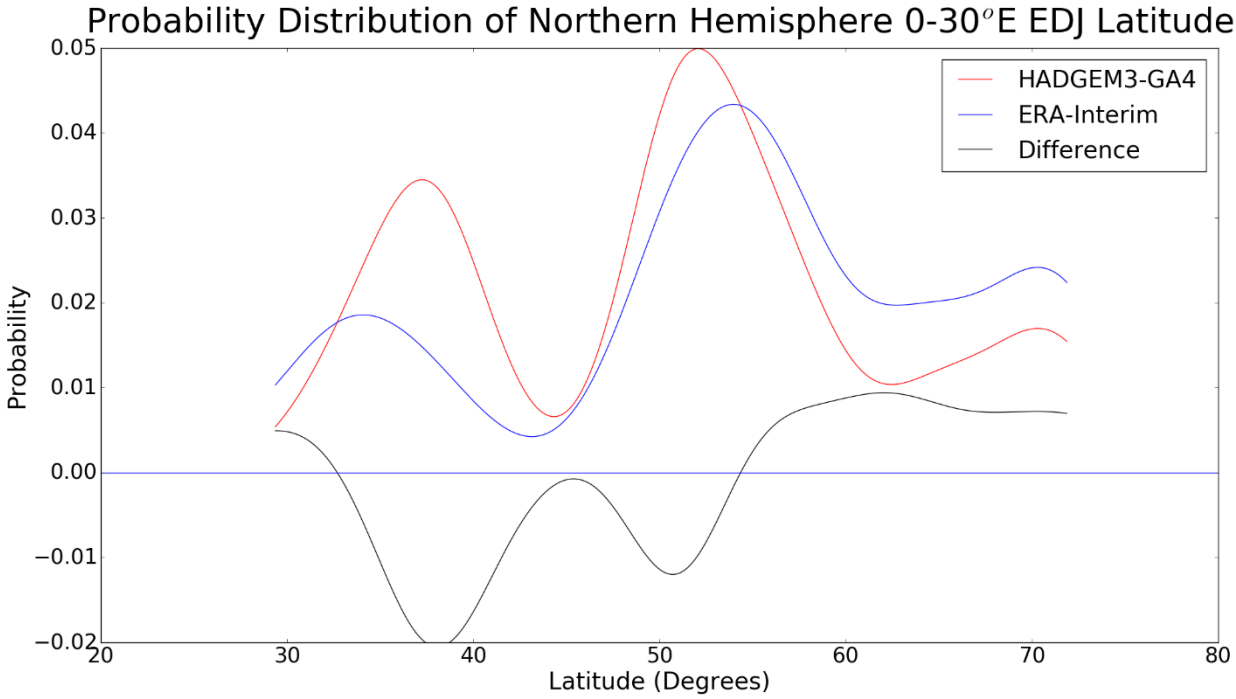

Figure E.1 The probability distribution of Eddy Driven Jet latitude, averaged between 0º E -30º E, in the present-day free-running HADGEM3-GA4 simulation (red) and ERA-Interim dataset (blue). The difference between the two distributions is shown by the black line. Data was obtained from both datasets for winter months (DJF) between January 1999 and December 2008.

Figure E.1 was included in this analysis to evaluate model biases in EDJ variability at a longitude that coincides with the RWB frequency biases in Fig. 6.2. The most important result from Fig. E.1 is that a positive model bias exists in the latitudinal probability distribution of the EDJ between 33ºN and 54ºN. This region coincides with the region of negative RWB frequency model bias seen in Fig. 6.2. This result highlights that the RWB frequency biases are predominantly dictated by mean-state biases in the latitude of the EDJ.

Appendix F

Probability Density Functions (PDFs) for Four Modelled Tracers

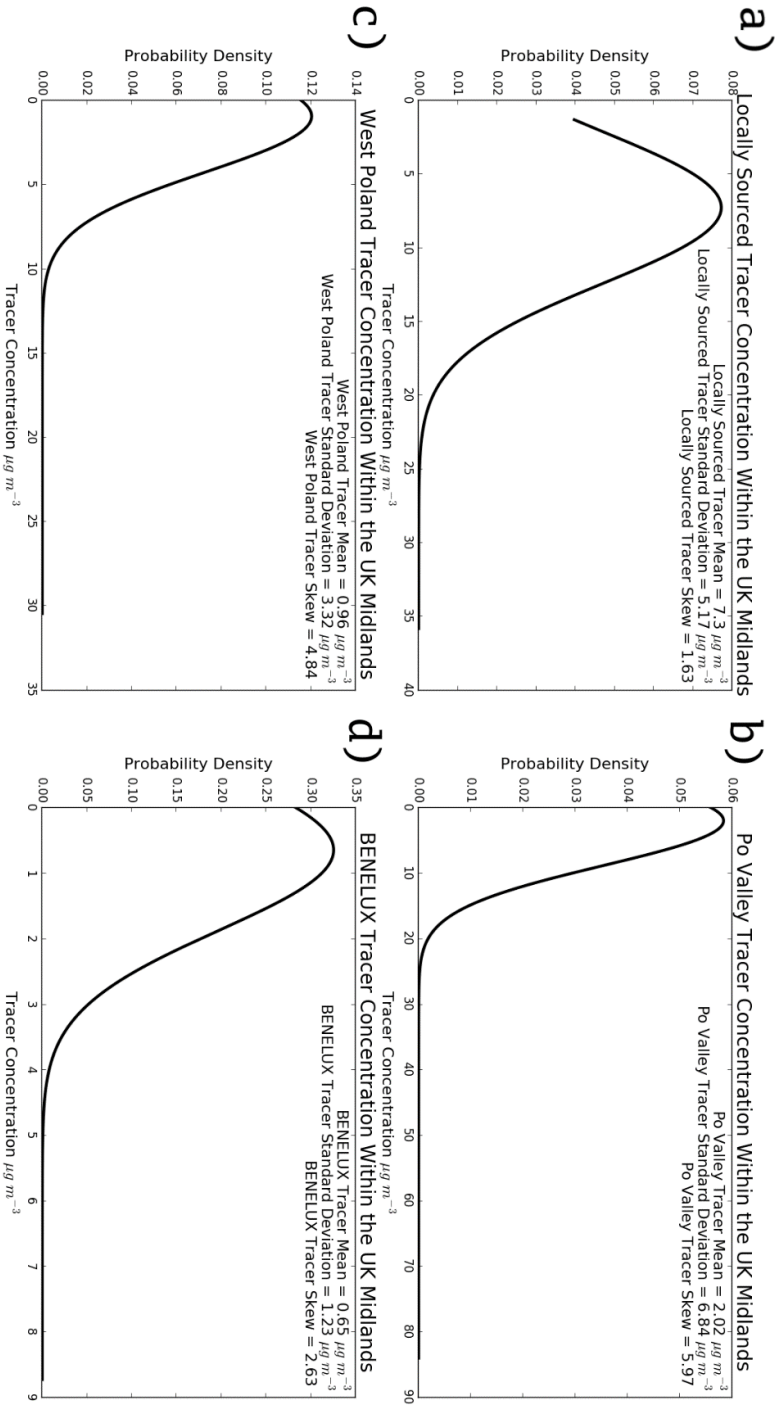

Figure F.1 The probability density functions for the UK concentration of four modelled tracers: **(a)** Locally Sourced Tracer, **(b)** Po Valley Tracer, **(c)** West Poland Tracer and **(d)** BENELUX Tracer. Included within each figure are the mean, standard deviation and Skew for each tracer concentration distribution.

Figure F.1 shows the probability density functions (PDF) of the four tracers emitted within HADGEM3-GA4. A quantitative description of each PDF is included on each figure, with the first (mean), second (variance, presented as the square root of the variance) and third (skew) moments of each distribution presented.

The distributions are included to show the increased variance in the UK concentration of two long-range advected tracers (Po Valley and West Poland tracers). The standard deviation of the Po Valley and West Poland tracers present the greatest percentage of the respective mean UK concentrations in Fig. F.1 (339% and 349% respectively). Consequently, the UK concentrations of these two tracers are highly variable.

The largest values of skew in Fig. F.1 are seen for the Po Valley and West Poland tracers (5.97 and 4.84 respectively). A large positive skew indicates that very occasionally the Po Valley and West Poland tracers are measured at very high UK concentrations. This again highlights the increased variability in the UK concentration of these two tracers. Given specific meteorological conditions, the advection of these two tracers can be optimised and high UK concentrations can be measured. This result highlights the sensitivity of the two long-range European tracers to synoptic flow regime.